Doctoral Dissertation
Doctoral Program in Materials Science and Technology (38th Cycle)

Advanced Porous Materials for Energy Transition: Synthesis and Characterization of Electrocatalysts for Electrochemical Reduction of CO_2 and O_2

By

Mitra Bagherikerachi

******

Supervisors:
Prof. Candido Pirri
Prof. Juqin Zeng
Dr. Adriano Sacco

Doctoral Examination Committee:

Professor Shangfeng Du

Professor Guillermo Díaz-Sainz

Politecnico di Torino
2026

Declaration

I hereby declare that the contents and organization of this dissertation constitute my own original work and do not compromise in any way the rights of third parties, including those relating to the security of personal data.

Mitra Bagherikerachi

October 2026

* This dissertation is presented in partial fulfilment of the requirements for the **Ph.D. degree** in the Graduate School of Politecnico di Torino (ScuDo).

Dedication

I would like to dedicate this thesis to my family.

And to my husband, thank you for standing beside me throughout this journey. Your support, patience, and belief in me carried me through some of the most challenging moments of my PhD.

Acknowledgment

First of all, I would like to express my sincere gratitude to my supervisor, Prof. Juqin Zeng, for giving me the opportunity to carry out this thesis and for her guidance and support throughout my research whenever I needed her. I am also grateful to Adriano Sacco for his assistance in resolving technical issues in the laboratory and for his help with practical aspects of my work. In addition, I would like to thank Professor Candido Pirri for his continuous support of the research group and for providing the resources and environment that made this research possible.

I would also like to thank Professor Shangfeng Du (University of Birmingham) and Professor Guillermo Díaz-Sainz (University of Cantabria) for their critical evaluation of this thesis. Their insightful comments, constructive suggestions, and valuable scientific feedback have helped to improve the clarity, rigor, and overall quality of this work.

I would like to sincerely thank all members of the CSFT@Polito (Center for Sustainable Future Technologies) for their support, and collaboration, especially the technician Denis Perrone and the administrative staff, Lidia Calleri and Sara Perrucci, for their assistance in managing official and organizational matters.

I would also like to express my gratitude to CICECO-Aveiro Institute of Materials, Department of Chemistry, University of Aveiro (Portugal), for hosting me during my six-month secondment. In particular, I thank Mirtha Lourenço and Luís Mafra for their support and collaboration.

Finally, I would like to thank my family and friends for all the support they provided during these years of studies; without whom this work would not have been possible.

Abstract

The growing urgency of climate change and the rising atmospheric concentration of CO_2 have necessitated the development of sustainable energy solutions, positioning the electrochemical CO_2 reduction reaction as a promising route for producing carbon-neutral fuels and value-added chemicals. In parallel, the oxygen reduction reaction is likewise a key process in sustainable energy conversion and storage systems, including fuel cells and metal-air batteries. This dissertation focuses on the rational synthesis and structural tuning of novel electrocatalysts, emphasizing the relationship between material structure, product selectivity, and reaction kinetics within the framework of the sustainable energy transition.

This thesis integrates a range of advanced characterization techniques to elucidate catalyst properties, including X-ray diffraction (XRD) for crystallinity analysis, Scanning Electron Microscopy (SEM) for morphological evaluation, and X-ray Photoelectron Spectroscopy (XPS) for surface chemical state determination. Electrochemical testing was performed in both three-compartment flow cells and zero-gap membrane electrode assemblies (MEA), while product distribution was analysed using Gas Chromatography (GC) for gas-phase species and High-Performance Liquid Chromatography (HPLC) for liquid-phase species.

The research first investigates Zeolitic Imidazolate Frameworks (ZIFs) prepared via a green, solvent-free steam-assisted dry-gel synthesis route. It is demonstrated that while ZIF-8 (Zn-based) achieves selective CO production with a Faradaic efficiency of approximately 60%, the isostructural ZIF-67 (Co-based) predominantly favours the competing hydrogen evolution reaction, highlighting the decisive role of the metal centre over surface area or CO_2 adsorption capacity alone. Expanding toward multi-carbon products, a nitrogen-coordinated Cu-MOF with a hierarchical flake morphology was engineered. In MEA, this catalyst achieved a maximum ethylene Faradaic efficiency of 51.6% at 200 mA cm^{-2}, with operando X-ray absorption spectroscopy revealing reversible Cu redox transitions during the reaction.

To address operational robustness, the study explores nickel sulfide (NiS_x) nanostructures supported on nitrogen-doped mesoporous carbon (NiS_x@NMC). Following strategic acid leaching, the resulting NiS_x@NMC_AL catalyst exhibits near-unity CO selectivity across a broad pH range, including under strongly acidic conditions with a pH of 1, while significantly outperforming sulfur-free Ni-based samples and the non-acid-treated NiS_x@NMC. The sulfur-enriched NiS_x surface effectively suppresses the competing hydrogen evolution reaction and promotes selective CO_2-to-CO conversion. By adjusting the anolyte to a mildly acidic pH of

3, salt deposition at the cathode is effectively mitigated, enabling stable continuous operation for 450 minutes at 100 mA $cm^{-2}$with a sustained full-cell energy efficiency of 43.7%. Finally, the thesis examines Fe-doped nitrogen-rich mesoporous carbons for the oxygen reduction reaction, showing that Fe_3C active sites promote an efficient four-electron pathway, particularly in alkaline media.

Publication and conferences

Publications in Peer-Reviewed Journals

1. M. Bagheri, M. A. O. Lourenço, J. K. Dangbegnon, N. B. D. Monti, L. Mafra, F. Pirri, and J. Zeng. *"Green Synthesis of MOF-Based Materials for Electrochemical Reduction of Carbon Dioxide"*. *ChemSusChem*, 2024.
2. N. B. D. Monti, J. Zeng, M. Castellino, S. Porro, M. Bagherikerachi, C. F. Pirri, A. Chiodoni, and K. Bejtka. *"Effects of Annealing Conditions on the Catalytic Performance of Anodized Tin Oxide for Electrochemical Carbon Dioxide Reduction"*. *Nanomaterials*, 2025.
3. M. Bagheri, M. A. O. Lourenço, M. Castellino, S. Nappini, F. Di Costola, J. K. Dangbegnon, E. Magnano, L. Mafra, F. Pirri, A. Sacco, and J. Zeng. *"Mesoporous Cu-MOF flakes as a promising platform for electrosynthesis of ethylene from carbon dioxide"*. *Small Science*, 2026.

Manuscripts Ready for Submission

1. M. Bagheri, M. A. O. Lourenço, L. Mafra, F. Pirri, A. Sacco, and J. Zeng. *"Ni_3S_2 anchored on N-Doped Mesoporous Carbon for Selective and Stable CO_2 Reduction"*.
2. M. Bagheri et al. *"Synergistic Fe_3C Active Sites in N-Doped Mesoporous Carbon Enable ORR Activity"*.

Conference Contributions

1. Oral presenter and organizing committee assistant, Materials for Sustainable Development Conference (MATSUS Fall 2024), Lausanne, Switzerland, November 2024.
2. Oral presenter and organizing committee assistant, Materials for Sustainable Development Conference (MATSUS Fall 2025), Valencia, Spain, October 2025.
3. Oral presenter, ECCE15 & ECAB8 & CIBIQ 2025, Lisbon, Portugal, September 2025.

International Research Experience

1. Invited research visitor, BACH Beamline, Elettra Synchrotron Facility, Trieste, Italy (January 2025). Performed in-operando X-ray Absorption Spectroscopy (XAS) on MOF-based CO_2 reduction catalysts.

2. Research secondment, University of Aveiro (CICECO), Portugal (March – June 2025). Conducted research on mesoporous nitrogen-doped carbon materials for CO_2 capture and electrochemical conversion.

Table of contents

Chapter 1. Introduction 14

1.1. Global Carbon Challenge 15

1.2. Electrochemical CO_2 Reduction 17

1.3. Mechanistic Pathways 17

1.4. Thermodynamic and Kinetic 20

1.5. Catalyst 22

1.5.1. Zeolitic imidazolate frameworks 24

1.5.2. Copper-Based Metal-Organic Frameworks 26

1.5.3. Ni-based materials 27

1.6. Electrolyte 28

1.6.1. Alkaline electrolyte 29

1.6.2. Neutral-buffered electrolyte 30

1.6.3. Interfacial electrolyte-electrode interactions 31

1.7. Electrochemical Cell Design 32

1.7.1. Cathode 34

1.7.2. Anode 34

1.7.3. Membrane electrode assembly 35

1.7.4. Flow channels and electrolyte compartments 36

1.7.5. Reference electrode 38

1.7.6. Gaskets 38
1.8. Research Questions Addressed 40
1.9. Layout of the work 41
1.9.1. Publication and conferences 41
Chapter 2. Methodologies 42
2.1. Electrochemical Testing Setups 43
2.1.1. Three-compartment flow cell assembly 43
2.1.2. Zero-gap assembly 46
2.2. Electrode Preparation 48
2.2.1. Binder effects and catalyst layer morphology 49
2.3. Electrochemical Techniques 49
2.3.1. Linear sweep voltammetry 50
2.3.2. Chronoamperometry and chronopotentiometry 51
2.3.3. Electrochemical impedance spectroscopy 51
2.4. Product Quantification 53
2.4.1. Gas-phase products quantification 54
2.4.2. Liquid chromatography 55
2.4.3. Liquid quantification 55
2.5. Structural Characterization 57
2.5.1. X-ray Diffraction 57
2.5.2. Electron Microscopy Characterization 59
2.5.3. Surface Area and Porosity Analysis 61
2.5.4. CO_2 Adsorption Isotherms 63
2.5.5. X-ray Photoelectron Spectroscopy 65
2.5.6. Elemental and Compositional Analysis 67
2.5.7. Vibrational Spectroscopy: 68
2.5.8. Thermogravimetric Analysis 70

2.5.9. X-ray Absorption Spectroscopy 70
2.5.10. In Situ and Operando XAS 71
Chapter 3. ZIF-Based Materials 73
3.1. Materials and Synthesis Methods 74
3.2. Results and Discussion 75
3.2.1. Physicochemical properties 75
3.2.2. Electrocatalytic performance 80
3.2.3. Conclusions 84
Chapter 4. Mesoporous Cu-MOF 85
4.1. Materials and Synthesis Methods 86
4.2. Results and Discussion 87
4.2.1. Physicochemical properties 87
4.2.2. Electrocatalytic performance 96
4.2.3. Conclusions 104
Chapter 5. Ni based on Nitrogen-doped mesoporous carbon 105
5.1. Materials and Synthesis Methods 106
5.2. Results and discussion 108
5.2.1. Physicochemical properties 108
5.2.2. Electrocatalytic performance 118
Chapter 6. The oxygen reduction reaction (ORR) 123
6.1. Materials and Synthesis Methods 125
6.2. Results and discussion 126
6.2.1. Physicochemical properties 126
6.3. RRDE Analysis of ORR Performance 135
Chapter 7. Final remarks 141
7.1. Conclusions and addressed research questions 142
7.2. Future Works 143

Bibliography 144

List of abbreviations

Core Research

CO_2RR: Electrochemical CO_2 Reduction Reaction

FE: Faradaic Efficiency

HER: Hydrogen Evolution Reaction

ORR: Oxygen Reduction Reaction

Characterization Techniques

BET: Brunauer-Emmett-Teller (Surface Area Analysis)

CA: Chronoamperometry

CP: Chronopotentiometry

CV: Cyclic Voltammetry

EA: Elemental Analysis

EDS: Energy Dispersive X-Ray Spectroscopy

EIS: Electrochemical Impedance Spectroscopy

FESEM: Field Emission Scanning Electron Microscope

FTIR: Fourier Transform Infrared (Analysis)

HAXRD: High-Angle X-Ray Diffraction

ICP-OES: Inductively Coupled Plasma Optical Emission Spectroscopy

IUPAC: International Union of Pure and Applied Chemistry

LAXRD: Low-Angle X-Ray Diffraction

LSV: Linear Sweep Voltammetry

NLDFT: Non-Local Density Functional Theory

RRDE: Rotating Ring-Disk Electrode

SEM: Scanning Electron Microscopy

TEM: Transmission Electron Microscopy

TGA: Thermogravimetric Analysis

TXRF: Total Reflection X-ray Fluorescence

XAS: X-ray Absorption Spectroscopy

XPS: X-ray Photoelectron Spectroscopy

XRD: X-Ray Diffraction

Materials and Chemical Frameworks

BE: Binding Energy

EPDM: Ethylene propylene diene monomer

HOMO: Highest Occupied Molecular Orbital

LUMO: Lowest Unoccupied Molecular Orbital

mIm: 2-methylimidazolate

MMO: Mixed Metal Oxide

MOFs: Metal-Organic Frameworks

NMC: Nitrogen-doped mesoporous carbon

PTFE: Polytetrafluoroethylene

SAC: Single-Atom Catalysts

ZIF-67: Cobalt-based Zeolitic Imidazolate Framework

ZIF-8: Zinc-based Zeolitic Imidazolate Framework

ZIFs: Zeolitic Imidazolate Frameworks

Electrochemical Cell Components

AEM: Anion Exchange Membrane

CEM: Cation Exchange Membrane

CL: Catalyst Layer

EDL: Electric Double Layer

GC: Gas Chromatography

GDE: Gas Diffusion Electrode

GDL: Gas Diffusion Layer

HPLC: High-Performance Liquid Chromatography

MEA: Membrane Electrode Assembly

MFC: Mass Flow Controller

MPL: Microporous Layer

MPS: Macroporous Substrate

OCP: Open-circuit potential

OCV: Open-circuit voltage

OER: Oxygen Evolution Reaction

PCET: Proton-coupled electron transfer

PEM: Polymer Electrolyte Membrane

RSF: Relative Sensitivity Factor

General and Institutional Abbreviations

CSFT: Center for Sustainable Future Technologies

DISAT: Department of Applied Science and Technology of PoliTo

ScuDo: Graduate School of Politecnico di Torino

List of figures

Figure 1-1. Schematic representation of the overall perturbation of the global carbon cycle caused by anthropogenic activities, averaged globally for the decade 2013-2022. Fluxes are in gigatonnes of carbon per year (GtC yr^{-1}) and reservoirs in gigatonnes of carbon (Gt C) (1) .. 15
Figure 1-2. Proposed mechanism for carbon dioxide electroreduction. a) The pathway to C_1 products (formate, carbon monoxide, and methane) and b) the pathway to C_2 products (ethylene and ethanol) (35). 20
Figure 1-3.(a) MOF-derived porous semiconductor heterostructures. (b) Nitrogen-doped carbon derived SBA-15. 24
Figure 1-4. Structure of ZIF-8 sodalite (SOD) net. On the left, the sodalite-like β-cage (11.6 Å) with the yellow sphere representing the van der Waals surface within the pore, and with the ZnN_4 tetrahedra highlighted and General structural model of ZIFs showing angle similarities with the aluminosilicate zeolites on the right. 24
Figure 1-5. Crystal structures and topologies of ZIF-8 and ZIF-67 (57). 25
Figure 1-6. Solubility of CO_2, H_2CO_3, HCO_3 and CO_3^{2-} as a function of pH. 29
Figure 1-7. Schematic diagrams of CO_2 electrolyzers. (a) H-cell, (b) flow-cell and (c) MEA-cell (131). 33
Figure 1-8. (a) Layered GDE between gas flow field and electrolyte, comprising a gas diffusion layer (MPS + MPL) and a catalyst layer (CL), (b) CO_2 diffuses through porous carbon-based MPS/MPL to the nanoparticle CL, while electrons are conducted to the catalyst. 34
Figure 1-9. Schematic representation of the working principles of two types of membrane under an electric field. (AEM anion exchange membrane, CEM cation exchange membrane) (137) 35
Figure 1-10. Illustration of the components of an exchange MEA cell with the catalyst layer on a carbon gas-diffusion layer. Shown here are the three different flow patterns at the cathode: (b) serpentine, (c) parallel, and (d) interdigitated flow patterns. 37
Figure 1-11.Schematic illustration of a flow-cell configuration for CO_2 electroreduction, showing separate catholyte and anolyte circulation loops, gas inlet and outlet streams, and membrane separation between the cathode and anode compartments 38
Figure 2-1. three-compartment flow cell, ... 44
Figure 2-2. Schematic diagrams of 3-compartment flow cell 44
Figure 2-3. Preparation of the catalyst-coated gas diffusion electrode (GDE). 45
Figure 2-4. Sequential assembly of the three-compartment electrochemical flow cell, illustrating the ordered stacking of sealing frames, electrodes, membrane, and flow-field components. 46
Figure 2-5. Schematic diagrams of zero-gap electrochemical cell (MEA-cell). 47
Figure 2-6. Stepwise assembly of the MEA electrochemical cell. 48

Figure 2-7. Nyquist plot showing key impedance contributions. 52
Figure 2-8. Sample mounting for (a) HAXRD and (b) LAXRD analysis 59
Figure 2-9. Sample preparation procedures for (a) SEM on conductive carbon tape and (b) on a holey carbon film supported on a 300-mesh copper grid. 60
Figure 2-10. Schematic depiction of the six fundamental gas physisorption isotherm categories according to the IUPAC classification (165) 62
Figure 2-11. Schematic of the XPS photoelectric process showing core-level electron emission and subsequent Auger electron generation. 65
Figure 2-12. Scheme of the EC-cell and measurement setup for operando soft-XAS experiments implemented at the BACH beamline, Elettra Sincrotrone Trieste, reproduced from: Napal Azcona, I. X-Ray Spectroscopies for .Hydrogen Based Economy (Doctoral Dissertation). 72
Figure 3-1. Schematic illustration of the steam-assisted dry-gel synthesis setup for ZIF materials. 75
Figure 3-2. XRD pattern of (a) ZIF-8 synthesized with different volumes of water and its commercial analogue, (b) ZIF-8 and ZIF-67 synthesized with 20 mL of water (189). 76
Figure 3-3. SEM images of (a) ZIF-8_2, (b) ZIF-8_10, (c-d) ZIF-8_20 (low and high magnification), (e- f) ZIF-8_30 (low and high magnification) and (g-h) ZIF-67_20 (low and high magnification) (189) 77
Figure 3-4. FESEM images and corresponding particle size distribution histograms of (a,b) ZIF-8_20, (c,d) ZIF-8_30, and (e,f) ZIF-67_20, showing the influence of water vapor volume and metal center on particle morphology and size distribution. 78
Figure 3-5. -196 N_2 adsorption-desorption isotherms for a) ZIF-8_20 and b) ZIF-67_20 materials. Closed symbols correspond to the adsorption process, whereas empty symbols are associated with the desorption process. The inset shows the pore size distribution curve for the respective sample (189) 79
Figure 3-6. . Adsorption isotherms of pure CO_2 at 25 °C in ZIF-8_20 (red symbols) and ZIF-67_20 (black symbols) (189) 80
Figure 3-7. Current densities recorded for ZIF-8_2, ZIF-8_10, ZIF-8_20, and ZIF-8_30 electrodes at different applied potentials in 2M $KHCO_3$ electrolyte. (b) Corresponding Faradaic efficiency for CO production and CO:H_2 ratio as a function of potential. The dotted lines in panel (a) serve as visual aids to highlight trends (189). 81
Figure 3-8. a) comparison of the Faradaic efficiency of ZIF-8_20 in 2M $KHCO_3$ and 1M KOH at different potentials vs RHE and b) Faradaic efficiency of ZIF-67_20 in 2M $KHCO_3$ at different potentials vs RHE (189). 82
Figure 3-9. Stability test of ZIF-8_20 at -60 mA cm^{-2} in 0.5M $KHCO_3$ by MEA cell (189) 84
Figure 4-1. XRD patterns of Cu-MOF (solid line) and 2-methylimidazole (dashed line) 87
Figure 4-2. FESEM images of Cu-MOF: (a) top view of the particles and (b) lateral view of the particles. 88
Figure 4-3. (a) SEM image of Cu-MOF under EDS condition and (b) EDS mapping. 89

Figure 4-4. (a) -196 N_2 adsorption-desorption isotherms (Closed symbols correspond to the adsorption process, whereas empty symbols are associated with the desorption process) and (b) NLDFT pore size distributions of Cu-MOF. 89
Figure 4-5. TGA up to 800 °C under the air atmosphere of steam-assisted hydrothermal Cu-MOF. 91
Figure 4-6. FTIR of steam-assisted hydrothermal Cu-MOF and 2-methylimidazole. 92
Figure 4-7. Raman spectrum of steam-assisted hydrothermal Cu-MOF and 2-methylimidazolem. 92
Figure 4-8. XPS spectra of the Cu-MOF: (a) survey spectrum showing the presence of C, N, O, and Cu elements; (b) high-resolution C 1s spectrum with fitted components corresponding to sp^2 C-C (284.5 eV), sp^3 C-C/C-N (285.3 eV), C-N/C=N (286.1 eV), and π-π* shake-up features (291.1 and 292.8 eV); (c) N 1s spectrum showing pyridinic N (398.6 eV) and Cu-coordinated N (399.9 eV); (d) Cu 2p spectrum displaying Cu^{2+} features with characteristic satellite peaks. 94
Figure 4-9. (a) Cu L-edge soft XAS spectra of the steam-assisted Cu-MOF in TEY and FY modes compared with Cu, Cu_2O, and CuO references, showing characteristic Cu(II) features and LMCT-related satellites. (b) N K-edge spectra in TEY(red solid line) and FY(red dashed line) modes displaying three main absorption features consistent with nitrogen coordination in the Cu-imidazolate framework. 96
Figure 4-10. Schematic diagrams of 3-compartment flow cell 97
Figure 4-11. (a) Faradaic efficiencies of CO_2 reduction products and corresponding total current density of Cu-MOF in a flow-cell at different applied potentials in 1M KOH catholyte. (b) Faradaic efficiencies and the C_2/C_1 product ratio derived from the data shown in (a). 98
Figure 4-12. Schematic diagrams of zero-gap electrochemical cell (MEA-cell). 98
Figure 4-13. (a) Faradaic efficiencies of CO_2 reduction products on Cu-MOF gas diffusion electrodes in a zero-gap cell at different current densities using 0.5M KOH as anolyte. (b) Corresponding Faradaic efficiencies and C_2/C_1 product ratio derived from the data in (a)..... 99
Figure 4-14. (a) Faradaic efficiencies of CO_2 reduction products for Cu-MOF electrodes with different loadings (1.6 and 0.25 mg cm^{-2}) in a flow cell at various applied current densities in 1M KOH, including the corresponding electrode potentials. (b) Corresponding Faradaic efficiencies and C_2/C_1 product ratio derived from the data shown in (a). 100
Figure 4-15. Salt deposition on the flow channel. 101
Figure 4-16. Time-dependent Faradaic efficiencies in the zero-gap cell at 200 $mA \cdot cm^{-2}$: (a) with 0.5M KOH anolyte, (b) with 0.1M KOH, (c) at 100 $mA \cdot cm^{-2}$ (0.5M KOH), and (d) with 0.1M $CsHCO_3$ (200 $mA \cdot cm^{-2}$). 102
Figure 4-17.Operando soft XAS measurements performed in an EC-cell on a spray-coated Cu-MOF electrode dried at 60 °C: Cu L-edge spectra collected in FY mode for the dry electrode and their evolution from OCP to −1.4 V vs Ag/AgCl; (b) Comparison of Cu L-edge spectra. 103

Figure 5-1. Schematic synthesis of SBA-15 via P123-templated self-assembly, hydrothermal treatment, extraction, and calcination 107
Figure 5-2. Schematic synthesis of Ni-based species anchored on nitrogen-doped mesoporous carbon using SBA-15 as a hard template, involving sequential impregnation, pyrolysis, template removal, and acid treatment. 108
Figure 5-3. (a) Low-angle and (b) High-angle XRD patterns of NMC, Ni@NMC, Ni_3S_2@NMC and after acid leaching..... 109
Figure 5-4. Low-angle XRD of SBA-15. 110
Figure 5-5. N_2 adsorption–desorption isotherms of NMC, Ni@NMC, Ni@NMC_AL, Ni_3S_2@NMC, and Ni_3S_2@NMC_AL measured at −196 °C. 113
Figure 5-6. Pore size distributions of NMC, Ni@NMC, Ni@NMC_AL, Ni_3S_2@NMC, and Ni_3S_2@NMC_AL derived from NLDFT analysis of N_2 adsorption data. 114
Figure 5-7. XPS survey of NMC (a) and Ni_3S_2@NMC-AL (b). a) wide-scan XPS survey of nitrogen-rich mesoporous carbon, b) Ni_3S_2 embedded in nitrogen. 115
Figure 5-8. High-resolution XPS spectra of NMC and Ni_3S_2@NMC-AT: (a) N 1s spectra and (b) C 1s spectra. 116
Figure 5-9. High-resolution XPS spectra of Ni_3S_2@NMC: (a) Ni 2p region and (b) S 2p region. 118
Figure 5-10. CO_2 electroreduction performance of NMC, Ni@NMC (with and without acid leaching), and Ni_3S_2@NMC (with and without acid leaching) in 0.1 M $KHCO_3$ (pH ≈ 8.3) under zero-gap MEA operation a) 100 mA cm^{-2} and (b) 150 mA cm^{-2}. 119
Figure 5-11. CO_2RR performance in a zero-gap MEA.(a) FE in current density (25–200 mA cm^{-2}) in 0.1 M $KHCO_3$.(b) Time-dependent FE in 0.1M $KHCO_3$ at 100 mA cm^{-2}, (c) FE at 100 and 150 mA cm^{-2} in 0.05 M K_2SO_4.(d) Time-dependent FE in K_2SO_4 at 100 mA $cm^{-2.}$..... 120
Figure 5-12. CO_2RR performance under acidic conditions in a zero-gap MEA. (a) FE at pH ≈ 3 at 100 and 150 mA cm^{-2},(b) Time-dependent FE at pH ≈ 3, (c) FE of CO and H_2 at pH ≈ 1 under the same conditions and (d) Time-dependent FE at pH ≈ 1. 121
Figure 6-1. a) Low-angle and b) High-angle XRD of NMC, Fe_3C@NMC and Fe_3C@NMC_AL 127
Figure 6-2. Raman spectroscopy of NMC, Fe_3C@NMC and Fe_3C@NMC_AL 128
Figure 6-3.a) N_2 adsorption–desorption isotherms measured at −196 °C, b) pore size distribution of NMC, Fe_3C@NMC and Fe_3C@NMC_AL 129
Figure 6-4. Thermogravimetric analysis of NMC, Fe_3C@NMC and Fe_3C@NMC_AL. 130
Figure 6-5. Wide-scan XPS survey of Fe_3C@NMCN and b) Fe_3C@NMC-AL. 132
Figure 6-6. High-resolution XPS spectra of the a) N 1s, b) O 1s, and c) Fe 2p of Fe_3C@NMC. 134
Figure 6-7. High-resolution XPS spectra of the C 1s and N 1s regions for the Fe_3C@NMC_AL. 135

Figure 6-8. CVs recorded at 50 mV s^{-1} in N_2- and O_2-saturated electrolytes to evaluate cathodic currents associated with the ORR. Measurements were conducted in 0.1 M KOH and 0.1 M $HClO_4$ for NMC, Fe_3C@NMC and Fe_3@NMC_AL. 136
Figure 6-9: ORR electrocatalytic activity measured at 1600 rpm: (a) Disk current density in 0.1 M KOH, (b) Disk current density in 0.1 M $HClO_4$. 137
Figure 6-10: ORR selectivity expressed in terms of electron transfer number and peroxide yield, measured in the 4-electrodes configuration (RRDE setup) at 1600 rpm in (a) 0.1 M KOH and (b) 0.1 M $HClO_4$. 139

List of tables

Table 1-1. Standard Reduction Potentials (36)..... 20
Table 2-1. Key components of a Gas Chromatography system used for CO_2 electroreduction product analysis, along with their specific functions in the detection and quantification process. 54
Table 2-2. common liquid-phase products generated in electrochemical CO_2 reduction (CO_2RR), including their chemical formulas, number of electrons transferred (n), typical detection method (e.g., HPLC or NMR), and technical remarks relevant to analysis and system performance. 56
Table 5-1. Elemental composition (wt%) of MC and Ni-based composites before and after acid leaching. EA (C, H, N, S) and TXRF (Ni) 112
Table 5-2. Surface elemental composition from XPS survey spectra (At.%) 115
Table 5-3.Relative distribution of nitrogen species (N 1s)..... 117
Table 5-4.Relative distribution of carbon species (C 1s) 116
Table 6-1. Quantification of Fe content in Fe_3C@NMC and after acid treatment (aqua regia digestion: 10 mL aqua regia under reflux, then diluted with 40 mL ultrapure water to 50 mL total) 130
Table 6-2: Surface atomic composition in wt. % from XPS survey spectra. 132
Table 6-3: C 1s peak assignments before and after acid treatment. 133
Table 6-4:) onset and halfwave potentials in both alkaline and acidic media. 137
Table 6-5. Electron transfer numbers and peroxide yields (H_2O_2 %) at 0.5 V for various synthesized catalysts in 0.1 M KOH and 0.1 M $HClO_4$ media. 139
Table 6-6. Brief literature review of Fe_3C-based electrocatalysts for ORR applications. 140

Chapter 1. Introduction

1.1. Global Carbon Challenge

The growing urgency of climate change and the increasing demand for sustainable energy solutions have placed carbon dioxide (CO_2) at the centre of the global energy and materials transition. As a long-lived greenhouse gas with a steadily increasing atmospheric concentration, surpassing 420 ppm in 2023 and standing 51% above pre-industrial levels, CO_2 is both a major environmental threat and, paradoxically, an underutilized chemical feedstock (1,2). Anthropogenic CO_2 emissions continue to increase atmospheric concentrations, altering carbon uptake by land and ocean reservoirs in response to climate change, natural variability, and other human-driven factors (Figure 1-1). Transforming CO_2 from waste into a resource is therefore not only a scientific challenge, but also a key element of circular carbon strategies for a sustainable energy future

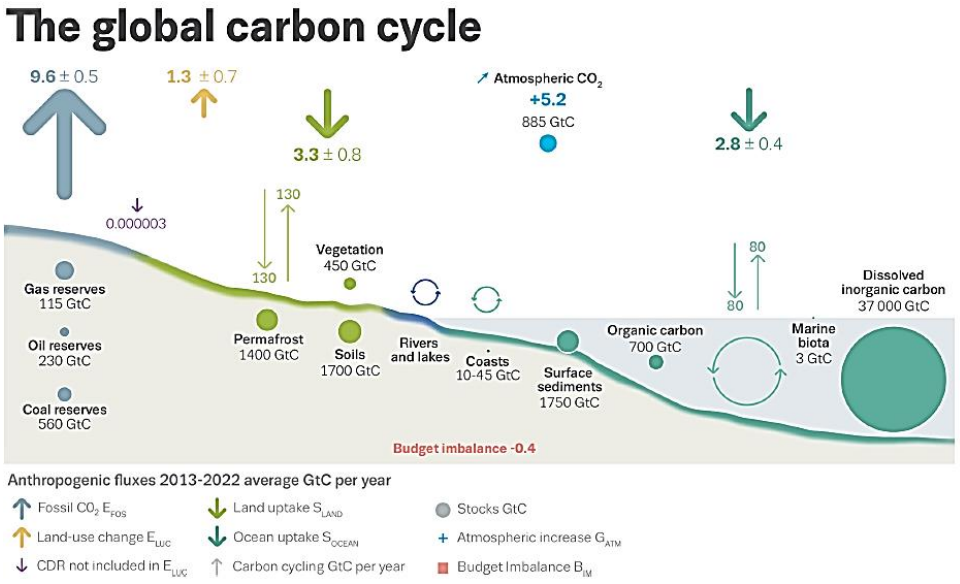


Figure 1-1. Schematic representation of the overall perturbation of the global carbon cycle caused by anthropogenic activities, averaged globally for the decade 2013-2022. Fluxes are in gigatonnes of carbon per year (GtC yr^{-1}) and reservoirs in gigatonnes of carbon (Gt C) (1)

Among carbon management technologies, the electrochemical CO_2 reduction reaction (CO_2RR) has emerged as a promising route for producing carbon-neutral fuels and value-added chemicals directly from CO_2, water, and renewable electricity (3,4). CO_2RR offers a modular, low-temperature pathway that can be integrated with intermittent renewable energy sources such as wind and solar, making it an attractive alternative to fossil-based thermochemical processes (5). In principle, CO_2RR enables the production of a wide range of compounds, from carbon monoxide and formate to hydrocarbons and oxygenates, through controlled multi-electron, multi-proton transformations (6).

Despite this promise, CO_2RR remains fundamentally challenging. CO_2 is a linear, thermodynamically stable molecule (with a standard heat of formation $\Delta_f H^0$ = -394.4 kJ mol^{-1})[1], and its electrochemical conversion is kinetically sluggish and highly sensitive to reaction conditions and catalyst properties. In aqueous electrolytes, CO_2RR takes place alongside the hydrogen evolution reaction (HER), which can decrease both the energy efficiency and the selectivity toward the desired CO_2 reduction products (7,8). Overcoming this competition requires not only improvements in reactor design and operating conditions, but also the development of electrocatalysts that can favour the desired reaction pathway while maintaining high activity, selectivity, and stability. In recent years, considerable effort has therefore been devoted to tailoring catalyst structure and composition to improve CO_2RR performance. Early work by Hori showed that Cu is particularly distinctive among metallic catalysts because it can produce C_2 and C_3 products, including ethylene and ethanol, under ambient conditions (9). Since then, a wide range of strategies have been explored, including oxide-derived structures, high-index facets, subsurface modification, bimetallic systems, defect engineering in two-dimensional materials, and atomically dispersed active sites (10–14). These studies have shown that CO_2RR performance is influenced not only by the chemical identity of the catalyst, but also by its structure, coordination environment, electronic properties, and interaction with the surrounding electrolyte.

From a synthetic perspective, these insights have driven a new generation of catalyst design strategies in which rational synthesis, in situ characterization, and mechanistic modelling are closely integrated. High-surface-area nanostructures, facet-controlled crystals, and defect-engineered materials are being tailored to tune the binding strengths of key intermediates such as *COOH, *CO[2], and *CHO, with the aim of selectively promoting C–C coupling and multi-proton/electron transfer pathways (15–17). At the same time, the field is increasingly embracing more sustainable materials synthesis approaches based on earth-abundant elements, green solvents, low-temperature processing, and scalable fabrication routes aligned with broader energy-transition goals (18).

Catalyst development must also be considered at the system level. The performance of a CO_2RR catalyst is strongly influenced by electrolyte composition, mass-transport behaviour, and reactor architecture, all of which shape the local reaction environment and determine practical viability (19). A materials-centred approach to CO_2RR therefore requires evaluation under realistic operating conditions, including operando spectroscopy, flow-cell testing, and long-term durability studies (20,21).

This thesis is positioned within this evolving framework at the interface of electrochemical science, materials engineering, and sustainable energy systems. It focuses on the rational

[1] $CO_2 + X \longrightarrow Y + Z \;\; \Delta_r H = \Delta_f H(Y) + \Delta_f H(Z) - \Delta_f H(CO_2) - \Delta_f H(X)$, shows a general reaction of carbon dioxide. The heat of reaction is determined by the difference between the heat of formation of all the products and that of all the reactants

[2] *CO refers to adsorbed carbon monoxide, that is, a CO molecule that is bound to the surface of a catalyst during the reaction process. The asterisk (*) denotes that the molecule is adsorbed on the catalyst surface.

synthesis and structural tuning of novel synthesis catalyst for CO_2RR, with dual emphasis on electrocatalytic performance and sustainability. Through controlled fabrication, advanced characterization, and mechanistic analysis, this thesis aims to clarify how material structure governs product selectivity and reaction kinetics. The broader objective is to contribute to materials-by-design strategies for scalable CO_2 utilization in future energy systems.

1.2. Electrochemical CO_2 Reduction

The CO_2RR has evolved from a scientific curiosity in the nineteenth century into a central topic in sustainable energy research. Early observations in simple electrolytic cells attracted limited interest because of sluggish kinetics, poor selectivity, and strong competition from HER (22). Major progress was achieved in the 1980s and 1990s through the systematic studies of Hori and co-workers, who examined CO_2 electroreduction on a wide range of metallic electrodes. Their work revealed the unique ability of Cu to reduce CO_2 to hydrocarbons and alcohols, unlike most other metals, and established the foundation for understanding material-dependent selectivity in CO_2RR (23). Several fundamental principles constrain this reaction. First, CO_2 is a linear, highly stable molecule, and the first electron transfer required to form the $*CO_2^-$ intermediate is energetically demanding. Second, CO_2RR proceeds through complex multi-step mechanisms involving coupled proton–electron transfer steps, often requiring between 2 and 12 electrons depending on the target product. Third, multiple competing pathways may occur in parallel, making selective product formation difficult. Finally, in aqueous media, HER often dominates at similar potentials, especially when catalysts do not selectively stabilize CO_2RR intermediates (24). To address these challenges, recent advances have focused on designing next generation electrocatalysts that tune the adsorption energetics of key intermediates. Recent approaches include nanostructuring, heteroatom doping, surface reconstruction, and the introduction of transition metals into single-atom catalysts (SACs) and porous materials such as metal–organic frameworks (MOFs) (25,26). Together, these strategies illustrate the broad range of approaches used to control CO_2RR activity and selectivity. The following sections discuss these aspects in more detail, starting with the reaction pathways and surface intermediates involved in CO_2 reduction.

1.3. Mechanistic Pathways

The electrochemical reduction of CO_2 starts with its adsorption and subsequent activation on the electrode surface. In aqueous solutions, CO_2 exists in equilibrium with bicarbonate (HCO_3^-) and carbonate (CO_3^{2-}); however, under most electrochemical conditions, the electroactive species is undissociated CO_2(g). Due to its linear geometry (O=C=O, 180°) and closed-shell electronic structure (HOMO-LUMO gap of ~12.5 eV), CO_2 is chemically inert and requires activation to form reactive surface-bound species.

The first electron transfer is often the rate-limiting step, leading to the formation of a bent radical anion ($*CO_2^-$):

$$CO_2 + e^- \rightarrow * CO_2^-$$ Eq. 1-1

These intermediate features a bent geometry (~133°) with the negative charge delocalized mainly on the oxygen atoms. The activation energy for this step is significant in the gas phase (~1.9 eV) but is reduced to ~0.6-1.1 eV in aqueous environments or on catalytic surfaces, especially those that stabilize the resulting negative charge via electron back-donation or local electrostatic fields (27,28). Studies using ab initio[3] molecular dynamics and Density Functional Theory (DFT) have shown that the activation is surface-specific, for example, Cu (100)[4], the interaction with $*CO_2^-$ is stronger than Cu(111), due to differences in orbital hybridization and local coordination (29). After activation, the mechanism diverges depending on catalyst composition, applied potential, and electrolyte environment. As shown in Figure 1-2, CO_2RR pathways can be broadly divided into those leading to C_1 products such as formate, carbon monoxide, and methane, and those leading to C_2 products such as ethylene and ethanol.
One common route is the *COOH pathway, typical of transition metals such as Cu, Ag, and Au. In this pathway, $*CO_2^-$ is protonated at the carbon atom to form the carboxyl intermediate *COOH:

$$* CO_2^- + H^+ + e^- \rightarrow * COOH$$ Eq. 1-2

$$* COOH + H^+ + e^- \rightarrow * CO + H_2O$$ Eq. 1-3

The *COOH intermediate is a key branching point. Its stability determines whether the reaction proceeds toward CO desorption, as on Au and Ag, or toward further reduction, as on Cu. In situ infrared spectroscopy has confirmed the formation of *COOH on both Au and Cu surfaces under applied bias (30). On Au, *CO binds relatively weakly, so it desorbs readily without further reduction (23). Under acidic or near-neutral conditions, where protons are readily available, the overall CO formation reaction is expressed as:

$$CO_2 + 2H^+ + 2e^- \rightarrow CO + H_2O$$ Eq. 1-4

Under alkaline conditions, free protons are scarce, and water acts as the proton donor. Therefore, the CO formation reaction is written as:

$$CO_2 + H_2O + 2e^- \rightarrow CO + 2OH^-$$ Eq. 1-5

An alternative route is the *OCHO pathway, which proceeds through protonation at the oxygen atom to form a bidentate *OCHO intermediate. This pathway is more favorable on p-block metals such as Sn, Bi, and In, where metal–oxygen interactions are energetically preferred:

[3] "ab initio" refers to methods based on quantum mechanical first principles, without empirical input.
[4] "Cu (100)" refers to the (100) crystallographic surface of a copper crystal, indicating the orientation of the surface with respect to its cubic lattice.

$$CO_2 + H^+ + e^- \rightarrow * OCHO \quad \text{Eq. 1-6}$$

$$* OCHO + H^+ + e^- \rightarrow HCOOH \quad \text{Eq. 1-7}$$

This route yields formate ($HCOO^-$) or formic acid (HCOOH), depending on electrolyte pH and buffering conditions.

$$CO_2 + 2H^+ + 2e^- \rightarrow HCOOH \quad \text{Eq. 1-8}$$

Or under alkaline conditions:

$$CO_2 + H_2O + 2e^- \rightarrow HCOO^- + OH^- \quad \text{Eq. 1-9}$$

DFT studies indicate that for example Sn(111) effectively stabilizes *OCHO while suppressing *CO formation, explaining its high Faradaic efficiency for formate production (31). Product speciation is also governed by acid–base equilibrium: below the pKa[5] of formic acid (~3.75), HCOOH predominates, whereas at higher pH, HCOO− is favoured (32). In Cu-based systems, the *CO pathway is central because *CO can accumulate on the surface under operating conditions. High *CO coverage opens two main possibilities. In the C_1 pathway, *CO is protonated further to form intermediates such as *CHO and *CH_2O, eventually leading to methane or methanol. In the C_2 pathway, two *CO species couple to form a *OCCO dimer, which is the key intermediate for multicarbon products such as ethylene and ethanol. Surface structure is crucial: Cu(100) facets favor *CO dimerization more strongly than Cu(111), which explains why nanocubes and stepped Cu surfaces often enhance C_2 product formation (33). Applied potential also influences selectivity, with methanol generally favored at moderate negative potentials and methane becoming more dominant at more negative potentials (34).

[5] Ka is the acid dissociation constant, which quantifies the extent to which an acid releases a proton (H^+) in solution. pKa is the negative logarithm of Ka ($pKa = -\log_{10}Ka$) and provides a more convenient way to express acid strength; lower pKa values indicate stronger acids.

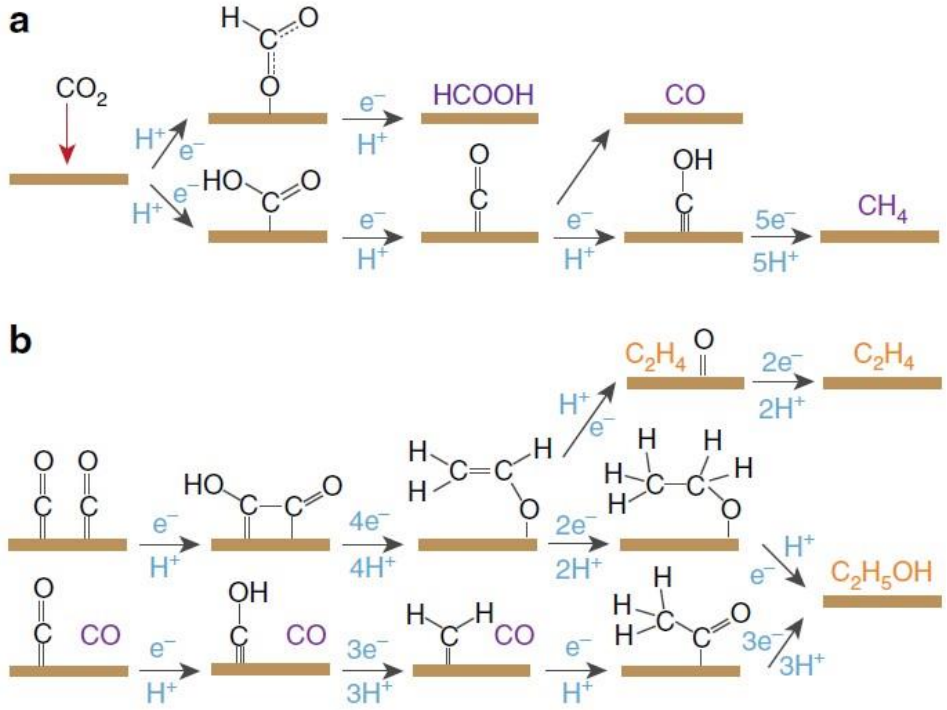


Figure 1-2. Proposed mechanism for carbon dioxide electroreduction. a) The pathway to C_1 products (formate, carbon monoxide, and methane) and b) the pathway to C_2 products (ethylene and ethanol) (35).

1.4. Thermodynamic and Kinetic

A key thermodynamic parameter in electrochemical systems is the open-circuit voltage (OCV), defined as the equilibrium potential of the cell when no net current flows. Under open-circuit conditions, no net current flows because the forward and reverse reactions occur at the same rate. The measured electrode potential therefore reflects the equilibrium between the oxidized and reduced species involved in the reaction. This relationship forms the basis of the Nernst description of electrochemical equilibrium, which connects thermodynamics with the potential measured in an electrochemical cell. Each CO_2RR product has its own standard reduction potential, E°, which indicates the potential required to drive its formation under standard conditions. These values are summarized in Table 1-1.

Table 1-1. Standard Reduction Potentials (36).

Reaction	**Electrolyte**	**Standard Potential (E° vs. RHE)**
$CO_2 + 2H^+ + 2e^- \rightarrow CO + H_2O$	Acid	–0.104

Reaction	Electrolyte	Standard Potential (E° vs. RHE)
$CO_2 + H_2O + 2e^- \rightarrow CO + 2OH^-$	Alkaline	–0.932
$CO_2 + 2H^+ + 2e^- \rightarrow HCOOH$	Acid	–0.171
$CO_2 + H_2O + 2e^- \rightarrow HCOO^- + OH^-$	Alkaline	–0.639
$CO_2 + 6H^+ + 6e^- \rightarrow CH_3OH + H_2O$	Acid	0.016
$CO_2 + 5H_2O + 6e^- \rightarrow CH_3OH + 6OH^-$	Alkaline	–0.812
$CO_2 + 8H^+ + 8e^- \rightarrow CH_4 + 2H_2O$	Acid	0.169
$CO_2 + 6H_2O + 8e^- \rightarrow CH_4 + 8OH^-$	Alkaline	–0.659
$2CO_2 + 12H^+ + 12e^- \rightarrow C_2H_4 + 4H_2O$	Acid	0.085
$2CO_2 + 8H_2O + 12e^- \rightarrow C_2H_4 + 12OH^-$	Alkaline	–0.743
$2CO_2 + 14H^+ + 14e^- \rightarrow C_2H_6 + 4H_2O$	Acid	0.144
$2CO_2 + 10H_2O + 14e^- \rightarrow C_2H_6 + 14OH^-$	Alkaline	–0.685
$2CO_2 + 12H^+ + 12e^- \rightarrow CH_3CH_2OH + 3H_2O$	Acid	0.084
$2CO_2 + 9H_2O + 12e^- \rightarrow CH_3CH_2 + 12OH^-$	Alkaline	–0.744
$2CO_2 + 8H^+ + 8e^- \rightarrow CH_3COOH + 2H_2O$	Acid	0.098
$2CO_2 + 5H_2O + 8e^- \rightarrow CH_3COO^- + 7OH^-$	Alkaline	–0.653
$2H^+ + 2e^- \rightarrow H_2$ (Hydrogen Evolution Reaction)	Acid	0.00
$2H_2O + 2e^- \rightarrow H_2 + 2OH^-$	Alkaline	–0.828

Although many products are thermodynamically accessible at relatively low potentials, large overpotentials are generally required because of kinetic barriers and poor stabilization of intermediates (37,38). In an electrolytic cell, non-spontaneous reactions are driven by electrical energy, which is converted into chemical energy. The Gibbs free-energy change is related to the applied potential by:

$$\Delta G = -nFE \qquad \text{Eq. 1-10}$$

Where n is the number of electrons transferred, F is the Faraday constant, and E is the electrode potential.

When current flows, the system departs from equilibrium and additional potential must be applied to overcome kinetic and transport limitations. The difference between the equilibrium

potential and the operating potential is defined as the overpotential (η). Overpotential represents the energetic penalty associated with irreversible processes including electron transfer, ionic conduction, and mass transport (39–41)

The cell voltage in Equation 1.8 is reported

$$V_c(T,P) = OCV + \sum_{n=1}^{3} \eta_n\,(i) \qquad \text{Eq. 1-11}$$

Equation 1.9 is reformulates of Equation 1.8 by separating individual overpotential contributions:

$$V_c(T,P) = OCV + \eta_{act}(i) + \eta_{ohm}\,(i) + \eta_{diff}\,(i) \qquad \text{Eq. 1-12}$$

The total cell voltage therefore consists of the equilibrium potential plus contributions from activation, ohmic, and diffusion overpotentials. Activation losses arise from sluggish charge-transfer kinetics and are commonly described by the Butler–Volmer equation through the exchange current density and charge-transfer coefficient. In CO_2RR, the rate-determining step often involves *COOH formation or C–C coupling, depending on the catalyst and local environment.(42). Ohmic losses originate from resistance to ion transport in the electrolyte, electron transport in electrodes, and resistance in the external circuit. These losses increase linearly with current density and are commonly expressed as the iR drop. Mass-transport losses become significant at high current density, when the supply of reactants and removal of products cannot keep pace with the reaction rate. These effects are especially important in gas-diffusion electrodes and zero-gap configurations (42).
In CO_2 reduction, the equilibrium potential depends on the selected half-reaction, electrolyte composition, and CO_2 partial pressure. For example, the reduction of CO_2 to CO is given by:

$$CO_2 + 2H^+ + 2e^- \rightarrow CO + H_2O \qquad \text{Eq. 1-13}$$

Although the thermodynamic potential for CO_2 reduction to CO is approximately −0.11 V vs RHE at pH 0, experimentally observed onset potentials are significantly more negative due to activation barriers associated with *COOH formation and competing hydrogen evolution. Therefore, the difference between the equilibrium potential and the operational potential directly reflects kinetic limitations of the system.

1.5. Catalyst

The performance of electrocatalysts for CO_2RR is governed not only by the intrinsic nature of the active site, but also by the surrounding structural and chemical environment. Parameters such as local pH, reactant accessibility, intermediate stabilization, and mass transport play a

critical role in determining catalytic activity and selectivity. These factors depend not only on catalyst composition, but also on the architecture of the supporting material and the microenvironment at the catalyst–electrolyte interface (43–45). Designing an efficient catalyst therefore requires looking beyond the active site itself and considering the environment in which the reaction takes place.

Porous materials are particularly useful in this regard. Their large surface area can provide more accessible sites for the reaction, while the interconnected pores can help CO_2, electrolyte ions, and reaction intermediates move through the catalyst layer. The pore structure can also affect the local concentration of reactants and how long intermediates remain near the active sites, which in turn can influence the reaction pathway and the products formed. In this context, micropores provide confinement and high surface area, whereas mesopores enable efficient mass transport, particularly under high current density conditions (46,47).

The pioneering work of Hori and co-workers identified Cu as the only pure metal capable of producing hydrocarbons and alcohols, while Ag and Au mainly yield CO at low overpotentials (48). Subsequent strategies, including alloying and nanostructuring, focused on tuning the adsorption energies of key intermediates such as *COOH and *CO (49). However, limitations related to mass transport and active-site utilization led to the development of porous and ligand-supported materials. Among these, metal–organic frameworks (MOFs), particularly zeolitic imidazolate frameworks (ZIFs), have emerged as versatile platforms due to their high surface area, well-defined metal–ligand coordination, and tunable pore structures (Figure 1-3a) (50). In parallel, nitrogen-doped mesoporous carbon (NMC) has gained increasing attention as a conductive and robust alternative. When NMC is prepared using a hard template such as SBA-15, the template helps form an ordered mesoporous structure with a relatively well-defined pore size and interconnected pore network. This structure can facilitate the transport of CO_2, ions, and reaction intermediates through the material. Nitrogen incorporation also changes the electronic properties of the carbon and creates sites that can interact with and anchor metal species, helping to distribute them throughout the carbon framework (Figure 1-3b). Compared with MOF-based materials, N-doped mesoporous carbon generally combines good electrical conductivity with good stability under electrochemical conditions, which makes it attractive for CO_2RR at relatively high current densities (51,52). In this context, this thesis focuses on the design of porous catalytic systems that integrate controlled structure, conductivity, and active-site dispersion. Specifically, Section 1.5.1 examines ZIF-based catalytic platforms, Section 1.5.2 focuses on Cu-based MOFs, while Section 1.5.3 examines Ni-based doped nitrogen mesoporous carbon, including nickel sulfides.(Ni_3S_2) Across these sections, the

structures, synthesis strategies, and design rationales that underpin their activity and selectivity toward CO_2 reduction are highlighted.

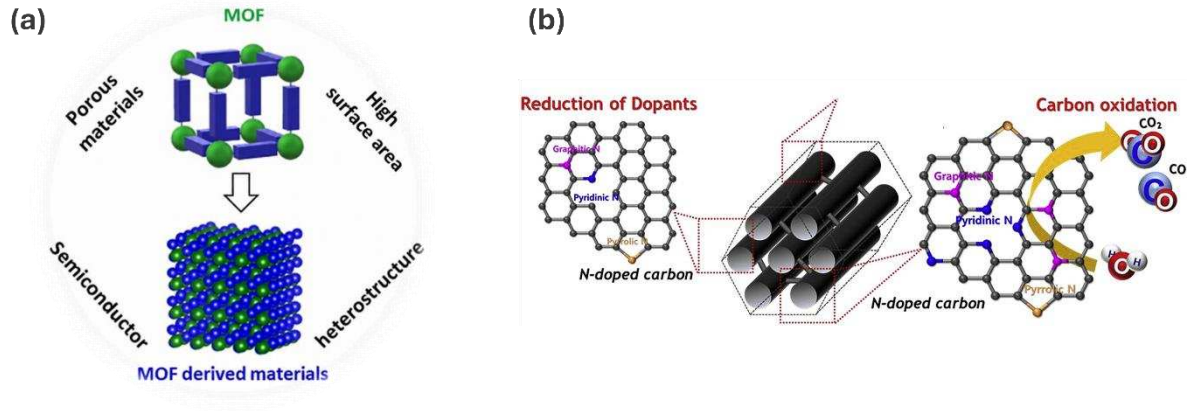


Figure 1-3. (a) MOF-derived porous semiconductor heterostructures. (b) Nitrogen-doped carbon derived SBA-15.

1.5.1. Zeolitic imidazolate frameworks

Zeolitic imidazolate frameworks (ZIFs) are a subclass of metal–organic frameworks composed of tetrahedrally coordinated metal ions, such as Zn^{2+}, Co^{2+}, or Fe^{2+}, linked by imidazolate ligands to form three-dimensional porous crystalline networks. A defining feature of ZIFs is their structural analogy to aluminosilicate zeolites: the M–Im–M bond angle of approximately 145° closely resembles the Si–O–Si angle in zeolites, allowing ZIFs to adopt similar topologies such as SOD, RHO, LTA, and GME (Figure 1-4) (53).

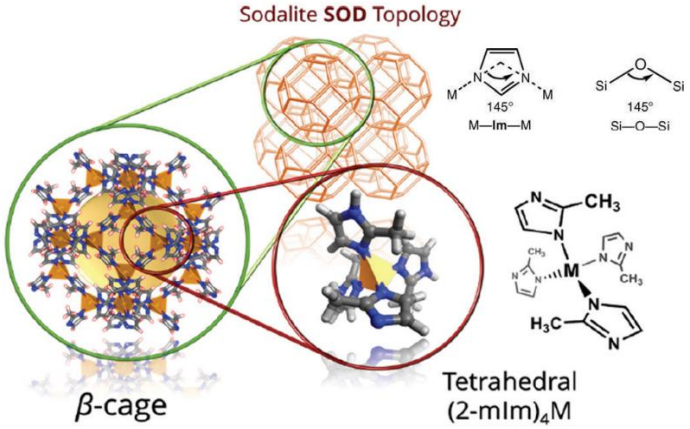


Figure 1-4. Structure of ZIF-8 sodalite (SOD) net. On the left, the sodalite-like β-cage (11.6 Å) with the yellow sphere representing the van der Waals surface within the pore, and with the ZnN_4 tetrahedra highlighted, and General structural model of ZIFs showing angle similarities with the aluminosilicate zeolites on the right.

Unlike conventional zeolites and many carboxylate-based MOFs, ZIFs combine zeolite-like rigidity and shape selectivity with the chemical tunability of organic frameworks (54,55). Strong metal–imidazolate bonds provide high thermal and chemical stability, while the organic linkers introduce hydrophobicity and functional diversity. Among the most studied members are ZIF-8 ($Zn(mIm)_2$) and ZIF-67 ($Co(mIm)_2$) (Figure 1-5) both of which exhibit sodalite topology, surface areas above 1500 $m^2\ g^{-1}$, and excellent chemical stability (56).

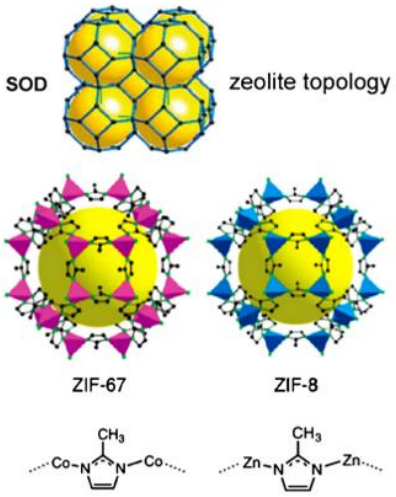


Figure 1-5. Crystal structures and topologies of ZIF-8 and ZIF-67 (57).

Their robust frameworks and tunable chemistry have made them central to applications in gas storage, separation, catalysis, and electrochemical energy conversion (58). The concept of ZIFs was first demonstrated in the mid-2000s by Huang et al., who reported ligand-directed synthesis of zeolite-type Zn-imidazolate frameworks (59). This was followed by the systematic development of ZIF families by Park et al., who demonstrated structural isomorphism with established zeolite nets (60). Subsequent work expanded the ZIF family through linker functionalization and mixed-metal strategies, enabling control over topology, pore size, and adsorption behaviour (61,62). ZIFs therefore occupy an intermediate position between zeolites and conventional MOFs, combining structural rigidity and stability with extensive opportunities for chemical modification (60,61). This combination enables fine tuning of adsorption, catalytic activity, and ion-transport properties (63,64).

ZIFs are typically microporous materials with pore widths below 2 nm and high internal surface areas (65,66). This microporosity allows selective adsorption of small molecules such as H2, CO2, and CH4 while excluding larger species, giving materials such as ZIF-8 strong molecular-sieving behavior. ZIF-8 commonly exhibits BET surface areas in the range of 1400–2000 m2 g−1, while ZIF-67 shows similar pore dimensions and can reach even higher surface areas (67,68). Across the broader ZIF family, pore size and surface area vary substantially depending on topology and activation conditions (69). ZIFs are among the most thermally and chemically

stable MOFs, with decomposition temperatures often above 500–600 °C (70,71). Their robustness arises from strong metal–nitrogen bonds and the hydrophobic character of the imidazolate linkers, which reduce susceptibility to hydrolysis and solvent intrusion (72). However, stability may decrease in frameworks bearing more polar or bulky substituents, particularly under harsh chemical conditions (73).

ZIFs, particularly ZIF-8, are widely used in gas separation, catalysis, and CO_2RR because of their stability, tunable porosity, and adaptable active sites (74) In gas separation, ZIF-8 acts as a molecular sieve that selectively separates CO_2 from larger gases such as N_2 and CH_4 through a combination of size exclusion and preferential adsorption (75,76). This behaviour has been exploited in CO_2 capture and mixed-matrix membranes to improve CO_2/N_2 and H_2/CO_2 separation performance (77). In catalysis and CO_2RR, ZIFs provide a versatile platform for incorporating catalytically active metals such as Zn, Co, Fe, Cu, and Ni. In ZIF-8, Zn^{2+} sites exhibit Lewis acidity and can coordinate intermediates, while metal doping or ion exchange introduces further catalytic functionality without necessarily disrupting the framework (78). ZIF-derived materials are particularly important electrocatalysts. Pyrolysis of ZIF-8 can generate nitrogen-doped porous carbons containing atomically dispersed metal sites (M–N–C), combining high conductivity, large surface area, and efficient active-site utilization (79). These features make them well suited for multi-electron CO_2RR pathways. For example, Cu-doped ZIF-8 derivatives have been reported to achieve high Faradaic efficiency for CO formation at low overpotentials (80). In addition, ZIF-based structures can act as confinement scaffolds, stabilizing intermediates such as *COOH and *CO while suppressing HER, thereby improving CO_2RR selectivity (81).

1.5.2. Copper-Based Metal-Organic Frameworks

Copper-based metal–organic frameworks (Cu-MOFs) are a versatile class of crystalline porous materials that combine the redox activity of copper centres with the structural tunability of organic linkers. Unlike MOFs based on redox-inactive metals such as Zn^{2+} or Mg^{2+}, Cu-MOFs can actively participate in catalytic transformations because of accessible Cu(I)/Cu(II) redox couples, making them promising for adsorption, separation, and especially CO_2RR (82). Among these materials, Cu-MOFs based on 2-methylimidazole (2-mIm), often referred to as ZIF-like frameworks, have attracted considerable attention because of their stability in aqueous media, nitrogen-rich coordination environment, and tunable electronic properties (83). n these structures, Cu^{2+} centres are coordinated mainly by nitrogen atoms from the imidazolate ligands, although the coordination number and geometry can change depending on the synthesis conditions and framework topology. The methyl group of 2-mIm also affects the local polarity, hydrophobicity, and electron density around the Cu centres, which can influence CO_2 adsorption and the stabilization of reaction intermediates during electroreduction (84). An important characteristic of Cu-MOFs is their ability to undergo structural and electronic changes under electrochemical conditions. During CO_2RR, Cu^{2+} centres can be partially reduced to Cu^{+} or Cu^{0}, forming catalytically active species while retaining a significant part of

the original framework structure. This in situ transformation is central to their activity (85). Cu-MOFs based on 2-mIm have shown activity toward a range of products including CO, formate, methane, ethylene, and ethanol. In particular, C_{2+} formation is promoted by adjacent Cu sites or Cu clusters that facilitate C–C coupling through CO dimerization. The porous structure can further enhance selectivity by confining intermediates, modulating local pH, and influencing diffusion (86). From a mechanistic perspective, Cu-MOFs offer atomic-level control over active-site geometry, spacing, and electronic structure that is difficult to achieve with conventional Cu catalysts such as polycrystalline foils (87). Reversible Cu(I)/Cu(II)/Cu(0) redox transitions further tune local electron density, helping to stabilize intermediates such as *COOH and *CHO and thus enabling deeper reduction pathways (88–90). Their performance can also be adjusted through linker substitution, post-synthetic modification, and incorporation of conductive supports such as carbon nanotubes or graphene to improve charge transport and site accessibility (91). Operando studies using X-ray absorption spectroscopy and surface-enhanced Raman scattering have confirmed dynamic changes in Cu oxidation state and active-site structure during catalysis (92).

1.5.3. Ni-based materials

In CO_2RR research, growing attention has shifted from noble metals toward catalysts based on earth-abundant transition metals. Although Cu remains central because of its unique ability to form multicarbon products, nickel-based systems have emerged as attractive alternatives for the selective production of carbon monoxide, an important intermediate and industrial feedstock. Nickel-based catalysts are promising for CO_2RR because of their electronic structure and their ability to interact with key reaction intermediates, particularly *COOH and *CO. Their properties can also be adjusted at both the atomic and nanoscale levels, allowing their catalytic behaviour to be tuned. In the CO_2-to-CO pathway, Ni can bind CO strongly enough to promote its formation while still allowing its subsequent desorption. The partially filled d band of Ni also enables interaction with the electronic states of CO_2-derived intermediates, which can help stabilize the reaction intermediates and facilitate the overall reaction process. favourable thermodynamics for CO_2-to-CO conversion without excessively strong HER activity (94) These intrinsic properties have motivated the development of Ni-based catalysts beyond bulk metallic forms, including nickel sulfides (Ni_3S_2) and nickel-containing nitrogen-doped mesoporous carbons (Ni@NMC). Each class uses a distinct structural strategy to tailor local coordination, adsorption energetics, and electron transfer:

- Ni_3S_2 exploits sulfur incorporation to tune the electron density of Ni sites, enhancing CO_2 adsorption and suppressing HER through ligand and interfacial polarization effects (95,96).
- Ni@NMC uses a mesoporous nitrogen-doped carbon matrix as a conductive, high-surface-area scaffold while encapsulated Ni nanoparticles provide catalytically active centres with improved stability and dispersion (97,98).

The design of Ni-based catalysts has further benefited from advanced synthesis methods such as MOF templating, wet impregnation, and pyrolysis, as well as operando spectroscopies and DFT calculations, which together enable detailed understanding of structure–activity relationships. Such systems also provide opportunities for heteroatom doping, defect engineering, and interface modulation to suppress HER and improve CO_2RR selectivity. For these reasons, Ni-based materials occupy a central position in current CO_2 electroreduction research. Ni_3S_2 is a crystalline transition-metal chalcogenide with a hexagonal-rhombohedral lattice (space group: R-3m), in which Ni atoms are coordinated by sulfur in trigonal prismatic environments (99,100). In contrast to many simple oxides, the covalent Ni–S bonding imparts moderate conductivity and partial metallic character, which improves charge transport during electrocatalysis. Ni_3S_2 also exhibits mixed Ni^0/Ni^{2+} character, providing redox-active centers that may promote CO_2 adsorption, stabilization of *COOH intermediates, and subsequent CO evolution (101,102) The surface of Ni_3S_2 exposes multiple crystallographic facets, such as (101) and (110), each providing distinct coordination environments and adsorption behavior. These facets influence the binding energies of intermediates such as *COOH and *CO, thereby affecting overpotential and selectivity. Sulfur not only modifies the electronic density at Ni centers but may also influence proton-transfer behavior and suppress HER relative to CO_2RR (102).

1.6. Electrolyte

In CO_2RR, the electrolyte is not merely an inert ion-conducting medium; it plays an active role in determining catalytic behaviour at the electrode–electrolyte interface. Parameters such as pH, ionic composition, and buffer strength influence reaction thermodynamics, kinetics, and competition with HER (103–105). One of the most important electrolyte effects is its control over the local reaction environment. Although bulk pH may be well defined, the local pH at the catalyst surface can differ substantially under operating conditions because of proton consumption or hydroxide generation (106,107). This local environment affects the speciation of dissolved carbon, including CO_2(aq), HCO_3^-, and CO_3^{2-}, with important consequences for adsorption and reaction pathways (108). Figure 1-6 clearly illustrates that the solubility of CO_2 in aqueous electrolytes is strongly influenced by pH. As the pH rises above 8.2, the amount of free CO_2 decreases significantly, nearly vanishing altogether. Consequently, during CO_2RR, the availability of reducible CO_2 is typically low because CO_2 is consumed by reacting with OH^- ions in the electrolyte, forming carbonate (CO_3^{2-}), especially in neutral and alkaline conditions

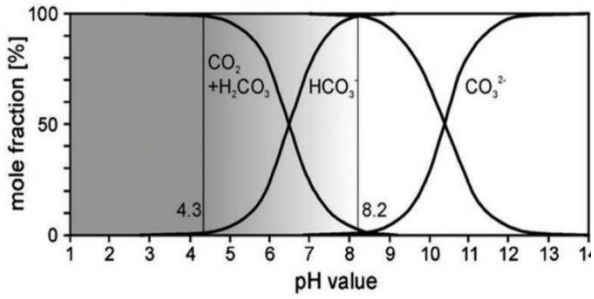


Figure 1-6. Solubility of CO_2, H_2CO_3, HCO_3 and CO_3^{2-} as a function of pH.

The structure of the electric double layer (EDL)[6] is also highly sensitive to electrolyte composition. In particular, the identity and hydration properties of cations strongly affect local electric fields and the stabilization of adsorbed intermediates through non-covalent interactions (109). Larger alkali cations such as Cs^+ and K^+ compress the EDL more effectively than smaller cations such as Li^+, which can favour multicarbon product formation on Cu by stabilizing *CO dimerization steps (110,111). The type of anion present in the electrolyte can also affect the conditions at the catalyst surface by changing the local solvation environment, the bicarbonate/carbonate equilibrium, and the competition between different species for surface sites (112). These effects can become even more pronounced at high current densities, where mass-transport limitations, carbonate formation, and gas evolution can progressively change the composition of the electrolyte close to the electrode (113). In a membrane-electrode assembly, the choice of electrolyte also has to be considered together with the ion-exchange membrane, since both influence ion transport, CO_2 crossover, and the pH gradient across the cell. Anion exchange membranes (AEMs), such as Sustainion®, are suitable for alkaline media due to their high OH^- conductivity and chemical stability, while cation exchange membranes (CEMs) like Nafion® facilitate proton transport and are more compatible with acidic or near-neutral environments (114,115). Taken together, these phenomena highlight the critical need to treat electrolyte selection as a design parameter rather than a background condition. A comprehensive understanding of electrolyte-catalyst-membrane interactions is essential for optimizing selectivity, activity, and stability in electrochemical CO_2 reduction systems.

1.6.1. Alkaline electrolyte

Alkaline electrolytes such as 1 M KOH (pH ≈ 13.7) are widely used in CO_2RR, particularly with Cu-based catalysts, because they strongly influence both reaction selectivity and system efficiency. One of the main advantages of this highly alkaline environment is suppression of HER. The very low proton availability significantly slows proton-driven side reactions, thereby shifting the reaction toward CO_2RR pathways that require fewer protons per electron

[66] The activity and selectivity of the cathode depend not only on the choice of catalyst but also on the composition of the electrolyte adjacent to the cathode (i.e., the electrical double layer (EDL)

transferred and improving selectivity toward C_1 and C_{2+} products (116). At the mechanistic level, the scarcity of protons hinders the Volmer step:

$$H^+ + e^- \rightarrow H^*$$

which is the initial and often rate-limiting step of HER. At the same time, the abundance of OH^- helps neutralize locally generated protons, maintaining a high interfacial pH near the catalyst surface even at high current densities. This localized alkaline microenvironment further reinforces CO_2RR selectivity by continuously suppressing hydrogen formation (116). However, these benefits come with an important trade-off: CO_2 availability near the electrode decreases because CO_2 readily reacts with hydroxide ions to form bicarbonate and carbonate species:

$$CO_2 + OH^- \rightarrow HCO_3^- \quad ; \quad HCO_3^- + OH^- \rightarrow CO_3^{2-} + H_2O \qquad \text{Eq. 1-14}$$

This conversion lowers the concentration of free CO_2 at the catalyst surface and introduces mass-transport limitations that can affect overall performance. Another major challenge in alkaline systems is carbonate accumulation. The formation and precipitation of carbonate species, particularly near the catalyst layer and membrane interface, can block active sites, increase transport resistance, and gradually degrade performance over time (117). Despite these limitations, 1 M KOH provides excellent ionic conductivity (~250 mS cm^{-1}), enabling low-resistance operation and supporting current densities above 200 mA cm^{-2}, which are relevant for industrial-scale electrolysis. Membrane selection is also critical in such systems. AEMs such as Sustainion® are commonly used because they combine high OH^- conductivity with good chemical stability in alkaline environments. They also reduce CO_2 crossover to the anode and generally offer better mechanical and chemical durability than many conventional AEMs, making them suitable for long-term CO_2RR operation (118).

1.6.2. Neutral-buffered electrolyte

Potassium bicarbonate ($KHCO_3$) is one of the most commonly used electrolytes for CO_2RR because it provides a buffered, near-neutral environment, with the pH typically remaining around 7.2–8.3. This helps maintain stable electrolysis conditions while supporting the formation of different products. A 2 M $KHCO_3$ solution can provide a suitable environment for both C_1 and C_{2+} products, particularly on polycrystalline Cu, where C–C coupling is strongly affected by the local CO coverage and pH. The buffering capacity of $KHCO_3$ mainly comes from the HCO_3^-/CO_2 equilibrium, which helps maintain the concentration of dissolved CO_2 during electrolysis and limits large changes in the local pH. The bicarbonate system can also act as both a proton donor and acceptor, participating in proton-coupled electron transfer (PCET) steps central to CO_2RR pathways (108). At the interface, 2 M $KHCO_3$ provides moderate ionic strength, which helps stabilize the EDL without causing excessive cation crowding near the catalyst surface. In this environment, K^+ ions play an important role in modulating catalytic behaviour. Because of their relatively large ionic radius and weak

hydration, K^+ ions accumulate near the electrode interface and enhance the local electric field. This effect strengthens CO adsorption and promotes C–C coupling, thereby favouring the formation of multicarbon products such as ethylene and ethanol (111). Membrane selection is also important in $KHCO_3$-based systems. Nafion® CEMs are frequently used because they allow selective cation transport while maintaining a proton gradient across the cell. However, long-term operation can lead to partial ion exchange within the sulfonic acid groups of Nafion, where K^+ ions, or Na^+ impurities, gradually replace H^+. This process may contribute to membrane degradation, pH drift, and a gradual decline in performance (114)

1.6.3. Interfacial electrolyte-electrode interactions

The electrode–electrolyte interface is the region where electrolyte composition directly interacts with the catalyst surface and therefore plays an important role in determining CO_2RR activity and selectivity. At this interface, solvated ions, water molecules, and adsorbed reaction intermediates are continuously rearranged in response to the applied potential and the local chemical environment. As a result, the behavior of the electrical double layer can affect both CO_2 activation and the subsequent conversion of surface intermediates (106,119). Alkali-metal cations are particularly relevant in this context. K^+ and Cs^+ can accumulate close to the electrode surface and modify the local electric field. These interfacial effects have been associated with changes in the stabilization of negatively charged intermediates, including $*CO_2^-$ and *COOH, and can consequently influence the surface coverage of *CO and the probability of C–C coupling. For Cu-based catalysts, the presence of K^+ has been linked to enhanced *CO dimerization, while the weaker hydration of Cs^+ allows it to approach the surface more closely and produce a different interfacial electric environment (120,121). In particular, K^+ ions present in both 1 M KOH and 2 M $KHCO_3$ preferentially accumulate near Cu surfaces, enhancing *CO dimerization and promoting ethylene formation (122). Larger cations such as Cs^+, because of weaker hydration, can approach the surface more closely than K^+, generating even stronger interfacial electric fields and further altering adsorption energetics, work function, and the potential of zero charge (123). The local pH at the electrode may also differ substantially from the bulk electrolyte. In alkaline operation, rapid proton consumption can increase the interfacial pH and thereby reduce the contribution of HER.(116). In acidic electrolytes, the high proton availability has the opposite tendency and can increase the competition from hydrogen evolution (124). Buffered electrolytes such as $KHCO_3$ can moderate these changes through the $CO_2/HCO_3^-/CO_3^{2-}$ equilibrium, although this buffering capacity may become insufficient at high current densities.

Ion-specific interactions provide an additional contribution. Cations may interact with adsorbed intermediates through outer-sphere interactions, while anions can modify interfacial hydration, surface charge, or adsorption behavior (125). Water itself is also an active component of the interface because it participates in proton-coupled electron-transfer steps and influences the stabilization of reaction intermediates through hydrogen bonding. These effects show that electrolyte selection cannot be separated completely from catalyst design: the local

environment established at the electrode surface is part of the catalytic system itself (126). Membrane transport is closely coupled to these interfacial phenomena. Proton-conducting Nafion® membranes can support acidic operation but may also facilitate water crossover and CO_2 loss, whereas anion-exchange membranes such as Sustainion® promote OH^- transport under alkaline conditions while introducing challenges related to carbonate accumulation and CO_2 crossover (127).

1.7. Electrochemical Cell Design

Catalyst performance cannot be considered independently of the reactor in which the electrochemical reaction takes place. The cell architecture determines how CO_2 reaches the catalyst, how ions move through the system, and how products and heat are removed. These effects become increasingly important as the current density increases because concentration gradients, local pH changes, gas evolution, and ion migration become more pronounced.
A typical CO_2RR electrolyzer contains a cathode, anode, ion-exchange membrane, gas diffusion layer, flow channels, and, depending on the configuration, one or more circulating electrolyte compartments. The relative arrangement of these components determines both mass transport and ohmic losses. Flow-cell and membrane-electrode-assembly configurations are particularly attractive for high-rate operation because gaseous CO_2 can be delivered directly to a gas diffusion electrode rather than relying exclusively on dissolution and diffusion through a bulk liquid electrolyte. (128). In a flow cell, continuous CO_2 feeding reduces the effective transport distance between the gas phase and catalyst layer and allows sustained product removal (129) Three-compartment designs provide additional control over the cathodic and anodic environments, while zero-gap architectures place the catalyst layer, membrane, and electrode in close contact and therefore reduce ionic transport distances. These configurations can support higher current densities, but they also introduce practical challenges, including water management, carbonate accumulation, membrane stability, and control of the local reaction environment (130). Consequently, the choice of electrochemical cell should be regarded as part of experimental design rather than simply as a hardware detail. Differences in transport conditions and interfacial composition can change the measured activity, selectivity, and stability of the same catalyst. Figure 1-7 shows representative CO_2RR cell configurations: (a) H-type, (b) three-compartment flow cell, and (c) zero-gap flow cell. Despite these advantages, challenges remain, including system complexity, cost, water management in GDLs (flooding vs. dehydration), electrolyte carbonation, and membrane degradation. At high current

densities, additional issues such as increased overpotential and heat generation arise, requiring careful optimization for stable long-term operation.

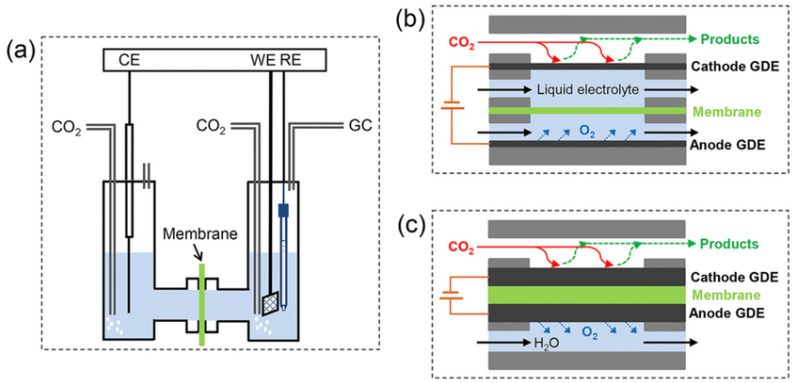


Figure 1-7. Schematic diagrams of CO_2 electrolyzers. (a) H-cell, (b) flow-cell and (c) MEA-cell (131).

1.7.1. Intrinsic Catalyst Activity versus Reactor Performance

The electrochemical response measured during CO_2 reduction reflects more than the chemistry of the catalyst itself. Catalyst composition and surface structure determine the intrinsic tendency of an active site to bind and transform reaction intermediates, but the experimentally observed response is also affected by catalyst loading, electrode morphology, electrolyte composition, gas transport, membrane properties, and operating conditions. (132). For this reason, geometric current density and Faradaic efficiency should be interpreted as measures of overall electrode performance rather than as direct descriptors of intrinsic catalytic activity. In principle, intrinsic activity is associated with the behavior of individual active sites under conditions where transport limitations and differences in accessible surface area are minimized. In practical CO_2RR experiments, however, these contributions are strongly coupled, particularly at high reaction rates. (132). This distinction becomes especially important when comparing different reactor configurations. In an H-cell, dissolved CO_2 must travel through the liquid electrolyte before reaching the catalyst surface, which can impose a strong mass-transfer limitation. A gas-diffusion electrode shortens this transport pathway by supplying CO_2 from the gas side of the electrode and can therefore sustain much higher reaction rates. However, the GDE introduces its own variables, including wetting, ion transport, gas permeability, and intermediate residence time. (133). Zero-gap MEA systems further increase this coupling because the catalyst, membrane, and gas-diffusion layer operate as a closely integrated unit. Consequently, changes in Faradaic efficiency or product distribution between an H-cell, flow cell, and MEA should not automatically be attributed to changes in intrinsic catalyst activity. The reactor itself can modify the local conditions under which the reaction proceeds.

1.7.2. Cathode

The cathode is the site of CO_2RR, where a catalyst deposited on a conductive substrate controls product selectivity. In gas-fed systems, gas diffusion electrodes (GDEs) are used to bring CO_2, the electrolyte, and the catalyst into close contact. The GDE is composed of a catalyst layer (CL) supported on a gas diffusion layer (GDL). The GDL provides a pathway for CO_2 to reach the active sites, while also maintaining electrical conductivity and reducing the risk of electrolyte flooding. Its hydrophobic nature is particularly important because it helps preserve the gas–liquid–solid interface needed for efficient CO_2RR. GDLs are typically made from porous carbon-based materials such as carbon paper or carbon cloth, which combine conductivity, porosity, and chemical stability (142). Structurally, single-layer GDLs consist only of a macroporous substrate (MPS), which allows direct gas transport but offers limited water management. GDL thickness generally ranges from 100 to 500 µm, with thinner layers often preferred to enhance mass transport (Figure 1-8). Hydrophobic treatment with PTFE, typically 10–30 wt%, is used to optimize wettability and balance gas permeability against flooding resistance, thereby maintaining efficient cell operation (143).

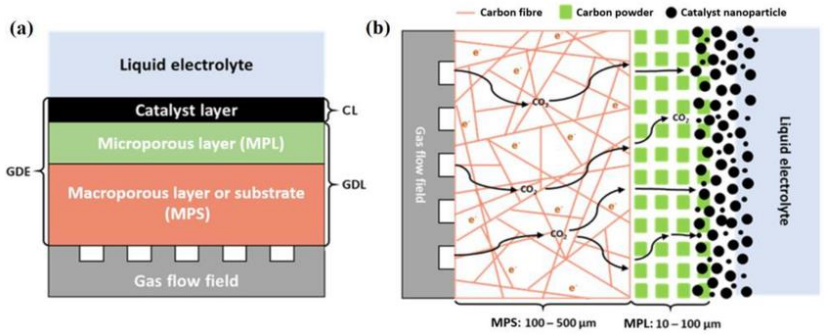


Figure 1-8. (a) Layered GDE between gas flow field and electrolyte, comprising a gas diffusion layer (MPS + MPL) and a catalyst layer (CL), (b) CO_2 diffuses through porous carbon-based MPS/MPL to the nanoparticle CL, while electrons are conducted to the catalyst.

1.7.3. Anode

In CO_2RR systems, the anode must exhibit high conductivity, chemical and electrochemical stability, and catalytic activity under strongly oxidative conditions. The most commonly used anode materials are iridium oxide (IrO_2) and mixed metal oxides (MMOs). IrO_2 is widely employed because it combines high catalytic activity for the oxygen evolution reaction (OER) with good stability in acidic and neutral media. Its relatively low OER overpotential and high resistance to corrosion can contribute to improved energy efficiency during electrolysis. The activity and long-term stability of IrO_2 also depend on the chemical environment and local structure of the Ir species, with Ir–Ir interactions playing an important role in these properties. (144,145). MMOs are often based on titanium substrates coated with oxides of Ir, Ru, or related noble metals. These coatings combine good electrocatalytic performance with reduced noble-

metal loading, lowering overall cost. MMOs also show stable performance in strong alkaline electrolytes and are therefore well suited for long-duration operation (146).

1.7.4. Membrane electrode assembly

Under an applied electric field, anion exchange membranes (AEM), and cation exchange membranes (CEM) exhibit distinct ion transport behaviors that strongly influence CO_2RR performance. Figure 1-9 illustrates the ion transport mechanisms and key differences between AEM, CEM.

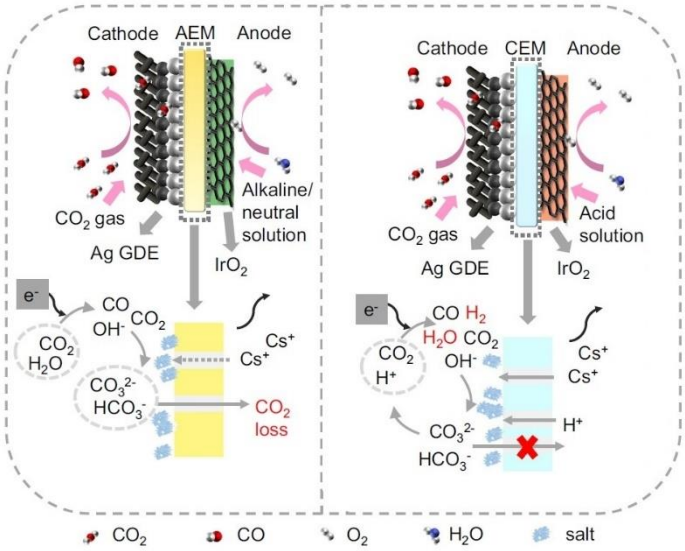


Figure 1-9. Schematic representation of the working principles of two types of membrane under an electric field. (AEM anion exchange membrane, CEM cation exchange membrane) (147)

AEMs are particularly important for CO_2RR under alkaline conditions, where they transport OH^- from cathode to anode, helping maintain a locally alkaline environment that suppresses the HER and enhances Faradaic efficiency for CO-derived products. However, AEM systems can suffer from unwanted transport of alkali metal ions, which may result in carbonate formation, salt precipitation, and loss of carbon during operation. CEM systems, on the other hand, mainly transport cations, but the accumulation of these ions near the cathode can cause local changes in pH and promote salt deposition. These effects can also increase competition from the hydrogen evolution reaction (HER) and eventually affect the stability of the gas diffusion electrode (147,148). Among the commercially available membranes, Sustainion® 37-50 is widely used because it combines good ionic conductivity with chemical stability and sufficient mechanical strength. It consists of a reinforced poly(phenylene) backbone functionalized with imidazolium groups and has a dry thickness of approximately 50 µm. In 1 M KOH at 60 °C, it exhibits a low area-specific resistance of about 0.045 $\Omega \cdot cm^2$ and ionic conductivity above 60 $mS \cdot cm^{-1}$, enabling efficient ion transport with limited ohmic loss (149).

CEMs conduct positively charged ions, primarily H^+, from the anode to the cathode. The most widely known example is Nafion®, a perfluorinated sulfonic acid polymer developed by DuPont. Nafion membranes are known for their chemical and thermal stability and their high proton conductivity, which makes them suitable for acidic CO_2RR systems and PEM electrolyzers. Nafion® 117 is one of the commonly used membrane grades, with a thickness of about 183 μm and an equivalent weight of 1100 g mol^{-1}. Depending on the temperature and hydration level, its proton conductivity is typically in the range of 0.1–0.2 $S \cdot cm^{-1}$. The sulfonic acid groups in the membrane facilitate proton transport, while the perfluorinated backbone provides the chemical stability needed under electrochemical operating conditions. However, in CO_2RR systems, CEMs such as Nafion® may favor HER over CO_2 reduction because of the high local proton concentration at the cathode interface. In addition, CO_2 crossover and carbonate formation in the anode compartment can cause performance losses and gas-management challenges. Despite these limitations, Nafion remains useful when acidic operation is required or when targeting specific products such as formic acid or methanol in tandem systems (150–152).

1.7.5. Flow channels and electrolyte compartments

Flow channels and electrolyte compartments are integral to the design and operation of electrochemical CO_2 reduction systems. Together, they control reactant delivery, product removal, ion transport, and the electrochemical environment at each electrode, thereby strongly influencing overall performance and efficiency. Flow channels are machined or molded into flow plates and direct the movement of gas and liquid reactants across the electrode surfaces. They also help remove the gaseous and liquid products generated during electrolysis. The geometry of the flow field has a direct effect on how evenly the reactants are distributed, the pressure drop across the cell, and the overall mass-transport behavior. Common configurations include serpentine, parallel, and interdigitated channels. As illustrated in Figure 1-10, each design creates different flow and transport conditions within the electrode. In particular, interdigitated channels can increase through-plane convection and provide more effective CO_2 transport to the catalyst layer than conventional serpentine channels. This effect was reported by Xing et al., who showed that flow-field architecture significantly influences CO_2 transport and CO_2RR performance in gas-diffusion electrolysis (153).

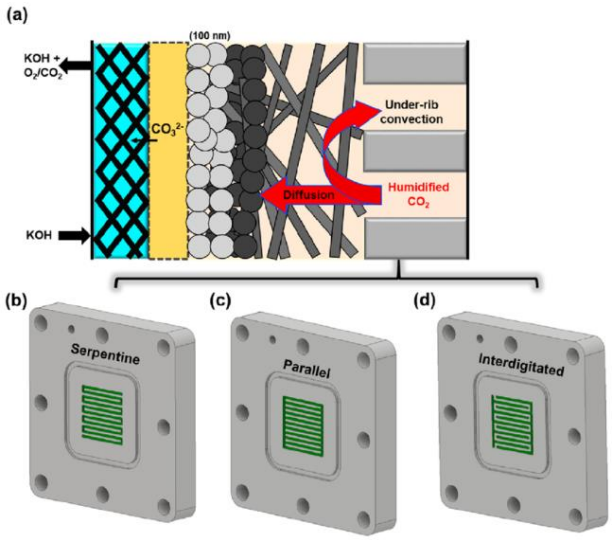


Figure 1-10. Illustration of the components of an exchange MEA cell with the catalyst layer on a carbon gas-diffusion layer. Shown here are the three different flow patterns at the cathode: (b) serpentine, (c) parallel, and (d) interdigitated flow patterns.

The electrolyte compartments, namely the anolyte at the anode and the catholyte at the cathode, complete the electrochemical circuit by enabling ion migration while supporting the respective half-reactions. In flow-cell configurations, these compartments also control electrolyte circulation, gas removal, and pH during electrolysis. As shown in Figure 1-11, the catholyte and anolyte are generally circulated through separate reservoirs, while the membrane allows ionic transport between the two sides and limits direct mixing of the products. Their design and operating conditions therefore have an important role in maintaining stable and efficient electrolysis. In CO_2RR systems, the anolyte is often an alkaline solution such as 0.5–1 M KOH, which provides a suitable environment for the OER at the anode. The alkaline conditions can improve OER kinetics and reduce the required overpotential (154). The anolyte is usually recirculated using a peristaltic or gear pump to maintain a relatively constant ionic strength, remove the O_2 produced at the anode, and limit pH gradients near the electrode surface. The catholyte, in contrast, can be operated either in recirculating or single-pass mode. In the recirculating configuration, the electrolyte continuously passes through the cathode compartment, giving better control over pH and ion concentration and helping to maintain stable catalytic conditions during operation (155). In single-pass operation, fresh electrolyte is continuously fed to the cathode, which can reduce product crossover and make the collection and analysis of liquid products such as formate or ethanol more straightforward. The choice between the two configurations depends on factors such as the product of interest, electrolyte consumption, and the overall design of the system. Recirculating catholytes are generally more suitable for extended operation, while single-pass operation can be more convenient when product collection and quantification are the main objectives.

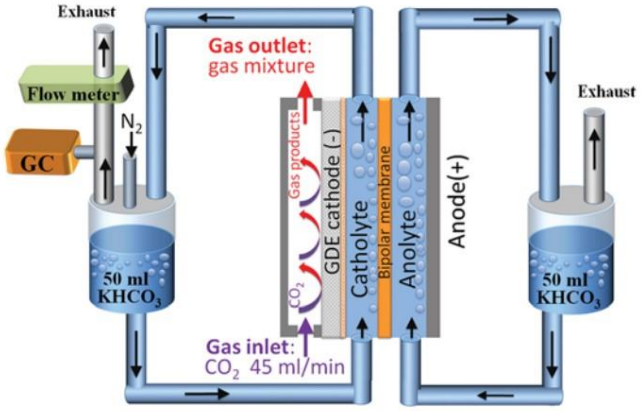


Figure 1-11. Schematic illustration of a flow-cell configuration for CO_2 electroreduction, showing separate catholyte and anolyte circulation loops, gas inlet and outlet streams, and membrane separation between the cathode and anode compartments

1.7.6. Reference electrode

The reference electrode provides stable potential against which the potential of the working electrode can be measured. In CO_2RR experiments, Ag/AgCl electrodes are commonly used because they provide a well-defined and reproducible reference potential, particularly in neutral and alkaline electrolytes (156). A limitation of conventional Ag/AgCl electrodes is that their porous junction can allow small amounts of Ag^+ to diffuse into the electrolyte. These Ag^+ ions may subsequently reach the working electrode and deposit on its surface. This can be particularly problematic for Cu electrodes, as the deposited Ag can influence the catalytic behavior and promote CO formation due to the intrinsic activity of Ag. Such contamination can therefore affect both product selectivity and the reproducibility of the measurements. To minimize this issue, leak-free Ag/AgCl electrodes, such as the LF-1 from BASi, can be used. Their non-porous junction prevents Ag^+ from leaking into the electrolyte, helping to maintain the composition of the electrolyte during long-term measurements. This is especially relevant in CO_2RR studies, where even small amounts of contamination can affect the observed product distribution. Double-junction Ag/AgCl electrodes provide another option, as an intermediate salt bridge further separates the internal reference electrolyte from the main electrolyte, although this design results in a larger and bulkier electrode. (157).

1.7.7. Gaskets

Gaskets are critical sealing components in electrochemical cells, serving to prevent gas and liquid leakage between compartments while maintaining uniform compression and mechanical stability across the cell assembly. They also help define the effective electrode area and ensure proper alignment of flow channels, membranes, and electrodes. The choice of gasket material must satisfy several requirements: chemical resistance to alkaline or acidic electrolytes, mechanical robustness under compression, low permeability to gases such as CO_2 or H_2, and

dimensional stability under operational temperatures and pressures. Common gasket materials used in electrochemical cells include polytetrafluoroethylene (PTFE), ethylene propylene diene monomer (EPDM), and silicone-based elastomers. PTFE is highly chemically inert and thermally stable, so it can be used under both acidic and alkaline conditions. Its main limitation is its low elasticity, which can make sealing more difficult when the cell is exposed to changes in pressure. EPDM is a synthetic rubber that combines good elasticity with resistance to KOH and acidic environments, and its ease of compression makes it widely used in fuel cells and CO_2 electrolyzers. Silicone-based elastomers are flexible and can withstand relatively high temperatures, although they may swell in some organic electrolytes, limiting their use in non-aqueous systems. In more advanced cell designs, gaskets are often custom-cut to match the shape and dimensions of the electrodes and membrane. This improves the seal and helps reduce the dead volume inside the cell. Choosing the appropriate gasket is important for maintaining stable operation over long periods and for preventing cross-leakage, particularly when the cell is operated at high current densities or under pressure.

1.8. Research Questions Addressed

These limitations point to the need for improved materials and a more systematic understanding of the factors that control CO_2RR performance. Based on these considerations, the following research questions were addressed in this thesis:

1. How can porous materials, including ZIF-derived and MOF-based catalysts, be designed and synthesized to improve CO_2 reduction activity and selectivity?
2. Which reaction pathways and intermediates play the main role in determining product distribution during electrochemical CO_2 reduction?
3. How do the electrolyte composition and operating conditions affect catalytic activity and product selectivity?
4. How can the electrode architecture and cell configuration be optimized to improve the efficiency and scalability of CO_2 electroreduction systems?
5. How can catalyst performance be systematically evaluated and related to the structural and surface properties of the material?

To address these questions, several catalyst systems were prepared and studied, including ZIF-based materials, mesoporous Cu-MOF flakes, and Ni_3S_2-derived nitrogen-doped mesoporous carbons. Their CO_2RR performance was evaluated using controlled electrochemical setups under different operating conditions. Electrochemical measurements together with product analysis were used to assess catalytic activity and selectivity, while structural and surface characterization was carried out to relate the observed performance to the properties of the materials. In addition, complementary studies on the oxygen reduction reaction (ORR) were performed to further examine catalytic behaviour and provide a basis for comparison and benchmarking.

1.9. Layout of the work

The current thesis is an effort to tackle the mentioned research questions. To address the questions properly, the thesis is divided in 7 chapters:

The **1st chapter** introduces the global carbon challenge and the fundamentals of electrochemical CO_2 reduction. It briefly covers reaction mechanisms, thermodynamic and kinetic aspects, catalyst development, electrolyte effects, and cell design, forming the foundation for the rest of the work.

2nd chapter describes the experimental and analytical methodologies used in this work. It details the electrochemical testing setups, along with operating conditions and electrode preparation techniques. The chapter also outlines the electrochemical methods employed, as well as product quantification, analysis, and structural and surface characterization techniques.

3rd chapter focuses on ZIF-based materials for electrochemical CO_2 reduction, presenting their synthesis methods followed by a discussion of the obtained results.

4th chapter explores mesoporous Cu-MOF flakes as a platform for the electrosynthesis of ethylene from CO_2, detailing the material preparation and corresponding performance results.

5th investigates Ni_3S_2 anchored nitrogen-doped mesoporous carbon for selective CO_2-to-CO conversion, including synthesis procedures and discussion of electrochemical performance.

6th chapter addresses the oxygen reduction reaction (ORR), covering material synthesis, performance evaluation, and RRDE analysis to assess catalytic activity.

Finally in the last chapter, some conclusions are brought, addressed research questions are highlighted, and possible future works are discussed.

1.10. Publication and conferences

Chapter 2. Methodologies

This chapter aims to provide a detailed overview of the principal methodologies employed for evaluating the performance of electrocatalysts in the context of CO_2 electrochemical reduction. We will delve into the electrochemical techniques used to assess activity, selectivity, and stability, alongside the analytical methods essential for identifying and quantifying the reaction products. Furthermore, the crucial role of surface characterization techniques in elucidating the catalyst's structural and chemical properties before and after electrochemical testing will be highlighted. By presenting a systematic examination of these evaluation methods, this chapter seeks to establish a foundational understanding for interpreting catalytic performance and comparing different catalytic systems reported in the literature. The challenges and important considerations associated with each methodology will also be discussed to promote rigor and reproducibility in the field.

The experimental measurements were carried out at Centre for Sustainable Future Technologies (CSFT) lab. It is located within the Environment Park of Turin through a collaboration between the IIT (Istituto Italiano di Tecnologia) Foundation and the Polytechnic of Turin, serves as an interdisciplinary hub dedicated to energy transition, sustainability, and the circular economy. Its research targets include reducing anthropogenic CO_2 emissions, improving renewable energy efficiency, and advancing green hydrogen technologies through the development of nanomaterials, catalysts, membranes, and integrated systems.





2.1. Electrochemical Testing Setups

2.1.1. Three-compartment flow cell assembly

Proper design and control of the electrochemical testing setup are essential for accurately evaluating catalyst performance in CO_2. In this thesis, two distinct electrochemical systems were employed: a three-compartment flow cell and a zero-gap MEA. The. Gas flow was regulated using computer-controlled mass flow controllers (MFCs), and liquid electrolytes were supplied via peristaltic pumps. Product gases were analyzed by gas chromatography (GC). When electrolyte was used, a mass flow meter was installed at the gas outlet to correct for deviations in gas flow caused by gas-liquid interactions within the system.

The three-compartment flow cell, illustrated in (Figure 2-1), was engineered to ensure a modular and efficient arrangement suitable for GDE testing. It comprises separate compartments for the anode, cathode, and gas handling, thereby enabling precise control of reactant and electrolyte flows.



Figure 2-1. three-compartment flow cell,

Gas diffusion electrodes were fabricated using Sigracet 28BC (SGL Technologies), with an active geometric area of 1.5 cm^2. The catalyst layer was deposited onto the microporous side of the GDE, which was oriented toward the membrane during assembly (Figure 2-2).

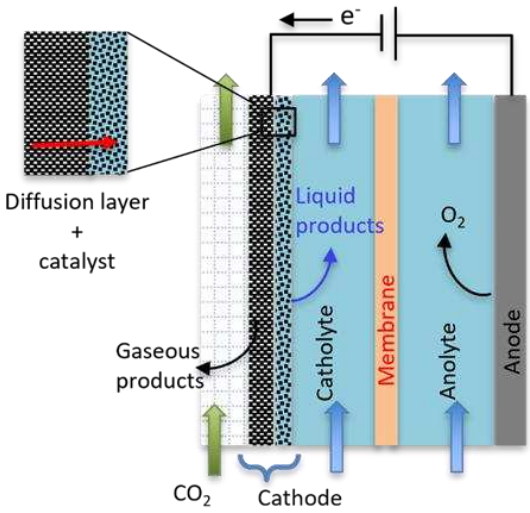


Figure 2-2. Schematic diagrams of 3-compartment flow cell

As shown in Figure 2-3, to ensure reliable electrical conduction between the GDE and the metallic flow field plate, copper tape was applied on the backside of the GDE, serving as a current collector. This configuration minimizes interfacial contact resistance and provides uniform current distribution across the active area while maintaining mechanical integrity under compression. A PTFE tape was applied to define the geometric active area, ensuring that only the exposed window participated in the electrochemical reaction. This approach allows precise control over the current density calculation by restricting the electrochemically accessible region.

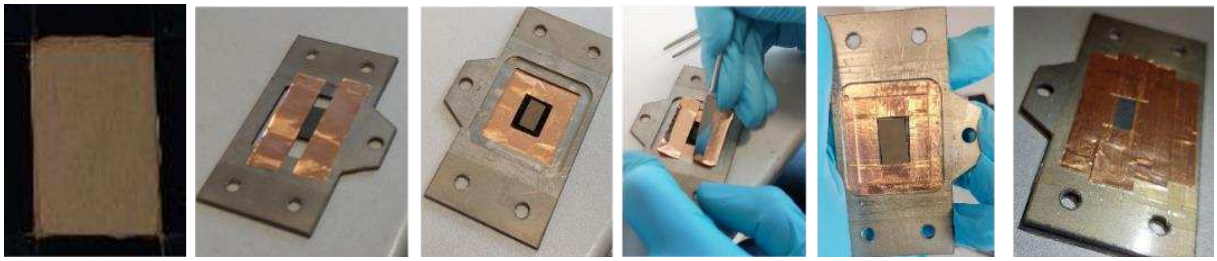


Figure 2-3. Preparation of the catalyst-coated gas diffusion electrode (GDE).

Following preparation of the catalyst-coated GDE, the assembly sequence of the electrochemical cell is illustrated in Figure 2-4 and was performed in a layered configuration using alignment pins to ensure precise positioning of all components.

A black sealing frame (gasket layer) was first positioned onto the white support plate and aligned using the guiding pins. This frame defines the outer boundary of the active region and provides the initial structural support for subsequent layers (Step 1). A central insert was then placed within the frame. This component does not function as a flow-field but rather acts as a spacer to adjust the chamber height and define the internal volume of the compartment (Step 2). A second black sealing frame was placed on top of the spacer to complete the base structure of the compartment and ensure proper sealing before inserting the electrode (Step 3). The anode electrode was positioned within the defined opening of the sealing frame, ensuring alignment with the active window. The anode electrode, consisting of an Ir-based mixed metal oxide (Ir-MMO, ElectroCell) coated on a titanium substrate, was positioned within the defined opening of the sealing frame. The anode was carefully aligned to match the membrane active area to ensure uniform current distribution and efficient oxygen evolution during operation (Step 4). The anolyte chamber was formed by placing the corresponding spacer frame. A plastic mesh was inserted inside the anolyte compartment to promote homogeneous electrolyte distribution and assist in bubble removal during operation (Step 5). The membrane separators included Nafion 117 (Ion Power) and Sustainion X37-RT (Dioxide Materials), chosen based on the desired pH and ion transport conditions; the separator was placed between two black sealing frames. These frames define the active area and control compression thickness, ensuring proper sealing and ionic conduction (Step 6). The catholyte chamber was assembled next. A reference electrode (1 mm mini-Ag/AgCl, leak-free type LF-1) was introduced into the catholyte compartment for three-electrode measurements. The catholyte inlet and outlet ports allowed continuous electrolyte circulation. A plastic mesh was again inserted to improve electrolyte flow distribution and facilitate removal of gas bubbles generated during CO_2 reduction (Step 7). A black sealing frame was positioned to define the cathode active area. The catalyst-coated GDE was then placed inside this frame, with the catalyst layer facing the membrane (Step 8). The backside of the cathode corresponds to the gas chamber through which CO_2 is supplied. The gas flow-field plate was positioned to distribute CO_2 uniformly across the electrode surface. To balance compression and maintain structural stability, an additional plastic mesh was inserted into this region (Step 9). A final black sealing frame was added, and

the top plate was positioned. The cell was then closed and compressed uniformly using bolts tightened in a cross-pattern to ensure homogeneous pressure distribution, stable electrical contact, and leak-free operation (Step 10). The system was equipped with peristaltic pumps to control the flow of the liquid electrolyte at a rate of 5 mL min^{-1}, while MFCs were used to precisely regulate the gaseous CO_2 feed. A mass flow meter was also installed at the outlet of the gas line, prior to the GC. This configuration enabled real-time monitoring and correction of the actual gas output rate, which was critical due to the complex interaction between gas and liquid flows in the system.

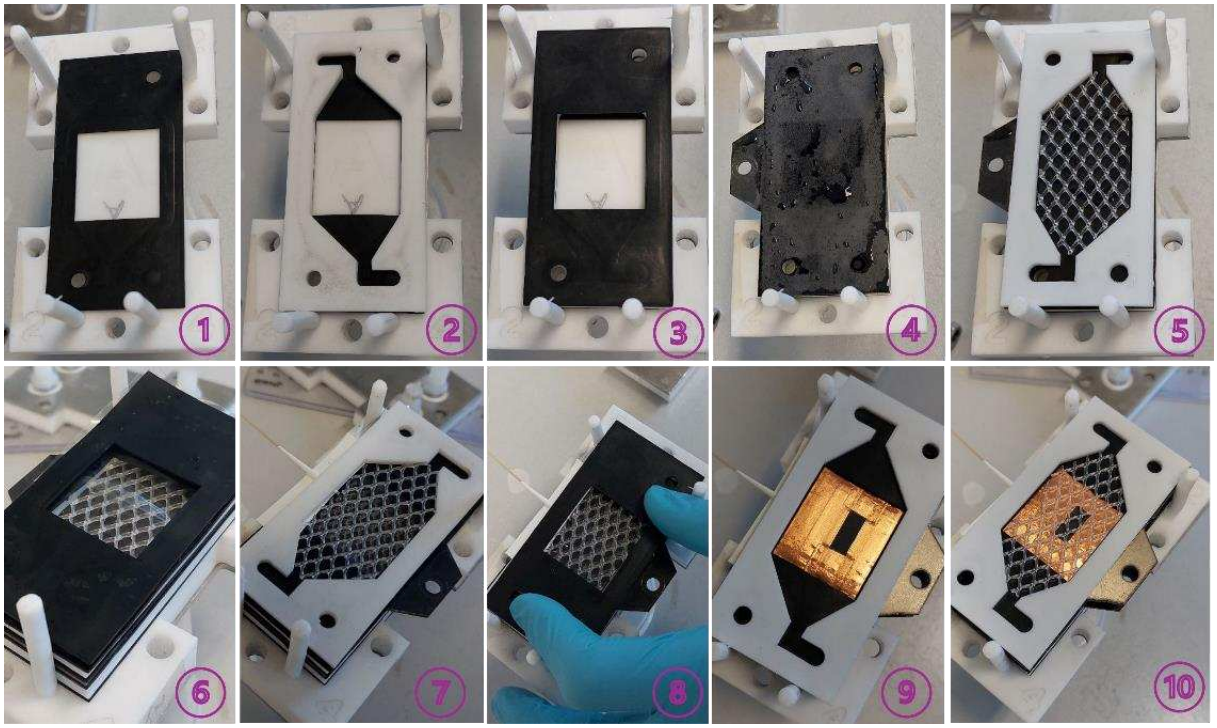


Figure 2-4. Sequential assembly of the three-compartment electrochemical flow cell, illustrating the ordered stacking of sealing frames, electrodes, membrane, and flow-field components.

2.1.2. Zero-gap assembly

In the zero-gap setup, the catalyst layer on the GDE was placed in direct contact with the ion-exchange membrane, eliminating the liquid electrolyte layer between them (Figure 2-5).

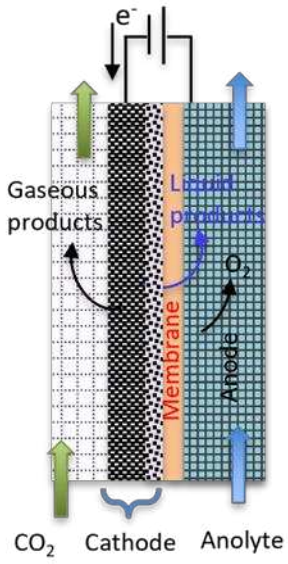


Figure 2-5. Schematic diagrams of zero-gap electrochemical cell (MEA-cell).

The same GDEs and membranes (Nafion or Sustainion) were used, ensuring consistency across setups. Gas and liquid feeds were similarly controlled with MFCs and peristaltic pumps, maintaining operational parity between both configurations.

Following preparation of the catalyst-coated GDE, the assembly sequence of the MEA electrochemical cell is illustrated in Figure 2-6 and was performed in a layered configuration using alignment pins to ensure precise positioning of all components. In contrast to the previously described flow-cell configuration, conventional gasket frames were not used. Instead, black sealing washers were employed to provide compression and prevent leakage of both gas and electrolyte during operation. The assembly begins from the liquid (anolyte) side. The front metallic plate containing the inlet and outlet ports was first positioned and aligned using the guiding pins (Step 1). These ports allow the connection of tubing for electrolyte circulation. A second plate containing elongated openings was then placed on top (Step 2). These openings function as flow distribution channels, ensuring homogeneous electrolyte access and minimizing concentration gradients across the electrode surface. Next, the serpentine flow-field plate was positioned (Step 3). This patterned structure promotes uniform liquid distribution across the electrode area while facilitating the removal of gas bubbles generated during operation. After forming the liquid distribution structure, the electrochemical layers were inserted. A metal mesh current collector (Ir-MMO) anode on titanium was first placed into the chamber (Step 4). This mesh ensures good electrical contact while maintaining an open structure that allows electrolyte transport. The ion-exchange membrane was then carefully positioned on top of the mesh (Step 5). The membrane separates the anode and cathode environments while allowing selective ion transport to maintain charge balance during electrolysis. Subsequently, the catalyst-coated GDE was placed on the cathode side with the catalyst layer facing the membrane (Step 6). The GDE provides a porous pathway for gas

transport and ensures effective contact between the catalyst layer, membrane, and gas phase. The gas-side distribution structure was then assembled. Two plates with channel patterns similar to those used on the liquid side were installed sequentially (Steps 7 and 8). These plates distribute the incoming CO_2 gas uniformly across the GDE surface and assist in the removal of gaseous reaction products during electrochemical operation. After all layers were aligned, the cell was mechanically sealed and compressed using bolts (Step 9). At this stage, the black sealing washers ensured tight sealing of the assembly and prevented leakage of both gas and liquid phases while maintaining uniform pressure across the MEA. Finally, the assembled cell was connected to the electrochemical measurement setup, including gas supply lines, tubing, and the potentiostat (Step 10). This configuration enabled stable operation of the MEA cell and efficient delivery of CO_2 directly to the catalyst layer during electrochemical CO_2 reduction experiments.



Figure 2-6. Stepwise assembly of the MEA electrochemical cell.

2.2. Electrode Preparation

Among the various techniques, drop casting remains one of the most widely adopted due to its simplicity, minimal equipment requirement, and suitability for small-scale research applications. Drop casting involves dispensing a measured volume of catalyst ink, typically containing catalyst particles, solvent (e.g., isopropanol or ethanol), and a polymeric binder such as Nafion, onto a substrate such as carbon paper, carbon cloth, or a gas diffusion layer. The ink is then allowed to dry under ambient or controlled conditions, forming a film on the surface. This method provides easy control over catalyst loading by adjusting the concentration and volume of the ink. However, challenges such as non-uniform film thickness, coffee-ring effects, and cracking during solvent evaporation may arise, particularly if the dispersion is not well-stabilized or drying is too rapid (158). Proper optimization of ink viscosity, solvent volatility, binder content, and drying environment (e.g., humidity, temperature) can mitigate these issues and produce more uniform films. The resulting morphology, especially for high-

loading electrodes, can influence gas diffusion, catalyst accessibility, and overall cell efficiency in CO_2RR applications. Drop casting is particularly advantageous for comparative studies where reproducible preparation and loading are critical. In contrast, Spray Coating offers improved layer uniformity and is more suitable for preparing large-area or scalable electrodes, especially in MEAs. The use of airbrush or ultrasonic sprayers allows fine control over film thickness and porosity. Electrodeposition, on the other hand, enables direct growth of catalyst layers onto conductive substrates, allowing precise control of metal loading, morphology, and oxidation state. This method is particularly effective for preparing nanostructured or crystalline films but requires electrical contact and more elaborate setups (159).

2.2.1. Binder effects and catalyst layer morphology

Binders play a crucial role in the fabrication of catalyst layers for CO_2RR., particularly in gas-diffusion electrode configurations. They serve mechanically anchoring the catalyst particles to the substrate, ensuring structural integrity, and providing ionic conductivity by forming percolating ion-conductive networks within the catalyst layer. Nafion® is one of the most commonly used binders in CO_2RR studies. It is a perfluorinated sulfonic acid ionomer with high proton conductivity, good mechanical stability, and wide commercial availability. However, its use can also have drawbacks in neutral and alkaline CO_2RR conditions. The hydrophilic sulfonic acid domains can create water-rich regions within the catalyst layer, which may favor the hydrogen evolution reaction (HER). A high Nafion content can also cover part of the catalyst surface and hinder gas transport. For this reason, Nafion is generally added at a binder-to-catalyst weight ratio of about 1:10 to 1:20, which provides sufficient mechanical cohesion while limiting its impact on gas and ion transport. For alkaline CO_2RR systems, particularly those based on anion-exchange membranes (AEMs), anion-conducting binders such as Sustainion® ionomer have also been introduced. Sustainion® is a quaternary ammonium-functionalized polymer that provides OH^- conductivity and good chemical stability under alkaline conditions. Its compatibility with the catalyst layer can improve ion transport and, under suitable operating conditions, support higher CO_2RR selectivity while limiting HER. These binders are particularly suited for gas-fed and zero-gap electrolyzers, where maintaining high local pH and minimizing parasitic reactions are essential for performance (160,161). In this work to avoid excessive ionomer coverage and mass-transport limitations, Nafion and Sustainion were incorporated as a binder 18.9 wt %.

2.3. Electrochemical Techniques

Electrochemical characterization is a central component in the development and benchmarking of catalysts for the CO_2RR. These techniques are used to evaluate the main performance parameters of a CO_2RR catalyst, including activity, selectivity, energy efficiency, and stability under both kinetic and mass-transport-limited conditions. The main aim of electrochemical testing is to understand how the applied potential affects the catalytic response, identify the onset potential and current density associated with specific products, and gain information

about the reaction pathway and possible rate-determining steps. A systematic electrochemical assessment can also provide information on electrode–electrolyte interactions, catalyst degradation, and the influence of operating parameters such as electrolyte composition, gas pressure, and temperature. Linear sweep voltammetry (LSV) and cyclic voltammetry (CV) are commonly used to examine electrochemical behavior and determine onset potentials, whereas chronoamperometry (CA) and chronopotentiometry (CP) are mainly applied to evaluate steady-state performance and long-term stability. Electrochemical impedance spectroscopy (EIS) provides mechanistic and kinetic information by analyzing charge transfer and mass transport processes at the electrode, electrolyte interface.
The following subsections detail the principles, applications, and methodological considerations of the key electrochemical techniques employed across the broader field of CO_2RR research.

2.3.1. Linear sweep voltammetry

LSV is fundamental electrochemical technique employed in the evaluation of electrocatalysts for the CO_2RR. This method provides useful information about the electrochemical behavior of a catalyst, including its onset potential, overpotential, redox activity, and overall catalytic response. During LSV, the potential of the electrode is swept linearly from an initial to a final value at a fixed scan rate, typically between 1 and 10 $mV \cdot s^{-1}$, while the resulting current is measured. One of the main purposes of this measurement in CO_2RR is to identify the onset potential (E-onset), which corresponds to the potential where the current begins to deviate noticeably from the capacitive response, indicating the start of Faradaic reactions. LSV can also be used to compare the electrochemical activity of different catalysts under the same experimental conditions. (162).
The current (i) response in LSV can be described by the Butler-Volmer equation, which relates the electrochemical reaction rate to overpotential (η):

$$i = i_0 \left[exp\left(\frac{(1-\alpha)nF\eta}{RT}\right) - exp\left(-\frac{\alpha nF\eta}{RT}\right)\right] \quad \text{Eq. 2-1}$$

Where:

- i_0 is the exchange current density ($A \cdot cm^{-2}$),
- α is the charge transfer coefficient,
- n is the number of electrons transferred,
- F is the Faraday constant (96485 $C \cdot mol^{-1}$),
- R is the universal gas constant (8.314 $J \cdot mol^{-1} \cdot K^{-1}$),
- T is the temperature (K),
- η is the overpotential (V).

For mass-transport-limited systems, such as gas-fed CO_2RR cells, the observed current often approaches a diffusion-limited plateau described by the Levich equation under hydrodynamic conditions. However, in stationary systems, a clear diffusion limit can also be inferred from the saturation current in the voltammogram.

2.3.2. Chronoamperometry and chronopotentiometry

CA and CP are time-resolved electrochemical techniques widely employed in the evaluation of catalyst stability, activity, and product distribution during CO_2RR. These methods enable the investigation of dynamic behavior under constant potential or constant current, respectively, and are particularly relevant for assessing long-term performance in both flow cells and MEAs. In chronoamperometry, the electrode potential is held constantly at a value determined from LSV or CV while the resulting current is monitored over time. This method is instrumental in determining FE when coupled with product analysis, evaluating catalyst stability under steady-state operation and assessing electrolyte compatibility and mass transport behavior. A declining current over time may indicate catalyst deactivation, electrode flooding, or product accumulation effects, especially in gas-fed systems. The total charge passed (Q) during CA can be calculated using:

$$Q = \int_0^t I(t)dt \qquad \text{Eq. 2-2}$$

Where t represents the elapsed time (in seconds) from the start of the chronoamperometry experiment (from when the potential is applied), Which, when combined with product quantification, allows for Faradaic efficiency calculations.
In CP, a constant current is applied while the resulting potential is monitored over time. This technique provides complementary insights into system behavior. For instance, potential drift can indicate catalyst degradation, changes in membrane resistance, or mass transport limitations. CP is also widely used for accelerated stress testing, as it simulates prolonged operation under industrially relevant current densities (>200 $mA \cdot cm^{-2}$). In gas-fed systems, potential oscillations observed during CP may signal various dynamic phenomena, including gas bubble accumulation and release, periodic electrolyte intrusion (flooding), and delamination or morphological instability of the catalyst layer. The choice between CA and CP ultimately depends on the objective of the measurement. CA is generally preferred for product quantification under controlled potential conditions, whereas CP is more suitable for assessing device robustness under application-relevant load conditions.(163).

2.3.3. Electrochemical impedance spectroscopy

EIS is an indispensable technique for dissecting the complex interplay of kinetic and transport phenomena in electrochemical systems, particularly in the context of the CO_2RR. Specifically, EIS facilitates the deconvolution of processes such as charge transfer, mass transport, and interfacial capacitance, which are critical for optimizing catalyst performance and reactor

design. In EIS, a small sinusoidal voltage perturbation is applied over a wide frequency range (typically 100 kHz to 0.1 Hz), and the resulting current response is measured. The system impedance Z(ω) is expressed as a complex function:

$$Z(\omega) = Z'(\omega) + jZ''(\omega) \qquad \text{Eq. 2-3}$$

where:

- Z' is the real (resistive) part,
- Z'' is the imaginary (capacitive or inductive) part,
- ω is the angular frequency, and
- j is the imaginary unit.

Nyquist plots (imaginary vs. real impedance) are commonly used to visualize the data (Figure 2-7). The high-frequency intercept with the Real axis corresponds to the solution resistance Rs, A semicircle (when observed) corresponds to charge transfer resistance (Rct), reflecting reaction kinetics at the catalyst surface. In GDE-based systems, this feature is often distorted or absent due to porous structures and coupled transport effects. At lower frequencies, deviations may indicate mass transport limitations, such as restricted CO_2 diffusion, although these features depend strongly on operating conditions. (164).

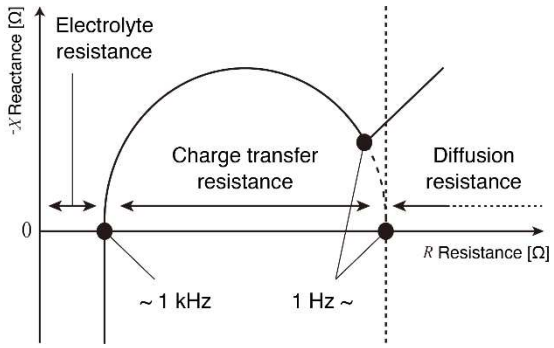


Figure 2-7. Nyquist plot showing key impedance contributions.

The Warburg impedance is given by:

$$Z_W = \sigma(1 - j)\omega^{-1/2} \qquad \text{Eq. 2-4}$$

σ is the Warburg coefficient, a constant that quantifies the strength of diffusion-related impedance in the system.

Unlike simple steady-state techniques, EIS enables a frequency-resolved analysis of processes such as charge transfer, double-layer formation, and gas/product diffusion, all of which are

critical in determining the efficiency, selectivity, and durability of CO_2RR systems (165). In high-current-density CO_2RR systems, especially in zero-gap cells, solution resistance (R_s) can result in substantial ohmic drops. Correcting the applied potential using iR compensation (typically 85-95%) is critical to isolate true electrocatalytic behavior. Without this, the potential applied to the working electrode may be significantly overestimated, leading to misinterpretation of reaction mechanisms or selectivity trends. To correct for this, iR compensation is applied:

$$E_{corrected} = E_{applied} - i \cdot R_s \quad \text{Eq. 2-5}$$

where:

- $E_{corrected}$ is the corrected potential,
- $E_{applied}$ is the measured potential,
- i is the current,
- R_s is the solution resistance.

2.4. Product Quantification

The column is coated with a stationary phase that interacts differently with the compounds in the sample depending on properties such as polarity, volatility, and molecular weight. As the gas mixture passes through the column, the individual compounds are distributed between the carrier gas and the stationary phase to different extents, causing them to leave the column at different times. The column is placed inside an oven where the temperature is carefully controlled, either at a constant value or using a programmed temperature ramp, depending on the volatility range of the analytes. The temperature profile affects the retention time of the compounds and therefore the separation quality and total analysis time. After separation, the compounds leave the column one after another and enter the detector, such as a Thermal Conductivity Detector (TCD) or Flame Ionization Detector (FID). The detector converts the response to each compound into an electrical signal, producing a chromatogram in which the signal intensity is plotted against retention time. The area of each peak is related to the amount of the corresponding compound and can be quantified using calibration curves prepared from standard gas mixtures. The main components of the GC system and their functions in the detection and quantification of CO_2RR products are summarized in Table 2-1. For CO_2RR measurements, reliable GC analysis requires careful calibration and correction for factors such as baseline drift, temperature changes, and variations in carrier-gas flow. The technique is particularly useful in flow-cell and zero-gap configurations, where gas products can be sampled continuously to monitor product distribution and determine Faradaic efficiency.

Table 2-1. Key components of a Gas Chromatography system used for CO_2 electroreduction product analysis, along with their specific functions in the detection and quantification process.

Component	Function
Carrier Gas	An inert gas (e.g., He, Ar, N_2) transports the sample through the system.
Sample Injector	Introduces the gas sample into the carrier stream.
GC Column	The heart of separation , packed or capillary tube with a stationary phase.
Oven	Maintains controlled temperature for efficient separation.
Detector	Detects separated components and converts them into electrical signals.
Data System	Outputs a chromatogram (peak vs. time), where peak area = component amount.

2.4.1. Gas-phase products quantification

Gas-phase products such as CO, CH_4, C_2H_4, and H_2 are commonly analyzed using GC. The total gas flow exiting the electrolyzer is monitored, and the molar fractions of products are determined by GC, calibrated against standard gas mixtures. The FE for gaseous products is calculated using:

$$FE_i = \frac{n_i . F . \chi_i . \dot{V} . P}{R . T . I} \times 100\% \quad \text{Eq. 2-6}$$

Or using molar flow rate directly:

$$FE_i = \frac{n_i . F . \dot{n}_\iota}{I} \times 100\% \quad \text{Eq. 2-7}$$

Where:

- χ_i = molar fraction of gas *i* in the outlet stream (from GC)
- $\dot{V}$ = volumetric flow rate (e.g., mL min^{-1})
- $\dot{n}_\iota = \chi_i . \dot{V_{gas}} / V_m$ = molar production rate (mol s^{-1})
- R = ideal gas constant (8.314 J $mol^{-1}K^{-1}$)
- T = temperature (K)
- P = pressure (Pa)

This approach requires accurate gas flow control, GC calibration, and iR-compensated voltage measurements to ensure reliability.

Drying tubes and gas sampling valves are essential to prevent moisture interference during gas analysis. Online GC enables real-time monitoring of product evolution, which is particularly important for capturing transient behaviors during CO_2RR. Accurate quantification requires proper calibration that accounts for detector response as well as gas matrix effects. In addition, mass flow controllers (MFCs) are employed to maintain stable and well-defined gas flow conditions throughout the experiment. (166).

2.4.2. Liquid chromatography

High-performance liquid chromatography (HPLC) is widely used for the separation, identification, and quantification of dissolved species in complex liquid mixtures. In CO_2RR studies, it is commonly employed to detect liquid products such as $HCOO^-$, CH_3COO^-, and oxalate ($C_2O_4^{2-}$), and in some cases alcohols (e.g., ethanol, propanol) with appropriate columns and detectors. HPLC operates by injecting a small sample into a high-pressure mobile phase that carries analytes through a stationary phase column, where separation occurs based on differences in polarity, charge, and hydrophobic interactions. A typical HPLC system consists of a pump, an injector, a chromatographic column, such as a C18 or ion-exchange column, a detector (UV–Vis, RI, or conductivity), and a data acquisition system. Compounds are generally identified from their retention times and quantified using calibration curves. In CO_2RR studies, ion-exclusion and ion-exchange columns are commonly used to separate short-chain carboxylic acids. Depending on the compounds being analyzed, detection can be carried out by UV absorption, usually around 210–220 nm, by refractive index detection (RI) for neutral species, or by conductivity detection in IC-HPLC systems. HPLC provides good sensitivity, reaching the millimolar to micromolar range, and usually requires only limited sample preparation. It is also compatible with a range of electrolyte compositions. One limitation is that volatile compounds and some alcohols are not always well suited to HPLC and may be better analyzed using NMR. For example, methanol may show poor retention under some conditions. In addition, relatively long elution times and peak overlap can occur, so the separation method may need to be adjusted depending on the products of interest.Liquid quantification

Liquid-phase products such as formate, acetate, ethanol, and propanol are typically dissolved in the catholyte. An overview of commonly detected liquid CO_2RR products, including their chemical formulas, electron transfer numbers, typical analytical techniques (e.g., HPLC or NMR), and relevant analytical considerations, is provided in (Table 2-2)

The FE for these products is calculated as:

$$FE_i = \frac{n_i.F.C_i.V_{elec}}{I.t} \times 100\% \qquad \text{Eq. 2-8}$$

Where:

- C_i = concentration of product *i* (mol/L)
- V_{elec} = electrolyte volume (L)

Table 2-2. Common liquid-phase products generated in electrochemical CO_2 reduction (CO_2RR), including their chemical formulas, number of electrons transferred (n), typical detection method (e.g., HPLC or NMR), and technical remarks relevant to analysis and system performance.

Product	Formula	e^- Transferred (n)	Detection (HPLC/NMR)	Remarks
Formate	$HCOO^-$	2	HPLC, NMR	Major product on Sn, Bi catalysts; stable in alkaline media
Methanol	CH_3OH	6	NMR, HPLC (RI detector)	Requires proper suppression of evaporation during sampling
Ethanol	C_2H_5OH	12	NMR, HPLC (UV/RI)	Dominant C_{2+} liquid on Cu; may appear in both catholyte and anolyte
Acetate	CH_3COO^-	8	HPLC, NMR	Stable under basic conditions; pH-dependent speciation
n-Propanol	C_3H_7OH	18	NMR	Minor C_3 product; indicative of advanced C–C coupling
Glycolaldehyde	$C_2H_4O_2$	10	HPLC (UV), NMR	Intermediate or trace product; may degrade in basic media
Acetaldehyde	CH_3CHO	10	HPLC (UV), NMR	Volatile; must be rapidly analyzed post-electrolysis

For HPLC, samples should be collected immediately after electrolysis to prevent post-electrolysis transformations such as CO_2 reabsorption or further reactions of intermediates like formate or acetate. Electrolyte samples are usually collected by taking a known volume with a gas-tight syringe or pipette. When needed, the sample is filtered immediately to remove suspended particles or catalyst residues that could interfere with the analysis. Internal standards, such as benzoic acid or dimethyl sulfoxide, can be added to improve the reliability of the measurements by accounting for variations in injection volume and detector response. After sampling, the solutions are stored in sealed containers, typically at around 4 °C, to limit the loss of volatile products such as ethanol and acetaldehyde. Moreover, pH fluctuations

during long-term CO_2RR can shift product distributions, particularly for weak acids (formic acid, acetic acid), making it necessary to monitor and, if needed, adjust pH before HPLC analysis to ensure consistent peak retention and quantification accuracy.

2.5. Structural Characterization

This section outlines the suite of advanced analytical techniques employed to probe the physicochemical properties of synthesized catalysts. A range of characterization techniques is used to understand the structural and chemical properties of the catalysts. X-ray diffraction (XRD) is used to determine crystallinity and identify the different phases present in the material. Scanning and transmission electron microscopy (SEM/TEM) provide information on particle size, morphology, and dispersion. Brunauer–Emmett–Teller (BET) analysis is used to measure the specific surface area and pore structure, both of which can affect reactant accessibility and mass transport. X-ray photoelectron spectroscopy (XPS) gives information about the surface composition and oxidation states, which is important for understanding the nature of potential active sites. X-ray absorption spectroscopy (XAS), particularly when performed under operando conditions, can further provide information on changes in the catalyst structure and oxidation state during CO_2RR.

2.5.1. X-ray Diffraction

XRD is a non-destructive analytical technique used to probe the long-range order of crystalline materials. XRD is employed to identify crystalline phases, assess phase purity, quantify crystallite size, and monitor structural transformations during synthesis or operation. These structural parameters are intrinsically linked to catalytic activity and selectivity, particularly in transition metal and metal oxide systems such as Cu, Ag, Sn, and Zn, where phase and oxidation state control are essential for product distribution (e.g., CO vs C_{2+} products) (167).

High-Angle XRD:

High-angle XRD (typically $2\theta > 20°$) probes short interplanar spacings, providing information on well-ordered atomic planes. It is governed by Bragg's Law, which defines the condition for constructive interference of incident X-rays scattered by crystal planes:

$$n\lambda = 2d\,sin\,\theta \qquad \text{Eq. 2-9}$$

Where:

- n is the diffraction order (typically 1),
- λ is the wavelength of the incident X-rays,
- d is the interplanar spacing,
- θ is the diffraction angle.

Crystalline materials diffract X-rays at specific angles corresponding to their unique lattice spacings, producing a pattern of peaks that serve as a structural fingerprint. The resulting diffractogram allows phase identification by matching with standard reference databases (e.g., JCPDS/ICDD).

Peak broadening in XRD patterns provides insights into nanocrystalline domain size and lattice strain. The average crystallite size can be estimated using the Scherrer equation:

$$D = \frac{K\lambda}{\beta \cos\theta} \qquad \text{Eq. 2-10}$$

Where:

- K is the shape factor (typically 0.89-0.94),
- β is the full width at half maximum (FWHM) of the diffraction peak (in radians),
- λ and θ are as defined above.

XRD is limited in detecting amorphous phases and surface-anchored nanoclusters (<2-3 nm). It is therefore often used together with TEM to obtain a more complete picture of the structure and composition of the material. The intensity of the diffraction peaks can also provide useful information about the structural features of the sample. For example, differences in the relative intensity of the peaks, especially when compared with standard powder diffraction patterns, can indicate preferred orientation or texture, which may result from anisotropic crystal growth. The shape and intensity of the peaks can also give an indication of the material's crystallinity. In general, broader and weaker peaks are associated with lower crystallinity or smaller crystallite sizes, as commonly observed in nanostructured materials. Such features can increase the accessible surface area and may provide a greater number of sites for catalytic reactions.

Low-Angle X-ray Diffraction :

Low-angle X-ray diffraction (LAXRD), typically measured over a 2θ range of 0.5° to 10°, is useful for studying long-range structural order in materials with periodic features on the nanometre scale, corresponding to d-spacings of approximately 2–50 nm. It is particularly useful for mesostructured materials because the resulting diffraction pattern can provide information about pore arrangement, interlayer spacing, and the overall periodicity of the structure. In mesoporous materials such as mesoporous carbons (CMK-3 and CMK-5) and silica-based materials (SBA-15 and SBA-3), the LAXRD pattern can show Bragg reflections arising from the regular arrangement of the pores. For example, CMK-5 shows several reflections at low angles that can be indexed to a hexagonal structure, indicating a well-ordered mesoporous framework. Similarly, SBA-1 materials prepared under controlled conditions can show well-defined reflections between 2θ = 1.5° and 3°, which are assigned to planes such as (200), (210), and (211) and confirm the cubic mesostructure.

In this thesis, HAXRD measurements were performed using a Rigaku Geigerflex D/Max-C series diffractometer with Cu-Kα radiation (λ = 1.5406 Å). The diffraction patterns were collected with a step size of 0.02° (2θ) and a counting time of 197 s per step. Prior to analysis, the powdered samples were finely ground in an agate mortar to ensure compositional homogeneity and reduce particle size effects. The powders were then carefully spread onto a zero-background silicon sample holder to minimize background scattering and enhance peak resolution. The sample surface was gently leveled to obtain a smooth and uniform layer, thereby ensuring reliable and accurate diffraction measurements. LAXRD measurements were performed using a PANalytical Empyrean powder diffractometer (Malvern PANalytical, United Kingdom) equipped with a PIXcel3D detector. The LAXRD patterns were collected in transmission mode using focusing mirror geometry with Cu $K\alpha_{1/2}$ radiation. The instrument was operated at an accelerating voltage of 45.0 kV and a tube current of 40.0 mA. Data acquisition was conducted in continuous scanning mode with a step size of 0.0131° (2θ) and a counting time of 50 s per step. Figure 2-8 shows the powdered sample mounted on the zero-background silicon holder prior to measurement, where (a) corresponds to the sample prepared for HAXRD analysis and (b) corresponds to the sample prepared for LAXRD analysis.



Figure 2-8. Sample mounting for (a) HAXRD and (b) LAXRD analysis

2.5.2. Electron Microscopy Characterization

SEM is employed to evaluate the morphological structure of electrocatalysts and catalyst layers, which directly influences electrochemically active surface area, mass transport, and long-term stability. SEM imaging is based on the interaction between a focused electron beam and the solid surface, generating secondary and backscattered electrons that provide topographical and compositional contrast with nanometer-scale resolution (168,169). SEM provides a direct way to examine the morphology of both the catalyst and the electrode. Parameters such as particle size, pore structure, film thickness, cracks, and surface roughness can be observed, and these features can affect the distribution of local current density and the paths available for CO_2 transport in gas diffusion electrodes (170,171). The depth of information obtained by SEM depends on the electron interaction volume, which changes with the accelerating voltage and the density of the material. Secondary electrons mainly originate

from the surface region, typically within the first few nanometers, while backscattered electrons come from a deeper region and can provide contrast related to composition. This difference is useful when comparing the material before and after electrolysis, since particle growth or agglomeration, pore collapse, and delamination of the catalyst layer may be associated with changes in catalytic performance or product selectivity (172,173). SEM can also be coupled with Energy-Dispersive X-ray Spectroscopy (EDS) to examine the elemental composition. The characteristic X-rays detected by EDS are generated within a micrometre-scale interaction volume, making it possible to map the distribution of different elements and obtain semi-quantitative compositional data. This is useful for checking features such as dopant distribution, phase segregation, and the homogeneity of alloyed materials. In CO_2RR catalysts, uniform elemental dispersion and absence of segregation are critical for maintaining consistent active-site chemistry and stable catalytic behavior (174). Together, SEM and EDS provide structural, compositional correlation, enabling identification of degradation mechanisms and verification of catalyst integrity before and after electrochemical operation.

In this thesis the morphology of the materials was examined using a Field Emission Scanning Electron Microscope (FESEM, Supra 40, Carl Zeiss) operated at 5 kV. SEM images were collected at magnifications between 1,000× and 250,000× to examine the particle size, morphology, and overall structural uniformity of the samples. For SEM analysis, the catalyst powder was dispersed in ethanol and gently sonicated before being drop-cast onto conductive carbon tape fixed to an aluminium sample holder. Elemental analysis was carried out using a Hitachi SU8600 SEM equipped with an EDS detector (XFlash® 7). Measurements were performed at an accelerating voltage of 10 kV to determine the elemental composition and its distribution within the sample. Figure 2-9 shows the sample mounting protocols for SEM electron microscopy

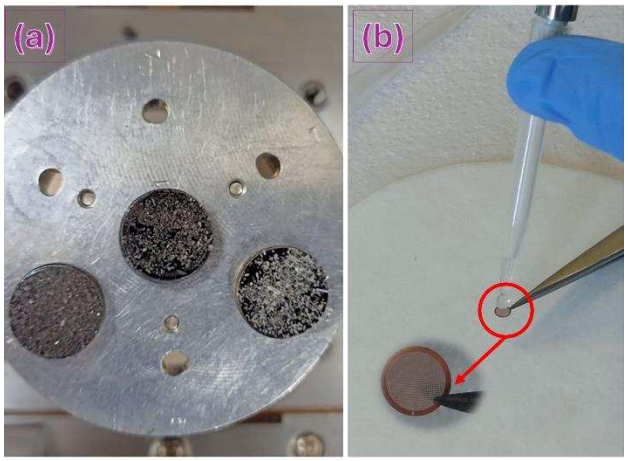


Figure 2-9. Sample preparation procedures for (a) SEM on conductive carbon tape and (b) on a holey carbon film supported on a 300-mesh copper grid.

2.5.3. Surface Area and Porosity Analysis

The BET method, based on physical adsorption of N_2 at 77 K, is a foundational technique to evaluate the specific surface area, total pore volume, and, when combined with advanced modeling, pore size distribution. These characteristics directly influence the accessibility of active sites, reactant transport, and stabilization of intermediates during electrochemical processes. The BET method quantifies the surface area by measuring the amount of nitrogen adsorbed on the material at different relative pressures. The general equation used for BET surface area determination is:

$$\frac{1}{\left[V\left(\frac{1}{P/P_0 - 1}\right)\right]} = \frac{C-1}{V_m C}\left(\frac{P}{P_0}\right) + \frac{1}{V_m C} \qquad \text{Eq. 2-11}$$

Where:

- V is the volume of adsorbed nitrogen at a given relative pressure P/P_0,
- V_m is the monolayer adsorption capacity,
- C is the BET constant related to the heat of adsorption,
- P is the equilibrium pressure,
- P_0 is the saturated vapor pressure of nitrogen.

The BET surface area is calculated from the linear part of the adsorption isotherm, typically within the relative pressure range of $P/P_0 = 0.05–0.30$. The total pore volume is estimated from the amount of N_2 adsorbed at $P/P_0 \approx 0.99$, assuming that the pores are filled with condensed nitrogen. The adsorption isotherm also gives information about how the gas interacts with the surface and the pore structure of the material. According to the International Union of Pure and Applied Chemistry (IUPAC) classification, the isotherm types most relevant to CO_2RR catalysts are shown in Figure 2-10.

- **Type I**: Characteristic of microporous materials (pore width <2 nm), with steep uptake at low relative pressures and a plateau indicating saturation. This is often observed in zeolites, carbon molecular sieves, and microporous metal organic frameworks.
- **Type II (Non-porous materials)**: A typical shape for materials with no significant porosity.
- **Type III (Weak adsorbent)**: Exhibited by hydrophobic materials, where the surface energy of adsorbent is lower than that of the adsorbate.
- **Type IV (Mesoporous materials)**: Characterized by a hysteresis loop in the desorption branch, indicative of mesoporosity (2-50 nm) These materials, such as mesoporous silica, carbon, and metal oxides, which are highly relevant for CO_2 electroreduction

catalysts. Mesopores provide substantial surface area for catalytic reactions, facilitating CO_2 diffusion and reducing diffusion resistance.

- **Type V (Microporous materials)**: Materials exhibiting very high adsorption capacity at low P/P_0, typical for microporous materials (pores <2 nm), which are also important for selective CO_2RR products.
- **Type II/III**: Represent macroporous or nonporous solids and are less relevant to CO_2RR catalyst optimization.

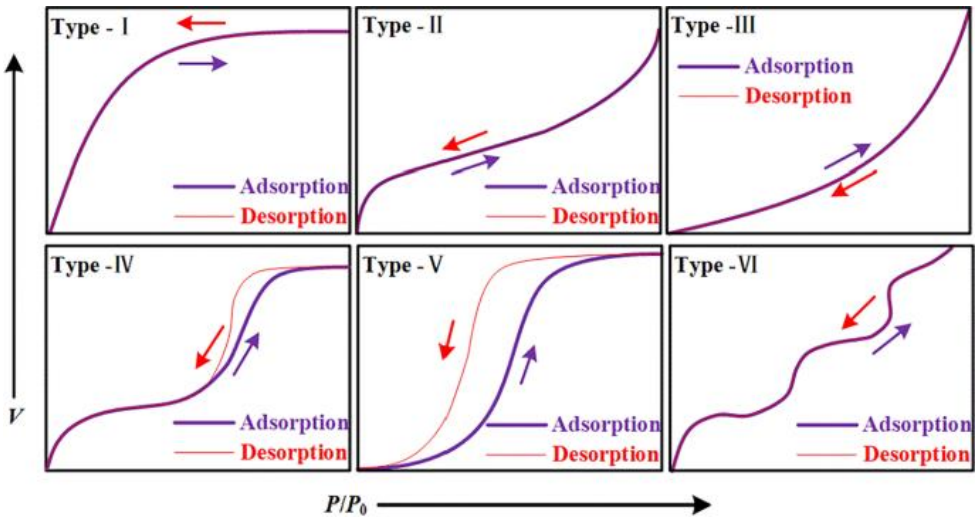


Figure 2-10. Schematic depiction of the six fundamental gas physisorption isotherm categories according to the IUPAC classification (175)

For mesoporous and microporous catalysts, the adsorption isotherms can show Type IV behavior, with a clear hysteresis loop associated with capillary condensation in the mesopores. The shape and size of the hysteresis loop can provide useful information about the pore structure and the connectivity between pores. Although the BET method is used to determine the specific surface area, it does not directly provide the pore size distribution (PSD). For a more detailed analysis of pore sizes, complementary methods such as Non-Local Density Functional Theory (NLDFT) are commonly applied to the adsorption data. The NLDFT approach is based on molecular-level simulations and is particularly useful for mesoporous and microporous materials. It considers factors such as pore geometry, surface roughness, and structural heterogeneity, which can be important when analyzing materials with more complex pore structures. The pore size distribution obtained using NLDFT can be derived from the adsorption branch of the isotherm by fitting the experimental data with NLDFT theory. This is often presented as a histogram showing the distribution of pore sizes across the sample, which is essential for understanding the diffusion and adsorption behavior of CO_2 in the catalyst pores. Other two features can be extracted from this characterization:

- **Pore Volume**: The total pore volume is typically calculated from the amount of adsorbed nitrogen at the highest relative pressure P/P_0 using the BET method. It is

indicative of the total volume of voids in the material, which can affect the rate of mass transport during electrochemical reactions.

- **Mesopore and Micropore Analysis**: Mesopores (2-50 nm) are particularly important for electrochemical reactions, as they allow for efficient transport of CO_2 and reduction intermediates. Micropores (<2 nm) are often associated with high selectivity but may limit the overall reaction rate due to slow mass transport. Understanding the pore size distribution helps in optimizing catalyst architecture to balance mass transport with reaction efficiency (176).

In CO_2RR systems, high mesoporosity is often desirable for enabling efficient CO_2 diffusion to the catalyst surface and facilitating bubble removal during reaction. Additionally, the presence of micropores may aid in stabilizing reaction intermediates, which is particularly important for selective production of higher-order products like C_2H_4 or C_2H_5OH on copper-based catalysts. A combination of mesopores and micropores can be useful for CO_2RR because the two pore sizes can contribute differently to the catalytic environment. Mesopores can facilitate CO_2 transport to the active sites and improve electrolyte access, which can support higher reaction rates. Micropores, in contrast, provide more confined environments that may affect the stabilization of reaction intermediates and, consequently, product selectivity. Materials that contain both mesoporous and microporous structures have therefore been reported to benefit from a balance between reactant transport and control of the local reaction environment, leading to improved CO_2RR performance. For example, mesoporous copper catalysts exhibit enhanced activity for the CO_2-to-C_2H_4 conversion, which is often associated with copper-based materials with tailored porous structures (226).

2.5.4. CO_2 Adsorption Isotherms

CO_2 adsorption isotherms provide essential insights into the surface affinity, adsorption capacity, and interaction strength of catalysts toward CO_2 molecules under ambient or near-operational conditions. Unlike N_2 adsorption, which is mainly used to determine textural properties such as surface area and pore size, CO_2 adsorption–desorption measurements can provide information about the affinity of the catalyst surface for CO_2 and the interactions between adsorbed CO_2 and the surface. This is particularly useful for microporous and surface-functionalized materials, where CO_2 adsorption can help evaluate the accessible pore volume as well as the nature of surface–CO_2 interactions. CO_2 adsorption measurements are commonly performed at 273 or 298 K by progressively increasing the CO_2 pressure from 0 to 1 atm and recording the amount adsorbed. The resulting adsorption isotherm is expressed as a function of the relative pressure, P/P_0, where P_0 is the saturation pressure of CO_2 at the measurement temperature (approximately 34 atm at 298 K).

Because CO_2 has a quadrupole moment and a relatively small kinetic diameter of about 0.33 nm, it can access ultra micropores smaller than 0.7 nm that may be difficult to probe using N_2 adsorption at 77 K. The resulting isotherms commonly show Type I(a) or Type I(b) behavior according to the IUPAC classification, which is characteristic of microporous materials (176).

The pronounced uptake at low pressure reflects the relatively strong interaction of CO_2 with the surface. This can be particularly relevant for N-doped carbons, where electron-rich sites can interact with CO_2, as well as for MOFs containing open metal sites and metal oxides with surface defects such as oxygen vacancies in CuO or TiO_2. To analyse the adsorption data in more detail, different isotherm models can be applied, including the Langmuir, Freundlich, Sips, and dual-site Langmuir models:

- The Langmuir model assumes monolayer adsorption on a surface with a uniform set of adsorption sites.

$$q = \frac{q_m b P}{1 + bP} \qquad \text{Eq. 2-12}$$

Where q is the amount adsorbed at pressure P, q_m is the maximum monolayer capacity, and b is the adsorption affinity constant. Dual-site Langmuir models accommodate heterogeneous adsorption centers (e.g., defect sites vs. basal surfaces):

$$q = \frac{q_1 b_1 P}{1 + b_1 P} + \frac{q_2 b_2 P}{1 + b_2 P} \qquad \text{Eq. 2-13}$$

This model is particularly useful in distinguishing between strong binding sites (e.g., nitrogen functionalities, metal defects) and weaker physisorption domains (177). The isosteric heat of adsorption (Q_{st}) is a critical descriptor reflecting the strength of interaction between CO_2 and the catalyst surface. It is determined from adsorption isotherms collected at multiple temperatures (e.g., 273 K and 298 K) using the Clausius-Clapeyron equation:

$$Q_{st} = -R \left(\frac{\partial \ln P}{\partial (1/T)} \right)_q \qquad \text{Eq. 2-14}$$

Where P is the equilibrium pressure, T the absolute temperature, and q the amount adsorbed.

- Q_{st} values of 25-40 kJ mol^{-1} typically indicate chemisorption or strong physisorption, beneficial for CO_2 capture and intermediate stabilization.
- Values <20 kJ mol^{-1} suggest weak van der Waals interactions and lower selectivity toward CO_2RR pathways.
- Values >40 kJ mol^{-1} may indicate chemical bonding, risking catalyst deactivation or slow desorption.

Notably, a decreasing Q_{st} with increasing coverage implies site heterogeneity, where stronger sites are filled first. Materials such as doped porous carbons and MOFs show such trends (178,179).

This thermodynamic descriptor is also correlated with the stabilization of reaction intermediates like $*CO_2^-$ or *COOH during CO_2RR, providing a bridge between adsorption studies and electrocatalytic performance.

2.5.5. X-ray Photoelectron Spectroscopy

XPS is a powerful surface-sensitive analytical technique extensively used in material science to investigate the elemental composition, chemical state, and electronic environment of elements present on the surface of solid materials. As catalytic processes such as the electrochemical CO_2RR occur at the catalyst-electrolyte interface, the surface properties of catalysts play a pivotal role in determining their activity, selectivity, and long-term stability. XPS, with a typical probing depth of 5-10 nm, provides direct insight into the surface chemistry of catalysts and supports the elucidation of structure-function relationships in catalytic systems. XPS relies on the photoelectric effect: a sample is irradiated with monochromatic X-rays (commonly Al Kα, 1486.6 eV), which leads to the emission of core-level electrons from specific atomic orbitals (e.g., 1s, 2p, 3d). The binding energy (BE) of each electron is calculated using the photoelectric equation:

$$E_B = h\nu - E_K - \phi \qquad \text{Eq. 2-15}$$

where E_B is the binding energy, hν the X-ray photon energy, E_K the kinetic energy of the emitted electron, and ϕ the work function of the spectrometer. Schematic representation of the XPS mechanism is reported in Figure 2-11. When monochromatic X-rays (hν) irradiate the sample, a core-level electron (e.g., 1s) is ejected if the photon energy exceeds its BE. The kinetic energy of the emitted photoelectron is measured and used to calculate the binding energy relative to the Fermi level and the spectrometer work function (Φ). The diagram also illustrates the relaxation process following core-hole formation, which can result in the emission of an Auger electron (180,181).

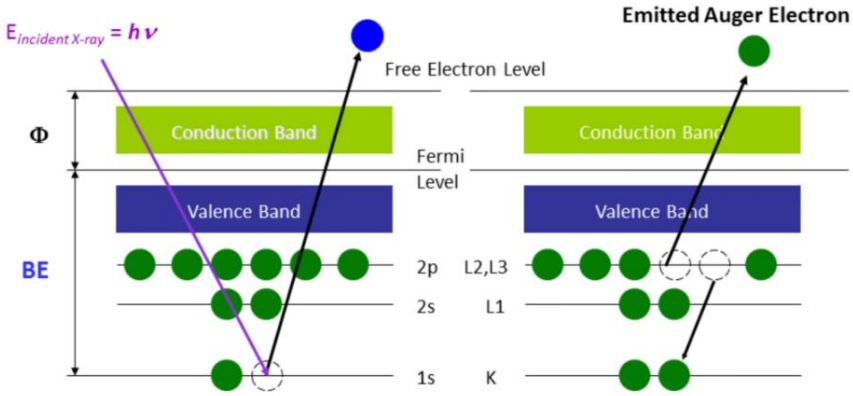


Figure 2-11. Schematic of the XPS photoelectric process showing core-level electron emission and subsequent Auger electron generation.

Each element exhibits characteristic core-level peaks, which are sensitive to both its oxidation state and chemical environment. This allows XPS to not only identify elements but also differentiate between chemical states, such as Cu^0, Cu^+, and Cu^{2+}, or different types of nitrogen species (e.g., pyridinic, graphitic, metal-bound).

XPS analysis generally begins with the acquisition of a survey spectrum, which covers a wide binding energy range (typically 0-1350 eV). This spectrum allows for the rapid identification of all elements present on the surface (excluding H and He, which are not detectable by XPS) and serves to verify elemental composition qualitatively. Following the survey, high-resolution (HR) spectra are collected for specific core-level regions of interest. These HR scans provide detailed chemical information by resolving peak shapes and potential satellite features. Deconvolution of these peaks using curve-fitting algorithms (e.g., Gaussian-Lorentzian functions) allows for the identification of specific oxidation states and coordination environments. Peak fitting is typically performed after Shirley or linear background subtraction, and the binding energies are referenced against adventitious carbon (C 1s at 284.8 eV).

Quantification and Relative Atomic Concentration

Semi-quantitative analysis is carried out by integrating the area under the HR peaks, corrected using relative sensitivity factors (RSFs). The relative atomic concentrations of elements present at the surface are calculated according to:

$$C_i = \frac{I_i/SF_i}{\sum I_j/SF_j} \qquad \text{Eq. 2-16}$$

where C_i is the atomic concentration of element *i*, I_i is the integrated peak area, and SF_i is the sensitivity factor for the corresponding orbital. This approach enables determination of surface elemental ratios (e.g., metal to nitrogen, metal to oxygen), which can then be compared with bulk measurements (e.g., from ICP-OES or EDS) to assess surface enrichment or depletion. In catalytic applications, this is critical to confirm the surface accessibility of active sites or to monitor post-reaction leaching or passivation effects.

Chemical State and Coordination Environment

One of the most valuable aspects of XPS lies in its ability to differentiate oxidation states and bonding environments. For instance:

- **Transition metals** such as Cu, Fe, Co, or Ni show characteristic core-level splitting (e.g., Cu $2p_{3/2}$and Cu $2p_{1/2}$) and satellite peaks that are diagnostic of valence states.
- **Nitrogen functionalities** (N 1s) in carbon-based catalysts may be deconvoluted into pyridinic, pyrrolic, graphitic, and metal-coordinated species.
- **Oxygen species** (O 1s) provide insights into surface hydroxylation, lattice oxygen, or adsorbed species.

These features are particularly informative when studying MOF-derived catalysts, heteroatom-doped carbons, or single-atom catalysts, where the coordination structure (e.g., M-N_4, M-O, or defect-bound species) dictates catalytic performance.

Post-Reaction Analysis and Stability Evaluation

XPS is also extensively employed in ex-situ post-electrolysis characterization to investigate potential changes in surface chemistry after catalysis. Shifts in oxidation state, the emergence of new chemical environments, or surface elemental redistribution (e.g., leaching, segregation, passivation) can all be monitored. This is especially important when evaluating catalyst stability, as structural transformations during CO_2RR, such as oxidation-reduction cycling, metal aggregation, or ligand degradation, can directly impact catalytic durability and selectivity. In certain cases, depth profiling by sequential argon-ion sputtering may be applied to differentiate between surface-only modifications and bulk structural changes, though care must be taken to avoid sputter-induced artifacts (182,183).
In this thesis XPS analysis was performed via a PHI 5000 Versaprobe analyzer, by using an Al k-alpha X-ray monochromated source (1486.6 eV), with a double neutralizer charge system (Ar ions and electrons beams) to compensate surface charging phenomena. Survey and HR scans have been collected choosing a Pass Energy (PE) equals to 187.85 and 23.50 eV respectively, a take-off angle of 45°, and an X-ray spot diameter of 100.0 μm. Binding energy scale was referred to C1s peak at 284.5 eV. MultiPak software (version 9.7.01) was used for data analysis.

2.5.6. Elemental and Compositional Analysis

EA, typically carried out via CHNS (Carbon, Hydrogen, Nitrogen, Sulfur) analysis, is a core technique used to determine the bulk elemental composition of a material, especially when organic frameworks or dopants are involved. CHNS analysis is based on the complete combustion of a carefully weighed sample, typically around 1–3 mg, in an oxygen-rich atmosphere. During combustion, the carbon, hydrogen, nitrogen, and sulfur present in the sample are converted into CO_2, H_2O, N_2, and SO_2, respectively. These gases are then detected using thermal conductivity detectors or infrared spectroscopy. From the measured amounts, the contents of C, H, N, and S are calculated as weight percentages relative to the total mass of the sample. Inductively Coupled Plasma Optical Emission Spectroscopy (ICP-OES) is a bulk elemental analysis technique commonly used to determine the concentration of metallic elements. In this method, the sample is first completely digested in acid and then introduced into a high-temperature argon plasma, typically at around 8000–10,000 K. The atoms and ions in the plasma become excited and emit radiation at wavelengths characteristic of each element. The intensity of these emissions is related to the concentration of the corresponding element and is determined using calibration standards (184). Total Reflection X-ray Fluorescence (TXRF) is another X-ray-based technique that is particularly useful for trace elemental analysis. The incident X-ray beam reaches the sample at a very small angle, below the critical angle for total reflection, which reduces background scattering and improves detection sensitivity. The excited elements then emit characteristic fluorescence radiation, which is quantified using an internal standard. Because TXRF requires relatively little sample preparation and is less affected by matrix effects, it allows rapid analysis of multiple elements

at trace levels and can be used alongside ICP-OES to verify the measured elemental concentrations. (185).
In this thesis, EA results helped assess the degree of carbonization in the catalysts and verified successful retention of nitrogen functionalities that are vital for CO_2RR selectivity. Elemental composition was also correlated with the XPS-derived surface atomic percentages to differentiate between surface enrichment or depletion phenomena. Combining EA with techniques like ICP-OES allows for full quantification of both non-metallic and metallic components, thereby ensuring accurate stoichiometric assessments of bimetallic or heteroatom-doped systems (186).
In this thesis Elemental Analysis was conducted by using a TruSpec 20 Micro 630-200-200 analyzer using 1-3 mg of sample. The combustion furnace was maintained at 1075 °C, and the afterburner operated at 850 °C. Carbon, hydrogen, and sulfur were detected via infrared absorption, while nitrogen was determined using thermal conductivity. The actual metal percentage was determined by ICP-OES on ICAP 7600 DUO spectrometer (Thermo Fisher Scientific). The ICP-OES measurements were performed using an auxiliary gas flow rate of 0.50 L min^{-1}, a cooling gas flow rate of 12 L min^{-1}, and a nebulizer gas flow rate of 0.50 L min^{-1}. The nebulizer gas pressure was set to 180 kPa, the RF power to 1150 W, and the peristaltic pump speed to 50 rpm. Elemental calibration was carried out using a four-point calibration curve, excluding the blank, with standard concentrations of 0.01, 0.1, 1, and 10 ppm. TXRF measurements were performed using a Bruker S2 Picofox spectrometer. For the analysis, approximately 2.5 mg of sample was placed in a 25 mL round-bottom flask and digested under reflux for 4 h using 10 mL of freshly prepared aqua regia (HNO_3:HCl = 1:3). After digestion, 40 mL of ultrapure water was added, and the solution was passed through a 0.45 µm nylon syringe filter to remove any remaining undissolved material. Yttrium (Y) was used as an internal standard for the quantification. The concentrations of the metal elements were then determined, with a detection limit of 0.011 ppm.

2.5.7. Vibrational Spectroscopy:

Raman spectroscopy is a vibrational spectroscopic technique that probes the inelastic scattering of monochromatic light (commonly from a laser source) when it interacts with molecular vibrations or phonons in a solid. The majority of scattered light remains at the same energy (Rayleigh scattering), but a small fraction is scattered with a shift in energy corresponding to specific vibrational modes of the sample, this is known as the Raman effect. The resulting spectrum provides a detailed molecular fingerprint and is sensitive to bonding, crystallinity, defects, doping, and chemical modifications. The intensity and position of Raman peaks reveal information about the atomic arrangement, making it ideal for characterizing carbon-based materials, metal oxides, and composites.
In carbon materials such as graphene, carbon nanotubes, amorphous carbon, or carbon supports in hybrid catalysts, two dominant features are usually observed in the Raman spectrum:

- **G-band (~1580 cm^{-1})**: Arises from the E_2g phonon of sp^2 carbon atoms in a hexagonal lattice. It is associated with the in-plane stretching vibration of C-C bonds in graphitic domains. A sharp G-band indicates high graphitization and crystalline ordering (187).
- **D-band (~1350 cm^{-1})**: Originates from the A_1g breathing mode of six-membered carbon rings and becomes Raman-active only in the presence of defects, such as edge planes, vacancies, heteroatoms (e.g., N, B, S), or sp^3-hybridized carbon atoms (188).

The intensity ratio between the D band and G band (I_D/I_G) is a critical parameter for quantifying structural disorder. An increase in I_D/I_G signifies a higher degree of defects and disruption of the extended π-conjugated network, while a lower ratio reflects a more ordered, graphitic structure. From an electronic perspective, excessive structural disorder interrupts π-electron delocalization and may reduce intrinsic electrical conductivity. However, in electrocatalytic systems such as electroreduction CO_2RR, a moderate level of defects is often beneficial. Defective sites can serve as adsorption centers for CO_2 and reaction intermediates, facilitating charge transfer and enhancing catalytic activity (239). Nitrogen doping, for example, increases I_D/I_G by introducing lattice distortions and modifying local electronic structure, which can improve CO_2 binding affinity and intermediate stabilization. (240). The I_D/I_G ratio is also related to the in-plane crystallite size (L_a) of graphitic domains through the Tuinstra-Koenig relation:

$$L_a(nm) = C(\lambda) \times \left(\frac{I_D}{I_G}\right)^{-1} \quad \text{Eq. 2-17}$$

where C(λ) is a wavelength-dependent constant (e.g., 4.4 nm for 514 nm excitation) (189). (18).

Complementary to Raman spectroscopy, FTIR spectroscopy probes vibrational transitions that involve changes in dipole moment. While Raman spectroscopy is sensitive to changes in molecular polarizability, FTIR detects vibrational modes associated with polar functional groups, making the two techniques fundamentally complementary. FTIR is particularly useful for identifying surface functionalities such as C=O, C-O, O-H, N-H, and metal-ligand bonds, which may not always be Raman-active. In carbon-based CO_2RR catalysts, FTIR enables verification of heteroatom incorporation, surface oxidation states, and functional groups that influence wettability, CO_2 adsorption, and interfacial charge transfer. In doped carbon materials, FTIR bands corresponding to C-N, C=N, or pyridinic/pyrrolic nitrogen species provide additional confirmation of successful heteroatom incorporation, supporting Raman-derived structural disorder analysis. Moreover, in MOF-derived or composite catalysts, FTIR allows identification of metal–oxygen or metal–nitrogen coordination environments, contributing to a comprehensive understanding of active site chemistry (190). By combining Raman and FTIR spectroscopy, both structural ordering (graphitic domains, defect density) and surface chemical functionalities can be simultaneously evaluated. This dual vibrational approach provides a more complete picture of catalyst structure, property relationships,

particularly in systems where electronic conductivity, defect density, and surface chemistry collectively determine CO_2RR activity and selectivity.
In this thesis Raman spectra were acquired in a Raman-FT Bruker RFS/100S instrument equipped with Nd:YAG (1064 nm) laser at 100 mW and 4 cm^{-1} for 1000 scans. FTIR spectroscopy was acquired using a Bruker Tensor 27 FTIR equipped with a SPECAC Golden Gate Diamond ATR accessory in the range of 4000-400 cm^{-1} and applying a resolution of 4 cm^{-1} and 256 scans.

2.5.8. Thermogravimetric Analysis

Thermogravimetric Analysis is a thermal analysis technique that measures the change in mass of a material as a function of temperature or time under a controlled atmosphere (e.g., air, O_2, N_2, or Ar). The mass change typically results from thermal decomposition, oxidation, desorption, or volatilization of components in the sample. In a typical TGA setup, the sample is placed on a high-precision balance inside a programmable furnace. The instrument records mass loss (or gain) while the temperature is ramped at a controlled rate (e.g., 5 °C min^{-1}), often up to 800-1000 °C, depending on the application. The resulting thermogram plots mass (%) versus temperature (or time), revealing the thermal stability, compositional information, and presence of labile species.
In this thesis TGA was performed using a Hitachi NEXTA STA 300 instrument under an air atmosphere between 25 and 800 ºC and at a heating rate of 5 °C min^{-1}.

2.5.9. X-ray Absorption Spectroscopy

X-ray Absorption Spectroscopy is an element-specific technique that probes the local electronic and atomic structure of materials by measuring the X-ray absorption coefficient as a function of photon energy across a core-level edge (191,192). When a core electron is excited, characteristic spectral features are generated that reflect oxidation state and local coordination. The X-ray absorption spectrum is generally divided into two main regions: the X-ray Absorption Near Edge Structure (XANES) and the Extended X-ray Absorption Fine Structure (EXAFS). The XANES region, extending roughly 50 eV around the absorption edge, is mainly related to the oxidation state and electronic structure of the absorbing atom. Changes in the edge position and white-line intensity can therefore provide information about the valence state and the covalency of the metal–ligand bonds. At higher energy, the EXAFS region extends several hundred eV above the absorption edge. It originates from the backscattering of the photoelectron by neighboring atoms and can be used to determine structural parameters such as interatomic distances and coordination numbers, as well as the degree of structural disorder. One advantage of EXAFS is that this information can also be obtained for materials that are amorphous or highly nanostructured. The probing depth depends on the detection mode. Transmission and fluorescence yield (FY) modes are bulk-sensitive, typically probing tens to hundreds of micrometers, whereas total electron yield (TEY) is surface-sensitive (~5-10 nm) due to the limited electron escape depth (193). For CO_2RR catalysts, XAS is particularly

valuable because it enables determination of oxidation states, identification of local bonding environments (e.g., metal-metal vs. metal-ligand coordination), and monitoring of structural evolution under operando conditions. These insights are essential for correlating atomic-scale structure with catalytic activity and selectivity.
In this thesis Soft XAS characterization was performed at the BACH beamline of IOM-CNR at the synchrotron radiation facility Elettra (Trieste, Italy). Measurements of the Cu L-edge and N K-edge were performed in both TEY mode, by recording the drain current through the sample using a Keithley 428 current amplifier, and FY mode, using a multichannel plate (MCP) detector (Hamamatsu, F4655-13) with an energy resolution better than 0.25 eV. The TEY and FY modes provide complementary information, probing the oxidation state of the Cu-MOF at the surface and in the bulk, respectively.

2.5.10. In Situ and Operando XAS

Operando XAS is a powerful, element-specific technique that provides direct insight into the electronic structure, oxidation state, and local atomic coordination of catalytic materials under real reaction conditions. In contrast to traditional ex-situ or static in-situ measurements, operando XAS is conducted while the catalyst is simultaneously undergoing electrochemical transformation, allowing the correlation of structural dynamics with catalytic performance metrics such as current density, product distribution, or Faradaic efficiency. One of the definitive advantages of operando XAS is its capability to elucidate transient states that arise only under applied potential and in the presence of electrolyte, which are often inaccessible by post-mortem or static characterization techniques (194). Electrocatalytic processes such as CO_2RR pose unique challenges for operando characterization due to the presence of electrolyte layers, gas evolution, and potential-dependent structural reconstruction. To address these challenges, custom electrochemical cells optimized for operando XAS have been developed. Such cells generally incorporate X-ray transparent windows and thin electrolyte paths to minimize absorption and scattering, while sustaining realistic reaction environments under applied potential. By integrating the operando cell into a synchrotron beamline setup, XAS measurements can be collected with minimal perturbation to the electrochemical interface and with sufficient signal-to-noise for both bulk and surface-sensitive observations (195). In copper systems central to CO_2RR research, operando XAS measurements at the Cu K-edge have revealed potential-dependent redox transitions that directly correlate with product selectivity and have demonstrated the persistence of oxidic Cu species even during active catalysis, pointing to dynamic bulk-surface relationships that traditional electrochemical characterization alone cannot resolve (196).
In this thesis operando XAS was used to monitor electronic and structural changes of a Cu-MOF during CO_2RR at the BACH beamline of Elettra Synchrotron, Trieste, Italy using a custom electrochemical cell optimized for soft X-ray operando studies (Figure 2-12). Cu L-edge spectra were acquired in fluorescence yield mode using an IRD AXUV100G photodiode at 25° to the incident beam. A 0.1 M CO_2-saturated $KHCO_3$ solution was flowed

through the cell with a peristaltic pump, and spectra were recorded at applied potentials from OCP to -1.4 V vs Ag/AgCl, enabling real-time observation of Cu oxidation state and coordination dynamics under operating conditions (197).

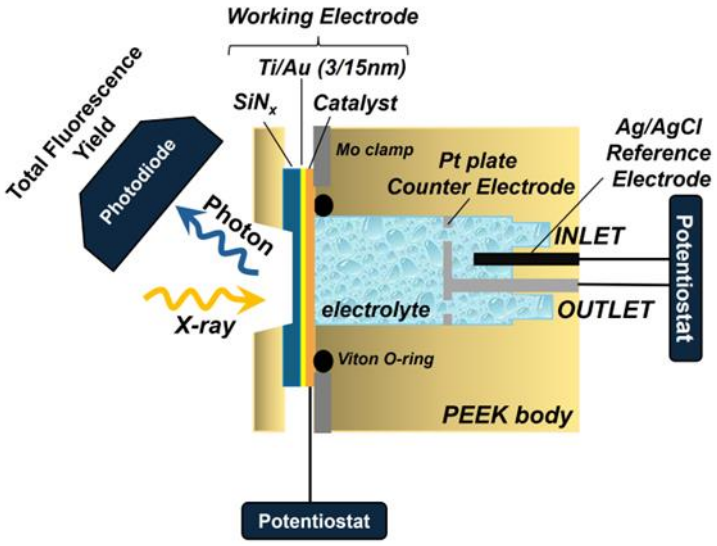


Figure 2-12. Scheme of the EC-cell and measurement setup for operando soft-XAS experiments implemented at the BACH beamline, Elettra Sincrotrone Trieste, reproduced from: Napal Azcona, I. X-Ray Spectroscopies for Hydrogen Based Economy (Doctoral Dissertation).

Chapter 3. ZIF-Based Materials

Building upon that general background in the previous chapters, the present chapter focuses specifically on the experimental work carried out during my PhD on ZIF-based materials synthesized via a green route and their application as electrocatalysts for CO_2RR. The core objective of this chapter is to investigate how an environmentally friendly steam-assisted dry-gel synthesis method can be used to tailor the structural, morphological, and electrochemical properties of ZIF materials. This chapter focuses in particular on ZIF-8 and ZIF-67, which have the same framework structure but differ in their metal centers, Zn^{2+} and Co^{2+}, respectively. This makes them a useful model system for examining how the metal center affects CO_2 activation and reduction. The chapter first describes the synthesis approach, in which the amount of water used to generate steam during the dry-gel process is systematically varied. The results show that this parameter has a strong effect on crystal growth, particle size distribution, and morphological uniformity, particularly in the case of ZIF-8. The synthesized materials are then examined through a series of physicochemical characterization techniques. Their electrochemical performance for CO_2 reduction is subsequently investigated using gas diffusion electrodes in flow-cell configurations. The effects of catalyst morphology, electrolyte composition, and applied potential on catalytic activity, product selectivity, and the CO:H_2 ratio of the resulting syngas are then discussed. A direct comparison between ZIF-8 and ZIF-67 highlights the contrasting electrocatalytic behaviors of Zn- and Co-based frameworks, despite their similar porous structures. Finally, the chapter addresses catalyst stability and discusses the limitations associated with MOF-based electrodes under continuous operation.

- Notice: Some of the material presented in this chapter has been previously published in "Green Synthesis of MOF-Based Materials for Electrochemical Reduction of Carbon Dioxide", ChemSusChem, 2024.

3.1. Materials and Synthesis Methods

ZIF-8 and ZIF-67 were synthesized using a solvent-free, environmentally benign steam-assisted dry-gel approach. Zinc acetate dihydrate (Zinc acetate dihydrate $(Zn(OAc)_2.2H_2O$, Sigma-Aldrich, ≥98%), and cobalt(II) acetate tetrahydrate $(Co(OAc)_2.4H_2O$, Sigma-Aldrich, ≥98%) were employed as the metal precursors for ZIF-8 and ZIF-67, respectively, while 2-methylimidazole (2-MeIm, Sigma Aldrich, 99%) served as the organic linker. All chemicals were used as received without further purification. Deionized water was utilized as the vapor source in the synthesis process. The synthesis was carried out in a Teflon-lined stainless-steel autoclave with a total volume of 100 mL, as schematically illustrated in (Figure 3-1). In a typical procedure, the metal salt (2.5 mmol) and 2-methylimidazole (25 mmol) were thoroughly mixed and placed into a quartz ceramic crucible. The crucible was then positioned at the center of the autoclave, while a controlled volume of deionized water was introduced at the bottom of the vessel, without direct contact with the solid reactants. The amount of water

was systematically varied to modulate the crystallization environment and investigate its influence on the resulting framework properties.
After sealing, the autoclave was heated in an oven at 120 °C for 3 h, allowing water vapor to act as a transient reaction medium and promote the formation of the ZIF structure through vapor-assisted coordination between the metal ions and imidazolate ligands. Upon completion of the thermal treatment, the autoclave was allowed to cool naturally to room temperature. The resulting solid product was collected by centrifugation and washed several times with a water–ethanol mixture to remove unreacted species and residual ligands. The recovered powders were subsequently dried under vacuum at 60 °C to obtain the final ZIF materials.
The synthesized samples were denoted as ZIF-8_X or ZIF-67_X, where X corresponds to the volume of water used during the steam-assisted synthesis. This notation was adopted to clearly distinguish samples prepared under different vapor conditions and to facilitate systematic comparison of their physicochemical properties. The steam-assisted dry-gel method offers significant advantages over conventional solvothermal routes, including the elimination of toxic organic solvents, improved control over crystal growth, and the ability to tailor particle morphology and size through simple adjustment of the water content. These features make this synthesis strategy particularly suitable for producing porous ZIF materials intended for electrochemical applications.

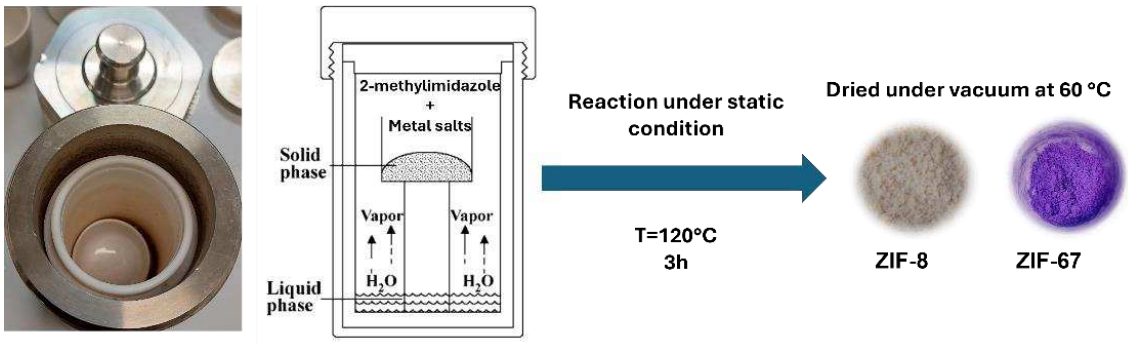


Figure 3-1. Schematic illustration of the steam-assisted dry-gel synthesis setup for ZIF materials.

3.2. Results and Discussion

3.2.1. Physicochemical properties

The physicochemical characterization results demonstrate that the steam-assisted dry-gel method successfully yields crystalline ZIF-8 and ZIF-67 materials, with their structural and morphological properties strongly influenced by the synthesis conditions. In fact, X-ray diffraction analysis confirms that all ZIF-8_X samples exhibit diffraction patterns consistent with the characteristic sodalite-type framework, indicating phase purity across the investigated water vapor volumes (Figure 3-2a). An increase in diffraction peak intensity with increasing water content suggests an enhancement in crystallinity, highlighting the critical role of water

vapor in facilitating framework growth and structural ordering during the dry-gel synthesis process. A direct comparison between ZIF-8_20 and ZIF-67_20 further confirms their isostructural nature, while differences in peak broadening indicate variations in crystallite size that can be attributed to the distinct metal precursors employed (Figure 3-2b) (198).

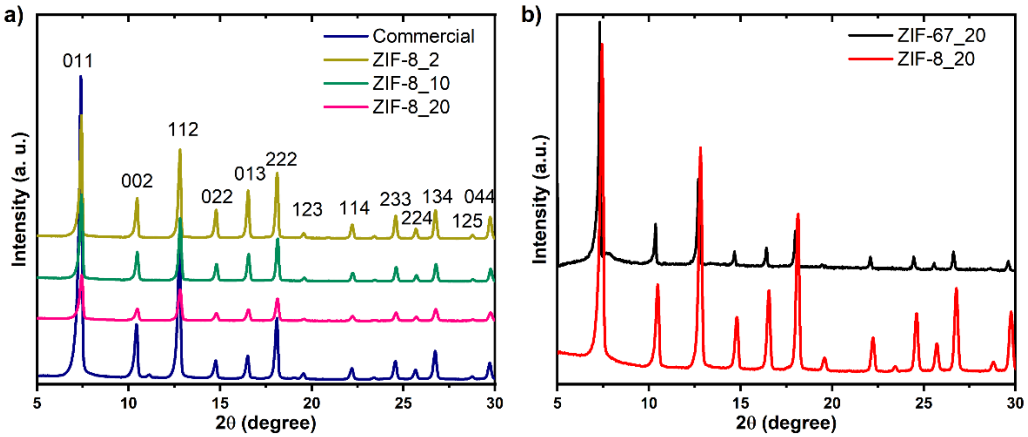


Figure 3-2. XRD pattern of (a) ZIF-8 synthesized with different volumes of water and its commercial analogue, (b) ZIF-8 and ZIF-67 synthesized with 20 mL of water (199).

On the other part, morphological analysis by FESEM reveals a strong dependence of particle size, shape, and homogeneity on the volume of water used during synthesis, as illustrated in (Figure 3-3). At low water content, ZIF-8_2 materials exhibit inhomogeneous crystal growth accompanied with an average size of 2 µm are observed. Many smaller particles are also displayed over the bigger crystals, probably due to unreacted salts resulting from the incomplete reaction (Figure 3-3a) These wide distributions are consistent with insufficient vapor-mediated mass transport and incomplete coordination between metal ions and imidazolate linkers. Increasing the water volume leads to progressively narrower and more symmetric size distribution histograms (Figure 3-3b), reflecting improved regulation of crystal growth. At intermediate water contents 20 mL, a well-defined unimodal distribution centered at smaller particle sizes is observed (Figure 3-3c and d), in agreement with the formation of uniform, well-faceted polyhedral crystals visible in the corresponding FESEM micrographs. This is further supported by the quantified particle size distribution plots (Figure 3-4b and c), which exhibit narrow, symmetric histograms with minimal skewness, indicating a high degree of size uniformity and controlled crystal growth. This behavior highlights the existence of an optimal vapor environment that balances nucleation and crystal growth, resulting in structurally homogeneous ZIF-8 particles. In contrast, excessive water vapor let to the coexistence of small crystallites and larger agglomerates, indicating accelerated growth and particle coalescence that compromise morphological uniformity (Figure 3-3e and f). This behavior is clearly reflected in the corresponding particle size distribution histograms (Figure 3-4e and f), which display wider, asymmetric profiles with extended tails toward larger particle sizes, confirming increased polydispersity and heterogeneous growth dynamics. The

morphology of ZIF-67_20 synthesized under comparable conditions exhibits distinct characteristics compared to ZIF-8_20, both in terms of particle size and crystal shape, despite being synthesized under the same water content (Figure 3-3g and h). The size distribution histograms are shifted toward larger particle sizes and remain relatively broader (Figure 3-4h and i) This further highlights the critical role of the metal precursor (salt nature) in tuning the morphology of ZIF materials. Moreover, these observations are consistent with the XRD results, which indicate smaller particle sizes for ZIF-8_20.

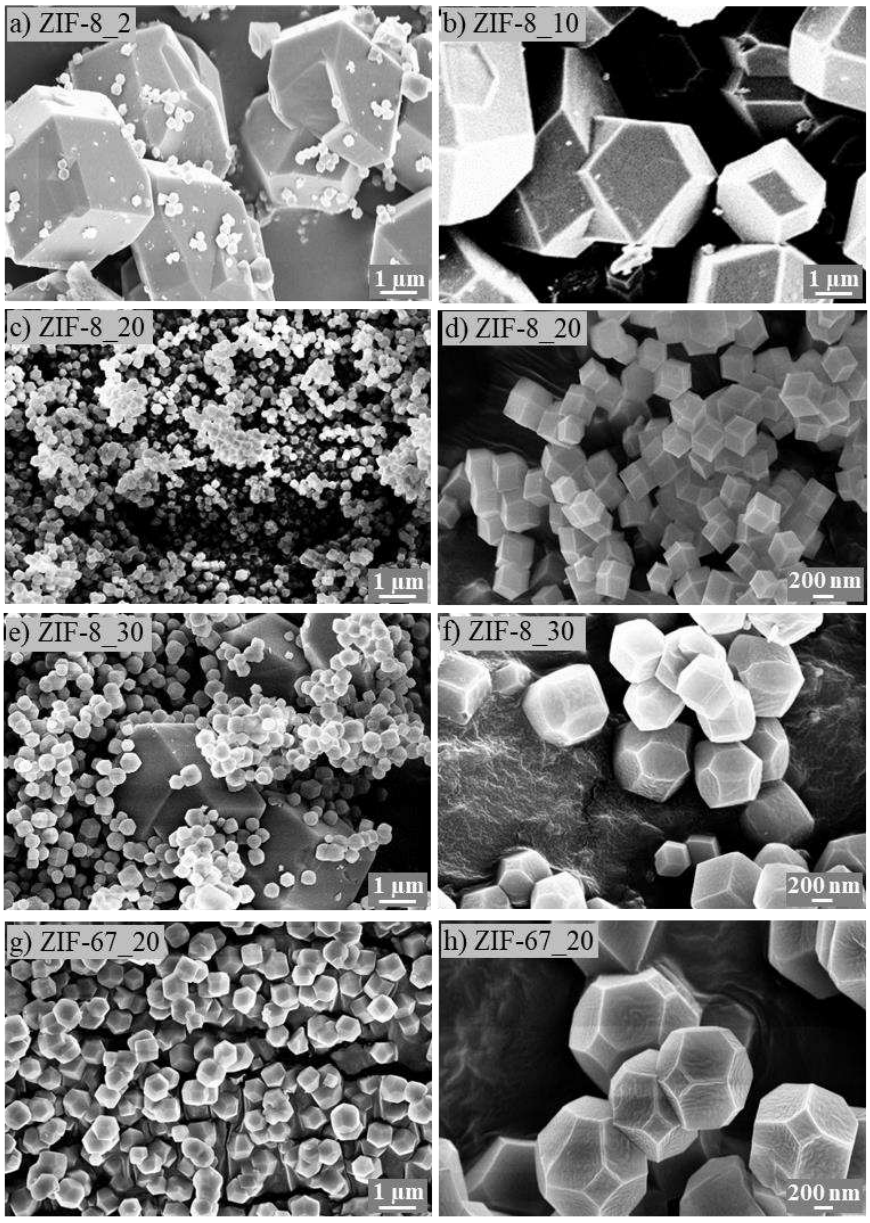


Figure 3-3. SEM images of (a) ZIF-8_2, (b) ZIF-8_10, (c,d) ZIF-8_20 (low and high magnification), (e,f) ZIF-8_30 (low and high magnification) and (g,h) ZIF-67_20 (low and high magnification) (199).

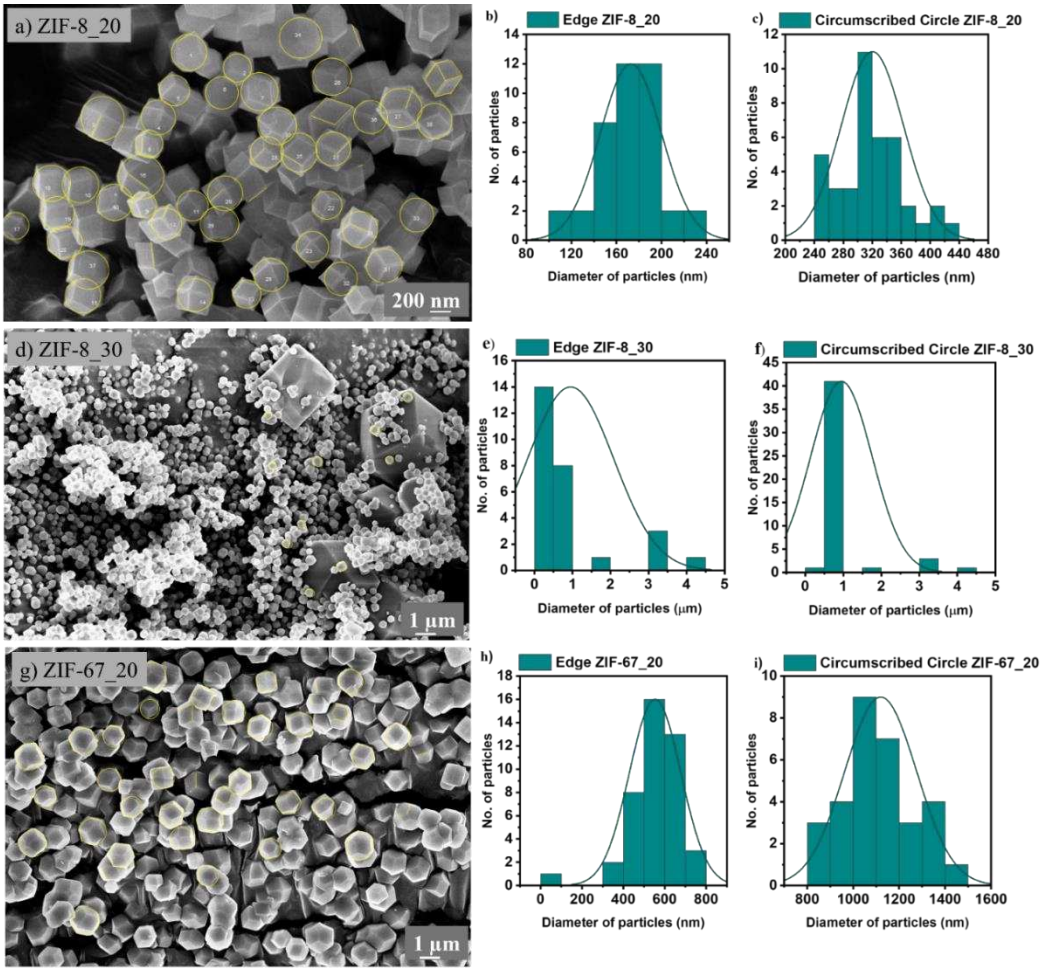


Figure 3-4. FESEM images and corresponding particle size distribution histograms of (a,b) ZIF-8_20, (c,d) ZIF-8_30, and (e,f) ZIF-67_20, showing the influence of water vapor volume and metal center on particle morphology and size distribution.

The textural properties of the synthesized ZIF-8_X and ZIF-67_X materials were systematically investigated by nitrogen adsorption-desorption measurements at -196 °C in order to evaluate their surface area, pore volume, and pore size distribution (Figure 3-5). All samples exhibit type I adsorption-desorption isotherms according to the IUPAC classification, confirming their predominantly microporous nature (175). This behavior indicates the successful formation of well-developed ZIF frameworks through the steam-assisted dry-gel synthesis route, independent of the metal center employed.

Within the ZIF-8_X series, the samples prepared with intermediate amounts of water show the most favorable textural properties. Among them, ZIF-8_20 has a relatively high BET specific surface area of about 1239 $m^2 g^{-1}$ and a total pore volume of 0.74 $cm^3 g^{-1}$. The pore size distribution obtained from the NLDFT analysis is relatively narrow, with a maximum around 1.7 nm, indicating fairly uniform access to the micropores. These values are comparable, and in some cases exceed those reported for ZIF-8 synthesized via conventional solvothermal or

ionothermal routes, despite the complete elimination of organic solvents in the present method (200,201). This observation highlights the effectiveness of the steam-assisted dry-gel approach in preserving the intrinsic porosity of ZIF-8 while enabling improved control over crystal growth.

ZIF-67 prepared under similar conditions, referred to as ZIF-67_20, shows an even higher BET surface area of about 1408 m^2 g^{-1}, together with a pore volume of 0.82 cm^3 g^{-1}. Its pore size distribution is also centered at around 1.7 nm, indicating a similar pore structure to that of ZIF-8_20. The higher surface area and pore volume observed for ZIF-67 may be related to differences in the strength of the metal–ligand interactions and the flexibility of the framework when Zn(II) is replaced by Co(II). Thus, despite having the same overall framework structure, the choice of metal center has a clear effect on the resulting textural properties of the two ZIF materials. The comparison with previously reported materials also shows the advantages of the steam-assisted dry-gel synthesis used here. The ZIF materials obtained with this approach have surface areas and pore volumes comparable to, and in some cases higher than, those reported for conventional DMF-based solvothermal synthesis, while producing smaller and more uniform particles (202–206). The combination of high porosity and small particle size is particularly useful for electrochemical applications, as it increases the accessible surface area and can facilitate mass transport between the catalyst and the electrolyte.

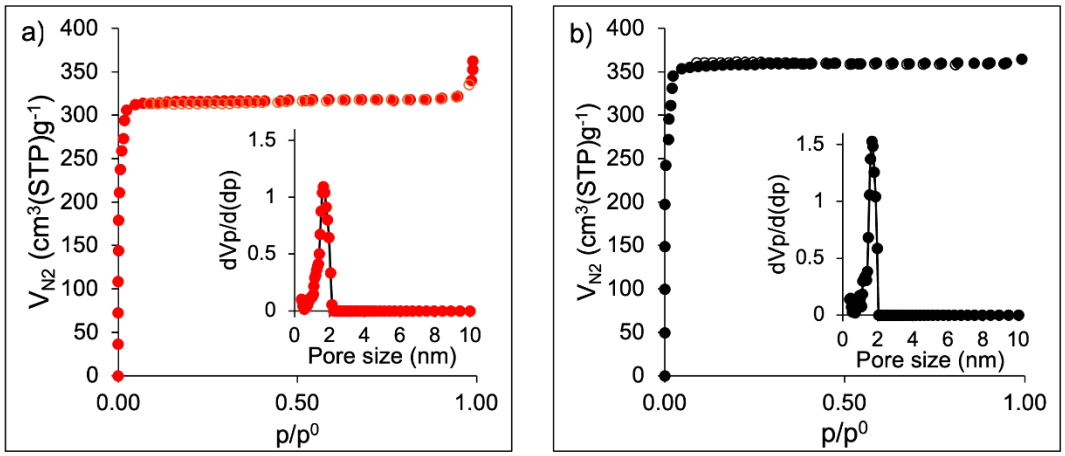


Figure 3-5. -196 °C N_2 adsorption-desorption isotherms for (a) ZIF-8_20 and (b) ZIF-67_20 materials. Closed symbols correspond to the adsorption process, whereas empty symbols are associated with the desorption process. The inset shows the pore size distribution curve for the respective sample (199)

The CO_2 adsorption behavior of the synthesized ZIF-8_X and ZIF-67_X materials were investigated to assess their affinity toward carbon dioxide and to provide insight into gas-framework interactions relevant to CO_2-related applications (Figure 3-6). The CO_2 adsorption isotherms were measured at 25 °C after the nitrogen adsorption–desorption experiments, using

the same sample pretreatment procedure. Both materials show the typical behavior of microporous ZIFs, with CO_2 uptake increasing progressively as the pressure increases, indicating that the internal pore network remains accessible.

The two ZIFs nevertheless show a clear difference in CO_2 uptake. ZIF-67_20 reaches an adsorption capacity of about 0.88 mmol g^{-1} at 100 kPa, compared with approximately 0.55 mmol g^{-1} for ZIF-8_20 under the same conditions. The higher uptake of ZIF-67_20 is mainly associated with its larger BET surface area and pore volume, together with the stronger interaction between CO_2 and the Co(II)-based framework. The smaller effective pore openings and the higher charge density around the Co(II) centers may further strengthen the host–guest interactions, favoring CO_2 adsorption under dry conditions.

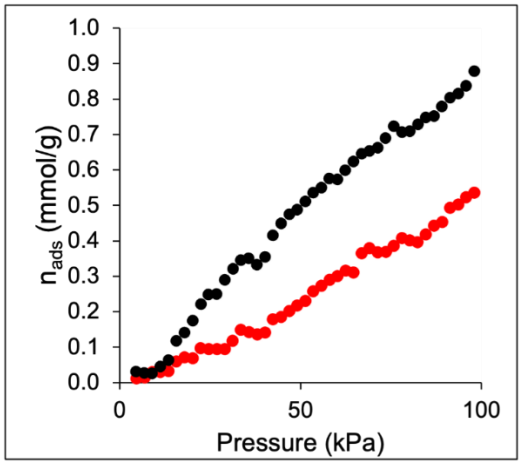


Figure 3-6. Adsorption isotherms of pure CO_2 at 25 °C in ZIF-8_20 (red symbols) and ZIF-67_20 (black symbols) (199).

3.2.2. Electrocatalytic performance

The electrochemical CO_2 reduction performance of the synthesized ZIF-8_X and ZIF-67_X materials was evaluated using gas diffusion electrodes in controlled electrochemical cell configurations in order to assess their catalytic activity, selectivity, and stability under relevant operating conditions.

Electrochemical measurements were conducted in flow-cell using $KHCO_3$ and KOH electrolytes, depending on the specific experiment. Chronopotentiometry tests were performed after iR compensation to evaluate the steady-state behavior of the catalysts at different applied potentials or current densities.

As is shown in (Figure 3-7), the electrochemical behavior of ZIF-8 is strongly influenced by synthesis conditions, particularly the volume of water used during the steam-assisted dry-gel process. ZIF-8_20 consistently delivers the most stable current response across the investigated potential range, indicating favorable charge transport and sustained catalytic activity. At increasingly negative potentials, the current density rises, reaching values on the order of tens

of mA cm^{-2}, which is notable considering the intrinsically insulating nature of pristine MOF materials. This behavior suggests that the porous structure and intimate contact with the gas diffusion layer effectively mitigate transport limitations during operation.

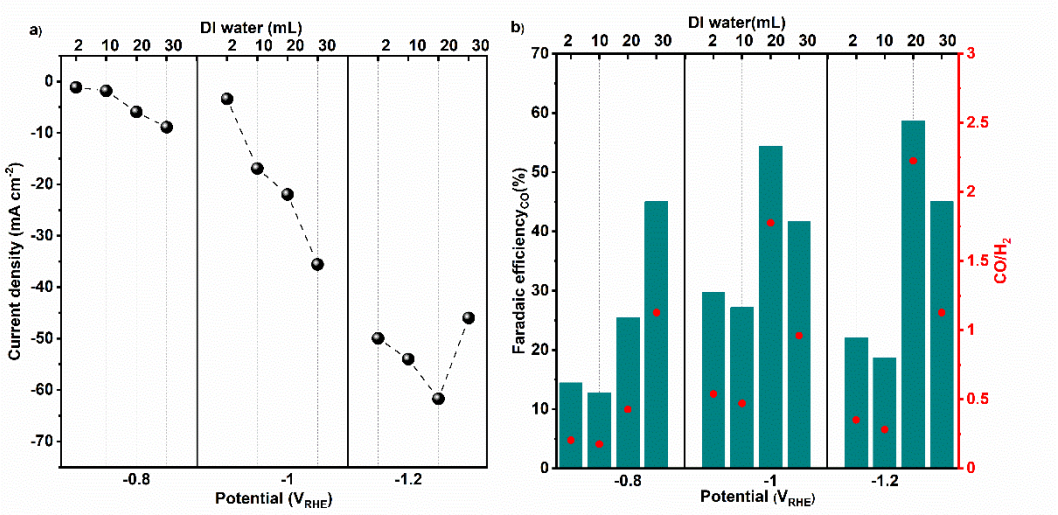


Figure 3-7. Current densities recorded for ZIF-8_2, ZIF-8_10, ZIF-8_20, and ZIF-8_30 electrodes at different applied potentials in 2 M $KHCO_3$ electrolyte. (b) Corresponding Faradaic efficiency for CO production and CO:H_2 ratio as a function of potential. The dotted lines in panel (a) serve as visual aids to highlight trends (199).

Product analysis reveals that ZIF-8_20 achieves the highest Faradaic efficiency for CO formation, reaching values close to 60% at sufficiently negative potentials. Samples prepared with either lower or higher water contents show lower CO selectivity, highlighting the effect of particle morphology and size distribution on the electrochemical response (Figure 3-4). The better performance of ZIF-8_20 can be related to its smaller particles and relatively narrow particle size distribution. These characteristics provide greater accessibility to the Zn(II) sites and help form a more effective three-phase interface. As a result, CO_2 activation is favored, while the competing hydrogen evolution reaction is reduced.

The electrochemical measurements also show that the CO:H_2 ratio can be adjusted by changing the synthesis conditions and the applied potential. This tunability allows ZIF-8_X to produce syngas with different compositions, which can be useful for subsequent energy and chemical conversion processes. Samples prepared under less favorable conditions generally show a higher contribution from H_2, whereas ZIF-8_20 gives a product stream with a larger CO fraction (Figure 3-7b). This tunability highlights the sensitivity of CO_2 electroreduction pathways to catalyst morphology and active-site accessibility. Besides CO and H_2, this process also drives formate production in a relatively lower proportion. Electrolyte composition exerts a pronounced influence on the electrochemical CO_2 reduction behavior of ZIF-based electrodes. As discussed so far, when CO_2 electroreduction is performed in near-neutral 2M $KHCO_3$ electrolyte, ZIF-8_20 exhibits a gradual increase in current density with increasing cathodic potential, achieving its highest CO selectivity at relatively negative potentials (around

-1.0 to -1.2 V vs RHE). Under these conditions, the bicarbonate buffer stabilizes the local pH at the cathode surface, enabling a balanced competition between CO_2 reduction and hydrogen evolution and allowing effective tuning of the CO:H_2 ratio through potential control. In comparison, using 1 M KOH shifts the onset of CO_2 reduction towards less negative overpotentials, while similar CO Faradaic efficiencies are obtained at around −0.7 V vs RHE (Figure 3-8a). The current densities are also higher at the same applied potentials, which is mainly related to the higher ionic conductivity of KOH and the more efficient transport of charged species through the electrolyte. The use of an alkaline electrolyte, however, also introduces some disadvantages. In 1 M KOH, the CO:H_2 ratio becomes less tunable and the range of potentials over which high CO selectivity is obtained is narrower. In addition, CO_2 reacts with OH^- to form carbonate species, leading to carbon loss and gradual changes in the electrolyte composition. Carbonate precipitation and water accumulation inside the gas diffusion electrode can further disturb the three-phase interface, eventually causing flooding and a loss of performance during longer electrolysis. These results show that the electrochemical response cannot be attributed to the catalyst alone. The electrolyte and the applied potential also play an important role, and catalyst performance therefore needs to be considered together with the transport and stability limitations associated with the electrolyte.
ZIF-67 behaves quite differently from ZIF-8. Only limited CO_2 reduction activity is observed over the investigated potentials and in both electrolytes (Figure 3-8b). The strong contribution of the hydrogen evolution reaction indicates that a high surface area and a relatively high CO_2 adsorption capacity are not sufficient to obtain selective CO_2 conversion. In the case of ZIF-67, the Co(II) centers appear to favor water and proton activation, which limits CO formation. This result further highlights the importance of the metal center in determining the electrochemical behavior and product selectivity of ZIF-based catalysts.

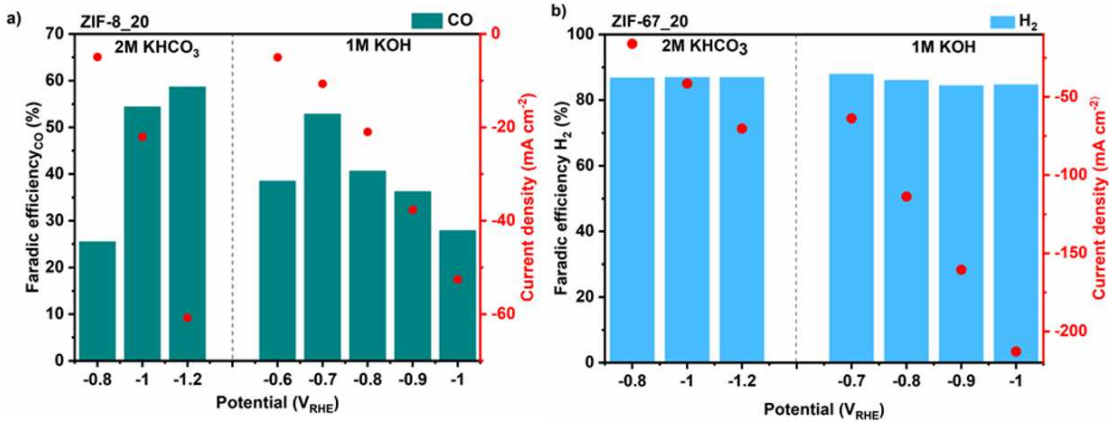


Figure 3-8. a) comparison of the Faradaic efficiency of ZIF-8_20 in 2 M $KHCO_3$ and 1 M KOH at different potentials vs RHE and b) Faradaic efficiency of ZIF-67_20 in 2M $KHCO_3$ at different potentials vs RHE (199).

The disparity between ZIF-8 and ZIF-67 further illustrates that strong CO_2 binding does not necessarily translate into efficient catalytic turnover. Although ZIF-67 exhibits enhanced CO_2 uptake under dry adsorption conditions, the stabilization of CO_2 within its ultramicropores may hinder the formation and evolution of key reaction intermediates, such as *COOH, that are required for CO production. In contrast, the Zn(II) centers in ZIF-8 provide a more favorable balance between CO_2 adsorption and activation, enabling effective electron transfer and timely desorption of intermediates. This balance is critical for sustaining selective CO formation during electrochemical operation.

The operational stability of the ZIF-8 catalyst was evaluated to assess its durability under continuous CO_2 electroreduction conditions. Stability tests were conducted using the ZIF-8_20 electrode, which exhibited the highest activity and selectivity in short-term measurements. Owing to the limited lifetime of the three-phase interface in flow-cell configurations, long-term electrolysis was performed in a zero-gap MEA configuration, which provides improved mechanical stability and controlled reactant transport during extended operation.

The stability test was carried out at a constant current of -300 mA, corresponding to a geometric current density of approximately -60 mA cm^{-2}, in 0.5 M $KHCO_3$ electrolyte. Under these conditions, the Faradaic efficiency for CO formation initially stabilized at around 60% after the first two hours of electrolysis, in agreement with the values obtained during short-duration experiments (

Figure 3-9). This stable response suggests that the ZIF-8 framework remains relatively stable under the applied reductive potentials, with the sites involved in CO formation still accessible during the initial period of electrolysis. After about five hours of continuous operation, however, the CO selectivity gradually decreases while H_2 production increases. This change does not appear to result from direct degradation of the catalyst, but rather from limitations in mass transport and changes in the wettability of the electrode. During CO_2 electroreduction, water is also produced at the cathode and can accumulate within the porous structure of the gas diffusion electrode. At the same time, pressure differences between the gas and liquid sides can drive electrolyte into the electrode and cause partial flooding of the catalyst layer. As the electrode becomes flooded, the solid–liquid–gas interface is disturbed and the amount of CO_2 reaching the active sites decreases, making hydrogen evolution more favorable. Overall, the stability results suggest that the loss of performance during extended operation is more closely related to the electrode structure and interfacial conditions than to chemical degradation of ZIF-8 itself. The continued formation of CO for several hours indicates that the ZIF-8 framework can remain functional under the electrochemical conditions used here. The later increase in H_2 production, however, shows that long-term performance also depends on factors such as the gas diffusion layer, membrane properties, and effective water management.

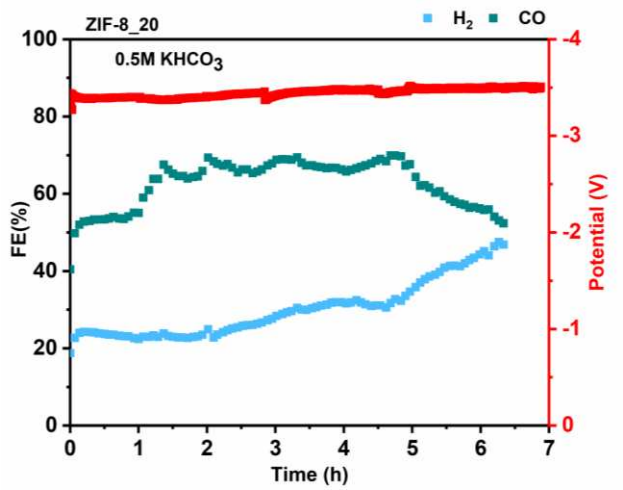


Figure 3-9. Stability test of ZIF-8_20 at -60 mA cm^{-2} in 0.5M $KHCO_3$ by MEA cell (199).

3.2.3. Conclusions

This work demonstrated that zeolitic imidazolate frameworks can be rationally designed through a green, steam-assisted synthesis route to achieve controlled morphology, high porosity, and tunable electrochemical performance for CO_2 reduction. By systematically varying the synthesis conditions, particularly the water vapor content, ZIF-8 materials with narrow particle size distributions and accessible microporosity were obtained, enabling selective CO production with tunable CO:H_2 ratios. In contrast, the isostructural ZIF-67 framework predominantly favored hydrogen evolution, highlighting that electrochemical selectivity is governed primarily by the nature of the metal center rather than surface area or CO_2 adsorption capacity alone. These findings establish clear structure–property–performance relationships and underline the importance of metal-node selection in MOF-based electrocatalysts. These results emphasize that high CO_2 adsorption capacity does not directly translate to improved electrochemical performance. Instead, effective CO_2 reduction requires a balance between adsorption strength, pore accessibility, and mass transport. In this context, the more accessible pore architecture of ZIF-8 provides a more favorable environment for CO_2 activation and conversion.

.

Chapter 4. Mesoporous Cu-MOF

The results obtained from ZIF-8, and ZIF-67 systems demonstrated that metal-ligand coordination environments critically dictate reaction pathways in CO_2 electroreduction. While Zn-based ZIF-8 showed selective CO formation and structural stability under electrochemical conditions, the formation of multi-carbon products requires active sites capable of promoting C-C coupling. Copper-based materials are widely recognized for their ability to generate C_2 products such as ethylene during CO_2 reduction. Therefore, building upon the coordination-driven design principles established in the previous chapter, this work shifts toward Cu-containing metal-organic frameworks.

This chapter focuses on the synthesis of a copper-imidazolate MOF using two greener hydrothermal approaches: a steam-assisted route and a microwave-assisted route. Both methods avoid the use of hazardous organic solvents and offer a practical way to produce the material while preserving its structural characteristics. The chapter first describes the synthesis procedures, including conventional steam-assisted hydrothermal treatment. The synthesized material is then examined using a range of physicochemical characterization techniques, including X-ray diffraction, FESEM with EDS mapping, nitrogen adsorption–desorption, FTIR, Raman spectroscopy, thermogravimetric analysis, elemental analysis, ICP-OES, XPS, and soft X-ray absorption spectroscopy. Particular attention is given to confirming the formation of the $Cu–N_4$ coordination environment and determining the oxidation state of Cu in both the bulk and surface regions. Operando soft-XAS measurements are also used to follow changes in the Cu species during CO_2 reduction. The electrochemical performance of the Cu-MOF is subsequently investigated in both flow-cell and zero-gap membrane-electrode assembly configurations. The effects of catalyst loading applied to current density, and cell configuration on Faradaic efficiency, the C_2/C_1 ratio, and overall product distribution are examined. Finally, the chapter considers the restructuring of the catalyst under operating conditions and its stability during continuous electrolysis.

4.1. Materials and Synthesis Methods

Copper (II) acetate tetrahydrate ($Cu(OAc)_2 \cdot 4H_2O$, ≥98%, Sigma-Aldrich) and 2-methylimidazole (2-MeIm, 99%, Sigma-Aldrich) were used as supplied. Deionized water and ethanol served as solvents. Cu-MOFs were synthesized via a steam-assisted technique in a 100 mL Teflon-lined stainless-steel autoclave. Briefly, $Cu(OAc)_2 \cdot 4H_2O$ (2.5 mmol) and 2-MeIm (25 mmol) were placed in a quartz crucible positioned at the center of the autoclave, while 20 mL of DI water was added at the bottom to generate steam. The sealed autoclave was heated at 120 °C for 3 h. The resulting product was collected by centrifugation, washed with a 2:1 (v/v) water/ethanol mixture, and dried under vacuum at 60 °C. Further experimental details are provided in 3.1.

4.2. Results and Discussion

4.2.1. Physicochemical properties

X-ray powder diffraction measurements were performed to verify the crystallinity and phase purity of the steam-assisted hydrothermal Cu-MOF. The diffraction pattern (Figure 4-1) displays a series of sharp and well-defined reflections at 2θ values of 14.6°, 29.8°, 31.5°, 33.3°, 35.7°, 38.8°, 44.9°, and 48.0°, which are indexed to the (022), (040), (006), (026), (226), (127), (356), and (019) crystallographic planes, respectively. The sharpness and intensity of these peaks confirm the formation of a well-crystallized framework (207).

A direct comparison between the XRD pattern of the synthesized Cu-MOF and that of the pristine 2-methylimidazole ligand reveals clear structural differences. The characteristic diffraction peaks of crystalline 2-methylimidazole are absent in the Cu-MOF pattern, indicating complete coordination of the ligand to Cu^{2+} centers and the formation of a new crystalline phase. This confirms that the product is not a physical mixture of precursors but a coordinated Cu-imidazolate framework.

Importantly, no additional peaks corresponding to copper oxides or other secondary phases are detected, demonstrating the high phase purity of the material synthesized via the steam-assisted hydrothermal route. These findings verify the successful formation of a crystalline Cu-MOF suitable for subsequent electrochemical investigation.

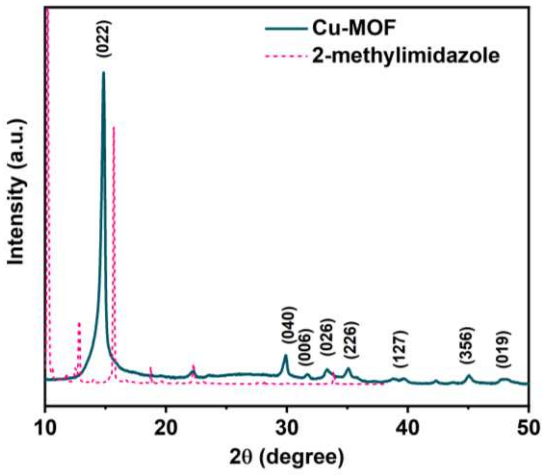


Figure 4-1. XRD patterns of Cu-MOF (solid line) and 2-methylimidazole (dashed line)

The FESEM micrographs (Figure 4-2**Error! Reference source not found.**) reveal that the Cu-MOF consists of densely packed, irregular flake-like nanostructures. In top-view images (Figure 4-2a), the crystals appear as plate-like flakes ranging from ~200 nm up to ~1.2 μm in lateral dimension. In side-view images (Figure 4-2b), these flakes are seen edge-on with thicknesses on the order of 50-80 nm. The flake surfaces and edges are noticeably rough and irregular, with nanoscale protrusions and indentations. These textural features indicate that the

flakes are highly porous: gaps and voids are visible between stacked layers, suggesting loosely stacked 2D sheets rather than solid blocks. Such a highly anisotropic morphology (large aspect-ratio flakes) greatly increases the exposed surface area and internal porosity.
These morphological characteristics can be rationalized by the steam-assisted growth mechanism. In our synthesis, a dry precursor mixture is exposed to water vapor (steam) in a sealed autoclave, rather than being dissolved in a large volume of solvent. This vapor-phase environment typically favors controlled diffusion of reactants and anisotropic crystal growth. As a result, metal ions and 2-methylimidazole molecules migrate through the steam to the nucleation sites, promoting two-dimensional growth of the Cu-imidazolate framework.

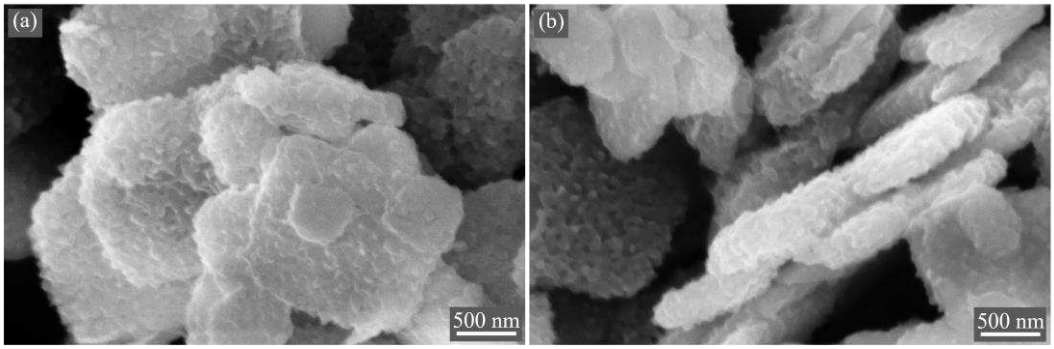


Figure 4-2. FESEM images of Cu-MOF: (a) top view of the particles and (b) lateral view of the particles.

EDS elemental analysis provides additional information on the composition of the material (Figure 4-3). The EDS spectrum in Figure 4-3b shows the presence of Cu, C, and N, with no other foreign elements detected. The corresponding elemental maps show a uniform distribution of all three elements, with the Cu, C, and N signals overlapping throughout the analyzed area. No clear segregation or formation of separate phases can be observed. In particular, there are no regions with a noticeable increase in oxygen or areas that could be associated with Cu oxide, suggesting that significant oxide impurities are not present in the as-synthesized MOF. The similar distribution of Cu, C, and N across the flakes also indicates a relatively uniform composition throughout the material. Overall, the EDS results support the homogeneous distribution of the elements within the Cu-imidazolate network and do not show detectable phase segregation.

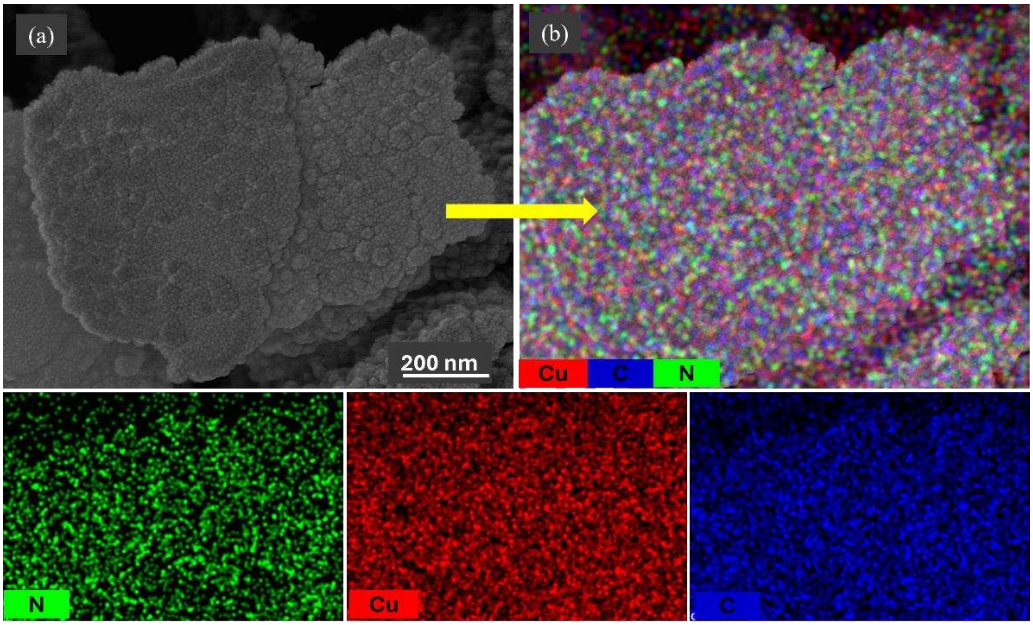


Figure 4-3. (a) SEM image of Cu-MOF under EDS condition and (b) EDS mapping.

N_2 adsorption-desorption isotherms were measured at -196 °C (Figure 4-4a). The Cu-MOF shows a classic type-IV isotherm with a hysteresis loop at high relative pressure ($P/P_0 > 0.8$), a hallmark of mesoporous materials (175). From the adsorption data, the BET surface area is calculated as 25.6 $m^2 \cdot g^{-1}$ and the total pore volume (at $P/P_0 = 0.98$) is 0.24 $cm^3 \cdot g^{-1}$. These values indicate significant porosity despite a modest overall area. The BJH analysis of the desorption branch yields an average pore diameter of ~19 nm, consistent with mesopores. NLDFT analysis (using a carbon slit-pore model) reveals the dominant pore widths are centered around 26 nm and 100 nm, reflecting a wide meso-macropore distribution (Figure 4-4b).

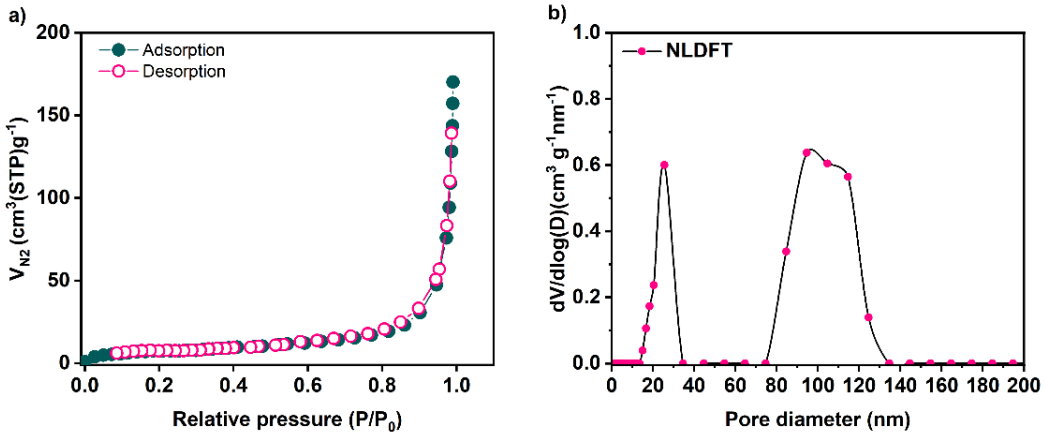


Figure 4-4. (a) -196 N_2 adsorption-desorption isotherms (Closed symbols correspond to the adsorption process, whereas empty symbols are associated with the desorption process) and (b) NLDFT pore size distributions of Cu-MOF.

Elemental analysis (CHNS) was performed to determine the bulk chemical composition of Cu-MOF. The measured weight percentages were carbon (40.6%), hydrogen (4.6%), and nitrogen (24.6%), confirming that the framework contains a substantial fraction of the imidazolate ligand. The significant nitrogen content is consistent with the incorporation of 2-methylimidazole within the structure and indicates successful coordination of the organic linker. The copper content was independently quantified by TGA and ICP-OES. The TGA curve, recorded under air atmosphere up to 800 °C (Figure 4-5), exhibits a multi-step weight loss profile. The material remains thermally stable up to approximately 225 °C. An initial weight loss of about 18% is attributed to the removal of adsorbed solvents and residual organic species. At higher temperatures (around 400 °C), a pronounced mass loss occurs due to decomposition of the organic framework. After complete decomposition, a residual mass of approximately 35.5% remains, corresponding to the formation of inorganic copper oxide species in air. Based on this residual weight, the copper content is estimated to be approximately ~28.4 wt.% in agreement with the values obtained from ICP-OES measurements. In fact, ICP-OES analysis showed that the Cu-MOF contains approximately 25-28 wt.% Cu, consistent with the TGA-derived estimation. The agreement between these independent techniques verifies the reliability of copper quantification. To assess coordination, we compute the atomic Cu:N ratio by combining the CHNS data with the measured copper content. To estimate the Cu:N atomic ratio, the following relationship was applied:

$$Cu{:}N = \left(\frac{Cu\ wt\%}{M(Cu)}\right){:}\left(\frac{N\ wt\%}{M(N)}\right) = \left(\frac{28.4}{63.55}\right){:}\left(\frac{24.6}{14.01}\right) = (0.447){:}(1.756)$$

Dividing both values by 0.447

$$Cu{:}N \approx 1{:}3.93 \quad therefore\ Cu{:}N \approx 1{:}4$$

This ratio suggests that each copper ion is coordinated by four nitrogen atoms from the imidazolate ligands, consistent with a Cu-N_4 coordination environment within the framework (208).

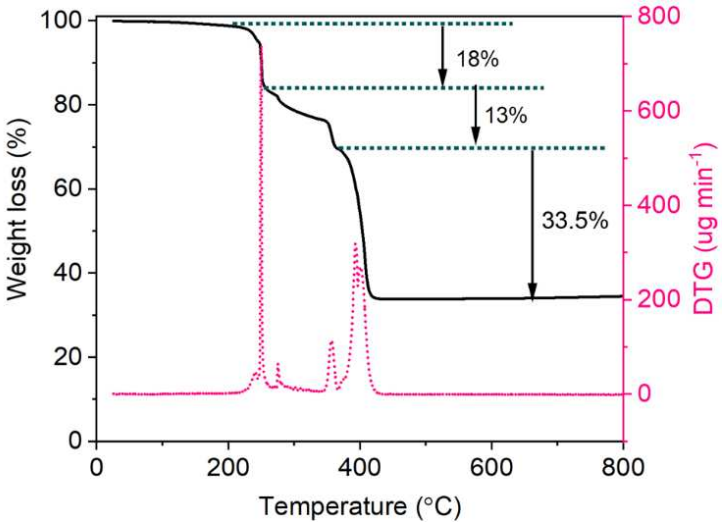


Figure 4-5. TGA up to 800 °C under the air atmosphere of steam-assisted hydrothermal Cu-MOF.

Spectroscopic techniques, including FTIR, Raman spectroscopy, XPS, and XAS, were employed to further investigate the chemical structure and coordination environment of the synthesized Cu-MOF.

FTIR spectroscopy was used to examine the interaction between Cu^{2+} ions and the 2-methylimidazole ligands. Comparing the spectra of pristine 2-methylimidazole and the Cu-MOF (Figure 4-6) shows several changes in the vibrational bands, supporting the formation of metal–ligand coordination. A broad O–H stretching band appears between 3100 and 3400 cm^{-1} in both spectra and is assigned to adsorbed water. The C–H stretching vibrations of the methyl and aromatic groups are observed in the 2900–3000 cm^{-1} region (209). After Cu coordination, the corresponding bands in the MOF become sharper, which may reflect a more ordered ligand environment and reduced vibrational freedom (210,211). In the 1600–1500 cm^{-1} region, strong bands are associated with the C=C and C=N stretching vibrations of the imidazole ring. For the Cu-MOF, these bands shift towards higher wavenumbers, which is consistent with changes in the C=N bond upon coordination of the nitrogen atoms with Cu(II) centers (209,212). The C–H bending vibrations appear between 1400 and 1300 cm^{-1}, while the C–N stretching bands are found in the 1100–1000 cm-1 region. A new sharp band at 433 cm^{-1} appears in the Cu-MOF spectrum and is assigned to Cu–N stretching. In addition, the peak around 1851 cm^{-1}, attributed to N–H-related vibrations, disappears or becomes much weaker after coordination. Taken together, these changes are consistent with the formation of Cu–N interactions within the framework.

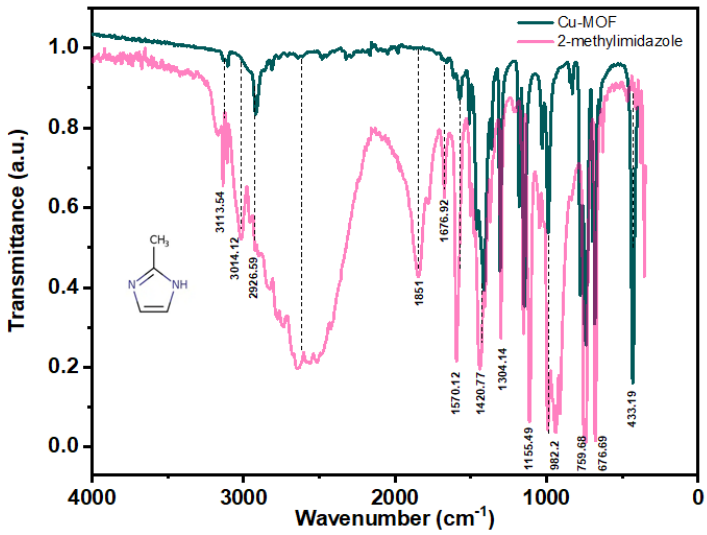


Figure 4-6. FTIR of steam-assisted hydrothermal Cu-MOF and 2-methylimidazole.

Raman spectroscopy further supports the successful formation of the Cu-MOF. The Raman spectrum exhibits distinct peaks at 690, 1023, 1183, 1462, and 2920 cm^{-1} (Figure 4-7), corresponding to characteristic vibrational modes of the 2-methylimidazole aromatic ring. Specifically, the peak at 690 cm^{-1} is assigned to C=C stretching, 1023 cm^{-1} to C-H bending, 1183 cm^{-1} to C-N stretching within the imidazole ring, 1462 cm^{-1} to methyl bending, and 2920 cm^{-1} to C-H stretching of methyl groups (209).
In the low-frequency region, a band at 293 cm^{-1} is attributed to Cu-N vibrations within the framework (213). Although vibrational modes in this region may overlap, the presence of this band provides additional evidence of coordination between Cu and nitrogen atoms.

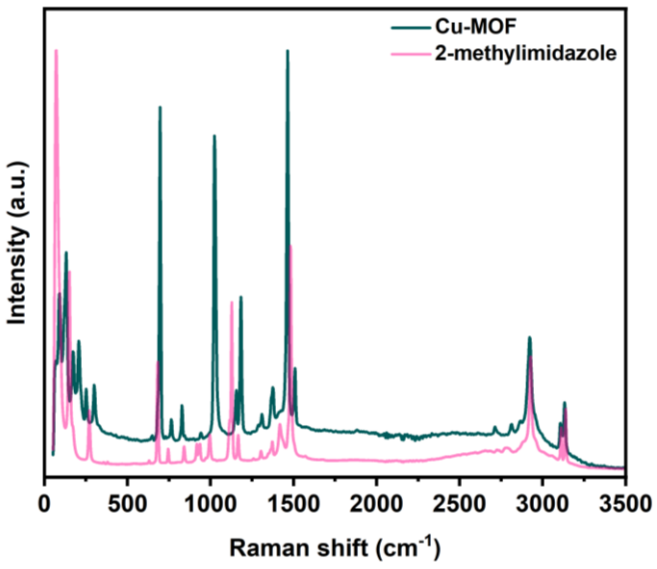


Figure 4-7. Raman spectrum of steam-assisted hydrothermal Cu-MOF and 2-methylimidazole.

XPS analysis was performed to obtain detailed information on the surface elemental composition and chemical environment of the Cu-MOF. The XPS survey spectrum (Figure 4-8a) shows the expected signals from C, O, N, and Cu, with no other elements detected within the sensitivity limit of the measurement (0.01 at.%). The relative atomic concentrations shown in the same figure were obtained from quantitative analysis of the corresponding high-resolution spectra (Figure 4-8b-d), This analysis provides more reliable information, particularly for elements present in smaller amounts.

The high-resolution C 1s spectrum (Figure 4-8b) contains several components, reflecting the different chemical environments of carbon in the material. The main peak at 284.5 eV is assigned to sp^2 C–C bonds. A second component at 285.3 eV can be related to sp^3 C–C as well as C–O and C–N bonds within the aromatic structure, although these contributions overlap and cannot be clearly separated (214). The component at 286.1 eV is assigned to C–N/C=N bonds associated with amino-type environments. At higher binding energies, peaks at 291.1 and 292.8 eV are observed and correspond to π–π* excitation and shake-up satellite features, respectively, which are characteristic of sp^2 carbon structures (215). Overall, the C 1s spectrum is consistent with the aromatic structure of the 2-methylimidazole ligand used to prepare the Cu-MOF.

The N 1s spectrum (Figure 4-8c) is dominated by a peak at 398.6 eV, together with a weaker component at 399.9 eV (216). These contributions are commonly assigned to pyridinic-N and pyrrolic-N species, respectively, in agreement with the imidazole-based structure indicated by the C 1s spectrum. A weaker and broader feature between 404 and 408 eV is also present and is attributed to π excitation. Literature values generally place uncoordinated pyridinic or aromatic N between about 398.3 and 399.5 eV, whereas coordination with Cu shifts the N 1s signal towards higher binding energies, typically within the 399.8–400.8 eV range (217–219). The expected shift is therefore around 0.5–1.5 eV. In the present sample, the component at 399.9 eV is 1.3 eV higher than the main peak at 398.6 eV. This difference is consistent with coordination of the nitrogen atoms to Cu^{2+}. The shift towards higher binding energy can be explained by donation of the nitrogen lone pair to Cu^{2+}, which lowers the electron density around N. The Cu 2p region was then examined in more detail to further support the Cu–N coordination assignment (Figure 4-8d). The spectrum contains the expected Cu $2p_{3/2}$ and Cu $2p_{1/2}$ peaks. For Cu^{2+}, the appearance of satellite peaks at higher binding energies is a well-known characteristic of this oxidation state, and these features are clearly visible in the present spectrum. At the same time, the Cu $2p_{3/2}$ peak is not fully symmetric, suggesting that more than one copper oxidation state may be present. A lower-binding-energy component is observed at around 933.4 eV. Because Cu^0 and Cu^+ have very similar binding energies in this region, they cannot be distinguished from the main Cu 2p peak alone. Following the approach reported by M. Biesinger et al. (220), the Cu $2p_{3/2}$ peak together with its associated satellite region between 940 and 950 eV was therefore deconvoluted to estimate the relative contributions of the different oxidation states. The analysis shows approximately 77% Cu(II) and 23% Cu(0/I), indicating that Cu(II) is the predominant oxidation state in the Cu-MOF.

The presence of mixed copper oxidation states has also been reported previously for Cu-MOF materials, although without quantitative determination of their relative contributions (213,221).

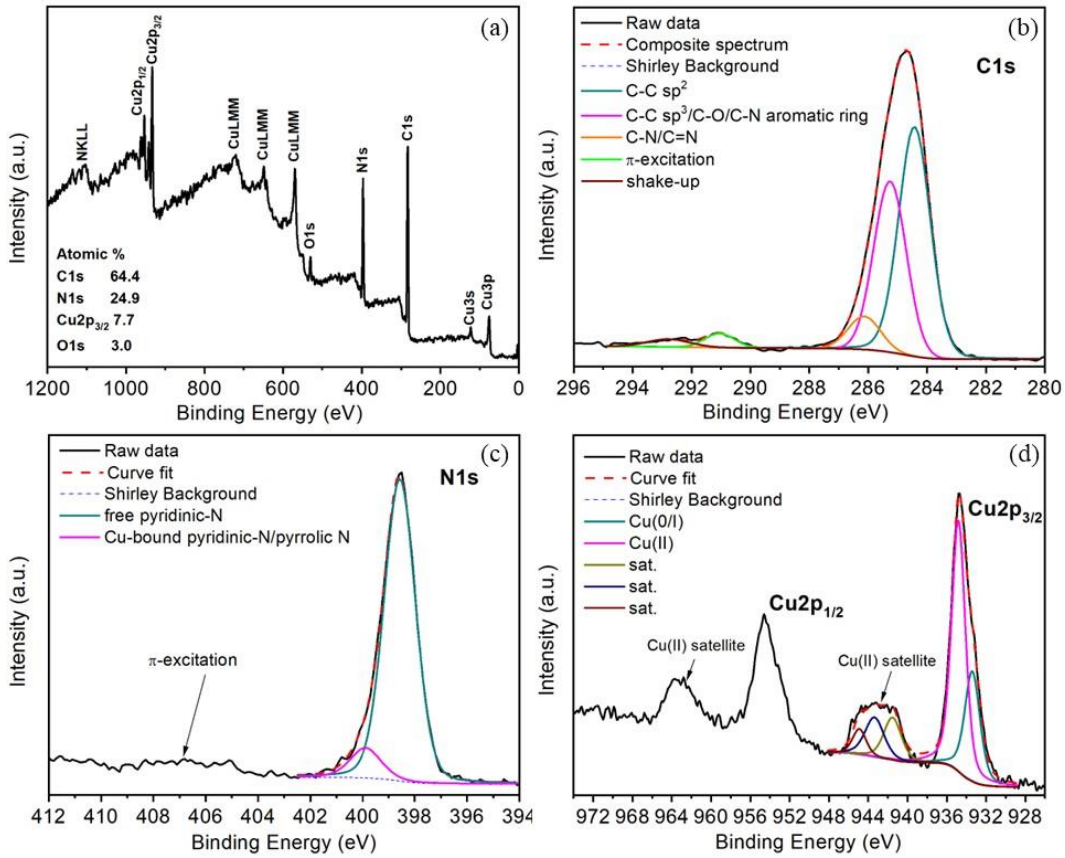


Figure 4-8. XPS spectra of the Cu-MOF: (a) survey spectrum showing the presence of C, N, O, and Cu elements; (b) high-resolution C 1s spectrum with fitted components corresponding to sp^2 C-C (284.5 eV), sp^3 C-C/C-N (285.3 eV), C-N/C=N (286.1 eV), and π-π* shake-up features (291.1 and 292.8 eV); (c) N 1s spectrum showing pyridinic N (398.6 eV) and Cu-coordinated N (399.9 eV); (d) Cu 2p spectrum displaying Cu^{2+} features with characteristic satellite peaks.

(Figure 4-9a) presents the Cu L-edge soft X-ray absorption spectra of the Cu-MOF powder, measured alongside reference spectra of metallic Cu, Cu_2O, and CuO. Measurements were performed in both TEY and FY modes, enabling depth-resolved analysis from the near-surface region (a few nanometers, TEY) to deeper layers (up to tens of micrometers, FY). The strong similarity between TEY and FY spectra indicates that both surface and bulk regions share a comparable chemical composition and coordination environment. In both detection modes, two principal absorption features are observed at 931.5 eV (L_3-edge) and 951.1 eV (L_2-edge), corresponding to Cu 2p → 3d electronic transitions. These peaks are characteristic of Cu(II) species and closely resemble those of the CuO reference(222). However, they are shifted by approximately +0.2 eV, suggesting a slightly more oxidized or covalently bound Cu environment within the MOF framework. Importantly, the Cu L_3-edge spectrum exhibits an

additional shoulder at approximately 938 eV (S3), which is absent in the CuO reference. This feature indicates increased spectral complexity and is attributed to ligand-to-metal charge transfer (LMCT) transitions involving nitrogen-based ligands in the Cu-MOF. Specifically, these LMCT satellites correspond to $3d^9 \rightarrow 3d^{10}L$ excitations. Such features have been widely reported in N-coordinated Cu(II) systems, including NH_3-dosed Cu(I)-MFU-4l, Cu-ZIF8, Cu-ZIOS, and Cu-ethylenediamine complexes (223–225). These LMCT-related shoulders, commonly linked to π-backbonding interactions between Cu(II) centers and nitrogen donors, have also been reported near 938.4 eV in Cu-based MOFs such as HKUST-1, where they are attributed to Cu-N or Cu-O charge transfer transitions (226). A corresponding satellite feature is observed at 957.8 eV in the Cu L_2-edge spectrum (S2), further supporting the presence of LMCT or multiplet effects arising from interactions between ligand π orbitals and Cu d orbitals. These broad satellite structures, unlike sharp single-electron transitions, originate from more delocalized or hybridized electronic states, consistent with ligand-to-metal charge transfer involving N-imidazole donors in the Cu(II) coordination environment (227–230). Although direct Cu L-edge soft XAS investigations of Cu-methylimidazole MOFs remain limited, the observed spectral characteristics are consistent with known Cu-N coordination environments in imidazole-based systems. DFT and EXAFS studies reported for related systems further support the occurrence of LMCT in Cu(II) frameworks coordinated by imidazole-type ligands (224,231). Therefore, despite the limited direct precedent, the combined Cu L-edge and N K-edge spectroscopic evidence strongly supports the formation of a nitrogen-coordinated Cu-MOF. Supporting this interpretation, (Figure 4-9b) presents the N K-edge spectra measured in both TEY and FY modes. The two spectra display nearly identical line shapes, confirming that the surface and bulk regions share the same coordination chemistry. Three distinct absorption features are observed at 399.1 eV (A), 400.6 eV (B), and 401.6 eV (C) (232). The low-energy feature at 399.1 eV is assigned to the N 1s → π* transition of nitrogen atoms within the imidazolate linker that are directly coordinated to Cu(II) centers. Coordination to Cu lowers the transition energy due to ligand-to-metal charge transfer and electron delocalization from the nitrogen lone pair into partially filled Cu d orbitals. Similar low-energy π* resonances have been reported in Cu-imidazole and Zn-imidazole frameworks. The second feature at 400.6 eV is attributed to non-coordinated or weakly interacting nitrogen atoms within the 2-methylimidazolate linker, such as pyridinic sp^2 nitrogen not directly bonded to copper. This assignment is consistent with literature reports indicating that uncoordinated imidazole typically exhibits π* transitions in the 400.5-401.0 eV range (233). The higher-energy feature at approximately 401.6 eV is attributed to π* transitions of pyrrolic nitrogen (N-H), hydrogen-bonded nitrogen sites (e.g., from coordinated H_2O or partially decomposed framework), or the onset of σ* transitions involving N-C or N-Cu bonds (234). Such features generally appear at higher energies due to reduced electron density at nitrogen or increased localization, as commonly observed in hydrogen-bonded nitrogen species or imidazole molecules. Together, the Cu L-edge and N K-edge spectra provide strong evidence for Cu-N

coordination within the Cu-MOF, with LMCT features further confirming electronic interaction between Cu(II) centers and nitrogen ligands in the framework (233,234).

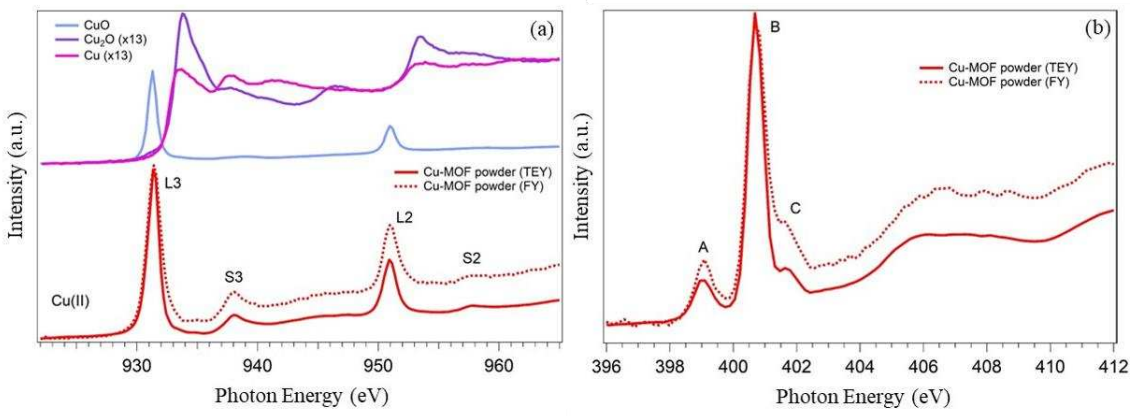


Figure 4-9. (a) Cu L-edge soft XAS spectra of the steam-assisted Cu-MOF in TEY and FY modes compared with Cu, Cu_2O, and CuO references, showing characteristic Cu (II) features and LMCT-related satellites. (b) N K-edge spectra in TEY (red solid line) and FY (red dashed line) modes displaying three main absorption features consistent with nitrogen coordination in the Cu-imidazolate framework.

4.2.2. Electrocatalytic performance

The electrochemical performance of the Cu-MOF was systematically evaluated using both flow-cell and zero-gap MEA configurations to assess activity, selectivity, and scalability under practical operating conditions.

In the flow-cell setup, an iridium-based mixed metal oxide anode (Ir-MMO, ElectroCell) served as the counter electrode, while a mini-Ag/AgCl reference electrode (1 mm, leak-free LF-1) was employed to control cathodic potential. The anolyte and catholyte were separated by an anion exchange membrane (Sustainion® 37-50, Dioxide Materials). The anolyte was 1 M KOH and was continuously recirculated, while the 1 M KOH catholyte was operated in single-pass mode. Both electrolytes were supplied at a flow rate of 4 mL min^{-1}. CO_2 was fed separately to the gas compartment at 25 mL min^{-1} and passed through the gas diffusion electrode (GDE) before reaching the catalyst layer. The CO_2 flow rate was controlled using Bruker mass flow controllers to maintain stable and reproducible operating conditions throughout the measurements. A schematic of the cell configuration is shown in Figure 4-10.

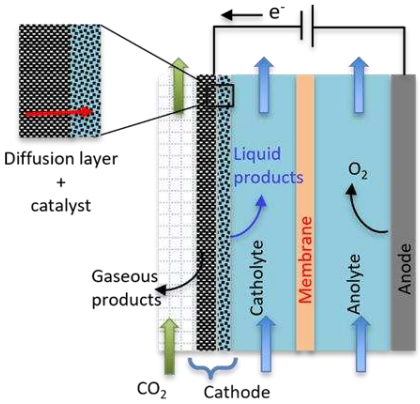


Figure 4-10. Schematic diagrams of 3-compartment flow cell

The catalytic response was investigated by varying the applied potential between -0.4 to -1.2 V vs RHE, thereby systematically tuning the thermodynamic driving force for CO_2 reduction (Figure 4-11). As the overpotential increased, the reaction rate was progressively enhanced, reaching a maximum current density of 220 mA cm^{-2} at -1.2 V_{RHE}. The Cu-MOF remains active even under strongly reducing conditions. Its product distribution, however, changes noticeably with the applied potential. At relatively low overpotentials, from −0.4 to −0.8 V_{RHE}, CO is the main product, with a nearly constant Faradaic efficiency of about 37%. A smaller amount of formate ($HCOO^-$) is also formed in this potential range. H_2 production remains relatively low, reaching a maximum FE of around 20%, which indicates that CO_2 reduction is able to compete effectively with HER under the alkaline conditions used here.

When the overpotential increases beyond 0.8 V_{RHE}, the product distribution changes. The contribution of the C_1 products, CO and $HCOO^-$, gradually decreases, while C_2 formation becomes more pronounced (Figure 4-11a). The FE for ethylene (C_2H_4), in particular, reaches about 35% at −1.2 V_RHE. Ethanol (C_2H_5OH) is also produced and contributes to the overall C_2 selectivity. Methane (CH_4) and acetate ($CH3COO^-$) remain minor products over the whole potential range. Although the H_2 contribution changes only slightly, the C_2/C_1 ratio increases with increasing overpotential and reaches 1.3 at −1.2 V_RHE (Figure 4-11b). At this potential, the combined FE for C_2 products reach 47%, meaning that almost half of the charge converted during electrolysis is directed towards multi-carbon products.

This potential-dependent transition from C_1-dominated chemistry at low overpotentials to enhanced C_2 selectivity at higher overpotentials suggests that elevated driving force promotes surface accumulation of *CO intermediates, facilitating C-C coupling pathways. The sustained hydrogen suppression, even at high current densities, further highlights the favorable CO_2RR selectivity of the Cu-MOF in alkaline media.

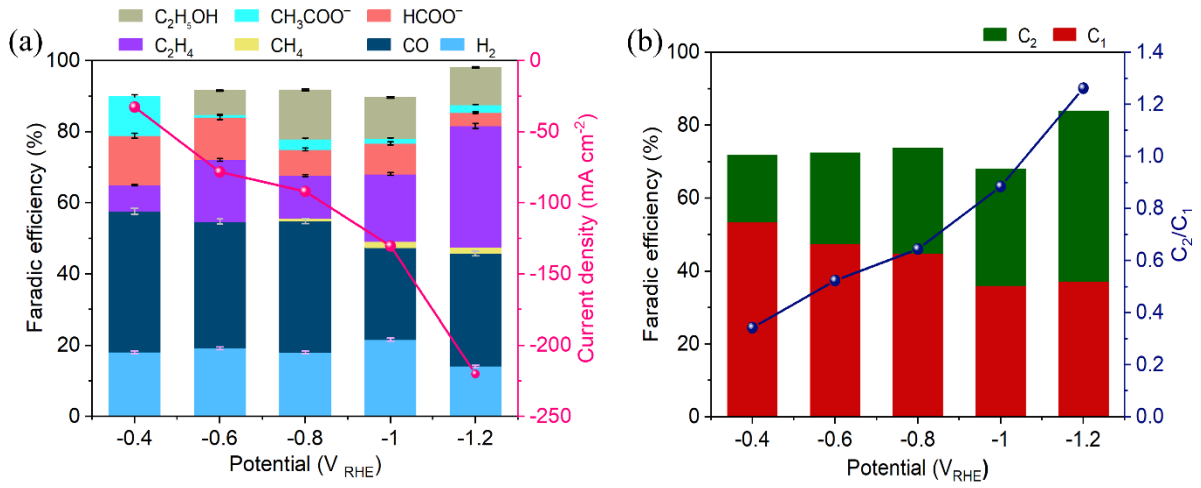


Figure 4-11. (a) Faradaic efficiencies of CO_2 reduction products and corresponding total current density of Cu-MOF in a flow-cell at different applied potentials in 1M KOH catholyte. (b) Faradaic efficiencies and the C_2/C_1 product ratio derived from the data shown in (a).

To evaluate the catalytic performance under industrially relevant operating conditions, the Cu-MOF was further tested in a zero-gap electrolyzer cell. The membrane-electrode assembly consisted of the Cu-MOF catalyst deposited onto a gas diffusion layer at the cathode, while a commercial Ir-based anode was used for oxygen evolution (Figure 4-12). The cathode was supplied with humidified CO_2 gas, and the anode was fed with 0.5M KOH electrolyte. The cell voltage and product distribution were monitored under galvanostatic conditions at current densities of 100, 150, 200, and 300 mA cm^{-2}

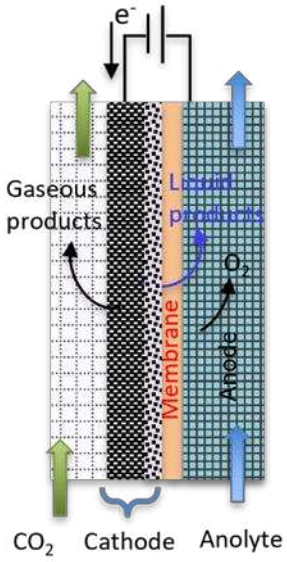


Figure 4-12. Schematic diagrams of zero-gap electrochemical cell (MEA-cell).

As shown in (Figure 4-13a), hydrogen production remains nearly constant across all investigated current densities, with a Faradaic efficiency of approximately 19%, consistent with the behavior observed in the flow-cell measurements. This indicates that hydrogen evolution does not scale proportionally with increasing current density and does not dominate the reaction under these alkaline conditions. In contrast, the distribution of carbon-containing products exhibits a pronounced dependence on current density. With increasing current density, Faradaic efficiency for CO decreases significantly, while selectivity toward C_2H_4 increases markedly. This trend culminates at 200 mA cm^{-2}, where a maximum Faradaic efficiency of 51.6% for C_2H_4 is achieved. Ethylene thus becomes the dominant carbon-containing product under zero-gap operation. When considering the total C_2 product formation (including C_2H_4 and other minor C_2 species), C_2 products account for 67% of the total products in the zero-gap cell (Figure 4-13b). This clearly demonstrates that multi-carbon formation dominates under these conditions.

Importantly, a clear selectivity shift is observed when transitioning from the liquid-phase flow-cell to the zero-gap architecture. At comparable current densities, the zero-gap cell suppresses CO formation and enhances C_2 selectivity, particularly toward C_2H_4. This shift arises from fundamental differences between the two architectures (235–238). In the zero-gap cell, the local CO_2 availability at the catalyst-membrane interface, the carbonate formation dynamics in alkaline media, water management within the GDE, and the retention of key intermediates at high surface coverage differ significantly from the liquid-phase flow-cell environment. These factors favor higher *CO surface coverage and promote C-C coupling pathways under zero-gap operation.

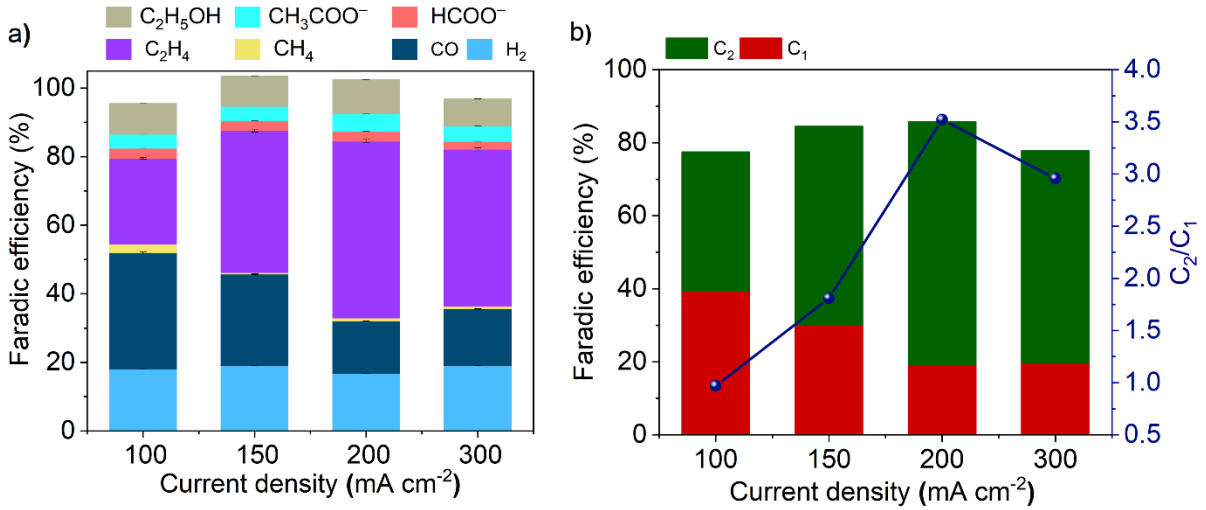


Figure 4-13. (a) Faradaic efficiencies of CO_2 reduction products on Cu-MOF gas diffusion electrodes in a zero-gap cell at different current densities using 0.5M KOH as anolyte. (b) Corresponding Faradaic efficiencies and C_2/C_1 product ratio derived from the data in (a).

To further understand the influence of catalyst layer thickness on CO_2 electroreduction performance, gas diffusion electrodes with two loadings were prepared: a diluted ink (0.25 mg cm^{-2}) and the standard ink (1.6 mg cm^{-2}). Both were tested in the flow-cell at different current density under identical conditions (1M KOH, 25 mL·min^{-1} CO_2) to isolate the effect of catalyst loading on activity and selectivity. As shown in (Figure 4-14a), no significant variation in the electrode potential is observed at the same current density except the highest one. However, decreasing the catalyst loading from 1.6 to 0.25 mg cm^{-2} leads to a substantial increase in C_1 products and a decrease in C_2 products. The low-loading electrode (0.25 mg cm^{-2}) exhibits higher Faradaic efficiencies for H_2 and CH_4, while its C_2H_4 FE is low. The high-loading electrode (1.6 mg cm^{-2}) shows the opposite, CH_4 FE is negligible, and C_2H_4 FE is much higher. Quantitatively, ethylene FE is larger at 1.6 mg·cm^{-2} than at 0.25 mg·cm^{-2}. The CO FE is moderate for both cases, but the C_2/C_1 ratio increases dramatically with loading (Figure 4-14b). Increasing the catalyst loading increases the thickness of the porous layer, which likely leads to higher *CO surface concentration and longer residence time for intermediates. This promotes the C-C coupling steps needed for C_2H_4 formation. In contrast, the thinner (0.25 mg·cm^{-2}) layer allows intermediates to diffuse away more readily or be flushed by the flow, favoring C-C termination at C_1 products (CO, CH_4). These results align with known behavior of Cu catalysts: low metal loading favors hydrogenation to CH_4, whereas higher loading enables carbon-carbon coupling (239).

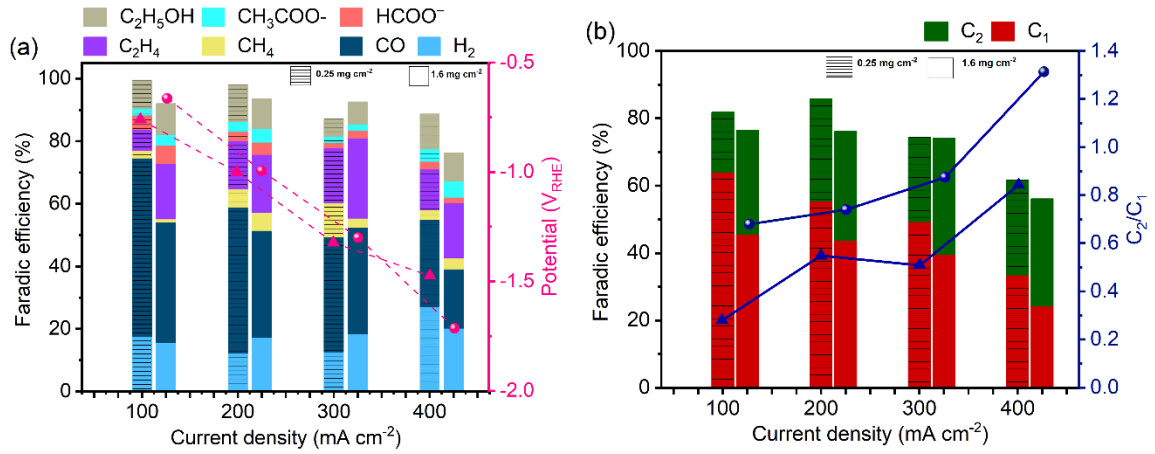


Figure 4-14. (a) Faradaic efficiencies of CO_2 reduction products for Cu-MOF electrodes with different loadings (1.6 and 0.25 mg cm^{-2}) in a flow cell at various applied current densities in 1M KOH, including the corresponding electrode potentials. (b) Corresponding Faradaic efficiencies and C_2/C_1 product ratio derived from the data shown in (a).

A stability test was carried out in the zero-gap electrolyzer (as above) using a 0.5M KOH anolyte. The Cu-MOF GDE was operated at a fixed current density (200 mA·cm^{-2}) for 1 hour while monitoring product distribution. The cell was then disassembled for post-test inspection. Additional experiments were performed under varied conditions (lower KOH concentration,

reduced current, $CsHCO_3$ electrolyte) to assess their effect on stability. (Figure 4-16) shows that with 0.5M KOH, the Cu-MOF achieves ~51% C_2H_4 FE after 1 hour. However, beyond 1 h a rapid increase in H_2 FE is observed, accompanied by a drop in C_2H_4 selectivity. Upon disassembling the cell, substantial salt deposits were visible in the cathode flow channels (Figure 4-15), especially near the gas inlet. These salts (mainly K_2CO_3) form in situ from CO_2 reacting with OH^- in the alkaline electrolyte. The precipitated carbonate physically blocks CO_2 access to parts of the catalyst layer, creating localized CO_2 starvation. Under these starved conditions, the kinetics favor the hydrogen evolution reaction, explaining the observed surge in H_2 production over time.

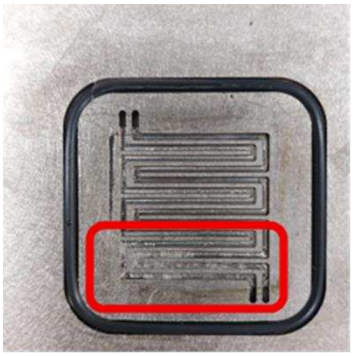


Figure 4-15. Salt deposition on the flow channel.

(Figure 4-16b-d) demonstrate that this degradation can be mitigated: (b) using a lower anolyte concentration (0.1M KOH) slows carbonate accumulation, (c) operating at lower current density (100 $mA \cdot cm^{-2}$) reduces OH^- generation rate, and (d) using Cs^+ instead of K^+ ($CsHCO_3$ anolyte) increases the solubility of the carbonate salt. Each strategy leads to a more stable C_2H_4 FE over time by limiting salt precipitation at the cathode.

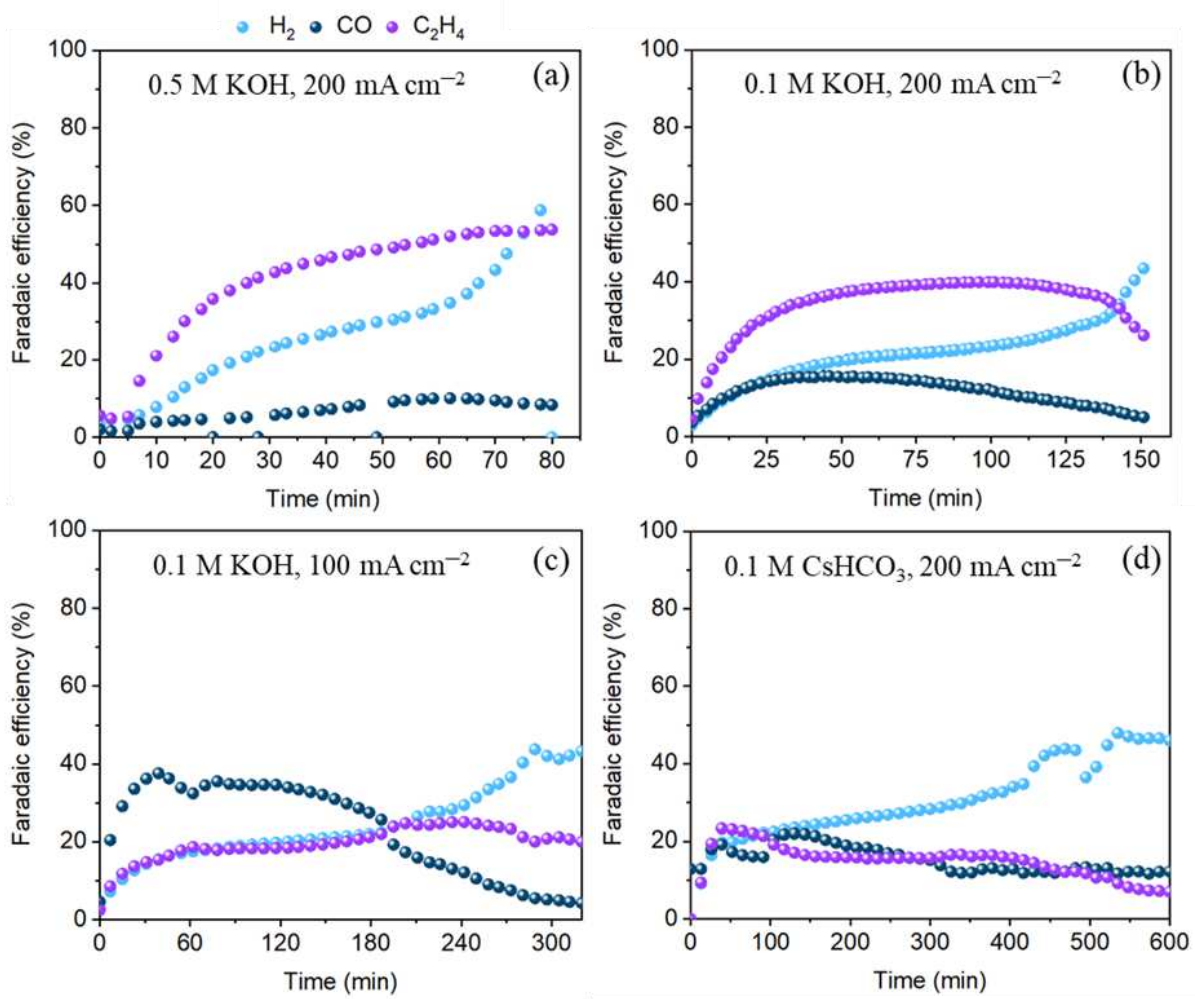


Figure 4-16. Time-dependent Faradaic efficiencies in the zero-gap cell at 200 mA·cm^{-2}: (a) with 0.5M KOH anolyte, (b) with 0.1M KOH, (c) at 100 mA·cm^{-2} (0.5M KOH), and (d) with 0.1M $CsHCO_3$ (200 mA·cm^{-2}).

Operando XAS measurements were performed to understand the changes in the electronic structure of Cu-MOF under CO_2RR conditions using a dedicated electrochemical cell (EC-cell) optimized for soft X-ray experiments (Figure 2-12) (240). The data reveal that Cu^{2+} centers in the Cu-MOF are gradually reduced to metallic Cu under CO_2RR conditions, consistent with previous reports (241). The catalyst ink was prepared via standard procedures by sonicating the material in a hydroalcoholic Nafion solution, followed by spray-coating onto a 15 nm Au-coated SiNx membrane (100 nm thick) and drying at 60 °C. The Cu L-edge spectrum of the pristine film confirms the presence of Cu^{2+} in the as-fabricated electrode (Figure 4-17a). Compared to the powder sample (Figure 4-17a), the S3 satellite peak (associated with ligand-to-metal charge transfer (LMCT) from N to Cu) shows a slight shift toward lower photon energy. This indicates a weaker ligand field and reduced Cu–N covalency within the MOF framework (242,243). This spectral shift is likely due to partial interactions

with Nafion functional groups, as well as the acidic and polar nature of the ionomer environment, which can influence ligand-field splitting without compromising the structural integrity of the MOF. Introducing CO_2-saturated 0.1 M $KHCO_3$ electrolyte into the EC-cell does not alter the catalyst's electronic structure, as the spectral intensity remains unchanged at open circuit potential (OCP, −0.1 V vs Ag/AgCl).

As increasingly negative potentials are applied, down to −1.4 V vs Ag/AgCl, the Cu^{2+} signal progressively diminishes, while features corresponding to metallic Cu emerge (Figure 4-17a). The metallic Cu signal appears relatively weak due to its significantly lower absorption transition probability (approximately 13 times lower than that of Cu^{2+}) and is partially obscured by background noise (244). Despite this, complete reduction to metallic Cu is clearly evident at −1.2 V vs Ag/AgCl, a potential at which CO_2RR is already active. When the potential is returned to −0.1 V vs Ag/AgCl, the original Cu^{2+} spectral features are fully restored. A comparison of the Cu L-edge spectra before and after CO_2RR (Figure 4-17b) shows no notable differences in peak shape or intensity, suggesting that the catalyst's electronic structure remains intact and that significant Cu dissolution does not occur.

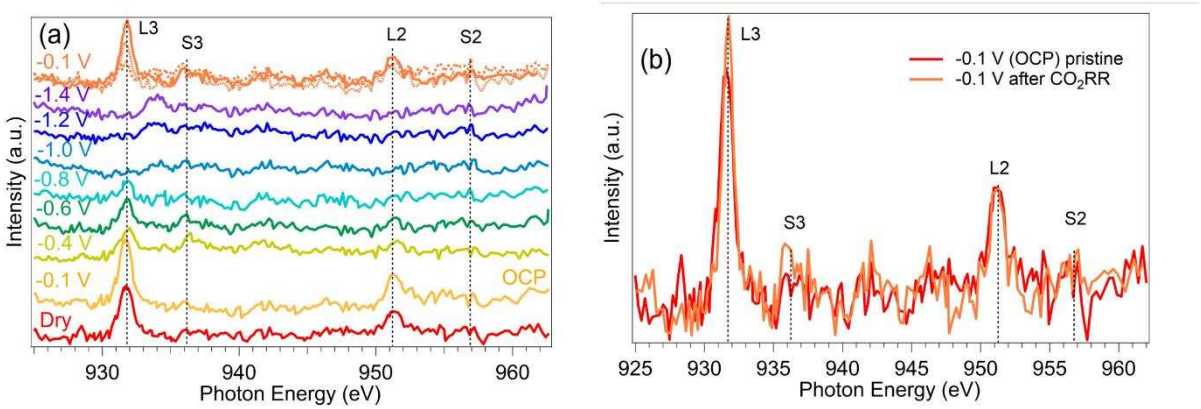


Figure 4-17. Operando soft XAS measurements performed in an EC-cell on a spray-coated Cu-MOF electrode dried at 60 °C: Cu L-edge spectra collected in FY mode for the dry electrode and their evolution from OCP to −1.4 V vs Ag/AgCl; (b) Comparison of Cu L-edge spectra.

Operando XAS reveals reversible changes in the electronic structure of Cu-MOF, specifically the reduction to metallic Cu under CO_2RR conditions and its recovery at OCP, occurring on a timescale of minutes. In contrast, salt precipitation is irreversible and accumulates over time, causing a progressive loss of C_2H_4 selectivity and eventual cell failure over hours. Mitigating salt formation under optimized zero-gap operating conditions could significantly enhance the long-term stability of CO_2RR on Cu-MOF electrodes.

4.2.3. Conclusions

In this chapter, a nitrogen-coordinated Cu-MOF was successfully synthesized via a green steam-assisted hydrothermal route, extending the solvent-minimized strategy previously applied to ZIF materials. Cu-MOF exhibits a well-defined Cu-N_4 coordination environment and a hierarchical flake porous morphology that together enable efficient CO_2 electroreduction. FESEM and BET measurements show that the Cu-MOF consists of a network of thin imidazolate nanosheets, with thicknesses of about 50–80 nm and lateral dimensions ranging from 200 to 1200 nm. The material also shows meso/macroporosity, with a specific surface area of 25.6 m^2 g^{-1} and a pore volume of 0.24 cm^3 g^{-1}. These structural features provide accessible active sites while also facilitating mass transport through the catalyst layer. CHNS, ICP-OES, and TGA analyses give a composition consistent with the expected material, including a Cu content of about 28 wt% and a Cu:N ratio of approximately 1:3.93. The FTIR, Raman, XPS, and XAS results further support the presence of the imidazole ligands and Cu(II)–N coordination. These structural characteristics are also reflected in the electrochemical results. In the flow-cell experiments, the Cu-MOF reaches a current density of 220 mA cm^{-2} at −1.2 V, with a clear change from mainly CO formation towards C_2 products as the overpotential increases. Ethylene reaches a Faradaic efficiency of about 35% at the highest overpotential investigated. Higher C_2H_4 selectivity, up to 51.6%, is obtained when the catalyst is tested in a zero-gap MEA, although longer operation requires careful electrolyte management to limit carbonate deposition. Changing the catalyst loading also affects product distribution. Thicker catalyst layers favor higher *CO coverage and C–C coupling, whereas thinner layers show a greater contribution from H_2 and CH_4. The stability tests show that the initial C_2H_4 selectivity, around 51% after 1 h, decreases during prolonged operation in concentrated alkaline electrolyte. This decline is associated with salt deposition in the cathode flow channels, resulting from the reaction between CO_2 and OH^- during electrolysis. The accumulated deposits can locally limit CO_2 transport to the catalyst and eventually shift the reaction towards hydrogen evolution. Mitigation strategies, including lowering anolyte concentration, reducing current density, and replacing K^+ with Cs^+ cations, significantly improve operational stability by limiting salt precipitation. Importantly, post-electrolysis SEM, XPS, and operando XAS analyses confirm that the Cu-MOF framework remains structurally intact and that Cu redox transitions are reversible under applied bias.

Chapter 5. Ni based on Nitrogen-doped mesoporous carbon

The studies of ZIF-8, ZIF-67, and Cu-MOF showed that the metal–ligand coordination environment can strongly influence the CO_2RR pathway and can be used to tune the formation of C1 and C2 products. However, maintaining high selectivity toward one product over a wide range of operating conditions remains difficult. In MOF-based catalysts, the product distribution can change with the electrolyte composition, local pH, accumulation of reaction intermediates, and structural changes under applied potential. Strongly alkaline conditions can also lead to carbonate formation and salt precipitation, whereas acidic conditions may affect the stability of the framework and increase the contribution of the hydrogen evolution reaction. These observations point to a trade-off between the well-defined structure offered by coordination-based materials and their stability under practical operating conditions.

Electrochemical CO_2 reduction in membrane-electrode assemblies (MEAs) is a promising approach for producing CO at higher current densities, but maintaining both high selectivity and long-term stability remains challenging. In this thesis, a heterogeneous nickel sulfide catalyst supported on N-doped mesoporous carbon (NiS_x@NMC) was prepared by nanocasting and subsequently modified by acid leaching. This treatment selectively removed unstable Ni-rich species while retaining the crystalline Ni_3S_2 phase, resulting in a Ni-deficient and sulfur-enriched surface. This surface modification improved both the catalytic performance and the stability of the material under acidic conditions.

The resulting NiS_x@NMC_AL catalyst showed near-unity CO selectivity in a zero-gap MEA, with CO Faradaic efficiencies above 90% and values close to 100% at current densities of 100–150 mA cm^{-2}. High CO selectivity was maintained over a wide pH range, including strongly acidic conditions at pH 1. This behavior indicates that the sulfur-coordinated Ni sites can effectively suppress the competing HER.

Operation with neutral anolytes was affected by carbonate salt accumulation, while adjusting the anolyte to pH 3 reduced salt deposition and allowed stable operation for 450 min at 100 mA cm^{-2}, while maintaining near-unity CO selectivity. Under these conditions, the catalyst also achieved a full-cell energy efficiency of 43.7%.

Overall, the results show that combining acid-leached nickel sulfides with controlled acidic operation can improve CO_2RR selectivity while limiting HER and salt deposition. This approach also enabled stable CO_2-to-CO electrolysis at relatively high current density and with good full-cell energy efficiency.

5.1. Materials and Synthesis Methods

All samples were prepared via a nanocasting method using SBA-15 as a sacrificial hard template. D-Glucosamine and urea were used as the carbon and nitrogen sources, while nickel nitrate and H_2SO_4 served as the nickel and sulfur sources, respectively. By varying the precursor solution composition, nitrogen-doped mesoporous carbon (NMC) support, NMC supported NiS_x (NiS_x@NMC), and NMC supported Ni (Ni@NMC) counterparts were

synthesized. An acid leaching (AL) step was applied to the Ni@NMC and NiS_x@NMC samples to obtain Ni@NMC_AL and NiS_x@NMC_AL, respectively.

As shows in Figure 5-1, SBA-15 was synthesized via a modified sol-gel method, adapting the procedure described by Choi et al.(245). Briefly, 6.92 g of P123 was dissolved in a solution of 125.6 g distilled water and 3.78 g HCl (37%). 14.88 g of TEOS was rapidly introduced under vigorous stirring at 35 °C. The resulting mixture was aged at 35 °C for 24 h, followed by static hydrothermal leaching at 100 °C for 24 h. The solid product was recovered by filtration and dried at 100 °C without washing. Notably, filtration was significantly expedited compared to conventional SBA-15 syntheses. Template removal was achieved by a solvent extraction process. The as-synthesized material was refluxed in a solution of 250 mL ethanol and 3.67 mL HCl (37%) within a round-bottom flask equipped with a condenser to prevent evaporation. The extraction was conducted under magnetic stirring at 80 °C for 6, followed by filtration, drying at 100 °C, and calcination at 550 °C in air for 6h.

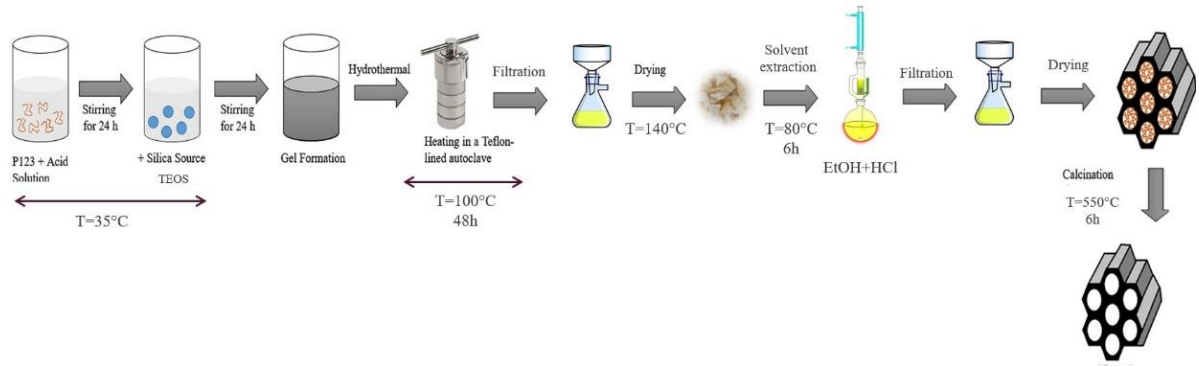


Figure 5-1. Schematic synthesis of SBA-15 via P123-templated self-assembly, hydrothermal treatment, extraction, and calcination

Nitrogen-doped mesoporous carbon (NMC) and Ni-containing NMC were synthesized using SBA-15 as a hard template following a modified procedure reported by Maruccia et al (246). For the synthesis of NiS_x supported on NMC (NiS_x@NMC), SBA-15 was impregnated in two successive steps with aqueous solutions containing D-glucosamine, urea, nickel (II) nitrate hexahydrate, and H_2SO_4 (Figure 5-2). In the first impregnation, 0.3962 g D-glucosamine, 1.14 g urea, and 0.2664 g nickel (II) nitrate hexahydrate were dissolved in 3 mL deionized water containing 0.0485 mL H_2SO_4 and added dropwise to 500 mg SBA-15 under stirring. After 1 h stirring, the material was heated from room temperature to 100 °C for 6 h, from 100 to 140 °C for 2 h, and from 140 to 160 °C for 6 h at a heating rate of 3 °C min^{-1}. In the second impregnation, 0.243 g D-glucosamine, 0.0756 g urea, and 0.164 g nickel (II) nitrate hexahydrate were dissolved in 1.84 mL deionized water containing 0.03 mL H_2SO_4 and introduced into the intermediate product. After stirring for 1 h, the sample was heated from room temperature to 100 °C for 6 h and from 100 to 140 °C for 2 h. The resulting solid was ground and pyrolyzed under inert atmosphere to 900 °C at 3 °C min^{-1}. The silica template was

removed using 6 M NaOH, and the product was washed to neutral pH and dried at 70–80 °C overnight.

For the synthesis of Ni supported on NMC (Ni@NMC), the same procedure was followed, except that H_2SO_4 was omitted from both impregnation steps. The acid-leached samples, denoted NiS_x@NMC_AL and Ni@NMC_AL, were obtained by treating the corresponding pyrolyzed and template-removed materials with 37% HCl for 3 h at room temperature. The acid-treated products were then washed repeatedly with deionized water until neutral pH and dried at 70–80 °C overnight. For comparison, the pristine NMC support was synthesized by the same hard-template route in the absence of the nickel precursor

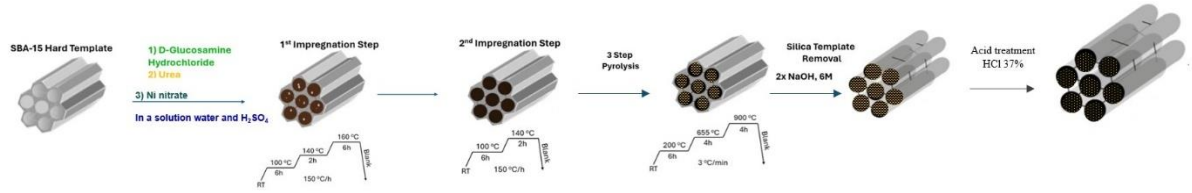


Figure 5-2. Schematic synthesis of Ni-based species anchored on nitrogen-doped mesoporous carbon using SBA-15 as a hard template, involving sequential impregnation, pyrolysis, template removal, and acid treatment.

5.2. Results and discussion

5.2.1. Physicochemical properties

Figure 5-3a shows the low-angle X-ray diffraction (XRD) patterns of all samples. With respect to the SBA-15 template (Figure 5-4), the resulting materials exhibit less ordered porosity, probably due to the excess quantity of urea used in precursor solution. The high-angle XRD patterns of all samples are shown in (Figure 5-3b). The pristine NMC exhibits a broad diffraction band centered at 2θ = ~25°, characteristic of amorphous/turbostratic carbon, confirming the disordered graphitic framework of the carbon support. Upon incorporation of Ni, the Ni@NMC sample displays intensive diffraction peaks corresponding to metallic Ni phase (JCPDS No. 04-001-3331), along with small reflections at 2θ = 25.4° and 36.3° related to Ni_3Si_2 (JCPDS No. 04-006-9134). Following the acid leaching step, these Ni related crystalline peaks completely disappear in the Ni@NMC_AL sample, consistent with their poor stability in acidic conditions (247,248). Concurrently, a peak at 2θ = 26.3° emerges, corresponding to the characteristic reflection of crystalline carbon (JCPDS No. 01-086-8298). The simultaneous incorporation of Ni and S results in the formation of NiS_x@NMC, which exhibits well-defined diffraction peaks indexed to two crystalline Ni_3S_2 phases (JCPDS No. 00-044-1418 and JCPDS No. 04-017-4589). Furthermore, weak diffraction peaks associated with metallic Ni indicates the presence of a minor fraction of this phase. Additional reflections are assigned to the presence of carbon (at 2θ = 26.1° for JCPDS card No. 04-014-0362, and graphitic carbon nitride (g-C_3N_4, at 2θ = 27.5° for JCPDS card No. 04-021-6536), likely

originating from the thermal polymerization of the urea precursor (249,250). After acid leaching, the NiS_x@NMC_AL sample retains the primary diffraction pattern of NiS_x@NMC but displays a noticeable increase in peak intensities. This behavior indicates that the overall crystallinity is enhanced likely due to the preferential removal of less stable, non-crystalline Ni species during AL process (251). In contrast to metallic Ni, transition metal sulfides generally exhibit enhanced chemical stability due to strong metal–sulfur interactions, which reduce susceptibility to complete oxidative dissolution (252,253). The persistence of metallic Ni after acid leaching can be attributed to confinement and encapsulation of Ni nanoparticles within the carbon framework and/or graphitic carbon nitride domains and/or NiS_x particles, which hinder access to the leaching medium (254,255).

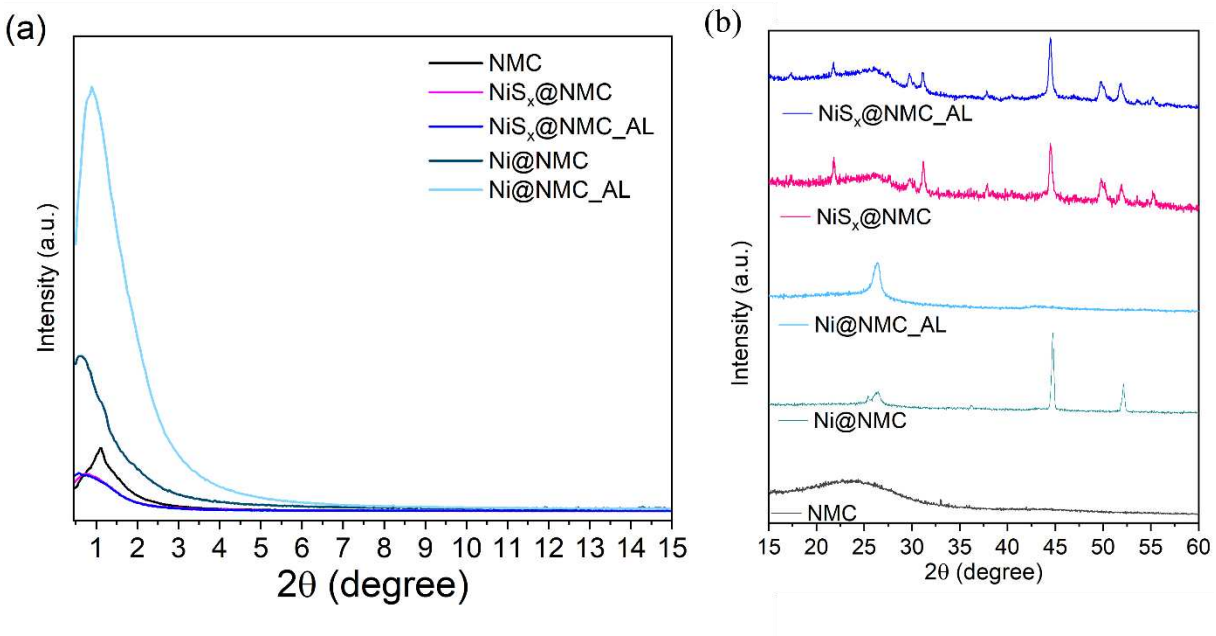


Figure 5-3. (a) Low-angle and (b) High-angle XRD patterns of NMC, Ni@NMC, NiS_x@NMC and after acid leaching

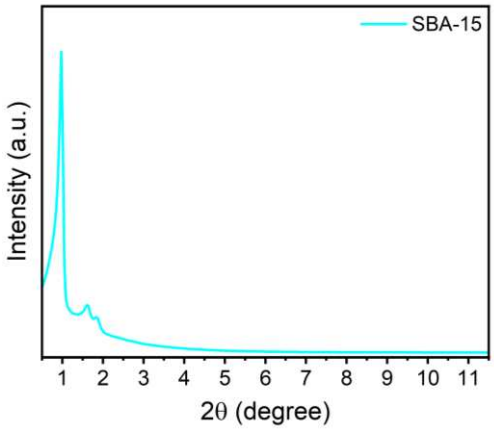


Figure 5-4. Low-angle XRD of SBA-15.

To comprehensive evaluate the microstructural properties of the catalysts, transmission electron microscopy (TEM) and energy-dispersive X-ray spectroscopy (EDS) mapping were performed, as illustrated in **Error! Reference source not found.**. The results reveal a profound morphological evolution induced by the incorporation of sulfur and the subsequent acid leaching process.

A stark contrast is observed between the Ni@NMC and Ni@NMC_AL samples. For the as-prepared Ni@NMC, surface-bound crystalline particles are clearly visible throughout the matrix (Figure 5-5a and e). Following the acid leaching step, these surface particles are entirely absent on Ni@NMC_AL sample, while the underlying mesoporous carbon channels derived from the SBA-15 template remain structurally intact (Figure 5-5). Corresponding EDS elemental maps show a continuous and uniform distribution of carbon (C) and nitrogen (N) in both Ni@NMC and Ni@NMC_AL, but no resolvable nanoparticles are observed in the latter. These results are consistent with XRD analysis, confirming the effective removal of surface-exposed metallic Ni with the acid leaching step. In contrast, both the NiS_x@NMC (Figure 5-5c and f) and NiS_x@NMC_AL (Figure 5-5d and g) samples show a dense distribution of robust, well-defined nanoparticles throughout the N-doped carbon matrix. Elemental mapping confirms that Ni and S signals are exclusively localized on these nanoparticles with a strong spatial correlation, while C and N remain homogeneously distributed throughout the graphitic framework. This result suggests that NiS_x constitutes the predominant Ni-containing species and is well retained after acid leaching. However, metallic Ni particles are not observed in element mapping (Figure 5-5c and d), which appears inconsistent with the XRD results showing a minor metallic Ni phase in both the NiS_x@NMC and NiS_x@NMC_AL samples. This apparent discrepancy may be attributed to the encapsulation of metallic Ni particles within the carbon matrix of NiS_x particles, which could limit their detection by EDS mapping. The TEM images in Figure 5-5f and g show distinctive core-shell and confined nano-topographies, where core particles are tightly enveloped within graphitic carbon sheets.

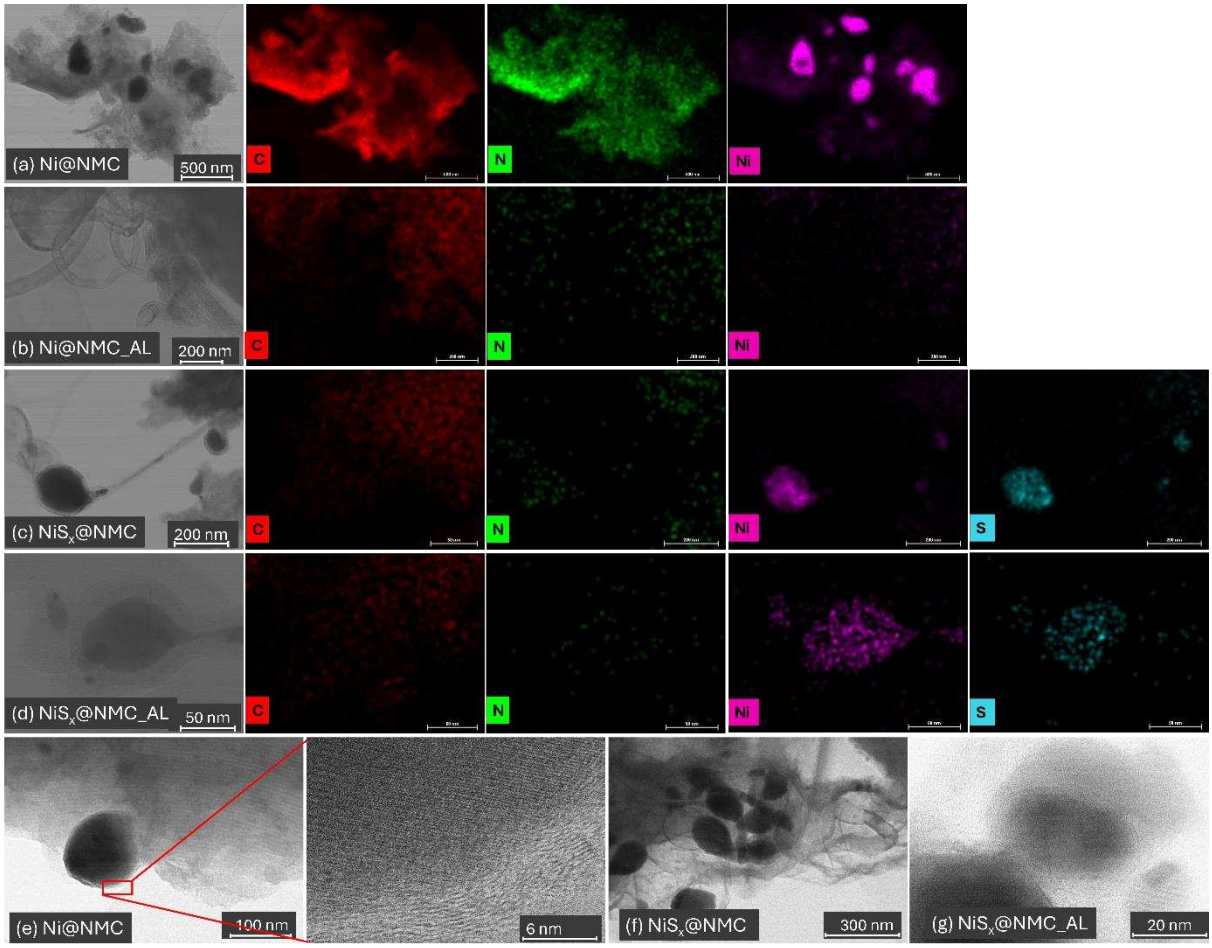


Figure 5-5. TEM images and elemental mapping of various catalysts: (a) Ni@NMC, (b) Ni@NMC_AL, (c) NiS_x@NMC and (d) NiS_x@NMC_AL. HR-TEM images of the Ni containing samples: (e) Ni@NMC, (f) NiS_x@NMC and (g) NiS_x@NMC_AL

To analyze the textural properties and pore size distributions of the catalysts, N_2 adsorption–desorption measurements were performed. Detailed textural parameters and NLDFT−derived pore size distributions for all samples are provided in the Figure 5-6-Figure 5-7. All catalysts exhibit type IV isotherms with H3-type hysteresis loops, according to the IUPAC classification (175). The materials possess a hierarchical pore structure consisting of a dominant mesopore peak centered at about 3–4 nm and significant microporosity originating from the carbon channels. The pristine NMC exhibits a specific surface area (S_{BET}) of 263 $m^2\ g^{-1}$. Upon incorporation of Ni species, both Ni@NMC and NiS_x@NMC show a reduction in S_{BET} (228 $m^2\ g^{-1}$ and 245 $m^2\ g^{-1}$, respectively) and decreased pore volumes (0.190 and 0.211 $cm^3\ g^{-1}$, respectively), indicating partial pore blocking. A significant divergence in textural evolution was observed after the acid leaching step. Ni@NMC_AL exhibits a significant increase in S_{BET} (up to 683 $m^2\ g^{-1}$) and a pronounced enhancement in mesopore volume, reflecting the efficient removal of metallic Ni and the reopening of blocked pores (256). In contrast, NiS_x@NMC_AL shows only moderate changes in isotherm and pore size distribution, indicating that the NiS_x

species are structurally acid-resistant and remains embedded within the carbon framework. These results are consistent with the XRD, TEM and elemental mapping analyses, confirming the robustness of the NiS_x@NMC_AL catalyst in strong acid.

The chemical composition of the samples was further analyzed using elemental analysis for S and N quantification and total reflection X-ray fluorescence (TXRF) for Ni loading determination., as summarized in The pristine NMC contains 5.2 wt% N and a minor amount of S (0.7 wt%), likely reflects minor doped S in carbon matrix or residual precursor (H_2SO_4). Upon the incorporation of nickel, the Ni@NMC sample shows 2.4 wt% N and a substantial Ni loading of 19.1 wt%. Following the acid leaching step, the N content remains largely preserved at 3.0 wt%, whereas the Ni content undergoes a sharp reduction to 1.0 wt% (Ni@NMC_AL). This significant decrease confirms the effective removal of metallic Ni species, consistent with XRD and TEM analyses. The simultaneous introduction of Ni and S results in the formation of NiS_x@NMC, which exhibits an enhanced nitrogen content of 7.2 wt% and significant sulfur incorporation (7.0 wt%), while maintaining a high Ni loading of 19.5 wt%, comparable to the sulfur-free Ni@NMC. After acid leaching, the NiS_x@NMC_AL sample retains N and S contents of, 7.0 wt% and 6.6 wt%, respectively, while its Ni content decreases drastically to 9.6 wt%. Given that no significant changes are observed between NiS_x@NMC and NiS_x@NMC_AL samples by XRD and TEM analyses, it is reasonable to infer that the dissolved Ni species originate primarily from amorphous Ni-rich phases or surface-accessible Ni species, rather than from the bulk crystalline Ni_3S_2 phase. It is worth to note that the NiS_x@NMC_AL shows a bulk Ni:S atomic ratio of 0.79, nearly half of the value of 1.52 measured for NiS_x@NMC and substantially lower than the stoichiometric value of 1.5 for Ni_3S_2. Given that the NMC support contains only 0.7 wt% of S, it is reasonable to assume that S in the NiS_x@NMC_AL sample is predominantly bonded to Ni rather than C. Therefore, the much lower Ni:S ratio in NiS_x@NMC_AL compared with the stoichiometric value in Ni_3S_2 suggests the formation of a nickel-deficient, sulfur-rich phase, likely at the Ni_3S_2 surface during acid leaching.

Table 5-1. Elemental composition (wt%) of MC and Ni-based composites before and after acid leaching. EA (C, H, N, S) and TXRF (Ni). The pristine NMC contains 5.2 wt% N and a minor amount of S (0.7 wt%), likely reflects minor doped S in carbon matrix or residual precursor (H_2SO_4). Upon the incorporation of nickel, the Ni@NMC sample shows 2.4 wt% N and a substantial Ni loading of 19.1 wt%. Following the acid leaching step, the N content remains largely preserved at 3.0 wt%, whereas the Ni content undergoes a sharp reduction to 1.0 wt% (Ni@NMC_AL). This significant decrease confirms the effective removal of metallic Ni species, consistent with XRD and TEM analyses. The simultaneous introduction of Ni and S results in the formation of NiS_x@NMC, which exhibits an enhanced nitrogen content of 7.2 wt% and significant sulfur incorporation (7.0 wt%), while maintaining a high Ni loading of 19.5 wt%, comparable to the sulfur-free Ni@NMC. After acid leaching, the NiS_x@NMC_AL sample retains N and S contents of, 7.0 wt% and 6.6 wt%, respectively, while its Ni content decreases drastically to 9.6 wt%. Given that no significant changes are observed between

NiS_x@NMC and NiS_x@NMC_AL samples by XRD and TEM analyses, it is reasonable to infer that the dissolved Ni species originate primarily from amorphous Ni-rich phases or surface-accessible Ni species, rather than from the bulk crystalline Ni_3S_2 phase. It is worth to note that the NiS_x@NMC_AL shows a bulk Ni:S atomic ratio of 0.79, nearly half of the value of 1.52 measured for NiS_x@NMC and substantially lower than the stoichiometric value of 1.5 for Ni_3S_2. Given that the NMC support contains only 0.7 wt% of S, it is reasonable to assume that S in the NiS_x@NMC_AL sample is predominantly bonded to Ni rather than C. Therefore, the much lower Ni:S ratio in NiS_x@NMC_AL compared with the stoichiometric value in Ni_3S_2 suggests the formation of a nickel-deficient, sulfur-rich phase, likely at the Ni_3S_2 surface during acid leaching.

Table 5-1. Elemental composition (wt%) of MC and Ni-based composites before and after acid leaching. EA (C, H, N, S) and TXRF (Ni)

Samples	Elemental analysis				TXRF
	C (wt%)	H (wt%)	N (wt%)	S (wt%)	Ni (wt%)
NMC	40.87	0.13	5.19	0.74	0
Ni@NMC	44.36	0.66	2.38	0.	19.1
Ni@NMC_AL	56.33	1.33	3.04	0	1.03
NiS_x@NMC	42.94	2.81	7.13	6.95	19.5
NiS_x@NMC_AL	47.95	0.98	7.12	6.38	9.6

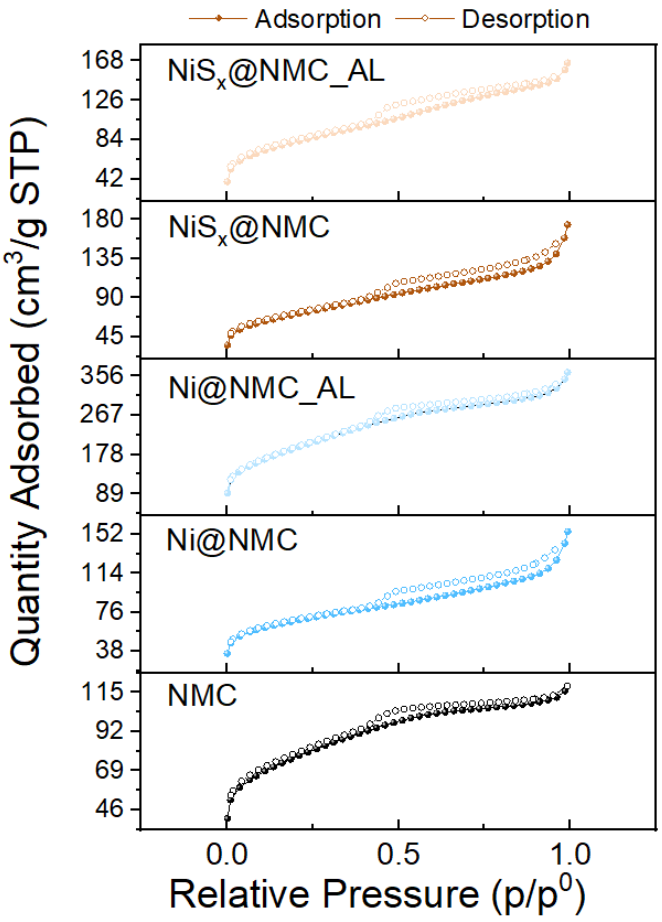


Figure 5-6. N_2 adsorption–desorption isotherms of NMC, Ni@NMC, Ni@NMC_AL, NiS_x@NMC, and NiS_x@NMC_AL measured at −196 °C.

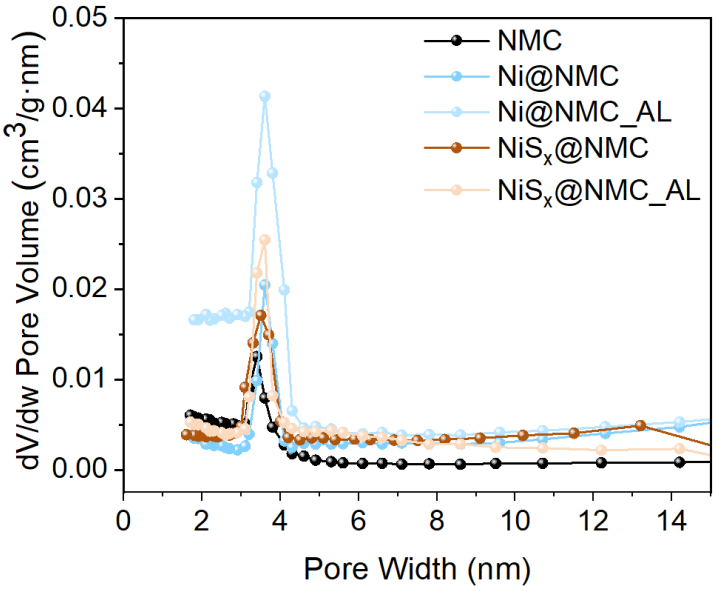


Figure 5-7. Pore size distributions of NMC, Ni@NMC, Ni@NMC_AL, NiS_x@NMC, and NiS_x@NMC_AL derived from NLDFT analysis of N_2 adsorption data.

To investigate the surface composition, X-ray photoelectron spectroscopy (XPS) was performed on selected samples NMC and NiS_x@NMC_AL. The survey spectrum of NMC (Figure 5-8a) shows dominant peaks corresponding to C 1s (~284 eV), O 1s (~531 eV) and N 1s (~399 eV) (257). A small Si 2p signal (~103 eV) is also detected, which can be attributed to residual silica template used during the synthesis of NMC-based materials. After incorporation of NiS_x followed by acid leaching, the survey spectrum of NiS_x@NMC_AL (Figure 5-8b) exhibits additional peaks corresponding to Ni 2p (~855 eV) and S 2p (~162 eV), confirming the successful introduction of Ni and S species on the mesoporous carbon support (258,259). In addition, an increase in the O 1s signal intensity is observed after the acid leaching. This increase can be attributed to the formation of oxygen-containing surface

functional groups or partial surface oxidation of sulfide species when exposed to air, a phenomenon frequently reported for transition-metal sulfide catalysts (260).

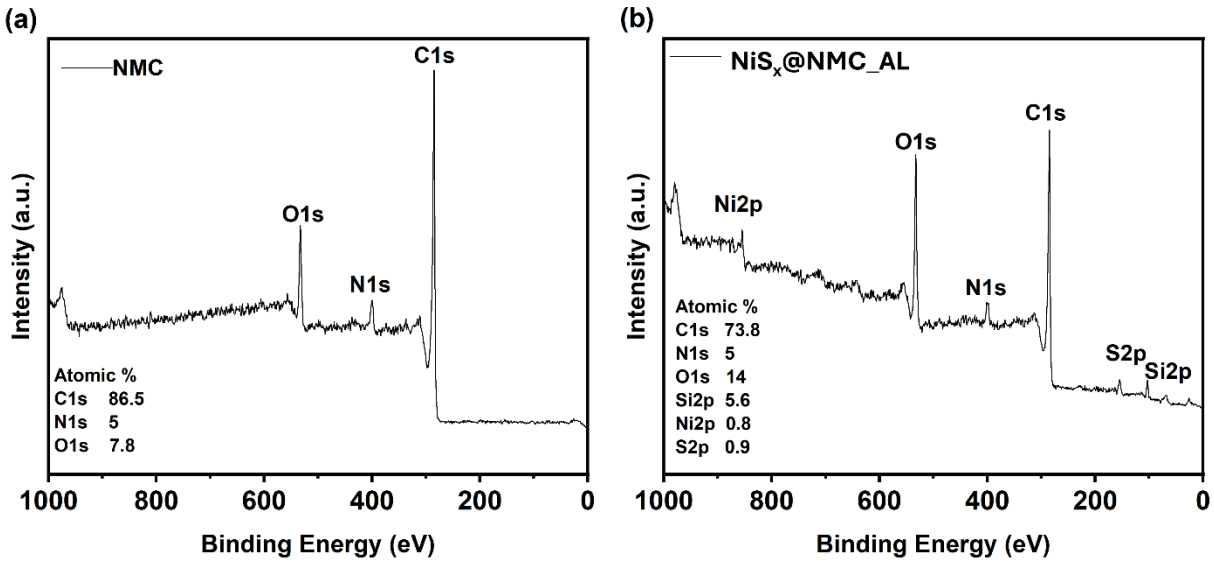


Figure 5-8. XPS survey of NMC (a) and NiS_x@NMC-AL (b). a) wide-scan XPS survey of nitrogen-rich mesoporous carbon, b) NiS_x embedded in nitrogen.

Table 5-2. Surface elemental composition from XPS survey spectra (At.%)

Element At%	C	O	Ni	N	S	Si
NMC	86.6	7.8	-	5	-	0.5
NiS_x@NMC_AL	73.8	13.9	0.8	4.9	0.9	5.6

The high-resolution C1s spectra of NMC and NiS_x@NMC_AL exhibited similar carbon bonding environments, dominated by graphitic carbon with contributions from nitrogen- and oxygen-containing functionalities (Figure 5-9a and Table 5-3. Relative distribution of carbon species (C 1s)). No significant shifts in binding energy or substantial changes in the relative distribution of carbon species were observed after NiS_x incorporation and acid leaching, indicating that the conjugated N-doped mesoporous carbon framework was largely preserved. The high-resolution N1s spectra of NMC and NiS_x@NMC_AL exhibit similar nitrogen functionalities, including pyridinic, pyrrolic, graphitic, and oxidized nitrogen species (Figure 5-9b and Table 5-4). The overall spectral profiles and binding energies remain largely unchanged after NiS_x incorporation and acid leaching, indicating that the nitrogen-doped carbon framework is preserved. Quantitative analysis shows that pyridinic and pyrrolic nitrogen

remain the dominant species, while the observed changes in their relative abundance suggest subtle modifications of the local nitrogen environment.

Table 5-3. Relative distribution of carbon species (C 1s)

Carbon species	NMC (%)	NiS_x@NMC_AT (%)
Graphitic C	30.2	30.7
sp^3 carbon	19.8	19.1
Secondary carbon	17.7	21.9
C–O / C–N	12.1	10.2
C=O	6.0	4.7
COOH	8.4	8.2
π–π* shake-up	3.6	3.2
π–π* shake-up	2.2	2.0

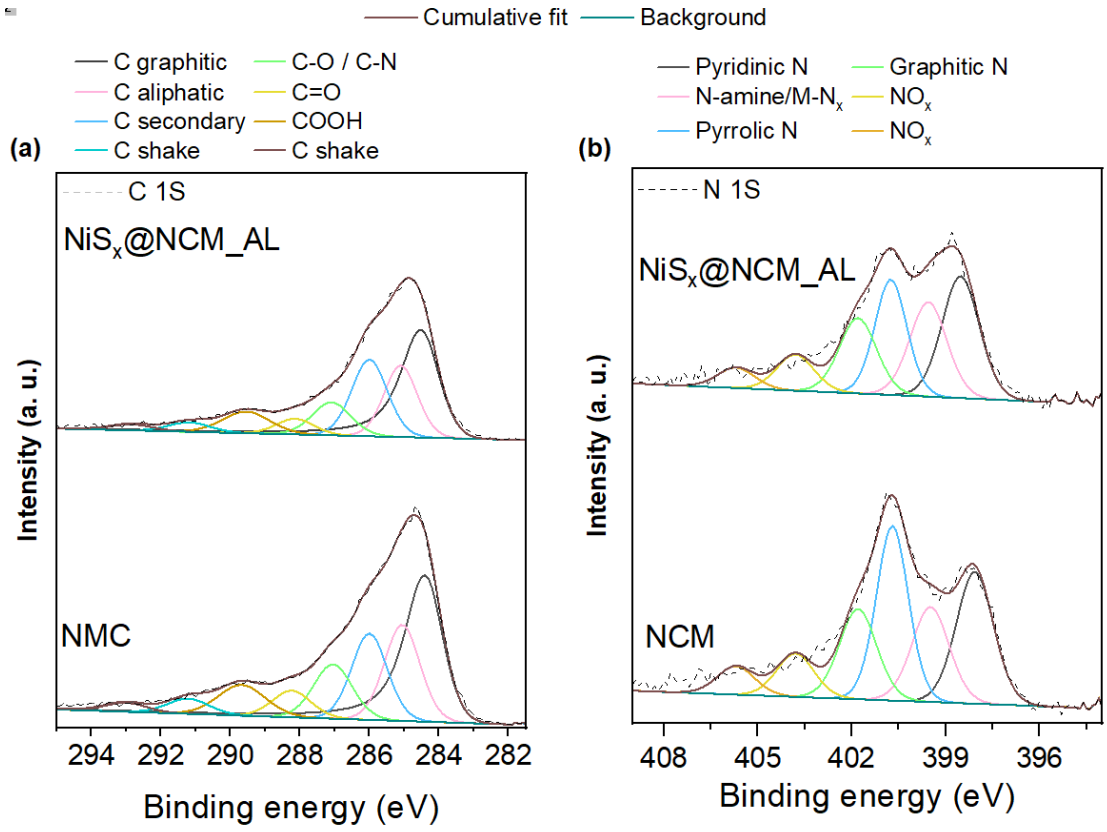


Figure 5-9. High-resolution XPS spectra of NMC and NiS_x@NMC_AT: (a) N 1s spectra and (b) C 1s spectra.

Table 5-4. Relative distribution of nitrogen species (N 1s)

N species	NMC (%)	NiS_x@NMC_AL (%)
Pyridinic N	24.4	27.3
N-amine/Metal–N_x	17.6	21.1
Pyrrolic N	27.8	22.1
Graphitic N	16.8	16.9
NO_x (403.8 eV)	8.1	8.1
NO_x (405.7 eV)	5.3	4.5

The Ni 2p spectrum (**Error! Reference source not found.**a) displays characteristic spin-orbit doublet for Ni $2p_{3/2}$ and Ni $2p_{1/2}$ at approximately 855 eV and 872–873 eV, respectively. The observed spin–orbit splitting of 17.35 eV, is characteristic of nickel sulfide species within a non-stochiometric NiS_x framework (261–263). The presence of weak shake-up satellite features at higher binding energies further suggests a heterogeneous chemical environment, involving partially oxidized Ni species and charge-transfer interactions between Ni 3d orbitals and the surrounding sulfur coordination (264). Notably, no signals corresponding to metallic nickel (Ni^0) were detected in the surface-sensitive XPS spectra (265,266). This observation is highly significant when contrasted with the bulk-sensitive XRD results, which clearly identify a crystalline Ni^0. The discrepancy suggests that the Ni^0 particles are likely encapsulated by the surrounding nickel sulfide or graphitic carbon framework or are otherwise present at a surface concentration below the XPS detection limit. In either case, the lack of surface-exposed metallic nickel explains why these species remain stable against oxidative dissolution during the strategic acid leaching process, in agreement with XRD and TEM analyses. The high-resolution S 2p spectrum was deconvoluted into three distinct spin-orbit doublets to accurately reflect the complex surface chemistry of the NiS_x@NMC_AL catalyst (Figure 3b). The primary doublet, positioned at 162.1/163.3 eV, is assigned to lattice sulfide sulfur within the crystalline Ni_3S_2 framework, showing excellent agreement with established literature for nickel sulfide standards (267–269). The intermediate doublet at 163.9/165.1 eV is conservatively assigned to a S-rich/S-S-like chemical environment, consistent with the formation of a Ni-deficient, S-enriched reconstructed Ni_3S_2 surface during acid leaching, as suggested by the bulk compositional analysis, although contributions from carbon-bound sulfur or partially oxidized S–Ni–O environments cannot be excluded (270). Finally, a third contribution at higher binding

energies (168.4/169.6 eV) corresponds to oxidized S(VI) sulfate-like species, likely resulting from partial surface oxidation during air exposure or residual precursors (271).

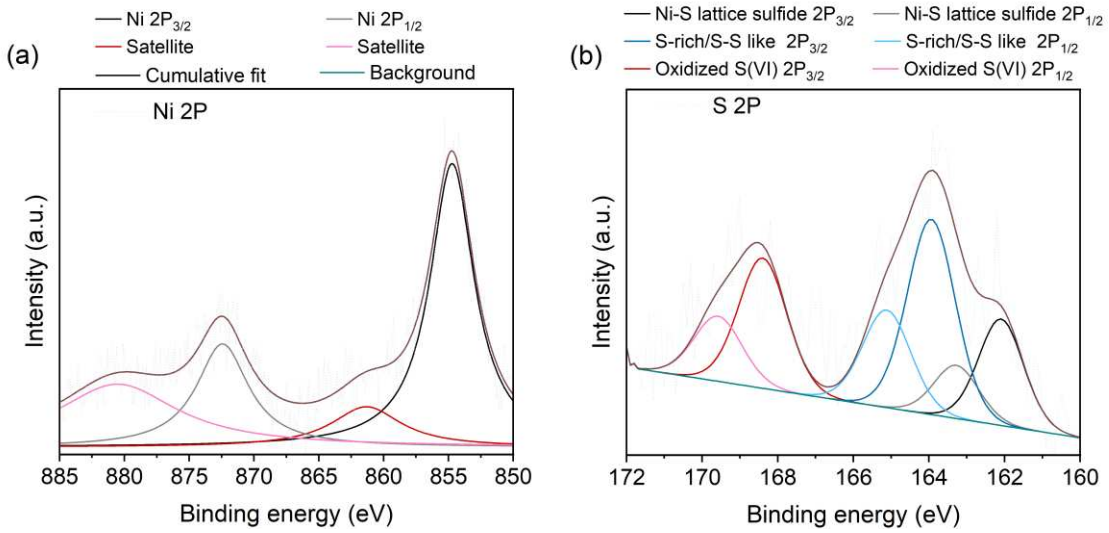


Figure 5-10. High-resolution XPS spectra of NiS_x@NMC: (a) Ni 2p region and (b) S 2p region.

5.2.2. Electrocatalytic performance

The CO_2RR performance of the catalysts was first evaluated in a zero-gap MEA at current densities of 100 and 150 mA cm^{-2}, utilizing a neutral anolyte (0.1 M $KHCO_3$, pH ≈ 8.3). As shown in **Error! Reference source not found.**, the pristine NMC support exhibits negligible selectivity, with H_2 evolution dominating at both current densities. Upon incorporation of Ni species (~19 wt% loading), both Ni@NMC and NiS_x@NMC samples exhibit similar CO selectivity (40-50% FE) and comparable cell voltages, indicating that both metallic Ni and Ni_3S_2 nanoparticles serve as active sites. A pronounced divergence in catalytic behavior emerges following the strategic acid leaching. The Ni@NMC_AL sample suffers a near-total loss of CO_2RR selectivity, with H_2 evolution becoming dominant, closely resembling the behavior of the NMC support. This is consistent with their similar physicochemical properties following the extensive removal of Ni during acid leaching. In contrast, the NiS_x@NMC_AL catalyst exhibits an enhancement in CO selectivity, achieving a FE exceeding 90%. Furthermore, the cell voltage slightly decreases at each current density for NiS_x@NMC_AL, suggesting that the acid leaching also activates NiS_x catalyst or enhances electronic conductivity due to the amorphous phase removal [31,32]. This activation is driven by the unique structural transformation of the Ni_3S_2 surface induced by the acid leaching, which serves as an interface engineering tool rather than a mere cleaning step (270). The reconstructed Ni-deficient, S-enriched layer on Ni_3S_2 provides an optimal platform for CO_2RR activation and drives the selectivity toward CO (267). Similar surface reconstruction-induced activity enhancements in nickel sulfides have been observed where surface transformation creates new

coordination environments that stabilize key reduction intermediates (268,272,273). Moreover, the removal of less-stable Ni species by acid leaching could also increase the exposure of highly active, well-coordinated sites within N-doped carbon frameworks (274,275).

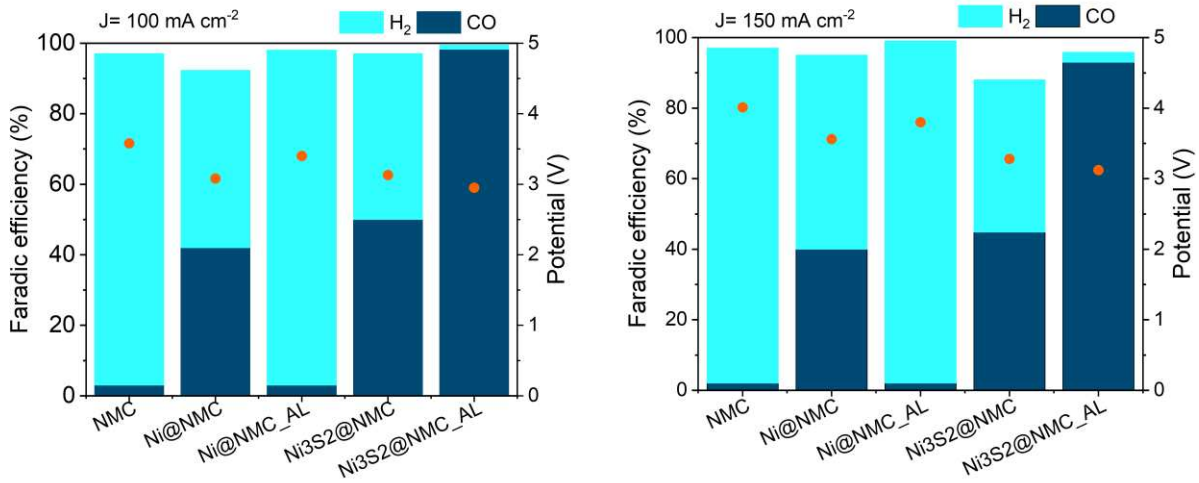


Figure 5-11. CO_2 electroreduction performance of NMC, Ni@NMC (with and without acid leaching), and NiS_x@NMC (with and without acid leaching) in 0.1 M $KHCO_3$ (pH ≈ 8.3) under zero-gap MEA operation (a) 100 mA cm^{-2} and (b) 150 mA cm^{-2}.

The catalytic performance of the NiS_x@NMC_AL was further investigated across a broad current density range in 0.1 M $KHCO_3$ anolyte. As shown in Figure 5-12a, CO remains the dominant product throughout the entire tested range. Even at a low current density of 25 mA cm^{-2}, the FE for CO exceeds 85%, indicating efficient CO_2 activation at a low overpotential. Selectivity further improves at higher reaction rates, achieving near-unity FE_{CO} at100 and 150 mA cm^{-2}. At 200 mA cm^{-2}, CO remains the major product, although a moderate increase in H_2 is observed, reflecting the increased kinetic competition from the HER under high-rate operation.

The time-dependent stability was also explored at 100 mA cm^{-2} using a 0.1 M $KHCO_3$ anolyte (Figure 5-12b). The catalyst maintained near-unity CO selectivity for 150 min with negligible H_2 evolution. By replacing $KHCO_3$ anolyte with a non-buffered 0.05 M K_2SO_4 (pH ≈ 7), **Error! Reference source not found.**the catalyst exhibits nearly identical performance, reaching ~95-97% FE_{CO} at both 100 and 150 mA cm^{-2} (Figure 5-12c) and maintaining stable production for 150 min (Figure 5-12d). These results demonstrate that the anolyte anions (HCO_3^- and SO_4^{2-}) does not significantly impact the selectivity or stability of catalyst. Crucially, all stability tests in neutral anolytes were terminated not due to catalyst degradation, but because of electrode choking caused by massive salt deposition. This interfacial salt accumulation, clearly visible upon cell disassembly, blocks active sites and gas diffusion channels, a common failure mode in zero-gap MEAs. While the zero-gap configuration lacks

a bulk catholyte, the anolyte pH serves as a vital control knob for the cathodic microenvironment. It directly regulates the rate of proton migration and diffusion across the membrane to cathode. By transitioning to acidic anolyte conditions, it is possible to increase the proton flux to the cathode, thereby promoting the dissolution of carbonate precipitates and extending operational longevity. However, the acidic environment poses severe challenges to catalyst stability while simultaneously favoring HER kinetics, thereby requiring catalysts that combine high acid resistance with intrinsically low HER activity.

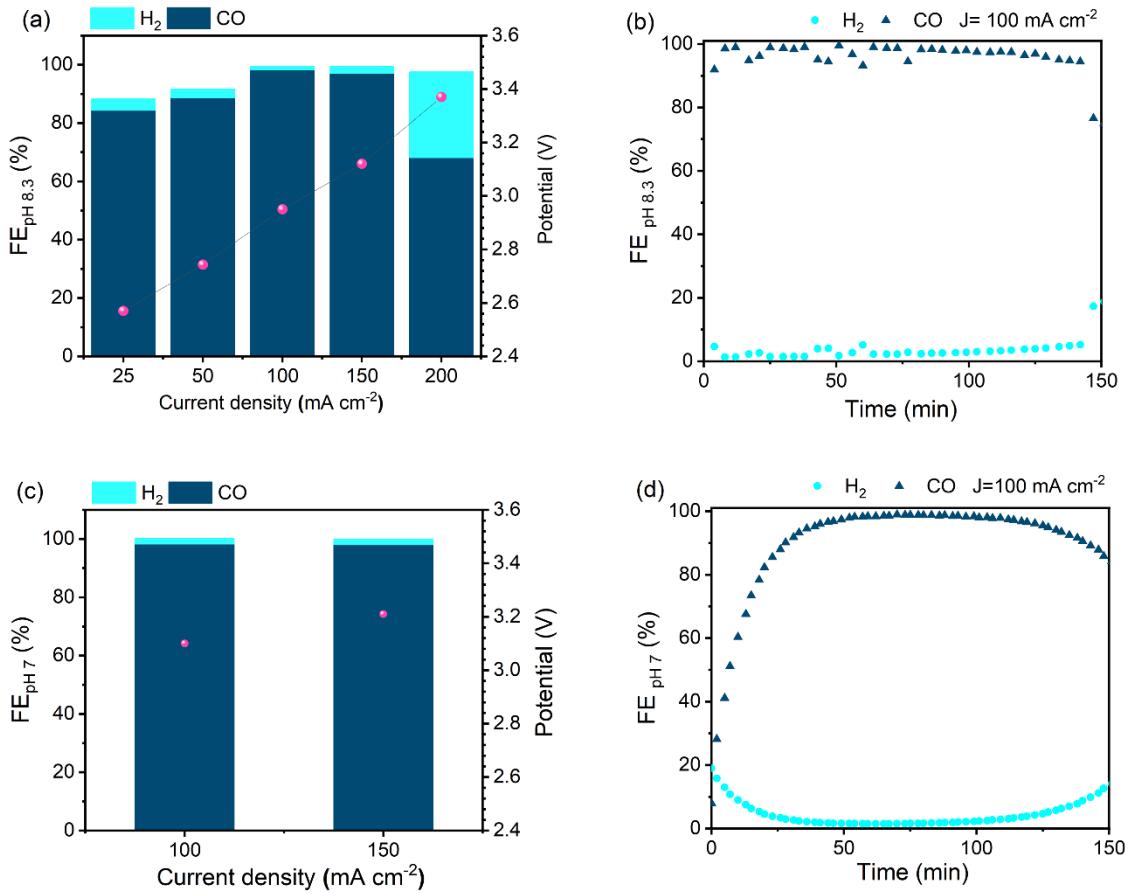


Figure 5-12. CO_2RR performance in a zero-gap MEA. (a) FE at different current density (25–200 mA cm^{-2}) in 0.1 M $KHCO_3$. (b) Time-dependent FE in 0.1M $KHCO_3$ at 100 mA cm^{-2}, (c) FE at 100 and 150 mA cm^{-2} in 0.05 M K_2SO_4.(d) Time-dependent FE in K_2SO_4 at 100 mA cm^{-2}.

To investigate the CO_2RR performance of NiS_x@NMC_AL in acidic condition, the anolyte composition was tuned by adding concentrated H_2SO_4 into 0.05 M K_2SO_4 to obtain moderate acidic (pH 3) and strongly acidic (pH 1) solutions. Since the added H_2SO_4 volumes were

negligible with respect to the solution volume, the K^+ concentration was approximately kept at 0.1 M.

As shown in Figure 5-13a and c, the NiS_x@NMC_AL catalyst maintains near-unity CO selectivity across the investigated current density range for both acidic anolytes. This exceptional selectivity in proton-rich environments is primarily attributed to the reconstructed sulfur-coordinated Ni sites, which weaken hydrogen adsorption and effectively suppress the competing HER (276). Furthermore, rapid proton consumption during the reduction reactions creates a locally less acidic microenvironment at the electrode-electrolyte interface, thereby helping to suppress the HER and favor the CO_2RR (277–279). Notably, the use of a pH 3 anolyte substantially enhances durability, enabling stable continuous operation for 450 min (Figure 6b), three times as long as the 150 min achieved with the neutral anolyte. This enhanced durability highlights the effectiveness of acidic conditions in suppressing salt deposition, while also demonstrating the robust stability of the NiS_x@NMC_AL catalyst under these operating conditions, which can be attributed to the stable and active NiS_x species formed during the acid-leaching step. However, a noticeable decrease in operational stability is observed under strongly acidic conditions (pH 1) (Figure 5-13d) compared with that achieved using the pH 3 anolyte. This decline in lifespan is likely due to the accelerated catalyst degradation such as metal leaching and restructuring under the combined cathodic bias and strong acidity (278–280). These findings underscore a critical trade-off in acidic electrolysis, while acidic anolytes are vital for mitigating the carbonate issue, excessive acidity can compromise the physical integrity of even robust catalysts. Consequently, pH 3 anolyte is identified as an optimal condition, providing the necessary proton flux for salt management while preserving the engineered catalyst interface. The near-unity selectivity and sustained high-performance

highlight the significant potential of the NiS_x@NMC_AL catalyst for practical, durable acidic CO_2–to–CO conversion.

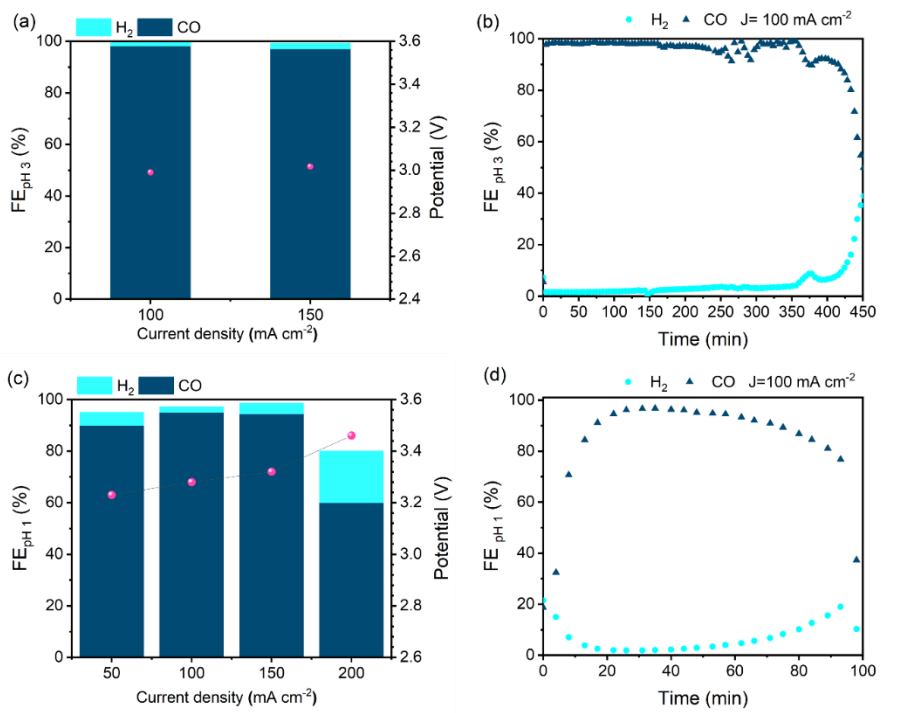


Figure 5-13. CO_2RR performance under acidic conditions in a zero-gap MEA. (a) FE at pH ≈ 3 at 100 and 150 mA cm^{-2}, (b) Time-dependent FE at pH ≈ 3, (c) FE of CO and H_2 at pH ≈ 1 under the same conditions and (d) Time-dependent FE at pH ≈ 1.

The practical potential of the NiS_x@NMC_AL catalyst is further highlighted by its exceptional full-cell EE. With pH 8.3 anolyte, the system achieves a peak EE of 44.3% (100 mA cm^{-2}), facilitated by the low cell voltage and near-unity CO selectivity. Remarkably, this high EE is largely preserved when transitioning to acidic conditions, which is 43.7% at pH 3 and 38.5% at pH 1 (100 mA cm^{-2}).

5.2.3. Conclusion

In this chapter, we demonstrate that acid-leaching-induced surface reconstruction provides an effective strategy for engineering Ni sulfide catalysts toward selective and durable CO_2 electroreduction under acidic conditions. A heterogeneous NiS_x catalyst supported on N-doped mesoporous carbon was synthesized through a hard-template route followed by acid leaching. This treatment preserves the crystalline Ni_3S_2 framework while inducing the formation of a Ni-deficient, S-enriched reconstructed surface, thereby creating a chemically distinct and acid-resistant catalytic interface.

This controlled surface reconstruction translates directly into enhanced CO_2RR performance. NiS_x@NMC_AL achieves near-unity CO selectivity at 100–150 mA cm^{-2} across a broad pH range, demonstrating that acid leaching functions as an effective surface-engineering strategy

that selectively removes unstable Ni-rich species and generates a highly selective Ni–S environment for CO_2 reduction.

Beyond catalytic selectivity, modulation of anolyte acidity addresses a critical limitation of zero-gap CO_2 electrolyzers carbonate salt accumulation. At pH 3, NiS_x@NMC_AL sustains continuous operation for 450 min, three times as long as that achieved under neutral conditions, while maintaining high CO selectivity. Moreover, the catalyst couples high-rate CO production with low cell voltages, delivering a full-cell energy efficiency of 43.7% at pH 3. These results identify moderate acidity as an effective operating window that balances carbonate management with catalyst stability.

In general, this work establishes surface-reconstructed Ni sulfides as robust, pH-tolerant catalytic phases for CO_2-to-CO electrolysis and highlights the interplay between catalyst surface chemistry and electrolyte management in determining electrolyzer performance. The ability to simultaneously suppress the competing HER, mitigate salt deposition and sustain high energy efficiency under acidic operation provides a compelling strategy for advancing durable and practically relevant zero-gap CO_2 electrolyzers.

Chapter 6. The oxygen reduction reaction (ORR)

The oxygen reduction reaction (ORR) is a crucial electrochemical process that plays a vital role in sustainable energy conversion and storage systems, such as fuel cells and metal-air batteries. To date, platinum (Pt)-based materials have been widely recognized as the most efficient electrocatalysts for ORR due to their high catalytic activity (281). However, the widespread commercialization of these technologies is hindered by the high cost and limited reserves of Pt (282,283). Therefore, the development of cost-effective and high-performance non-precious metal catalysts (NPMCs) for ORR is of paramount importance (284–286).

Among the various NPMCs explored, iron Fe-based nitrogen-doped carbon materials, have attracted increasing attention as promising alternatives to Pt-based catalysts for ORR (287,288). Studies show that the ORR activity of these catalysts is governed by iron content (288,289), the type of ion species, the density of nitrogen functionalities (290), and microporous surface area (291). Despite decades of research, the precise nature of the active sites remains debated. Three main hypotheses prevail: nitrogen functionalities directly catalyze ORR (292), nitrogen groups coordinate Fe ions (Fe-N_x) where ORR occurs (293) and synergy between different Fe species such as Fe carbide (Fe_3C), Fe metal, and single-atom Fe-N_x (287,288,294,295). It is well-established that nitrogen doping in carbon matrices can significantly enhance the electrocatalytic activity for ORR (296,297). The incorporation of nitrogen atoms into the carbon framework can modify its electronic properties and create active sites, such as nitrogen-containing functional groups (N_x-C), which are believed to be crucial for ORR catalysis. The formation of Fe-Nx active sites, where iron is coordinated with nitrogen atoms in the carbon matrix, is widely considered to be a major contributor to the enhanced ORR performance of Fe-N-C catalysts (298–300). In particular, the last hypothesis has become the focus of study and has provided valuable insights for further improvement of Fe-based ORR catalysts. Yu et al. reported Fe/Fe_3C nanoparticles encapsulated in nitrogen-doped carbon, showing outstanding ORR activity with onset potential of 0.98 V_{RHE} and halfwave potential of 0.87 V_{RHE} in alkaline electrolyte due to the synergistic effects of Fe/Fe_3C and Fe-N_x (288). Wan et al. also considered that Fe/Fe_3C nanocrystals boost the activity of Fe-N_x, and the coexistence of high content of Fe-N_x and sufficient metallic iron nanoparticles is essential for the high ORR activity (301) These findings are further supported by numerous studies demonstrating that exposed Fe_3C nanodots markedly enhance the ORR activity of Fe-N_x-based catalysts (302,303).

In addition to the nature of the active sites, the porosity also plays a critical role in the performance of ORR electrocatalysts, due to their important role in the mass diffusion and active site distribution. Mesoporous structures, characterized by pore sizes between 2 and 50 nm, are particularly desirable as they provide a high surface area, facilitating the dispersion of active sites and improving the mass transport of reactants and products during the ORR process (304,305). To achieve controlled porous architectures, template methods are frequently employed in the synthesis of nanomaterials. These methods allow for the creation of well-defined pore structures, maximizing the accessibility of active sites and ultimately enhancing catalytic performance (306,307).

In this thesis, we present a novel approach for the synthesis of Fe embedded in a mesoporous, nitrogen-rich carbon matrix using a nanocasting approach. This methodology involves impregnation of the SBA-15 hard template with D-glucosamine and urea, serving as carbon and nitrogen precursors, together with an iron precursor, followed by a series of thermal treatments

to form the target catalysts. The resulting materials are thoroughly characterized to elucidate their structural, textural, and chemical properties. Their electrocatalytic performance for the oxygen reduction reaction (ORR) is then systematically investigated. This study focuses particularly on understanding how the interplay between Fe-derived species and nitrogen functionalities influences ORR activity in a mesoporous carbon architecture.

6.1. Materials and Synthesis Methods

Poly(ethylene glycol)-block-poly(propylene glycol)-block-poly(ethylene glycol) (EO20PO70EO20, P123, Sigma-Aldrich MW∼5800), hydrochloric acid (HCl, VWR, 37%), tetraethyl orthosilicate (TEOS, Sigma-Aldrich 98%), D-glucosamine hydrochloride ($C_6H_{13}NO_5$·HCl, Alfa Aesar, >98%), urea ($CO[NH_2]_2$, Merck, 99%), sulfuric acid (H_2SO_4, VWR, 95%), sulfuric acid (H2SO4, VWR, 95%), Nickel(II) nitrate hexahydrate ($Ni(NO_3)_2.6H_2O$, Sigma-Aldrich, 99.999% trace metals basis), ethanol solution (C_2H_6O, EtOH, Brenntag, 96%).

SBA-15 was synthesized via a modified sol-gel method, adapting the procedure described by Choi et al.(245). Briefly, 6.92 g of P123 was dissolved in a solution of 125.6 g distilled water and 3.78 g HCl (37%). 14.88 g of TEOS was rapidly introduced under vigorous stirring at 35 °C. The resulting mixture was aged at 35 °C for 24 h, followed by static hydrothermal leaching at 100 °C for 24 h. The solid product was recovered by filtration and dried at 100 °C without washing. Notably, filtration was significantly expedited compared to conventional SBA-15 syntheses. Template removal was achieved by a solvent extraction process. The as-synthesized material was refluxed in a solution of 250 mL ethanol and 3.67 mL HCl (37%) within a round-bottom flask equipped with a condenser to prevent evaporation. The extraction was conducted under magnetic stirring at 80 °C for 6 h, followed by filtration, drying at 100 °C, and calcination at 550 °C in air for 6 h.

Nitrogen-doped mesoporous carbon (NMC) and Fe-containing NMC were synthesized using SBA-15 as a hard template following a modified procedure reported by Maruccia et al (246). For the synthesis of Fe_3C supported on NMC (Fe_3C@NMC), SBA-15 was impregnated in two successive steps with aqueous solutions containing D-glucosamine, urea, iron(III) nitrate nonahydrate, and H_2SO_4. In the first impregnation, 0.3962 g D-glucosamine, 1.14 g urea, and 0.2664 g iron(III) nitrate nonahydrate were dissolved in 3 mL deionized water containing 0.0485 mL H_2SO_4 and added dropwise to 500 mg SBA-15 under stirring. After 1 h stirring, the material was heated from room temperature to 100 °C for 6 h, from 100 to 140 °C for 2 h, and from 140 to 160 °C for 6 h at a heating rate of 3 °C min^{-1}. In the second impregnation, 0.243 g D-glucosamine, 0.0756 g urea, and 0.164 g iron(III) nitrate nonahydrate were dissolved in 1.84 mL deionized water containing 0.03 mL H_2SO_4 and introduced into the intermediate product. After stirring for 1 h, the sample was heated from room temperature to 100 °C for 6 h and from 100 to 140 °C for 2 h. The resulting solid was ground and pyrolyzed under inert atmosphere to 900 °C at 3 °C min^{-1}. The silica template was removed using 6 M NaOH, and the product was washed to neutral pH and dried at 70–80 °C overnight.

The acid-leached sample, denoted Fe_3C@NMC_AL was obtained by treating the corresponding pyrolyzed and template-removed materials with 37% HCl for 3 h at room temperature. The acid-treated products were then washed repeatedly with deionized water until neutral pH and dried at 70–80 °C overnight. For comparison, the pristine NMC support was synthesized by the same hard-template route in the absence of the nickel precursor.

6.2. Results and discussion

6.2.1. Physicochemical properties

The X-ray diffraction patterns of NMC, Fe_3C@NMC and Fe_3C@NMC_AL were recorded to assess pore organization and sample crystallinity, and the results are compared in (Figure 6-1). (Figure 5-3) shows that SBA-15 exhibits a prominent (100) diffraction peak at $2\theta = 1.0°$ and weaker (110) and (200) reflections near $2\theta \approx 2.0°$, confirming its highly ordered 2D hexagonal mesoporous structure (308–310). Despite the well-ordered structure of the SBA-15 template, the resulting NMC and Fe_3C@NMC materials did not exhibit any detectable pore ordering in the low-angle XRD patterns (Figure 6-1a). The high-angle XRD pattern of Fe_3C@NMC and Fe_3C@NMC_AL in (Figure 6-1b) displays a series of well-defined diffraction peaks at $2\theta \approx$ 37.71°, 39.85°, 40.66°, 42.93°, 43.75°, 44.62°, 45.90°, 48.62°, and 49.16°, which match the characteristic reflections of cementite (Fe_3C) reported in the JCPDS database (No. 04-014-3145). Converting those 2θ positions (Cu Kα, $\lambda = 0.15406$ nm) to d-spacings gives approximate interplanar distances of 0.238, 0.226, 0.222, 0.211, 0.207, 0.203, 0.198, 0.187, and 0.185 nm, respectively, values fully consistent with cementite crystallography and confirming that the dominant crystalline iron phase in the as-prepared composite is Fe_3C. The preferential formation of Fe_3C during the template-based synthesis can be ascribed to the combined thermodynamic and kinetic environment created by the NMC host: (i) elevated local carbon activity within the matrix (carbon availability from the template-derived), (ii) the temperature profile used during metal incorporation and annealing, and (iii) the nanoscale confinement imposed by the mesoporous network, all of which favor carbide nucleation and growth over exclusive metallic Fe formation under the applied conditions (311). NMC shows a weak and broad peak in high-angle signature, consistent with a more amorphous, less stacked carbon/nitride framework. An amorphous host NMC provides different local carbon reservoirs and defect sites that can either facilitate or hinder carbide formation depending on the exact thermal history. Following acid treatment, the XRD pattern of the iron carbide phase remains remarkably consistent, indicating a high degree of stability of the Fe_3C structure under these conditions. This resistance to acid attack is likely due to the inherent low reactivity of cementite with HCl and potentially the protective effect of the surrounding NMC matrix, which might hinder the direct access of the acid to the Fe_3C nanoparticles. Notably, a sharpening of the

diffraction peak observed around 25° (2θ) after treatment suggests changes within the carbonaceous component of the primarily affecting the non-iron carbide components.

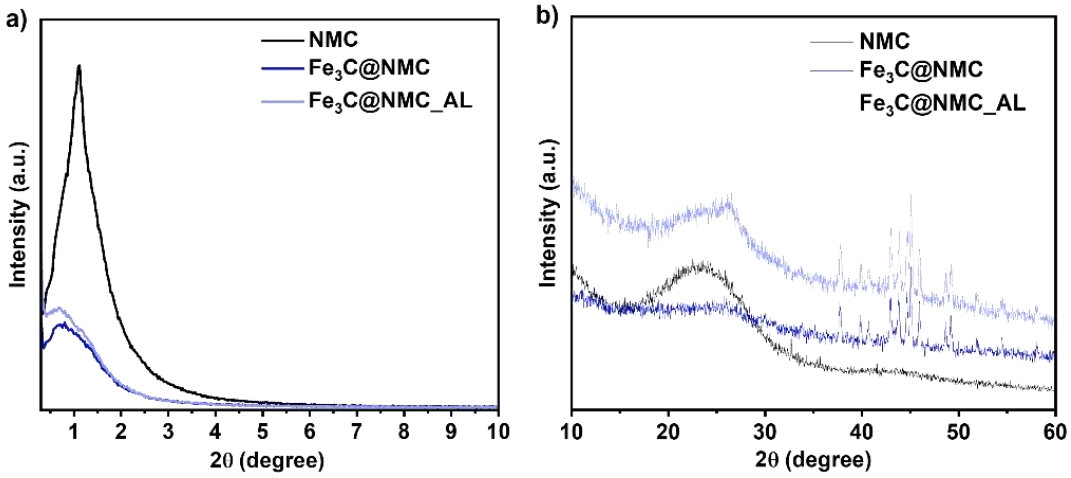


Figure 6-1. a) Low-angle and b) High-angle XRD of NMC, Fe_3C@NMC and Fe_3C@NMC_AL

The structural properties of Fe_3C@NMC, Fe_3C@NMC_AL and NMC were analyzed by Raman spectroscopy (Figure 6-2). Key features include the D band (~1350 cm^{-1}), indicating disordered carbon or defects, the G band (~1580 cm^{-1}), reflecting ordered graphitic (sp^2) carbon, and the 2D band (~2700 cm^{-1}), a second-order peak related to D, which assesses carbon layer stacking (312). All samples exhibit prominent D and G bands, with the D band slightly more intense, suggesting a significant degree of disorder in the carbon structure (313). The I_D/I_G ratio, a measure of defect density, appears similar across samples, indicating that Iron and acid treatments do not drastically alter the carbon framework's disorder (314). Additionally, a broad 2D band is observed, lacking sharpness, which suggests the carbon is not highly ordered, such as in multilayer graphene, with comparable intensity and shape across samples implying similar stacking characteristics (315). Comparing the samples, Fe_3C@NMC_AL shows a slight reduction in overall intensity compared to Fe_3C@NMC, possibly due to carbon or impurity removal during acid treatment (316), though the D/G ratio and peak positions remain largely unchanged, indicating a stable core carbon structure. The NMC sample displays a similar spectrum to the Fe-containing samples, suggesting that the carbon framework dominates the Raman signal, with Fe contributions being minimal or overlapping with carbon peaks. Overall, the spectra reveal a disordered carbon structure across all samples, consistent with mesoporous, N-rich carbon, where Fe presence is not distinctly visible due to weak or overlapping signals. Acid treatments have a limited impact, primarily affecting intensity rather than the fundamental carbon structure, as no significant peak shifts or new peaks are observed.

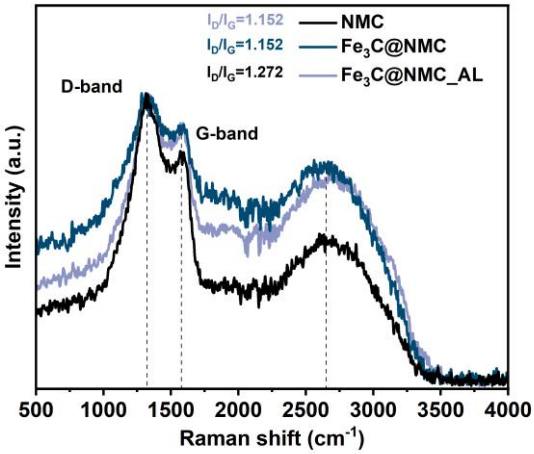


Figure 6-2. Raman spectroscopy of NMC, Fe_3C@NMC and Fe_3C@NMC_AL

The N_2 adsorption-desorption analysis confirms the mesoporous nature of all samples, with type IV isotherms and H2-type hysteresis loops (Figure 6-3a), characteristic of interconnected mesoporous networks (175,317,318). The sharp uptake at low relative pressures ($p/p^o < 0.1$) indicates the coexistence of microporosity, which is commonly introduced during carbonization and nitrogen doping due to defect formation and heteroatom incorporation from nitrogen-rich precursors such as urea and D-glucosamine (319,320). The preservation of the hysteresis loop after Fe loading and acid treatment suggests that the long-range mesostructural order of NMC is largely retained throughout impregnation and post-treatment processes (317,321). Compared with pristine NMC, Fe_3C@NMC shows a pronounced decrease in nitrogen uptake over the entire pressure range, indicating a reduction in BET surface area and pore volume. This behavior is attributed to partial pore blockage and pore filling by Fe species, as well as the occupation of micropores and pore entrances by Fe-Nx or Fe-Ox domains formed during impregnation and pyrolysis (322). Such pore blocking effects following metal impregnation have been widely reported for mesoporous carbons and are particularly significant for NMC due to its narrow and uniform pore channels (323). After acid treatment, Fe_3C@NMC_AL exhibits a substantial recovery of adsorption capacity, especially in the mesoporous pressure region, indicating reopening of blocked pores and improved pore accessibility. The corresponding pore size distributions (Figure 6-3b) show a dominant mesopore peak centered at ~3-4 nm for all samples, consistent with SBA-15-derived NMC materials (318,324). The restored pore volume and narrower distribution after acid treatment confirm the effective removal unstable or bulk Fe clusters and the leaching of any residual silica template that may have remained trapped. Additionally, nitrogen functionalities originating from urea and D-glucosamine are known to stabilize atomically dispersed or

coordinated Fe species, enabling selective removal of excess metal while preserving catalytically active Fe-N sites and hierarchical porosity (325–328).

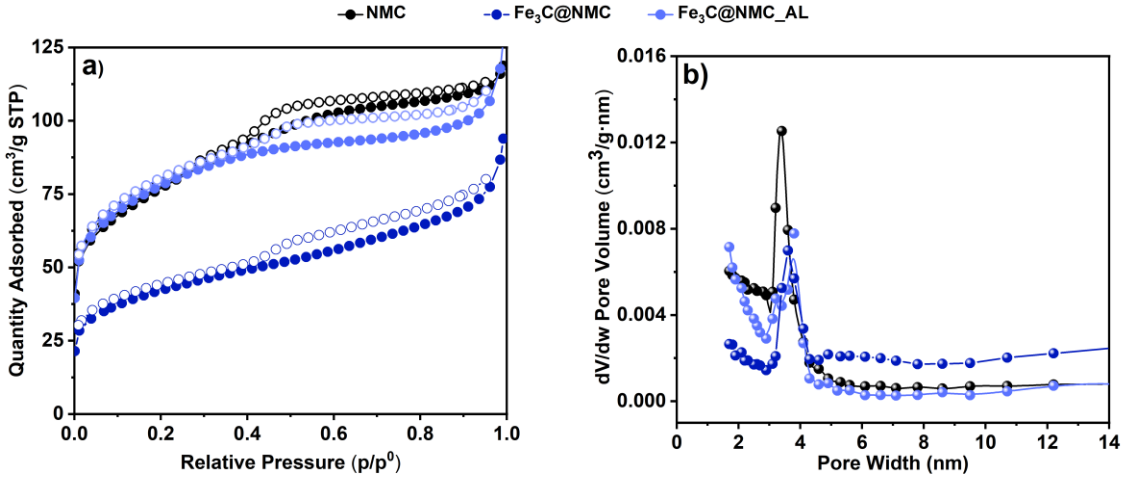


Figure 6-3. (a) N_2 adsorption–desorption isotherms measured at −196 °C, (b) pore size distribution of NMC, Fe_3C@NMC and Fe_3C@NMC_AL

Sample	BET Surface Area (m^2/g)	BJH Adsorption average pore width nm
NMC	263	3.4
Fe_3C@NMC	152	5.8
Fe_3C@NMC_AL	261	4.4

Thermogravimetric analysis (TGA) was employed to investigate the thermal decomposition behavior of NMC, Fe_3C@NMC, and Fe_3C@NMC_AL in air at a heating rate of 5 °C min^{-1}. The TGA results at 800°C showed residual masses of 16%, 46%, and 23% for NMC, Fe_3C@NMC, and Fe_3C@NMC-AT, respectively. Initial weight losses below 150°C, attributed to the desorption of physically adsorbed water and volatile species. The primary weight loss occurs between 350°C and 600°C, representing the combustion of the mesoporous carbon framework. Notably, the NMC support displays the highest thermal stability, with decomposition concluding near 600°C. In contrast, the iron-loaded samples (Fe_3C@NMC and Fe_3C@NMC_AL) exhibit a shift in the main decomposition temperature to lower values (400-600°C). This indicates that the embedded iron species act as a catalyst for carbon oxidation, accelerating the combustion of the framework. The residual mass at 800°C provides a direct window into the effectiveness of the purification and leaching processes. While the parent NMC leaves a residual mass of 16% (likely arising from trace silica or template ash), the significantly higher residue of 46% in Fe_3C@NMC confirms the successful incorporation of a high density of iron species within the mesoporous channels. The reduction of this residue

from 46% to 23% following acid treatment represents a selective refining process rather than a non-specific loss of material. This treatment effectively leaches away acid-labile bulk iron species and surface-bound carbides that obstruct mesopore accessibility, thereby exposing the stable, nitrogen-coordinated iron centers anchored within the carbon framework (329,330).

Samples	%C	%H	%N	%S
NMC	68	1	8	0.737
Fe_3C@NMC	43	1.3	7	2.51
Fe_3C@NMC -AL	53	1.5	8	1.11

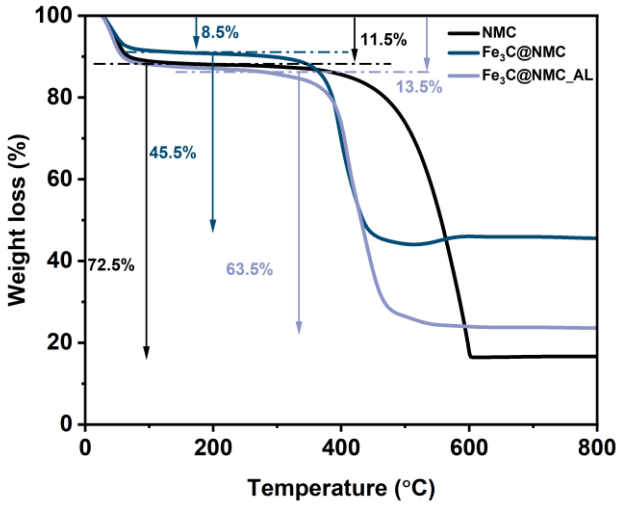


Figure 6-4. Thermogravimetric analysis of NMC, Fe_3C@NMC and Fe_3C@NMC_AL.

The selective removal of the iron phase is further validated by Total Reflection X-ray Fluorescence (TXRF).

The iron content of the and Fe_3C@NMC and Fe_3C@NMC_AL were quantitatively assessed using TXRF spectroscopy. To enable accurate comparison, both samples were digested in aqua regia under reflux for 4 hours, diluted to 40 mL with ultrapure water, and filtered prior to TXRF analysis. The measured Fe concentrations were 7.727 mg/L for the untreated sample and 4.028 mg/L for the acid-treated counterpart. These values were normalized to the original sample masses (2.8 mg and 2.4 mg, respectively) to calculate the iron content as a percentage by weight (wt%). The quantification results are summarized in Table 6-1:

Table 6-1. Quantification of Fe content in Fe_3C@NMC and after acid treatment (aqua regia digestion: 10 mL aqua regia under reflux, then diluted with 40 mL ultrapure water to 50 mL total)

Samples	Fe_3C@NMC	Fe_3C@NMC_AL

Sample mass (mg)	2.8	2.4
TXRF Fe concentration (mg/L)	7.727	4.028
Digest volume (mL)	50	50
Total Fe in solution (mg)	0.155	0.201
Fe content (wt%)	13.80	8.39

The results shown in Table 6-1 indicate that the Fe content in Fe_3C@NMC decreases from 13.80 wt% before acid treatment to 8.39 wt% after aqua regia digestion, corresponding to a ~39.2% loss of iron. The detection limit for Fe (0.011 mg/L) is well below the measured concentrations, confirming quantitative accuracy. This trend is mirrored in the TGA data, where the residual mass dropped from 46% to 23%, confirming the effective removal of acid-labile iron species. These leached components likely represent surface-exposed iron carbides (Fe_3C) or bulk oxide phases that are poorly integrated into the carbon framework. Despite the aggressive aqua regia digestion used for TXRF preparation, the retention of 8.39 wt% of iron highlights the exceptional stability of the remaining metal centers, which are presumably protected by the N-doped carbon matrix or stabilized via Fe-N_x coordination.
The discrepancy between the TXRF weight percentage and the TGA residue is attributed to the presence of residual silica template (16% residue in the parent NMC) and the oxidation of iron into heavier Fe_2O_3 phases during thermal decomposition in air.

X-ray photoelectron spectroscopy (XPS) was employed to investigate the surface chemical composition, elemental distribution, and bonding configurations of NMC, Fe_3C@NMC, and Fe_3C@NMC_AL. Owing to its intrinsic surface sensitivity (sampling depth < 5 nm, and < 2 nm for Fe 2p) (331,332). XPS provides complementary information to bulk-sensitive techniques such as XRD, TGA, and TXRF, enabling differentiation between surface-exposed species and bulk-embedded phases. Two independent XPS instruments were used for the measurements, Kratos Axis UltraDLD for Fe3C@NMC, and Kratos AXIS Supra for Fe_3C@NMC_AT. Although both instruments employ a monochromatic Al Kα source (hν = 1486.6 eV), minor variations in spectral features may arise from instrumental differences; however, all spectra were calibrated and interpreted to ensure that the observed trends reflect genuine chemical changes rather than instrumental artifacts. These effects are carefully considered below to ensure that the observed chemical trends reflect true material changes rather than instrumental artifacts. All spectra were analyzed using CasaXPS, with binding energies referenced to the C 1s peak at 284.5 eV (C-C/C-H). Background subtraction and peak fitting procedures were selected based on established best practices for each core level and applied consistently within each dataset.
The wide-scan (survey) spectra in Figure 6-5**,** confirm the presence of C, N, O, and Fe in Fe_3C@NMC prior to acid treatment, while after acid treatment the Fe signal is strongly attenuated at the surface. The lower Fe content derived from XPS compared to TXRF arises

from the shallow sampling depth of XPS (≈1-5 nm), which probes only the outermost surface layers rather than the bulk composition. XPS probes only the outermost atomic layers, whereas TXRF quantifies the total elemental content after complete digestion. Minor Si contributions originate from residual silica associated with the CMK-3 template, consistent with previous reports on hard-templated mesoporous carbons (333). The atomic concentrations derived from the survey spectra are summarized in Table 6-2.

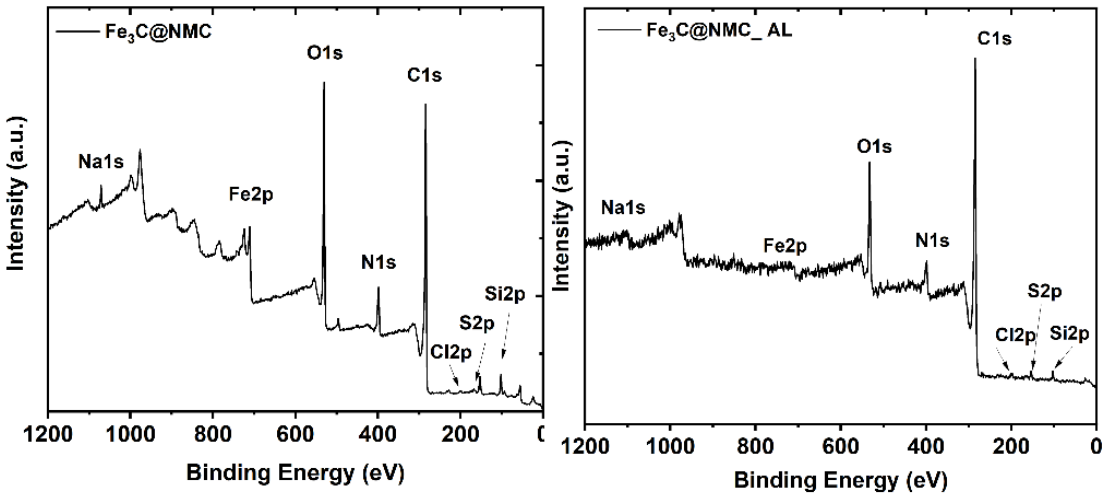


Figure 6-5. Wide-scan XPS survey of Fe_3C@NMCN and b) Fe_3C@NMC-AL.

Table 6-2. Surface atomic composition in wt. % from XPS survey spectra.

Element wt%	C	O	Fe	N	Si
Fe_3C@NMC	58.4	20.2	4.7	7.40	7.2
Fe_3C@NMC_AL	74.7	13	1.3	5.9	5.2

High-resolution C 1s spectra were recorded to elucidate the chemical environment of surface carbon before and after acid treatment. The deconvoluted components and their assignments are summarized in Table 6-3. In Fe_3C@NMC, the C 1s spectrum is dominated by a sharp peak centered at ~284.5 eV, corresponding to graphitic C-C/C=C and C-H bonds, characteristic of sp^2-hybridized carbon in extended aromatic frameworks (334,335). Additional components at ~285.7 eV and ~286.9 eV are assigned to C-N and C-O species, respectively, confirming successful nitrogen incorporation into the carbon lattice. A weak π-π* shake-up satellite at ~290.9 eV further indicates the presence of conjugated aromatic domains (336). Following acid treatment (Figure 6-7a), the C 1s envelope becomes broader and more complex, indicating significant surface oxidation. In addition to graphitic carbon at 284.4 eV, new components corresponding to aliphatic carbon (285.1 eV), secondary carbon (286.0 eV), C-O/C-N

functionalities (287.1 eV), carbonyl groups (C=O, 288.3 eV), and carboxyl groups (COOH, 289.5 eV) are observed. Weak shoulders at 291.2 eV and 293.0 eV are attributed to π-π* transitions and highly oxidized carbon species (335,337,338). The increased abundance of oxygen-containing groups after acid treatment contributes to enhanced surface polarity and may further attenuate photoelectrons have emitted from subsurface iron species.

Table 6-3. C 1s peak assignments before and after acid treatment.

Binding energy (eV)	Assignment	Fe_3C@NMC	Fe_3C@NMC_AL
284.4-284.5	C-C / C=C (graphitic)	✓	✓
285.1-285.7	Aliphatic C / C-N	✓	✓
286.0-286.9	Secondary C / C-O	✓	✓
287.1	C-O / C-N	-	✓
288.3	C=O	-	✓
289.5	COOH	-	✓
290.9-293.0	π-π* shake-up	✓	✓

The N 1s spectra provides insight into nitrogen bonding configurations and metal-nitrogen interactions. Prior to acid treatment (Figure 6-6a), the N 1s region can be deconvoluted into pyridinic N and Fe-N coordination (~398.3 eV), pyrrolic N (~399.5 eV), graphitic N (~400.6 eV), quaternary N (~402.5 eV), and oxidized N species (~405.3 eV). Pyridinic nitrogen species are widely recognized as preferential anchoring sites for transition metals into N-doped carbon frameworks and are closely associated with the formation of Fe-N_x coordination environments. After acid treatment (Figure 6-7b) (, pyridinic nitrogen remains at ~398.2 eV, while a distinct metal-nitrogen coordination feature is observed at ~399.5 eV. Pyrrolic and graphitic nitrogen components appear at ~400.6 eV and ~401.8 eV, respectively. The emergence of NOx species at ~403.8 and ~405.7 eV indicates partial oxidation of surface nitrogen functionalities during acid treatment. Importantly, the persistence of pyridinic nitrogen and metal-nitrogen coordination signals is consistent with the presence of acid-resistant Fe-N_x moieties embedded within the carbon matrix (339–342).

The highest binding energy component at ~533.2 eV is primarily assigned to C-O-type surface functionalities (alcohols and ethers), with a possible contribution from sulfate-related oxygen species (SO_4^-), consistent with the presence of sulfur in the survey spectrum and the use of sulfuric acid during synthesis (335). Given the shallow sampling depth of XPS, this

observation reflects surface depletion or encapsulation of iron species rather than complete loss of iron from the material, in agreement with TXRF and XRD analyses.

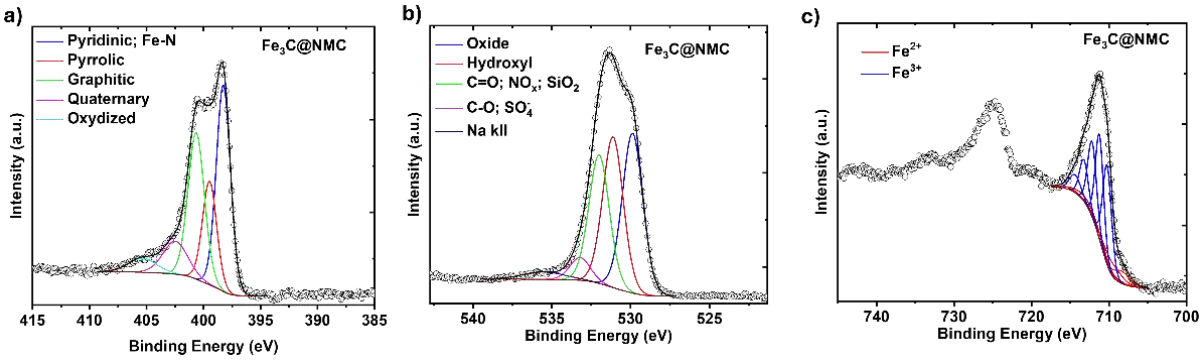


Figure 6-6. High-resolution XPS spectra of the a) N 1s, b) O 1s, and c) Fe 2p of Fe_3C@NMC.

The Fe 2p core-level spectrum of Fe_3C@NMC before acid treatment reveals detailed information on iron oxidation states and coordination environments (Figure 6-6c). The $Fe2p_{3/2}$ peak can be deconvoluted into two regions exhibiting a characteristic multiplet structure; the first region at lower binding energy is composed by the peaks at 708.4 eV, 709.7 eV, 710.8 eV, 712.1 eV and 715.4 eV. These binding energies positions correspond to Fe^{2+} iron oxide phase. The second region is composed by the peaks at binding energies of 710.2 eV, 711.2 eV, 712.2 eV, 713.3 eV and 714.4 eV typical of Fe^{3+} iron oxide in the form of FeOOH . The satellite peak at 719.5 eV is consistent with the Fe^{3+} iron hydroxide (343–345). Quantitative fitting indicates that Fe^{3+} accounts for approximately 77.5% of the surface iron, with Fe^{2+} contributing ~22.5%. This distribution demonstrates that prior to acid treatment, a significant fraction of iron exists as surface-exposed oxide or oxyhydroxide species rather than exclusively as Fe-Nx coordinated centers. Such surface-accessible iron phases have been widely reported to catalyze carbon oxidation and obstruct pore accessibility, in agreement with the trends observed in TGA and nitrogen sorption analyses (341,346–348). After acid treatment, the Fe 2p signal falls below the reliable detection limit of XPS, indicating the effective removal of surface-exposed iron oxides and carbides. Consequently, detailed Fe 2p fitting after AT was not meaningful. Instead, the evolution of nitrogen chemical states was used as the primary indicator of stabilized metal-nitrogen coordination. The O1s spectrum of Fe_3C@NMC (Figure 6-6c) consists of four main components. The lower binding energy peak at 529.9 eV is due to the lattice iron oxide. The second one at 531.1 eV corresponds to Hydroxyl group of iron hydroxide and defective oxide (349), the third at 532.0 eV to carbonyl group in O=C, oxidized

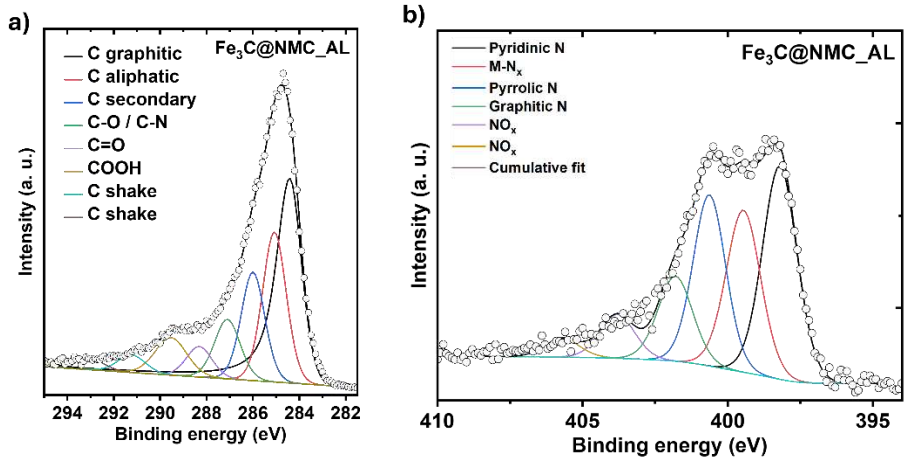


Figure 6-7. High-resolution XPS spectra of the C 1s and N 1s regions for the Fe_3C@NMC_AL.

6.3. RRDE Analysis of ORR Performance

The electrocatalysts' performance in terms of ORR activity, selectivity, and stability was evaluated in a RRDE setup in both alkaline (0.1 M KOH) and acidic media (0.1 M $HClO_4$). Figure 6-9 displays the CVs recorded in both N_2- and O_2-saturated electrolytes, to evaluate the occurrence of cathodic currents associated with oxygen reduction. In the O_2-saturated electrolyte, a pronounced reduction current is observed, indicative of electrochemical oxygen reduction activity. Specifically, in alkaline media, the reduction peaks appear within the potential window of 0.7-1.0 V_{RHE}, while in acidic media, they are observed in the range of 0.4-0.8 V_{RHE}, in agreement with previous studies on Fe-based materials (350,351). In contrast, the voltammograms recorded in the N_2-saturated electrolyte do not exhibit any significant cathodic features in the same potential window, due to the electrochemical inertness of nitrogen. This comparison confirms that the observed reduction current arises specifically from the presence of dissolved O_2 in the electrolyte. Notably, even from this preliminary assessment, it is evident that the metal-free sample (NMC) exhibits the lowest ORR activity, as highlighted by their more negative onset potentials compared to metal-containing counterparts, indicating that the oxygen reduction is less energetically favorable in this material. The ORR activity of the samples under study was better estimated by recording LSVs in the O_2-saturated electrolyte.

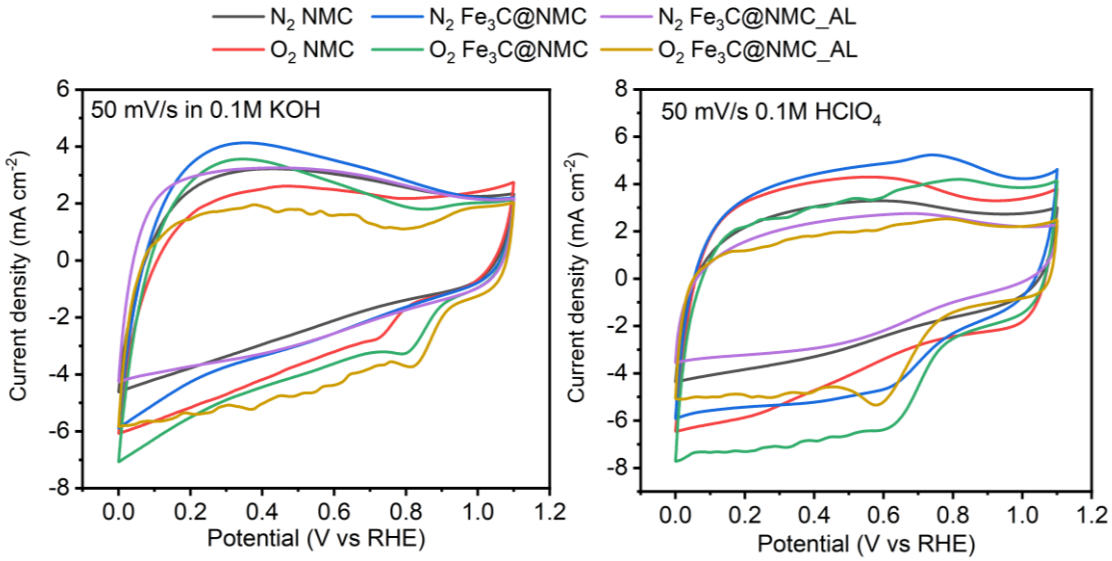


Figure 6-8. CVs recorded at 50 mV s^{-1} in N_2- and O_2-saturated electrolytes to evaluate cathodic currents associated with the ORR. Measurements were conducted in 0.1 M KOH and 0.1 M $HClO_4$ for NMC, Fe_3C@NMC and Fe_3C@NMC_AL.

LSVs acquired at 1600 rpm are reported in Figure 6-9 in both alkaline [Figure 6-9a] and acidic media [Figure 6-9b]. In both environments, the Fe-containing materials clearly outperform the metal-free mesoporous carbon, underlining the crucial role of Fe_3C active sites in driving the reaction. Among them, Fe_3C@NMC shows the most positive onset and half-wave potentials, reflecting superior intrinsic activity. The enhanced performance can be attributed to the synergistic interaction between the Fe_3C nanoparticles and the surrounding N-doped carbon shell, combined with the well-preserved mesoporosity revealed by the N_2-sorption analysis, which might provide a higher density of accessible active sites. The outstanding ORR performance of this sample can further be attributed to its highest pyridinic-N content (rel. at. % = 31.2), as revealed by the XPS analysis, since pyridinic-N is widely recognized as the most active nitrogen moiety (352). With a reduced amount of pyridinic-N (rel. at. % = 26.3), Fe_3C@NMC_AL exhibits reduced activity, which can be also ascribed to its less favorable textural framework. The metal-free carbons (NMC) display much lower onset and half-wave potentials despite their mesoporous structures, confirming that a well-developed textural framework alone is not sufficient to promote efficient ORR in the absence of Fe species. Interestingly, the performance gap between Fe-containing and metal-free samples becomes more pronounced in acidic electrolyte. In alkaline media, the ORR can proceed through different pathways and benefit from the contribution of nitrogen-doped carbon sites, which remain catalytically active (353,354). This is because under alkaline conditions, most nitrogen functionalities (such as pyridinic- and pyrrolic-N) are in their deprotonated form, allowing efficient electron donation to adjacent sites and facilitating oxygen reduction (355), possibly also through outer-sphere electron transfer mechanisms (356). In contrast, in acidic medium,

these nitrogen functionalities undergo protonation, becoming positively charged (357–359). This protonation not only diminishes their ability to delocalize charge but also favors anion adsorption (360), both of which hinder O_2 binding and reduce catalytic activity.

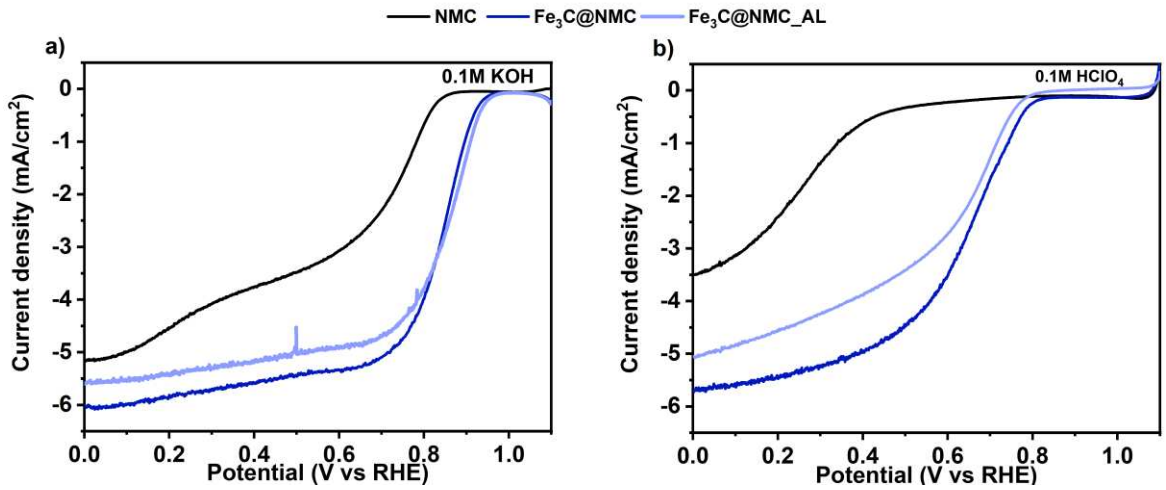


Figure 6-9. ORR electrocatalytic activity measured at 1600 rpm: (a) Disk current density in 0.1 M KOH, (b) Disk current density in 0.1 M $HClO_4$.

Table 6-4.Onset and half-wave potentials in both alkaline and acidic media.

Samples	Onset Potential (E_{on}, V)		Halfwave potential ($E_{1/2}$, V)	
	0.1M KOH	0.1M $HClO_4$	0.1M KOH	0.1M $HClO_4$
NMC	0.85	0.51	0.68	0.27
Fe_3C@NMC	0.95	0.82	0.85	0.62
Fe_3C@NMC_AL	0.96	0.80	0.84	0.64

As a result, the intrinsic contribution of N-doped carbon to the ORR is strongly suppressed in acidic conditions, and the reaction relies almost entirely on the presence of stable Fe_3C sites. In a similar manner, we can observe that the performance of the catalysts in alkaline medium outperforms that in acid, in trend with previous studies (361,362). Under alkaline conditions, the ORR mechanism at Fe_3C sites is generally more favorable: electron transfer is enabled by

the formation of O_2^- intermediates, which are stabilized in the presence of OH^- This stability allows efficient adsorption and stepwise reduction of oxygen at the Fe centers. In contrast, in acidic media, O_2^- is rapidly protonated and reduced, making it highly reactive and unstable, which hinders controlled electron transfer and reduces the overall catalytic activity (363). Consequently, Fe-based sites sustain faster ORR kinetics in alkaline electrolytes compared to acidic conditions. In conclusion, the onset (E_{on}) and half-wave ($E_{1/2}$) potentials extracted from the LSVs confirm the performance hierarchy of the samples, in agreement with previous studies reported in literature (

Table 6-6). The oxygen reduction pathway of the samples was probed by evaluating the electrocatalysts' selectivity toward the four-electron reaction using a rotating ring-disk electrode (RRDE). Hydrogen peroxide formed at the disk can diffuse to the ring, where it undergoes oxidation on the Pt surface through a two-electron pathway. Currents measured at disk [Figure 6-10] and ring are then used to calculate the number of electrons transferred (Eq. 6-1) and the amount of peroxide generated (Eq. 6-2), providing insight into the selectivity of the electrocatalysts

$$N = 4 \times \frac{I_D}{I_D + I_R/N} \qquad \text{Eq. 6-1}$$

$$HO_2^-\%\,(H_2O_2\,\%) = 200 \times \frac{I_R/N}{I_D + I_R/N} \qquad \text{Eq. 6-2}$$

I_D and I_R are the disk and ring current recorded at 1600 RPM, while N is the collection efficiency equal to 0.4.

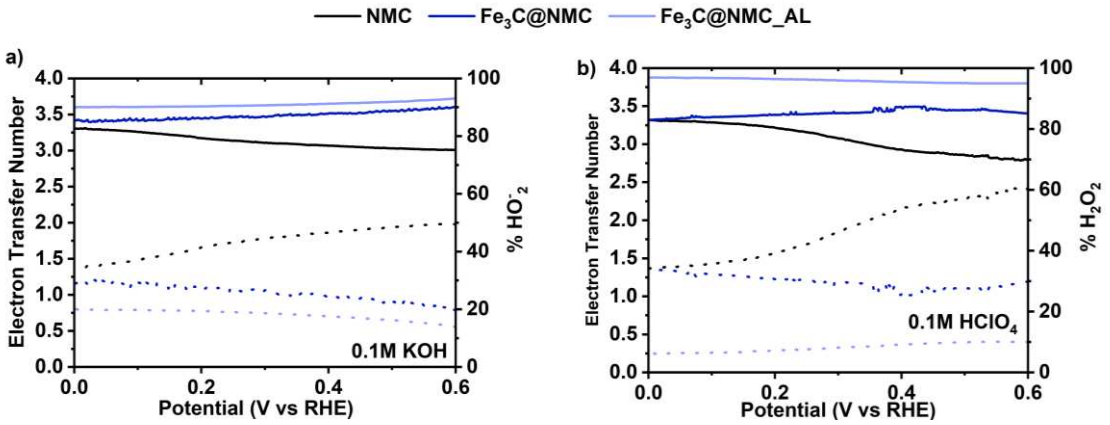


Figure 6-10. ORR selectivity expressed in terms of electron transfer number and peroxide yield, measured in the 4-electrodes configuration (RRDE setup) at 1600 rpm in (a) 0.1 M KOH and (b) 0.1 M $HClO_4$.

Table 6-5. Electron transfer numbers and peroxide yields (H_2O_2 %) at 0.5 V for various synthesized catalysts in 0.1 M KOH and 0.1 M $HClO_4$ media.

Samples	Electron Transfer Number @0.5 V		HO_2^-% or H_2O_2% @0.5 V	
	0.1M KOH	0.1M $HClO_4$	0.1M KOH	0.1M $HClO_4$
NMC	3	2.86	48.44	56.7
Fe_3C@NMC	3.5	3.45	22.66	28
Fe_3C@NMC_AL	3.7	3.79	16	10

The RRDE results confirm that the oxygen reduction on Fe-containing catalysts proceeds predominantly through the desirable four-electron pathway, with only minor production of hydrogen peroxide. In both media, Fe_3C@NMC-AT exhibits high disk currents and very low ring currents, translating into an electron transfer number close to 4 and low peroxide yields. By contrast, the metal-free carbons shows significantly higher ring currents, consistent with a two-electron dominated process leading to H_2O_2 formation. On the other hand, metal-free carbons exhibit electron transfer numbers well below 3 and peroxide yields exceeding 40%, further corroborating literature reports that highlight the crucial role of Fe incorporation not only in enhancing ORR activity, but also in steering the reaction toward the more efficient four-electron pathway (Table 6-5).

In alkaline conditions, the catalyst retains approximately 90% of its initial current density after 4 hours of operation, indicating excellent electrochemical stability. In contrast, a more pronounced degradation is observed under acidic conditions, with current density decreasing by over 50% in the same timeframe. This disparity highlights the greater resilience of Fe-based catalysts in alkaline environments, while the lower stability in acid is likely due to Fe demetallation. In acidic conditions, Fe_3C nanoparticles are thermodynamically unstable and can gradually corrode, releasing Fe^{2+}/Fe^{3+} ions into the electrolyte. These dissolved species may catalyze Fenton-type reactions with hydrogen peroxide, generating highly reactive hydroxyl radicals that accelerate carbon degradation and compromise catalyst durability (364). These results underscore the persistent challenge of implementing Fe-based electrocatalysts in proton exchange membrane fuel cells, where acidic conditions prevail. However, the high stability observed in alkaline media supports the promising potential of this material as a cathode catalyst for anion exchange membrane (AEM) fuel cells, where the operating environment is more compatible with the stability window of Fe-based materials.

Table 6-6. Brief literature review of Fe_3C-based electrocatalysts for ORR applications.

Electrocatalyst	*Electrolyte*	E_{on} (V_{RHE})	$E_{1/2}$ (V_{RHE})	*Transferred Electrons* (@ 0.5 V_{RHE})	*Ref.*
FeSA-Fe_3C/NC	0.1 M KOH	0.99	0.88	3.7	(365)
Fe−Fe_3C@C/CNT_Urea	0.1 M KOH	-	0.87	3.9	(366)
NFC@Fe/Fe_3C-9	0.1 M KOH	-	0.87	3.97	(367)
N-doped Fe/Fe_3C@C/RGO	0.1 M KOH	1	0.93	3.5	(368)
Fe_3O_4/Fe_3C@NC-1	0.1 M KOH	0.97	0.81	3.9	(369)
Fe_3C@NMC_AL	0.1 M KOH	0.98	0.87	3.6	This work

6.3.1. Conclusion

In this chapter, Fe_3C-containing nitrogen-doped mesoporous carbon catalysts were investigated for the oxygen reduction reaction in alkaline and acidic media. The incorporation of Fe_3C substantially enhanced ORR activity compared with metal-free NMC, with Fe_3C@NMC showing the most positive onset and half-wave potentials, demonstrating the

important role of Fe_3C sites and their interaction with the N-doped carbon framework. RRDE measurements further confirmed that Fe-containing catalysts preferentially promote the four-electron ORR pathway, with Fe_3C@NMC-AL reaching an electron-transfer number of 3.7 in alkaline and 3.79 in acidic media, together with substantially reduced peroxide formation compared with NMC. The catalysts also showed markedly better stability in alkaline conditions, retaining about 90% of the initial current after 4 h, whereas stronger degradation occurred in acidic media.

Chapter 7. Final remarks

7.1. Conclusions and addressed research questions

This doctoral dissertation has systematically investigated the rational design, green synthesis, and operational optimization of advanced porous electrocatalysts for key reactions in the sustainable energy transition. By integrating materials science with electrochemical engineering, the research established critical structure-performance relationships across four distinct catalytic systems:

1. Rational design and green synthesis strategies

A major contribution of this thesis is the development of solvent-free and environmentally benign synthesis routes. The implementation of the steam-assisted dry-gel approach for ZIFs and Cu-MOFs successfully eliminated toxic organic solvents while providing precise control over crystal growth. This methodology revealed that water vapor volume is a decisive parameter in modulating particle size distribution and morphological homogeneity, which are essential for creating an effective three-phase interface in gas-diffusion electrodes. The transition from 3D microporous ZIFs to hierarchical 2D Cu-MOF flakes further demonstrated how anisotropic growth enhances active-site exposure and mass transport.

2. Mechanistic insights into selectivity and coordination

This thesis provided fundamental insights into how the local coordination environment and metal centre identity steer reaction pathways. A direct comparison between isostructural ZIFs showed that while Zn-based ZIF-8 selectively produces CO, the Co-based ZIF-67 predominantly favours the hydrogen evolution reaction, proving that intrinsic electronic properties of the metal centre outweigh surface area or CO_2 adsorption capacity alone. The study of nitrogen-coordinated Cu-MOFs demonstrated that catalyst loading and layer thickness are critical for multi-carbon production. Thicker catalyst layers were found to enhance *CO surface coverage and residence time, facilitating the coupling steps required to achieve a maximum ethylene Faradaic efficiency of 51.6% in zero-gap assemblies Through operando soft-XAS, this study confirmed the reversible reduction of Cu^{2+} to metallic Cu during active CO_2RR, providing a real-time link between the catalyst's dynamic electronic state and its product selectivity.

3. Operational robustness and system engineering

To bridge the gap between lab-scale discovery and industrial viability, this thesis addressed the critical challenge of long-term operational stability. The investigation into Ni_3S_2 anchored on nitrogen-doped mesoporous carbon (showed that sulfur coordination modifies the electronic structure to suppress HER and favour CO_2-to-CO conversion with efficiencies above 90%. Mitigating. A significant finding was that controlling the anolyte pH is essential for preventing salt precipitation in zero-gap MEAs. By operating at a moderate acidity (pH ≈ 3), the NiS_x@NMC catalyst achieved an exceptional stability of 450 minutes, effectively managing the trade-off between proton availability and carbonate-related degradation. The shift from liquid-phase flow cells to zero-gap MEA architectures was shown to significantly alter the

local microenvironment, generally enhancing C_2 selectivity but requiring more sophisticated water and salt management strategies.
The studies on Fe-doped nitrogen-rich mesoporous carbons for the oxygen reduction reaction underlined the efficiency of Fe_3C active sites in driving the four-electron pathway.
In conclusion, this thesis offers materials-by-design framework for scalable CO_2 utilization. Collectively, these findings contribute to the development of a circular carbon economy, transforming CO_2 from an environmental threat into a valuable chemical resource.

7.2. Future Works

Although in this work fundamental goals have been achieved, there are several aspects that can still be improved and further developed to advance the understanding and performance of electrochemical CO_2 reduction systems.
A priority is the improvement of stability in Cu-based MOF systems. Future work should focus on structural modifications such as integration with conductive carbon supports, partial pyrolysis, or surface engineering to mitigate degradation under electrochemical conditions. Stabilizing the active Cu sites while preserving their ability to promote C–C coupling is essential for sustained C_{2+} product formation.
Secondly, the development of single-atom catalysts (SACs) based on the SBA-15 nanocasting approach represents a highly promising direction. This method can be adapted to produce atomically dispersed $M–N_x$ sites within nitrogen-rich mesoporous carbon. Such systems maximize atom efficiency, reduce material costs, and effectively suppress the competing hydrogen evolution reaction. Moreover, the well-defined nature of SACs enables clearer mechanistic insights and facilitates correlation with theoretical modelling (370,371).
Finally, efforts should focus on the scaling up of green and sustainable synthesis methods. Since the synthesis method developed for ZIFs and MOF-based materials is simple and environmentally friendly, it offers strong potential for scalability. The low-solvent and steam-assisted approach enables easier scale-up by reducing reactor volume requirements, energy consumption, and process complexity. Future work should focus on increasing batch size and optimizing process parameters while maintaining control over key properties such as morphology, porosity, and crystallinity.

Bibliography

1. Le Quéré C, Andrew RM, Friedlingstein P, Sitch S, Hauck J, Pongratz J, et al. Global Carbon Budget 2018. Earth Syst Sci Data. 2018 Dec 5;10(4):2141–94. doi:10.5194/essd-10-2141-2018
2. Friedlingstein P, O'Sullivan M, Jones MW, Andrew RM, Bakker DCE, Hauck J, et al. Global Carbon Budget 2023. Earth Syst Sci Data. 2023 Dec 5;15(12):5301–69. doi:10.5194/essd-15-5301-2023
3. Kondratenko E V., Mul G, Baltrusaitis J, Larrazábal GO, Pérez-Ramírez J. Status and perspectives of CO_2 conversion into fuels and chemicals by catalytic, photocatalytic and electrocatalytic processes. Energy Environ Sci. 2013;6(11):3112. doi:10.1039/c3ee41272e
4. Jhong HR "Molly," Ma S, Kenis PJ. Electrochemical conversion of CO_2 to useful chemicals: current status, remaining challenges, and future opportunities. Curr Opin Chem Eng. 2013 May;2(2):191–9. doi:10.1016/j.coche.2013.03.005
5. Dinh CT, Burdyny T, Kibria MG, Seifitokaldani A, Gabardo CM, García de Arquer FP, et al. CO_2 electroreduction to ethylene via hydroxide-mediated copper catalysis at an abrupt interface. Science (1979). 2018 May 18;360(6390):783–7. doi:10.1126/science.aas9100
6. Ross MB, De Luna P, Li Y, Dinh CT, Kim D, Yang P, et al. Designing materials for electrochemical carbon dioxide recycling. Nat Catal. 2019 Jul 1;2(8):648–58. doi:10.1038/s41929-019-0306-7
7. Hori Y, Wakebe H, Tsukamoto T, Koga O. Electrocatalytic process of CO selectivity in electrochemical reduction of CO_2 at metal electrodes in aqueous media. Electrochim Acta. 1994 Aug;39(11–12):1833–9. doi:10.1016/0013-4686(94)85172-7
8. Peterson AA, Nørskov JK. Activity Descriptors for CO_2 Electroreduction to Methane on Transition-Metal Catalysts. J Phys Chem Lett. 2012 Jan 19;3(2):251–8. doi:10.1021/jz201461p
9. Hori Y, Takahashi R, Yoshinami Y, Murata A. Electrochemical Reduction of CO at a Copper Electrode. J Phys Chem B. 1997 Sep 1;101(36):7075–81. doi:10.1021/jp970284i
10. Nitopi S, Bertheussen E, Scott SB, Liu X, Engstfeld AK, Horch S, et al. Progress and Perspectives of Electrochemical CO_2 Reduction on Copper in Aqueous Electrolyte. Chem Rev. 2019 Jun 26;119(12):7610–72. doi:10.1021/acs.chemrev.8b00705

11. Kibria MG, Edwards JP, Gabardo CM, Dinh C, Seifitokaldani A, Sinton D, et al. Electrochemical CO_2 Reduction into Chemical Feedstocks: From Mechanistic Electrocatalysis Models to System Design. Advanced Materials. 2019 Aug 16;31(31). doi:10.1002/adma.201807166

12. Kibria MG, Dinh C, Seifitokaldani A, De Luna P, Burdyny T, Quintero-Bermudez R, et al. A Surface Reconstruction Route to High Productivity and Selectivity in CO_2 Electroreduction toward C $_{2+}$ Hydrocarbons. Advanced Materials. 2018 Dec 9;30(49). doi:10.1002/adma.201804867

13. Creissen CE, Fontecave M. Keeping sight of copper in single-atom catalysts for electrochemical carbon dioxide reduction. Nat Commun. 2022 Apr 27;13(1):2280. doi:10.1038/s41467-022-30027-x

14. Fang W, Lu R, Li F, He C, Wu D, Yue K, et al. Low-coordination Nanocrystalline Copper-based Catalysts through Theory-guided Electrochemical Restructuring for Selective CO_2 Reduction to Ethylene. Angewandte Chemie. 2024 Apr 15;136(16). doi:10.1002/ange.202319936

15. López M, Exner KS, Viñes F, Illas F. Theoretical study of the mechanism of the hydrogen evolution reaction on the V2C MXene: Thermodynamic and kinetic aspects. J Catal. 2023 May;421:252–63. doi:10.1016/j.jcat.2023.03.027

16. Zhou L, Lv R. Rational catalyst design and interface engineering for electrochemical CO_2 reduction to high-valued alcohols. Journal of Energy Chemistry. 2022 Jul;70:310–31. doi:10.1016/j.jechem.2022.02.033

17. Choi W, Won DH, Hwang YJ. Catalyst design strategies for stable electrochemical CO_2 reduction reaction. J Mater Chem A Mater. 2020;8(31):15341–57. doi:10.1039/D0TA02633F

18. Voiry D, Chhowalla M, Gogotsi Y, Kotov NA, Li Y, Penner RM, et al. Best Practices for Reporting Electrocatalytic Performance of Nanomaterials. ACS Nano. 2018 Oct 23;12(10):9635–8. doi:10.1021/acsnano.8b07700

19. Nishikawa E, Islam S, Sleep S, Birss V, Bergerson J. Guiding research in electrochemical CO_2 conversion strategies through a systems-level perspective. Green Chemistry. 2023;25(1):229–44. doi:10.1039/D2GC01466A

20. Zhang X, Guo SX, Gandionco KA, Bond AM, Zhang J. Electrocatalytic carbon dioxide reduction: from fundamental principles to catalyst design. Mater Today Adv. 2020 Sep;7:100074. doi:10.1016/j.mtadv.2020.100074

21. Li Q, Jiang J, Jiang S, Liu D, Xu D, Chen Y, et al. Catalyst design for the electrochemical reduction of carbon dioxide: from copper nanoparticles to copper single atoms. Microstructures. 2025 Jan 17;5(1). doi:10.20517/microstructures.2024.69

22. Bard AJ. Elements of Molecular and Biomolecular Electrochemistry: An Electrochemical Approach to Electron Transfer Chemistry By Jean-Michel Savéant (Université de Paris 7, Denis Diderot). J. Wiley & Sons, Inc. Hoboken, NJ. 2006. xviii + 486 pp. $135. ISBN 0-471-44573-8. J Am Chem Soc. 2007 Jan 1;129(1):242–242. doi:10.1021/ja069754p

23. Hori Y. Electrochemical CO_2 Reduction on Metal Electrodes. In: Modern Aspects of Electrochemistry. New York, NY: Springer New York. p. 89–189. doi:10.1007/978-0-387-49489-0_3

24. Peterson AA, Nørskov JK. Activity Descriptors for CO_2 Electroreduction to Methane on Transition-Metal Catalysts. J Phys Chem Lett. 2012 Jan 19;3(2):251–8. doi:10.1021/jz201461p

25. Nitopi S, Bertheussen E, Scott SB, Liu X, Engstfeld AK, Horch S, et al. Progress and Perspectives of Electrochemical CO_2 Reduction on Copper in Aqueous Electrolyte. Chem Rev. 2019 Jun 26;119(12):7610–72. doi:10.1021/acs.chemrev.8b00705

26. Yan C, Li H, Ye Y, Wu H, Cai F, Si R, et al. Coordinatively unsaturated nickel–nitrogen sites towards selective and high-rate CO_2 electroreduction. Energy Environ Sci. 2018;11(5):1204–10. doi:10.1039/C8EE00133B

27. Garza AJ, Bell AT, Head-Gordon M. Mechanism of CO_2 Reduction at Copper Surfaces: Pathways to C_2 Products. ACS Catal. 2018 Feb 2;8(2):1490–9. doi:10.1021/acscatal.7b03477

28. Gauthier JA, Fields M, Bajdich M, Chen LD, Sandberg RB, Chan K, et al. Facile Electron Transfer to CO_2 during Adsorption at the Metal|Solution Interface. The Journal of Physical Chemistry C. 2019 Dec 5;123(48):29278–83. doi:10.1021/acs.jpcc.9b10205

29. Peterson AA, Abild-Pedersen F, Studt F, Rossmeisl J, Nørskov JK. How copper catalyzes the electroreduction of carbon dioxide into hydrocarbon fuels. Energy Environ Sci. 2010;3(9):1311. doi:10.1039/c0ee00071j

30. Hori Y. Electrochemical CO_2 Reduction on Metal Electrodes. In: Modern Aspects of Electrochemistry. New York, NY: Springer New York. p. 89–189. doi:10.1007/978-0-387-49489-0_3

31. Lim RJ, Xie M, Sk MA, Lee JM, Fisher A, Wang X, et al. A review on the electrochemical reduction of CO2 in fuel cells, metal electrodes and molecular catalysts. Catal Today. 2014 Sep;233:169–80. doi:10.1016/j.cattod.2013.11.037

32. Ramdin M, Morrison ART, de Groen M, van Haperen R, de Kler R, Irtem E, et al. High-Pressure Electrochemical Reduction of CO_2 to Formic Acid/Formate: Effect of pH on the Downstream Separation Process and Economics. Ind Eng Chem Res. 2019 Dec 26;58(51):22718–40. doi:10.1021/acs.iecr.9b03970

33. Montoya JH, Shi C, Chan K, Nørskov JK. Theoretical Insights into a CO Dimerization Mechanism in CO_2 Electroreduction. J Phys Chem Lett. 2015 Jun 4;6(11):2032–7. doi:10.1021/acs.jpclett.5b00722

34. Peterson AA, Abild-Pedersen F, Studt F, Rossmeisl J, Nørskov JK. How copper catalyzes the electroreduction of carbon dioxide into hydrocarbon fuels. Energy Environ Sci. 2010;3(9):1311. doi:10.1039/c0ee00071j

35. Ren D, Fong J, Yeo BS. The effects of currents and potentials on the selectivities of copper toward carbon dioxide electroreduction. Nat Commun. 2018 Mar 2;9(1):925. doi:10.1038/s41467-018-03286-w

36. Varhade S, Guruji A, Singh C, Cicero G, García-Melchor M, Helsen J, et al. Electrochemical CO_2 Reduction: Commercial Innovations and Prospects. ChemElectroChem. 2025 Jan 14;12(2). doi:10.1002/celc.202400512

37. Nitopi S, Bertheussen E, Scott SB, Liu X, Engstfeld AK, Horch S, et al. Progress and Perspectives of Electrochemical CO_2 Reduction on Copper in Aqueous Electrolyte. Chem Rev. 2019 Jun 26;119(12):7610–72. doi:10.1021/acs.chemrev.8b00705

38. Hori Y, Takahashi I, Koga O, Hoshi N. Electrochemical reduction of carbon dioxide at various series of copper single crystal electrodes. J Mol Catal A Chem. 2003 May;199(1–2):39–47. doi:10.1016/S1381-1169(03)00016-5

39. Bockris JO., Reddy AKN., Gamboa-Aldeco ME. Modern electrochemistry. Plenum Press; 1998. 2053 p.

40. Bard AJ., Faulkner LR. Electrochemical methods : fundamentals and applications. John Wiley & Sons, Inc.; 2001. 833 p.

41. Scholz F. Wilhelm Ostwald's role in the genesis and evolution of the Nernst equation. Journal of Solid State Electrochemistry. 2017 Jul 13;21(7):1847–59. doi:10.1007/s10008-017-3619-y

42. Ledezma-Yanez I, Wallace WDZ, Sebastián-Pascual P, Climent V, Feliu JM, Koper MTM. Interfacial water reorganization as a pH-dependent descriptor of the hydrogen evolution rate on platinum electrodes. Nat Energy. 2017 Mar 20;2(4):17031. doi:10.1038/nenergy.2017.31

43. She X, Zhai L, Wang Y, Xiong P, Li MMJ, Wu TS, et al. Pure-water-fed, electrocatalytic CO_2 reduction to ethylene beyond 1,000 h stability at 10 A. Nat Energy. 2024 Jan 5;9(1):81–91. doi:10.1038/s41560-023-01415-4

44. Wakerley D, Lamaison S, Ozanam F, Menguy N, Mercier D, Marcus P, et al. Bio-inspired hydrophobicity promotes CO_2 reduction on a Cu surface. Nat Mater. 2019 Nov 5;18(11):1222–7. doi:10.1038/s41563-019-0445-x

45. Nitopi S, Bertheussen E, Scott SB, Liu X, Engstfeld AK, Horch S, et al. Progress and Perspectives of Electrochemical CO_2 Reduction on Copper in Aqueous Electrolyte. Chem Rev. 2019 Jun 26;119(12):7610–72. doi:10.1021/acs.chemrev.8b00705

46. Lu S, Hu H, Sun H, Yang F, Zhu H, Du M, et al. Covalent porous catalysts for electrochemical reduction of CO2. Green Chemistry. 2024;26(10):5744–69. doi:10.1039/D4GC00717D

47. Rothschild DA, Cao Z, Xie F, Thomas B, Emge TJ, Li J, et al. Using Host-Guest Chemistry to Examine the Effects of Porosity and Catalyst-Support Interactions on CO_2 Reduction. Angew Chem Int Ed. 2025 May 19;64(21). doi:10.1002/anie.202504630

48. Hori Y, Kikuchi K, Suzuki S. production of co and ch4 in electrochemical reduction of co2 at metal electrodes in aqueous hydrogencarbonate solution. Chem Lett. 1985 Nov 5;14(11):1695–8. doi:10.1246/cl.1985.1695

49. Qiao J, Liu Y, Hong F, Zhang J. A review of catalysts for the electroreduction of carbon dioxide to produce low-carbon fuels. Chem Soc Rev. 2014;43(2):631–75. doi:10.1039/C3CS60323G

50. Furukawa H, Cordova KE, O'Keeffe M, Yaghi OM. The Chemistry and Applications of Metal-Organic Frameworks. Science (1979). 2013 Aug 30;341(6149). doi:10.1126/science.1230444

51. Wang S, Badreldin A, Li Y. Metal–nitrogen–carbon catalysts for electrochemical CO_2 reduction: from design to industrial applications. Chemical Communications. 2025;61(57):10484–504. doi:10.1039/D5CC02297E

52. Hu H, Liu J, Li W, Wen H, Yang X, Ke B, et al. MOF-derived doped porous carbon-based catalysts for CO_2 electroreduction: design, mechanisms, and scale-up. Mater Chem Front. 2026;10(6):888–921. doi:10.1039/D5QM00888C

53. Banerjee R, Phan A, Wang B, Knobler C, Furukawa H, O'Keeffe M, et al. High-Throughput Synthesis of Zeolitic Imidazolate Frameworks and Application to CO_2 Capture. Science (1979). 2008 Feb 15;319(5865):939–43. doi:10.1126/science.1152516

54. Park KS, Ni Z, Côté AP, Choi JY, Huang R, Uribe-Romo FJ, et al. Exceptional chemical and thermal stability of zeolitic imidazolate frameworks. Proceedings of the National Academy of Sciences. 2006 Jul 5;103(27):10186–91. doi:10.1073/pnas.0602439103

55. Zheng Z, Rong Z, Nguyen HL, Yaghi OM. Structural Chemistry of Zeolitic Imidazolate Frameworks. Inorg Chem. 2023 Dec 25;62(51):20861–73. doi:10.1021/acs.inorgchem.3c02322

56. Phan A, Doonan CJ, Uribe-Romo FJ, Knobler CB, O'Keeffe M, Yaghi OM. Synthesis, Structure, and Carbon Dioxide Capture Properties of Zeolitic Imidazolate Frameworks. Acc Chem Res. 2010 Jan 19;43(1):58–67. doi:10.1021/ar900116g

57. Phan A, Doonan CJ, Uribe-Romo FJ, Knobler CB, O'Keeffe M, Yaghi OM. Synthesis, Structure, and Carbon Dioxide Capture Properties of Zeolitic Imidazolate Frameworks. Acc Chem Res. 2010 Jan 19;43(1):58–67. doi:10.1021/ar900116g

58. Li JR, Kuppler RJ, Zhou HC. Selective gas adsorption and separation in metal–organic frameworks. Chem Soc Rev. 2009;38(5):1477. doi:10.1039/b802426j

59. Huang X, Lin Y, Zhang J, Chen X. Ligand-Directed Strategy for Zeolite-Type Metal–Organic Frameworks: Zinc(II) Imidazolates with Unusual Zeolitic Topologies. Angew Chem Int Ed. 2006 Feb 27;45(10):1557–9. doi:10.1002/anie.200503778

60. Park KS, Ni Z, Côté AP, Choi JY, Huang R, Uribe-Romo FJ, et al. Exceptional chemical and thermal stability of zeolitic imidazolate frameworks. Proceedings of the National Academy of Sciences. 2006 Jul 5;103(27):10186–91. doi:10.1073/pnas.0602439103

61. Banerjee R, Phan A, Wang B, Knobler C, Furukawa H, O'Keeffe M, et al. High-Throughput Synthesis of Zeolitic Imidazolate Frameworks and Application to CO_2 Capture. Science (1979). 2008 Feb 15;319(5865):939–43. doi:10.1126/science.1152516

62. Wang H, Pei X, Kalmutzki MJ, Yang J, Yaghi OM. Large Cages of Zeolitic Imidazolate Frameworks. Acc Chem Res. 2022 Mar 1;55(5):707–21. doi:10.1021/acs.accounts.1c00740

63. Thompson JA, Vaughn JT, Brunelli NA, Koros WJ, Jones CW, Nair S. Mixed-linker zeolitic imidazolate framework mixed-matrix membranes for aggressive CO_2 separation from natural gas. Microporous and Mesoporous Materials. 2014 Jul;192:43–51. doi:10.1016/j.micromeso.2013.06.036

64. Gong X, Wang Y, Kuang T. ZIF-8-Based Membranes for Carbon Dioxide Capture and Separation. ACS Sustain Chem Eng. 2017 Dec 4;5(12):11204–14. doi:10.1021/acssuschemeng.7b03613

65. Hayashi H, Côté AP, Furukawa H, O'Keeffe M, Yaghi OM. Zeolite A imidazolate frameworks. Nat Mater. 2007 Jul 27;6(7):501–6. doi:10.1038/nmat1927

66. Tan JC, Bennett TD, Cheetham AK. Chemical structure, network topology, and porosity effects on the mechanical properties of Zeolitic Imidazolate Frameworks. Proceedings of the National Academy of Sciences. 2010 Jun 17;107(22):9938–43. doi:10.1073/pnas.1003205107

67. Bergaoui M, Khalfaoui M, Awadallah-F A, Al-Muhtaseb S. A review of the features and applications of ZIF-8 and its derivatives for separating CO_2 and isomers of C3- and C4- hydrocarbons. J Nat Gas Sci Eng. 2021 Dec;96:104289. doi:10.1016/j.jngse.2021.104289

68. Kalauni K, Vedrtnam A, Wdowin M, Chaturvedi S. ZIF for CO_2 Capture: Structure, Mechanism, Optimization, and Modeling. Processes. 2022 Dec 13;10(12):2689. doi:10.3390/pr10122689

69. Ji Y, Liu X, Li H, Jiao X, Yu X, Zhang Y. Hydrophobic ZIF-8 covered active carbon for CO_2 capture from humid gas. Journal of Industrial and Engineering Chemistry. 2023 May;121:331–7. doi:10.1016/j.jiec.2023.01.036

70. Park KS, Ni Z, Côté AP, Choi JY, Huang R, Uribe-Romo FJ, et al. Exceptional chemical and thermal stability of zeolitic imidazolate frameworks. Proceedings of the National Academy of Sciences. 2006 Jul 5;103(27):10186–91. doi:10.1073/pnas.0602439103

71. Butt FS, Lewis A, Dingwall F, Mazlan NA, Radacsi N, Fan X, et al. ZIF-8 with exceptional thermal stability: Role of organic cosolvents in phase control and structure stabilization. Mater Today Chem. 2023 Dec;34:101804. doi:10.1016/j.mtchem.2023.101804

72. Ortiz AU, Freitas AP, Boutin A, Fuchs AH, Coudert FX. What makes zeolitic imidazolate frameworks hydrophobic or hydrophilic? The impact of geometry and functionalization on water adsorption. Phys Chem Chem Phys. 2014;16(21):9940–9. doi:10.1039/C3CP54292K

73. Xie L, Xu M, Liu X, Zhao M, Li J. Hydrophobic Metal–Organic Frameworks: Assessment, Construction, and Diverse Applications. Advanced Science. 2020 Feb 19;7(4). doi:10.1002/advs.201901758

74. Park KS, Ni Z, Côté AP, Choi JY, Huang R, Uribe-Romo FJ, et al. Exceptional chemical and thermal stability of zeolitic imidazolate frameworks. Proceedings of the National Academy of Sciences. 2006 Jul 5;103(27):10186–91. doi:10.1073/pnas.0602439103

75. Venna SR, Zhu M, Li S, Carreon MA. Knudsen diffusion through ZIF-8 membranes synthesized by secondary seeded growth. Journal of Porous Materials. 2014 Apr 14;21(2):235–40. doi:10.1007/s10934-013-9768-1

76. Zhu S, Lin Q, Huang X, Chen L, Liu L, Yao Z, et al. Efficient Separation of Acetylene-Containing Mixtures Using ZIF-8 Membranes. ACS Omega. 2021 Dec 7;6(48):33018–23. doi:10.1021/acsomega.1c05126

77. Bux H, Liang F, Li Y, Cravillon J, Wiebcke M, Caro J. Zeolitic Imidazolate Framework Membrane with Molecular Sieving Properties by Microwave-Assisted Solvothermal Synthesis. J Am Chem Soc. 2009 Nov 11;131(44):16000–1. doi:10.1021/ja907359t

78. Ali S, Ismail PM, Humayun M, Bououdina M, Qiao L. Tailoring 2D metal-organic frameworks for enhanced CO_2 reduction efficiency through modulating conjugated ligands. Fuel Processing Technology. 2024 May;255:108049. doi:10.1016/j.fuproc.2024.108049

79. Hu C, Bai S, Gao L, Liang S, Yang J, Cheng SD, et al. Porosity-Induced High Selectivity for CO_2 Electroreduction to CO on Fe-Doped ZIF-Derived Carbon Catalysts. ACS Catal. 2019 Dec 6;9(12):11579–88. doi:10.1021/acscatal.9b03175

80. Chen XL, Ma LS, Su WY, Ding LF, Zhu HB, Yang H. ZIF-derived bifunctional Cu@Cu–N–C composite electrocatalysts towards efficient electroreduction of oxygen and carbon dioxide. Electrochim Acta. 2020 Jan;331:135273. doi:10.1016/j.electacta.2019.135273

81. Tian H, Yang H, Liu X, Jia Y, Xu Q. Confinement effect on the electrochemical CO_2 reduction reaction. Green Chemistry. 2025;27(5):1238–53. doi:10.1039/D4GC05274A

82. Gholampour N, Ezugwu CI, Younus HA, Debecker DP, Al Abri M, Al hajri R, et al. Recent trends in CO_2 electroreduction over metal–organic framework-derived materials: a comprehensive review. J Mater Chem A Mater. 2024;12(41):27825–54. doi:10.1039/D4TA03502J

83. Liu X, Liu XH, Zhang X, Wang H, Zhao Q. Metal–organic frameworks and their derivatives for the electrochemical CO_2 reduction reaction: insights from molecular engineering. J Mater Chem A Mater. 2024;12(32):20578–605. doi:10.1039/D4TA01330A

84. Zhu L, Lin Y, Liu K, Cortés E, Li H, Hu J, et al. Tuning the intermediate reaction barriers by a CuPd catalyst to improve the selectivity of CO2 electroreduction to C_2 products. Chinese Journal of Catalysis. 2021 Sep;42(9):1500–8. doi:10.1016/S1872-2067(20)63754-8

85. Yang D, Wang X. 2D π-conjugated metal–organic frameworks for CO_2 electroreduction. SmartMat. 2022 Mar 28;3(1):54–67. doi:10.1002/smm2.1102

86. Pei Z, Li Y, Fan G, Guo Y, Luan D, Gu X, et al. Low-Coordinated Conductive ZnCu Metal-Organic Frameworks for Highly Selective H_2O_2 Electrosynthesis. Small. 2024 May 21. doi:10.1002/smll.202403808

87. Wang J, Deng D, Wu Q, Liu M, Wang Y, Jiang J, et al. Insight on Atomically Dispersed Cu Catalysts for Electrochemical CO_2 Reduction. ACS Nano. 2023 Oct 10;17(19):18688–705. doi:10.1021/acsnano.3c07307

88. Diercks CS, Liu Y, Cordova KE, Yaghi OM. The role of reticular chemistry in the design of CO_2 reduction catalysts. Nat Mater. 2018 Apr 26;17(4):301–7. doi:10.1038/s41563-018-0033-5

89. Singh HD, G M, Misra R, Sarkar S, Chakraborty D, Nandi S. Selective electroreduction of CO_2 to value-added C_1 and C_2 products using MOF and COF-based catalysts. Adv Compos Hybrid Mater. 2024 Dec 28;7(6):209. doi:10.1007/s42114-024-01016-z

90. Hu M, Li L, Li J, Zahra K, Zhang Z. Two-dimensional Cu-based materials for electrocatalytic carbon dioxide reduction. iScience. 2024 Mar;27(3):109313. doi:10.1016/j.isci.2024.109313

91. Kalaj M, Cohen SM. Postsynthetic Modification: An Enabling Technology for the Advancement of Metal–Organic Frameworks. ACS Cent Sci. 2020 Jul 22;6(7):1046–57. doi:10.1021/acscentsci.0c00690

92. Li J, Luo H, Li B, Ma JG, Cheng P. Application of MOF-derived materials as electrocatalysts for CO_2 conversion. Mater Chem Front. 2023;7(23):6107–29. doi:10.1039/D3QM00835E

93. Zhu Z, Li Z, Wei X, Wang J, Xiao S, Li R, et al. Achieving efficient electroreduction of CO_2 to CO in a wide potential window by encapsulating Ni nanoparticles in N-doped carbon nanotubes. Carbon N Y. 2021 Nov;185:9–16. doi:10.1016/j.carbon.2021.08.072

94. Peterson AA, Nørskov JK. Activity Descriptors for CO_2 Electroreduction to Methane on Transition-Metal Catalysts. J Phys Chem Lett. 2012 Jan 19;3(2):251–8. doi:10.1021/jz201461p

95. Lu S, Zhang Y, Mady MF, Egwu Eleri O, Mekonnen Tucho W, Mazur M, et al. Sulfur-Decorated Ni−N−C Catalyst for Electrocatalytic CO_2 Reduction with Near 100 % CO Selectivity. ChemSusChem. 2022 Oct 10;15(19). doi:10.1002/cssc.202200870

96. Parsons J, Alotaibi M. The Application of Transition Metal Sulfide Nanomaterials and Their Composite Nanomaterials in the Electrocatalytic Reduction of CO_2: A Review. Applied Sciences. 2023 Feb 26;13(5):3023. doi:10.3390/app13053023

97. Zhu J, Hu J, Wang Z, Lu Z, Das S, Cool P. Design of a new Ni@NCNT/graphene hybrid structured catalyst for high-performance electrochemical CO_2 reduction: unravelling the roles of N-doping. Chem Sci. 2025;16(6):2850–60. doi:10.1039/D4SC07354A

98. Zhang X, Ma G, Shui L, Zhou G, Wang X. Ni_3N nanoparticles on porous nitrogen-doped carbon nanorods for nitrate electroreduction. Chemical Engineering Journal. 2022 Feb;430:132666. doi:10.1016/j.cej.2021.132666

99. Yan B, Krishnamurthy D, Hendon CH, Deshpande S, Surendranath Y, Viswanathan V. Surface Restructuring of Nickel Sulfide Generates Optimally Coordinated Active Sites for Oxygen Reduction Catalysis. Joule. 2017 Nov;1(3):600–12. doi:10.1016/j.joule.2017.08.020

100. Anantharaj S, Kundu S, Noda S. Progress in nickel chalcogenide electrocatalyzed hydrogen evolution reaction. J Mater Chem A Mater. 2020;8(8):4174–92. doi:10.1039/C9TA14037A

101. Zhang B, Zhang J, Zhang H, Jiang H, Li C. Surface covalent sulfur enriching Ni active sites of Ni_3S_2 nanoparticles for efficient oxygen evolution. New Journal of Chemistry. 2021;45(6):3210–4. doi:10.1039/D0NJ06064J

102. Mukherjee A, Abdinejad M, Mahapatra SS, Ruidas BC. Metal sulfide-based nanomaterials for electrochemical CO $_2$ reduction. J Mater Chem A Mater. 2023;11(17):9300–32. doi:10.1039/D2TA08209H

103. Nitopi S, Bertheussen E, Scott SB, Liu X, Engstfeld AK, Horch S, et al. Progress and Perspectives of Electrochemical CO_2 Reduction on Copper in Aqueous Electrolyte. Chem Rev. 2019 Jun 26;119(12):7610–72. doi:10.1021/acs.chemrev.8b00705

104. Resasco J, Chen LD, Clark E, Tsai C, Hahn C, Jaramillo TF, et al. Promoter Effects of Alkali Metal Cations on the Electrochemical Reduction of Carbon Dioxide. J Am Chem Soc. 2017 Aug 16;139(32):11277–87. doi:10.1021/jacs.7b06765

105. Clark EL, Resasco J, Landers A, Lin J, Chung LT, Walton A, et al. Standards and Protocols for Data Acquisition and Reporting for Studies of the Electrochemical Reduction of Carbon Dioxide. ACS Catal. 2018 Jul 6;8(7):6560–70. doi:10.1021/acscatal.8b01340

106. Ringe S, Morales-Guio CG, Chen LD, Fields M, Jaramillo TF, Hahn C, et al. Double layer charging driven carbon dioxide adsorption limits the rate of electrochemical carbon dioxide reduction on Gold. Nat Commun. 2020 Jan 7;11(1):33. doi:10.1038/s41467-019-13777-z

107. Varela AS. The importance of pH in controlling the selectivity of the electrochemical CO_2 reduction. Curr Opin Green Sustain Chem. 2020 Dec;26:100371. doi:10.1016/j.cogsc.2020.100371

108. Dunwell M, Lu Q, Heyes JM, Rosen J, Chen JG, Yan Y, et al. The Central Role of Bicarbonate in the Electrochemical Reduction of Carbon Dioxide on Gold. J Am Chem Soc. 2017 Mar 15;139(10):3774–83. doi:10.1021/jacs.6b13287

109. Goyal A, Marcandalli G, Mints VA, Koper MTM. Competition between CO_2 Reduction and Hydrogen Evolution on a Gold Electrode under Well-Defined Mass Transport Conditions. J Am Chem Soc. 2020 Mar 4;142(9):4154–61. doi:10.1021/jacs.9b10061

110. Wu J, Li W, Liu K, Kucernak A, Liu H, Chai L, et al. Cation effects on electrochemical CO_2 reduction reaction. Next Energy. 2023 Sep;1(3):100032. doi:10.1016/j.nxener.2023.100032

111. Pérez-Gallent E, Marcandalli G, Figueiredo MC, Calle-Vallejo F, Koper MTM. Structure- and Potential-Dependent Cation Effects on CO Reduction at Copper Single-Crystal Electrodes. J Am Chem Soc. 2017 Nov 15;139(45):16412–9. doi:10.1021/jacs.7b10142

112. Liang S, Altaf N, Huang L, Gao Y, Wang Q. Electrolytic cell design for electrochemical CO_2 reduction. Journal of CO_2 Utilization. 2020 Jan;35:90–105. doi:10.1016/j.jcou.2019.09.007

113. Wakerley D, Lamaison S, Wicks J, Clemens A, Feaster J, Corral D, et al. Gas diffusion electrodes, reactor designs and key metrics of low-temperature CO_2 electrolysers. Nat Energy. 2022 Feb 17;7(2):130–43. doi:10.1038/s41560-021-00973-9

114. Qiu Z, Yun Y, He M, Wang L. Recent developments in ion conductive membranes for CO_2 electrochemical reduction. Chemical Engineering Journal. 2023 Jan;456:140942. doi:10.1016/j.cej.2022.140942

115. Lee J, Lim J, Roh CW, Whang HS, Lee H. Electrochemical CO_2 reduction using alkaline membrane electrode assembly on various metal electrodes. Journal of CO_2 Utilization. 2019 May;31:244–50. doi:10.1016/j.jcou.2019.03.022

116. Ma M, Seger B. Rational Design of Local Reaction Environment for Electrocatalytic Conversion of CO_2 into Multicarbon Products. Angew Chem Int Ed. 2024 Jun 3;63(23). doi:10.1002/anie.202401185

117. Kas R, Yang K, Bohra D, Kortlever R, Burdyny T, Smith WA. Electrochemical CO_2 reduction on nanostructured metal electrodes: fact or defect? Chem Sci. 2020;11(7):1738–49. doi:10.1039/C9SC05375A

118. Lee J, Lim J, Roh CW, Whang HS, Lee H. Electrochemical CO_2 reduction using alkaline membrane electrode assembly on various metal electrodes. Journal of CO_2 Utilization. 2019 May;31:244–50. doi:10.1016/j.jcou.2019.03.022

119. Bazant MZ. Theory of Chemical Kinetics and Charge Transfer based on Nonequilibrium Thermodynamics. Acc Chem Res. 2013 May 21;46(5):1144–60. doi:10.1021/ar300145c

120. Resasco J, Chen LD, Clark E, Tsai C, Hahn C, Jaramillo TF, et al. Promoter Effects of Alkali Metal Cations on the Electrochemical Reduction of Carbon Dioxide. J Am Chem Soc. 2017 Aug 16;139(32):11277–87. doi:10.1021/jacs.7b06765

121. Wuttig A, Yaguchi M, Motobayashi K, Osawa M, Surendranath Y. Inhibited proton transfer enhances Au-catalyzed CO_2 -to-fuels selectivity. Proceedings of the National Academy of Sciences. 2016 Aug 9;113(32). doi:10.1073/pnas.1602984113

122. Structure- and Potential-Dependent Cation Effects on CO Reduction at Copper Single-Crystal Electrodes.

123. Chen LD, Urushihara M, Chan K, Nørskov JK. Electric Field Effects in Electrochemical CO_2 Reduction. ACS Catal. 2016 Oct 7;6(10):7133–9. doi:10.1021/acscatal.6b02299

124. Li J, Kornienko N. Electrocatalytic carbon dioxide reduction in acid. Chem Catalysis. 2022 Jan;2(1):29–38. doi:10.1016/j.checat.2021.10.016

125. Chen X, Chen C, Wang Y, Pan Z, Chen J, Xu Y, et al. Interfacial microenvironment effects on electrochemical CO_2 reduction. Chemical Engineering Journal. 2024 Feb;482:148944. doi:10.1016/j.cej.2024.148944

126. Zeng D, Li C, Wang W, Zhang L, Zhang Y, Wang J, et al. Insights into the hydrophobic surface promoting electrochemical CO_2 reduction to ethylene. Chemical Engineering Journal. 2023 Apr;461:142133. doi:10.1016/j.cej.2023.142133

127. Rehberger H, Rezaei M, Aljabour A. Challenges and Opportunities of Choosing a Membrane for Electrochemical CO_2 Reduction. Membranes (Basel). 2025 Feb 8;15(2):55. doi:10.3390/membranes15020055

128. Lin J, Yan S, Zhang C, Hu Q, Cheng Z. Electroreduction of CO_2 toward High Current Density. Processes. 2022 Apr 22;10(5):826. doi:10.3390/pr10050826

129. Nitopi S, Bertheussen E, Scott SB, Liu X, Engstfeld AK, Horch S, et al. Progress and Perspectives of Electrochemical CO_2 Reduction on Copper in Aqueous Electrolyte. Chem Rev. 2019 Jun 26;119(12):7610–72. doi:10.1021/acs.chemrev.8b00705

130. Long-term-stability continuous flow CO_2 reduction electrolysers with high current efficiency.

131. Gao D, Wei P, Li H, Lin L, Wang G, Bao X. Designing Electrolyzers for Electrocatalytic CO_2 Reduction. Acta Physico Chimica Sinica. 2020;0(0):2009021–0. doi:10.3866/PKU.WHXB202009021

132. Zhang X, Guo SX, Gandionco KA, Bond AM, Zhang J. Electrocatalytic carbon dioxide reduction: from fundamental principles to catalyst design. Mater Today Adv. 2020 Sep;7:100074. doi:10.1016/j.mtadv.2020.100074

133. Liu K, Smith WA, Burdyny T. Introductory Guide to Assembling and Operating Gas Diffusion Electrodes for Electrochemical CO_2 Reduction. ACS Energy Lett. 2019 Mar 8;4(3):639–43. doi:10.1021/acsenergylett.9b00137

134. Weng LC, Bell AT, Weber AZ. Modeling gas-diffusion electrodes for CO_2 reduction. Physical Chemistry Chemical Physics. 2018;20(25):16973–84. doi:10.1039/C8CP01319E

135. Xing Z, Shi K, Hu X, Feng X. Beyond catalytic materials: Controlling local gas/liquid environment in the catalyst layer for CO_2 electrolysis. Journal of Energy Chemistry. 2022 Mar;66:45–51. doi:10.1016/j.jechem.2021.07.006

136. Ahangari HT, Portail T, Marshall AT. Comparing the electrocatalytic reduction of CO_2 to CO on gold cathodes in batch and continuous flow electrochemical cells. Electrochem commun. 2019 Apr;101:78–81. doi:10.1016/j.elecom.2019.03.005

137. Subramanian S, Yang K, Li M, Sassenburg M, Abdinejad M, Irtem E, et al. Geometric Catalyst Utilization in Zero-Gap CO_2 Electrolyzers. ACS Energy Lett. 2023 Jan 13;8(1):222–9. doi:10.1021/acsenergylett.2c02194

138. Lees EW, Mowbray BAW, Parlane FGL, Berlinguette CP. Gas diffusion electrodes and membranes for CO_2 reduction electrolysers. Nat Rev Mater. 2021 Sep 17;7(1):55–64. doi:10.1038/s41578-021-00356-2

139. Bagheri M, Lourenço MAO, Dangbegnon JK, Monti NBD, Mafra L, Pirri F, et al. Green Synthesis of MOF-Based Materials for Electrochemical Reduction of Carbon Dioxide. ChemSusChem. 2025 Jan 14;18(2). doi:10.1002/cssc.202400684

140. Bagheri M, Lourenço MAO, Castellino M, Nappini S, Di Costola F, Dangbegnon JK, et al. Mesoporous Copper-Based Metal-Organic Framework Flakes as a Promising Platform for Electrosynthesis of Ethylene from Carbon Dioxide. Small Science. 2026 Jun 11;6(6). doi:10.1002/smsc.70323

141. Lu XK, Seitz LC. Reactor operating parameters and their effects on the local reaction environment of CO_2 electroreduction. Chem Soc Rev. 2025;54(12):6088–121. doi:10.1039/D5CS00040H

142. Kutz RB, Chen Q, Yang H, Sajjad SD, Liu Z, Masel IR. Sustainion Imidazolium-Functionalized Polymers for Carbon Dioxide Electrolysis. Energy Technology. 2017 Jun 9;5(6):929–36. doi:10.1002/ente.201600636

143. Rabiee H, Ge L, Zhang X, Hu S, Li M, Yuan Z. Gas diffusion electrodes (GDEs) for electrochemical reduction of carbon dioxide, carbon monoxide, and dinitrogen to value-added products: a review. Energy Environ Sci. 2021;14(4):1959–2008. doi:10.1039/D0EE03756G

144. Chen Z, Duan X, Wei W, Wang S, Ni BJ. Iridium-based nanomaterials for electrochemical water splitting. Nano Energy. 2020 Dec;78:105270. doi:10.1016/j.nanoen.2020.105270

145. Nong HN, Falling LJ, Bergmann A, Klingenhof M, Tran HP, Spöri C, et al. Key role of chemistry versus bias in electrocatalytic oxygen evolution. Nature. 2020 Nov 19;587(7834):408–13. doi:10.1038/s41586-020-2908-2

146. Islam J, Kim SK, Thien PT, Kim MJ, Cho HS, Cho WC, et al. Enhancing the activity and durability of iridium electrocatalyst supported on boron carbide by tuning the chemical state of iridium for oxygen evolution reaction. J Power Sources. 2021 Nov;512:230506. doi:10.1016/j.jpowsour.2021.230506

147. Wei S, Hua H, Zhao Y, Luo J. Porous membranes enable selective and stable zero-gap acidic CO_2 electrolysers. Nat Commun. 2025 Oct 21;16(1):9299. doi:10.1038/s41467-025-64342-w

148. Verma S, Lu X, Ma S, Masel RI, Kenis PJA. The effect of electrolyte composition on the electroreduction of CO_2 to CO on Ag based gas diffusion electrodes. Physical Chemistry Chemical Physics. 2016;18(10):7075–84. doi:10.1039/C5CP05665A

149. Sajjad SD, Gao Y, Liu Z, Yang H, Masel R. Tunable-High Performance Sustainion^{TM} Anion Exchange Membranes for Electrochemical Applications. ECS Trans. 2017 Jul 7;77(11):1653–6. doi:10.1149/07711.1653ecst

150. Mauritz KA, Moore RB. State of Understanding of Nafion. Chem Rev. 2004 Oct 1;104(10):4535–86. doi:10.1021/cr0207123

151. Yang H, Kaczur JJ, Sajjad SD, Masel RI. Electrochemical conversion of CO_2 to formic acid utilizing Sustainion^{TM} membranes. Journal of CO_2 Utilization. 2017 Jul;20:208–17. doi:10.1016/j.jcou.2017.04.011

152. Rabinowitz JA, Kanan MW. The future of low-temperature carbon dioxide electrolysis depends on solving one basic problem. Nat Commun. 2020 Oct 16;11(1):5231. doi:10.1038/s41467-020-19135-8

153. Subramanian S, Yang K, Li M, Sassenburg M, Abdinejad M, Irtem E, et al. Geometric Catalyst Utilization in Zero-Gap CO $_2$ Electrolyzers. ACS Energy Lett. 2023 Jan 13;8(1):222–9. doi:10.1021/acsenergylett.2c02194

154. Rabiee H, Ge L, Zhang X, Hu S, Li M, Yuan Z. Gas diffusion electrodes (GDEs) for electrochemical reduction of carbon dioxide, carbon monoxide, and dinitrogen to value-added products: a review. Energy Environ Sci. 2021;14(4):1959–2008. doi:10.1039/D0EE03756G

155. Verma S, Hamasaki Y, Kim C, Huang W, Lu S, Jhong HRM, et al. Insights into the Low Overpotential Electroreduction of CO_2 to CO on a Supported Gold Catalyst in an Alkaline Flow Electrolyzer. ACS Energy Lett. 2018 Jan 12;3(1):193–8. doi:10.1021/acsenergylett.7b01096

156. Allen J. Bard LRF. Electrochemical Methods: Fundamentals and Applications, 2nd Edition. 2nd ed.

157. Troudt BK, Rousseau CR, Dong XIN, Anderson EL, Bühlmann P. Recent progress in the development of improved reference electrodes for electrochemistry. Analytical Sciences. 2022 Jan 28;38(1):71–83. doi:10.2116/analsci.21SAR11

158. Chae Y, Kim H, Lee DK, Lee U, Won DH. Exploring the critical role of binders in electrochemical CO2 reduction reactions. Nano Energy. 2024 Nov;130:110134. doi:10.1016/j.nanoen.2024.110134

159. Zanellato G, Schiavi PG, Zanoni R, Rubino A, Altimari P, Pagnanelli F. Electrodeposited Copper Nanocatalysts for CO_2 Electroreduction: Effect of

Electrodeposition Conditions on Catalysts' Morphology and Selectivity. Energies (Basel). 2021 Aug 15;14(16):5012. doi:10.3390/en14165012

160. Xue R, Yuan S, Wang R, Bi T, Zhang G, Li H, et al. The insights into ionomer-catalyst interactions enabling high-efficiency CO_2 electroreduction in pure water. Journal of Energy Chemistry. 2025 May. doi:10.1016/j.jechem.2025.04.057

161. Chen Y, Wrubel JA, Vise AE, Intia F, Harshberger S, Klein E, et al. The effect of catholyte and catalyst layer binders on CO_2 electroreduction selectivity. Chem Catalysis. 2022 Feb;2(2):400–21. doi:10.1016/j.checat.2022.01.011

162. Zhang F, Zhang H, Liu Z. Recent advances in electrochemical reduction of CO_2. Curr Opin Green Sustain Chem. 2019 Apr;16:77–84. doi:10.1016/j.cogsc.2019.02.006

163. Inzelt G. Chronoamperometry, Chronocoulometry, and Chronopotentiometry. In: Encyclopedia of Applied Electrochemistry. New York, NY: Springer New York; 2014. p. 207–14. doi:10.1007/978-1-4419-6996-5_217

164. J. Ross Macdonald WRK. Impedance Spectroscopy: Emphasizing Solid Materials and Systems.

165. Sacco A. Electrochemical impedance spectroscopy as a tool to investigate the electroreduction of carbon dioxide: A short review. Journal of CO_2 Utilization. 2018 Oct;27:22–31. doi:10.1016/j.jcou.2018.06.020

166. Diercks JS, Pribyl-Kranewitter B, Herranz J, Chauhan P, Faisnel A, Schmidt TJ. An Online Gas Chromatography Cell Setup for Accurate CO_2 -Electroreduction Product Quantification. J Electrochem Soc. 2021 Jun 1;168(6):064504. doi:10.1149/1945-7111/ac0363

167. Nitopi S, Bertheussen E, Scott SB, Liu X, Engstfeld AK, Horch S, et al. Progress and Perspectives of Electrochemical CO_2 Reduction on Copper in Aqueous Electrolyte. Chem Rev. 2019 Jun 26;119(12):7610–72. doi:10.1021/acs.chemrev.8b00705

168. Goldstein Joseph. Scanning electron microscopy and x-ray microanalysis. Springer-Verlag; 2018. 550 p.

169. Reimer L., Hawkes PW., Schawlow AL., Shimoda K., Siegman AE. Scanning Electron Microscopy : Physics of Image Formation and Microanalysis. Springer Berlin / Heidelberg; 2013. 538 p.

170. Vayenas CG., White RE., Gamboa-Aldeco ME. Modern aspects of electrochemistry. No. 42. Springer Science+Business Media; 2008. 420 p.

171. Nitopi S, Bertheussen E, Scott SB, Liu X, Engstfeld AK, Horch S, et al. Progress and Perspectives of Electrochemical CO_2 Reduction on Copper in Aqueous Electrolyte. Chem Rev. 2019 Jun 26;119(12):7610–72. doi:10.1021/acs.chemrev.8b00705

172. Möller T, Ju W, Bagger A, Wang X, Luo F, Ngo Thanh T, et al. Efficient CO_2 to CO electrolysis on solid Ni–N–C catalysts at industrial current densities. Energy Environ Sci. 2019;12(2):640–7. doi:10.1039/C8EE02662A

173. Kim D, Resasco J, Yu Y, Asiri AM, Yang P. Synergistic geometric and electronic effects for electrochemical reduction of carbon dioxide using gold–copper bimetallic nanoparticles. Nat Commun. 2014 Sep 11;5(1):4948. doi:10.1038/ncomms5948

174. Clark EL, Hahn C, Jaramillo TF, Bell AT. Electrochemical CO_2 Reduction over Compressively Strained CuAg Surface Alloys with Enhanced Multi-Carbon Oxygenate Selectivity. J Am Chem Soc. 2017 Nov 8;139(44):15848–57. doi:10.1021/jacs.7b08607

175. Thommes M, Kaneko K, Neimark A V., Olivier JP, Rodriguez-Reinoso F, Rouquerol J, et al. Physisorption of gases, with special reference to the evaluation of surface area and pore size distribution (IUPAC Technical Report). Pure and Applied Chemistry. 2015 Oct 1;87(9–10):1051–69. doi:10.1515/pac-2014-1117

176. Thommes M, Kaneko K, Neimark A V., Olivier JP, Rodriguez-Reinoso F, Rouquerol J, et al. Physisorption of gases, with special reference to the evaluation of surface area and pore size distribution (IUPAC Technical Report). Pure and Applied Chemistry. 2015 Oct 1;87(9–10):1051–69. doi:10.1515/pac-2014-1117

177. Sing KSW. Reporting physisorption data for gas/solid systems with special reference to the determination of surface area and porosity (Recommendations 1984). Pure and Applied Chemistry. 1985 Jan 1;57(4):603–19. doi:10.1351/pac198557040603

178. Walton KS, Snurr RQ. Applicability of the BET Method for Determining Surface Areas of Microporous Metal−Organic Frameworks. J Am Chem Soc. 2007 Jul 1;129(27):8552–6. doi:10.1021/ja071174k

179. Bae Y, Snurr RQ. Development and Evaluation of Porous Materials for Carbon Dioxide Separation and Capture. Angew Chem Int Ed. 2011 Dec 2;50(49):11586–96. doi:10.1002/anie.201101891

180. Matthew J. Surface analysis by Auger and x-ray photoelectron spectroscopy. D. Briggs and J. T. Grant (eds). IMPublications, Chichester, UK and SurfaceSpectra, Manchester, UK, 2003. 900 pp., ISBN 1-901019-04-7, 900 pp. Surface and Interface Analysis. 2004 Jan 29;36(13):1647–1647. doi:10.1002/sia.2005

181. Cramer SP. X-ray spectroscopy with synchrotron radiation : fundamentals and applications. Springer; 2020. 388 p.

182. John F. Moulder. Handbook of X-ray Photoelectron Spectroscopy: A Reference Book of Standard Spectra for Identification and Interpretation of XPS Data.

183. Wagner CD, Joshi A. The auger parameter, its utility and advantages: a review. J Electron Spectros Relat Phenomena. 1988 Jan;47:283–313. doi:10.1016/0368-2048(88)85018-7

184. Fassel VA, Kniseley RN. Inductively coupled plasma. Optical emission spectroscopy. Anal Chem. 1974 Nov 1;46(13):1110A – 1120a. doi:10.1021/ac60349a023

185. Rodríguez Alejandre JL, Sharma VR, Acosta Sánchez LA, Dasgupta-Schubert N. Total Reflection Xray Fluorescence (TXRF) spectrometry as a powerful and broad-spectrum analytical tool in the nuclear sciences. J Phys Conf Ser. 2023 Oct 1;2619(1):012014. doi:10.1088/1742-6596/2619/1/012014

186. Fadeeva VP, Tikhova VD, Nikulicheva ON. Elemental analysis of organic compounds with the use of automated CHNS analyzers. Journal of Analytical Chemistry. 2008 Nov 30;63(11):1094–106. doi:10.1134/S1061934808110142

187. Ferrari AC, Robertson J. Interpretation of Raman spectra of disordered and amorphous carbon. Phys Rev B. 2000 May 15;61(20):14095–107. doi:10.1103/PhysRevB.61.14095

188. Tuinstra F, Koenig JL. Raman Spectrum of Graphite. J Chem Phys. 1970 Aug 1;53(3):1126–30. doi:10.1063/1.1674108

189. Cançado LG, Takai K, Enoki T, Endo M, Kim YA, Mizusaki H, et al. General equation for the determination of the crystallite size La of nanographite by Raman spectroscopy. Appl Phys Lett. 2006 Apr 17;88(16). doi:10.1063/1.2196057

190. Stuart BH. Infrared Spectroscopy: Fundamentals and Applications. Wiley; 2004. doi:10.1002/0470011149

191. Rehr JJ, Albers RC. Theoretical approaches to x-ray absorption fine structure. Rev Mod Phys. 2000 Jul 1;72(3):621–54. doi:10.1103/RevModPhys.72.621

192. Bunker Grant. Introduction to XAFS : a practical guide to X-ray absorption fine structure spectroscopy. Cambridge University Press; 2010. 260 p.

193. Friebel D, Louie MW, Bajdich M, Sanwald KE, Cai Y, Wise AM, et al. Identification of Highly Active Fe Sites in (Ni,Fe)OOH for Electrocatalytic Water Splitting. J Am Chem Soc. 2015 Jan 28;137(3):1305–13. doi:10.1021/ja511559d

194. Timoshenko J, Roldan Cuenya B. *In Situ* / *Operando* Electrocatalyst Characterization by X-ray Absorption Spectroscopy. Chem Rev. 2021 Jan 27;121(2):882–961. doi:10.1021/acs.chemrev.0c00396

195. Paparoni F, Alizon G, Zitolo A, Rezvani SJ, Di Cicco A, Magnan H, et al. A novel electrochemical flow-cell for *operando* XAS investigations in X-ray opaque supports. Physical Chemistry Chemical Physics. 2024;26(5):3897–906. doi:10.1039/D3CP04701F

196. Matam SK, Sharma PK, Yu EH, Drivas C, Khan MD, Wilding M, et al. *Operando* X-ray absorption spectroscopic flow cell for electrochemical CO_2 reduction: new insight into the role of copper species. Catal Sci Technol. 2025;15(4):1070–81. doi:10.1039/D4CY00602J

197. Nappini S, D'Amario L, Favaro M, Dal Zilio S, Salvador F, Betz-Güttner E, et al. Soft x-ray spectroscopies in liquids and at solid–liquid interface at BACH beamline at Elettra. Review of Scientific Instruments. 2021 Jan 1;92(1). doi:10.1063/5.0025326

198. Drits V, Środoń J, Eberl DD. XRD Measurement of Mean Crystallite Thickness of Illite and Illite/Smectite: Reappraisal of the Kubler Index and the Scherrer Equation. Clays Clay Miner. 1997 Jun 28;45(3):461–75. doi:10.1346/CCMN.1997.0450315

199. Bagheri M, Lourenço MAO, Dangbegnon JK, Monti NBD, Mafra L, Pirri F, et al. Green Synthesis of MOF-based Materials for Electrochemical Reduction of Carbon Dioxide. ChemSusChem. 2024 Oct 4. doi:10.1002/cssc.202400684

200. Bergaoui M, Khalfaoui M, Awadallah-F A, Al-Muhtaseb S. A review of the features and applications of ZIF-8 and its derivatives for separating CO_2 and isomers of C_3- and C_4- hydrocarbons. J Nat Gas Sci Eng. 2021 Dec;96:104289. doi:10.1016/j.jngse.2021.104289

201. Duan C, Yu Y, Hu H. Recent progress on synthesis of ZIF-67-based materials and their application to heterogeneous catalysis. Green Energy & Environment. 2022 Feb;7(1):3–15. doi:10.1016/j.gee.2020.12.023

202. Yang L, Lu H. Microwave-assisted Ionothermal Synthesis and Characterization of Zeolitic Imidazolate Framework-8. Chin J Chem. 2012 May 10;30(5):1040–4. doi:10.1002/cjoc.201100595

203. Izadpanah Ostad M, Niknam Shahrak M, Galli F. The influence of different synthetic solvents on photocatalytic activity of ZIF-8 for methanol production from CO_2. Microporous and Mesoporous Materials. 2021 Oct;326:111363. doi:10.1016/j.micromeso.2021.111363

204. Payra S, Challagulla S, Indukuru RR, Chakraborty C, Tarafder K, Ghosh B, et al. The structural and surface modification of zeolitic imidazolate frameworks towards reduction of encapsulated CO_2. New Journal of Chemistry. 2018;42(23):19205–13. doi:10.1039/C8NJ04247K

205. Saliba D, Ammar M, Rammal M, Al-Ghoul M, Hmadeh M. Crystal Growth of ZIF-8, ZIF-67, and Their Mixed-Metal Derivatives. J Am Chem Soc. 2018 Feb 7;140(5):1812–23. doi:10.1021/jacs.7b11589

206. Zhou Y, Qiu J, Ding M, Zhang XF, Yao J. Electric current-assisted synthesis of ZIF-8 with stoichiometric metal and ligand precursors for CO_2 adsorption. Journal of Physics and Chemistry of Solids. 2022 Feb;161:110485. doi:10.1016/j.jpcs.2021.110485

207. Duan S, Wu L, Li J, Huang Y, Tan X, Wen T, et al. Two-dimensional copper-based metal−organic frameworks nano-sheets composites: One-step synthesis and highly efficient U(VI) immobilization. J Hazard Mater. 2019 Jul 5;373:580–90. doi:10.1016/j.jhazmat.2019.03.119 PubMed PMID: 30952003.

208. Franco A, Salatti-Dorado JÁ, García-Caballero V, Lorca S, Camacho L, Cano M, et al. A 2D copper-imidazolate framework without thermal treatment as an efficient ORR electrocatalyst for Zn–air batteries. J Mater Chem A Mater. 2022;10(46):24590–7. doi:10.1039/D2TA05988F

209. Majidi R, Farhadi A, Danaee I, Panah NB, Zarei D, Nikmanesh S. Investigation of synthesized planar Cu-MOF and spherical Ni-MOF nanofillers for improving the anti-corrosion performance of epoxy coatings. Prog Org Coat. 2023 Oct 1;183. doi:10.1016/j.porgcoat.2023.107803

210. Lv XL, Yuan S, Xie LH, Darke HF, Chen Y, He T, et al. Ligand Rigidification for Enhancing the Stability of Metal–Organic Frameworks. J Am Chem Soc. 2019 Jul 3;141(26):10283–93. doi:10.1021/jacs.9b02947

211. Smith BC. The Big Review III: Molecular Vibration Theory. Spectroscopy. 2024 Dec 1;31–4. doi:10.56530/spectroscopy.gn8689j7

212. Kale AM, Manikandan R, Justin Raj C, Dennyson Savariraj A, Voz C, Kim BC. Protonated nickel 2-methylimidazole framework as an advanced electrode material for high-performance hybrid supercapacitor. Mater Today Energy. 2021 Sep;21:100736. doi:10.1016/j.mtener.2021.100736

213. Lee J, Yoo J, Kim J. Copper 2-Methylimidazole Nanostructure-Based Colorimetric Fabric Sensor for Real-Time Monitoring of Ambient Sulfur Oxides. ACS Appl Nano Mater. 2022 Nov 25;5(11):17304–14. doi:10.1021/acsanm.2c04513

214. High Resolution XPS of Organic Polymers: The Scienta ESCA300 Database (Beamson, G.; Briggs, D.). J Chem Educ. 1993 Jan 1;70(1):A25. doi:10.1021/ed070pA25.5

215. Reed BP, Marchesini S, Chemello G, Morgan DJ, Vyas N, Howe T, et al. The influence of sample preparation on XPS quantification of oxygen-functionalised graphene nanoplatelets. Carbon N Y. 2023 Jun;211:118054. doi:10.1016/j.carbon.2023.118054

216. Miura Y, Kusano H, Nanba T, Matsumoto S. X-ray photoelectron spectroscopy of sodium borosilicate glasses. J Non Cryst Solids. 2001 Sep;290(1):1–14. doi:10.1016/S0022-3093(01)00720-7

217. Bulushev DA, Chuvilin AL, Sobolev VI, Stolyarova SG, Shubin Y V., Asanov IP, et al. Copper on carbon materials: stabilization by nitrogen doping. J Mater Chem A Mater. 2017;5(21):10574–83. doi:10.1039/C7TA02282D

218. Kirandeep, Kaur J, Sharma I, Zangrando E, Pal K, Mehta SK, et al. Fabrication of novel copper MOF nanoparticles for nanozymatic detection of mercury ions. Journal of Materials Research and Technology. 2023 Jan;22:278–91. doi:10.1016/j.jmrt.2022.10.167

219. Yan F, Dong L, Su J, Liu X, Han X, Zang J, et al. Copper coordinated with nitrogen in electrospun carbon nanofibers as a high-performance electrocatalyst for ORR. Electrochem commun. 2022 Mar;136:107245. doi:10.1016/j.elecom.2022.107245

220. Biesinger MC, Lau LWM, Gerson AR, Smart RStC. Resolving surface chemical states in XPS analysis of first row transition metals, oxides and hydroxides: Sc, Ti, V, Cu and Zn. Appl Surf Sci. 2010 Nov;257(3):887–98. doi:10.1016/j.apsusc.2010.07.086

221. Zhao C, Chen Y, Gong S, Tan W, Pan H, Liu X, et al. A water stable Cu-MOF/GO composite as a persulfate activator for efficient degradation of dye wastewater. Journal of Saudi Chemical Society. 2024 May;28(3):101856. doi:10.1016/j.jscs.2024.101856

222. Henzler K, Heilemann A, Kneer J, Guttmann P, Jia H, Bartsch E, et al. Investigation of reactions between trace gases and functional CuO nanospheres and octahedrons using NEXAFS-TXM imaging. Sci Rep. 2015 Dec 3;5(1):17729. doi:10.1038/srep17729

223. Su GM, Wang H, Barnett BR, Long JR, Prendergast D, Drisdell WS. Backbonding contributions to small molecule chemisorption in a metal–organic framework with open copper(i) centers. Chem Sci. 2021;12(6):2156–64. doi:10.1039/D0SC06038K

224. Lukens JT, DiMucci IM, Kurogi T, Mindiola DJ, Lancaster KM. Scrutinizing metal–ligand covalency and redox non-innocence *via* nitrogen K-edge X-ray absorption spectroscopy. Chem Sci. 2019;10(19):5044–55. doi:10.1039/C8SC03350A

225. Bui NT, Kang H, Teat SJ, Su GM, Pao CW, Liu YS, et al. A nature-inspired hydrogen-bonded supramolecular complex for selective copper ion removal from water. Nat Commun. 2020 Aug 7;11(1):3947. doi:10.1038/s41467-020-17757-6

226. Braglia L, Tavani F, Mauri S, Edla R, Krizmancic D, Tofoni A, et al. Catching the Reversible Formation and Reactivity of Surface Defective Sites in Metal–Organic Frameworks: An Operando Ambient Pressure-NEXAFS Investigation. J Phys Chem Lett. 2021 Sep 23;12(37):9182–7. doi:10.1021/acs.jpclett.1c02585

227. Hatsui T, Kosugi N. Metal-to-ligand charge transfer in polarized metal L-edge X-ray absorption of Ni and Cu complexes. J Electron Spectros Relat Phenomena. 2004 May;136(1–2):67–75. doi:10.1016/j.elspec.2004.02.133

228. Mangione G, Sambi M, Nardi M V., Casarin M. A theoretical study of the L_3 pre-edge XAS in Cu(ii) complexes. Phys Chem Chem Phys. 2014;16(37):19852–5. doi:10.1039/C4CP02441A

229. Grioni M, Goedkoop JB, Schoorl R, de Groot FMF, Fuggle JC, Schäfers F, et al. Studies of copper valence states with Cu L_3 x-ray-absorption spectroscopy. Phys Rev B. 1989 Jan 15;39(3):1541–5. doi:10.1103/PhysRevB.39.1541

230. Edzards J, Saßnick HD, Buzanich AG, Valencia AM, Emmerling F, Beyer S, et al. Effects of Ligand Substituents on the Character of Zn-Coordination in Zeolitic Imidazolate Frameworks. The Journal of Physical Chemistry C. 2023 Nov 2;127(43):21456–64. doi:10.1021/acs.jpcc.3c06054

231. Garetto B, Cao N, Finelli V, Aunan E, Signorile M, Olsbye U, et al. Pinpointing Cu-Coordination Motifs in Bio-Inspired MOFs by Combining DFT-Assisted XAS Analysis and Multivariate Curve Resolution. The Journal of Physical Chemistry C. 2025 Feb 20;129(7):3570–82. doi:10.1021/acs.jpcc.4c08029

232. Wang Q, Ina T, Chen WT, Shang L, Sun F, Wei S, et al. Evolution of Zn(II) single atom catalyst sites during the pyrolysis-induced transformation of ZIF-8 to N-doped carbons. Sci Bull (Beijing). 2020 Oct;65(20):1743–51. doi:10.1016/j.scib.2020.06.020

233. Al-Madhagi LH, Chang SY, Balasubramanian M, Kroner AB, Shotton EJ, Willneff EA, et al. X-ray Raman scattering: a new *in situ* probe of molecular structure during nucleation and crystallization from liquid solutions. CrystEngComm. 2018;20(43):6871–84. doi:10.1039/C8CE00929E

234. Thomason MJ, Seabourne CR, Sattelle BM, Hembury GA, Stevens JS, Scott AJ, et al. Self-association of organic solutes in solution: a NEXAFS study of aqueous imidazole. Faraday Discuss. 2015;179:269–89. doi:10.1039/C5FD00005J

235. Gabardo CM, O'Brien CP, Edwards JP, McCallum C, Xu Y, Dinh CT, et al. Continuous Carbon Dioxide Electroreduction to Concentrated Multi-carbon Products Using a Membrane Electrode Assembly. Joule. 2019 Nov;3(11):2777–91. doi:10.1016/j.joule.2019.07.021

236. Moore T, Xia X, Baker SE, Duoss EB, Beck VA. Elucidating Mass Transport Regimes in Gas Diffusion Electrodes for CO_2 Electroreduction. ACS Energy Lett. 2021 Oct 8;6(10):3600–6. doi:10.1021/acsenergylett.1c01513

237. García de Arquer FP, Dinh CT, Ozden A, Wicks J, McCallum C, Kirmani AR, et al. CO_2 electrolysis to multicarbon products at activities greater than 1 A cm^{-2}. Science (1979). 2020 Feb 7;367(6478):661–6. doi:10.1126/science.aay4217

238. Nam D, Shekhah O, Ozden A, McCallum C, Li F, Wang X, et al. High-Rate and Selective CO_2 Electrolysis to Ethylene via Metal–Organic-Framework-Augmented CO_2 Availability. Advanced Materials. 2022 Dec 16;34(51). doi:10.1002/adma.202207088

239. Zeng J, Mignosa M, Monti NBD, Sacco A, Pirri CF. Engineering copper nanoparticle electrodes for tunable electrochemical reduction of carbon dioxide. Electrochim Acta. 2023 Oct;464:142862. doi:10.1016/j.electacta.2023.142862

240. Nappini S, D'Amario L, Favaro M, Dal Zilio S, Salvador F, Betz-Güttner E, et al. Soft x-ray spectroscopies in liquids and at solid–liquid interface at BACH beamline at Elettra. Review of Scientific Instruments. 2021 Jan 1;92(1). doi:10.1063/5.0025326

241. Abid HMW, Balanay MP. Next-Generation Cu-MOF-based electrocatalysts for CO_2 reduction: Bridging mechanistic insights and rational design. Carbon Capture Science & Technology. 2025 Dec;17:100521. doi:10.1016/j.ccst.2025.100521

242. Shimizu K ichi, Maeshima H, Yoshida H, Satsuma A, Hattori T. Ligand field effect on the chemical shift in XANES spectra of Cu(II) compounds. Physical Chemistry Chemical Physics. 2001;3(5):862–6. doi:10.1039/b007276l

243. Sarangi R, Aboelella N, Fujisawa K, Tolman WB, Hedman B, Hodgson KO, et al. X-ray Absorption Edge Spectroscopy and Computational Studies on $LCuO_2$ Species: Superoxide−Cu^{II} versus Peroxide−Cu^{III} Bonding. J Am Chem Soc. 2006 Jun 1;128(25):8286–96. doi:10.1021/ja0615223

244. Arnouts S, Choukroun D, Napal I, Tajuelo Castilla G, Prieto J, Claes N, et al. Effective Utilization of Nanoporosity and Surface Area Guides Electrosynthesis over Soft-Landed Copper Oxide Catalyst Layers. Nano Lett. 2025 Feb 19;25(7):2670–7. doi:10.1021/acs.nanolett.4c05371

245. Choi M, Heo W, Kleitz F, Ryoo R. Facile synthesis of high quality mesoporous SBA-15 with enhanced control of the porous network connectivity and wall thickness. Chem Commun. 2003;(12):1340–1. doi:10.1039/B303696K

246. Maruccia E, Lourenço MAO, Priamushko T, Bartoli M, Bocchini S, Pirri FC, et al. Nanocast nitrogen-containing ordered mesoporous carbons from glucosamine for selective CO_2 capture. Materials Today Sustainability. 2022 Mar;17:100089. doi:10.1016/j.mtsust.2021.100089

247. Cherevko S, Zeradjanin AR, Topalov AA, Kulyk N, Katsounaros I, Mayrhofer KJJ. Dissolution of Noble Metals during Oxygen Evolution in Acidic Media. ChemCatChem. 2014 Aug 7;6(8):2219–23. doi:10.1002/cctc.201402194

248. Zhong G, Huang J, Yao Z, Luo B, Li K, Xu S, et al. Intrinsic acid resistance and high removal performance from the incorporation of nickel nanoparticles into nitrogen doped

tubular carbons for environmental remediation. J Colloid Interface Sci. 2020 Apr;566:46–59. doi:10.1016/j.jcis.2020.01.055

249. Thurston JH, Hunter NM, Wayment LJ, Cornell KA. Urea-derived graphitic carbon nitride (u-g-C_3N_4) films with highly enhanced antimicrobial and sporicidal activity. J Colloid Interface Sci. 2017 Nov;505:910–8. doi:10.1016/j.jcis.2017.06.089

250. Su Q, Sun J, Wang J, Yang Z, Cheng W, Zhang S. Urea-derived graphitic carbon nitride as an efficient heterogeneous catalyst for CO_2 conversion into cyclic carbonates. Catal Sci Technol. 2014;4(6):1556. doi:10.1039/c3cy00921a

251. Królikowski A, Karbownicka B, Jaklewicz O. Anodic dissolution of amorphous Ni–P alloys. Electrochim Acta. 2006 Aug;51(27):6120–7. doi:10.1016/j.electacta.2006.01.070

252. Jiao Y, Zheng Y, Jaroniec M, Qiao SZ. Design of electrocatalysts for oxygen- and hydrogen-involving energy conversion reactions. Chem Soc Rev. 2015;44(8):2060–86. doi:10.1039/C4CS00470A

253. Chen J, Sun T, Liu J, Yu H, Zang Q, Yuan T, et al. Recent Advances on Transition Metal Sulfides for Key Components of Lithium–Sulfur Batteries. Advanced Science. 2025 Oct 14;12(40). doi:10.1002/advs.202512191

254. Zhong G, Huang J, Yao Z, Luo B, Li K, Xu S, et al. Intrinsic acid resistance and high removal performance from the incorporation of nickel nanoparticles into nitrogen doped tubular carbons for environmental remediation. J Colloid Interface Sci. 2020 Apr;566:46–59. doi:10.1016/j.jcis.2020.01.055

255. Wang X, Niu J, Yang L, Guo X, Yu X, Yao B. Recent Advances on g-C_3N_4 Based Photocatalysts for Typical Antibiotics Photodegradation: Preparation, Mechanism and Influencing Factors. ChemistrySelect. 2023 Dec 18;8(47). doi:10.1002/slct.202301936

256. Blachnio M, Zienkiewicz-Strzalka M, Derylo-Marczewska A. Analysis of Physical Processes in Confined Pores of Activated Carbons with Uniform Porosity. Materials. 2026 Jan 4;19(1):191. doi:10.3390/ma19010191

257. Sevilla M, Mokaya R. Energy storage applications of activated carbons: supercapacitors and hydrogen storage. Energy Environ Sci. 2014;7(4):1250–80. doi:10.1039/C3EE43525C

258. Zhu J, Li Y, Kang S, Wei XL, Shen PK. One-step synthesis of Ni_3S_2 nanoparticles wrapped with in situ generated nitrogen-self-doped graphene sheets with highly improved electrochemical properties in Li-ion batteries. J Mater Chem A Mater. 2014;2(9):3142. doi:10.1039/c3ta14562j

259. Liu W, Zhang S, Almalki ASA, Fallatah AM, El-Bahy ZM, Ren J, et al. In Situ Synthesis of Honeycomb Nanorods Ni_3S_2 @NiCo-Layered-Double Hydroxide/Nickel

Foam Electrocatalysts with High Performance Electrocatalytic Hydrogen Production. ACS Appl Energy Mater. 2024 Oct 28;7(20):9223–31. doi:10.1021/acsaem.4c01501

260. Voiry D, Mohite A, Chhowalla M. Phase engineering of transition metal dichalcogenides. Chem Soc Rev. 2015;44(9):2702–12. doi:10.1039/C5CS00151J

261. Zhou W, Zhao J, Guan J, Wu M, Li GR. Ni_3S_2 in Situ Grown on Ni Foam Coupled with Nitrogen-Doped Carbon Nanotubes as an Efficient Electrocatalyst for the Hydrogen Evolution Reaction in Alkaline Solution. ACS Omega. 2019 Dec 3;4(23):20244–51. doi:10.1021/acsomega.9b02555

262. Qin S, Lei J, Xiong Y, Xu X, Geng X, Wang J. Synthesis of $Ni_{4.5}Fe_{4.5}S_8/Ni_3S_2$ film on Ni_3 Fe alloy foam as an excellent electrocatalyst for the oxygen evolution reaction. RSC Adv. 2019;9(18):10231–6. doi:10.1039/C9RA00724E

263. Zhang X, Guo L, Huang S, Han D. Three-Dimensional Nickel Foam-Based Lithiophilic LPP-Ni_3S_2@Ni Current Collector for Dendrite-Free Lithium Anode. Nanomaterials. 2024 Jul 7;14(13):1158. doi:10.3390/nano14131158

264. Peng Y, He H. Novel heterostructure Cu_2S/Ni_3S_2 coral-like nanoarrays on Ni foam to enhance hydrogen evolution reaction in alkaline media. RSC Adv. 2021;11(62):39493–502. doi:10.1039/D1RA07514D

265. Grosvenor AP, Biesinger MC, Smart RStC, McIntyre NS. New interpretations of XPS spectra of nickel metal and oxides. Surf Sci. 2006 May;600(9):1771–9. doi:10.1016/j.susc.2006.01.041

266. Mahala C, Devi Sharma M, Basu M. Fe-Doped Nickel Hydroxide/Nickel Oxyhydroxide Function as an Efficient Catalyst for the Oxygen Evolution Reaction. ChemElectroChem. 2019 Jul 10;6(13):3488–98. doi:10.1002/celc.201900857

267. Zhang Y, Chen C, Zheng QH, Guo ZK, Dong BX, Teng YL. S-Doped Ni ^{II} -Triazolate Derived Ni–S–C Catalyst for Electrochemical CO_2 Reduction to CO. ACS Appl Energy Mater. 2023 Sep 25;6(18):9065–73. doi:10.1021/acsaem.2c02333

268. Zhao X, Huang S, Chen Z, Lu C, Han S, Ke C, et al. Carbon nanosheets supporting Ni–N3S single-atom sites for efficient electrocatalytic CO_2 reduction. Carbon N Y. 2021 Jun;178:488–96. doi:10.1016/j.carbon.2021.03.017

269. Meyerson ML, Rosenberg SG, Wygant BR. Analysis of nickel sulfoselenide materials by XPS. Surface Science Spectra. 2024 Dec 1;31(2). doi:10.1116/6.0004063

270. Hu Q, Bai Y, Fang Y, Guo L, Li W. Acid- and alkaline-induced phase and structure reconstruction of nickel sulfide toward enhanced electrochemical performance. CrystEngComm. 2024;26(38):5393–404. doi:10.1039/D4CE00631C

271. Piontek S, junge Puring K, Siegmund D, Smialkowski M, Sinev I, Tetzlaff D, et al. Bio-inspired design: bulk iron–nickel sulfide allows for efficient solvent-dependent CO_2 reduction. Chem Sci. 2019;10(4):1075–81. doi:10.1039/C8SC03555E

272. Chen D, Yang S, Gao J, Zheng X, Mao J, Hu Q, et al. Electrochemical co-upgrading CO_2 and glycerol for selective formate production with 190% overall Faradaic efficiency. Nano Res. 2025 May;18(5):94907399. doi:10.26599/NR.2025.94907399

273. Hao S, Liu J, Cao Q, Zhao Y, Zhao X, Pei K, et al. In-situ electrochemical pretreatment of hierarchical Ni_3S_2-based electrocatalyst towards promoted hydrogen evolution reaction with low overpotential. J Colloid Interface Sci. 2020 Feb;559:282–90. doi:10.1016/j.jcis.2019.09.088

274. Wang SM, Yuan X, Zhou S, Li X, Han SG, Lin W, et al. Single-atomic-Ni electrocatalyst derived from phthalocyanine-modified MOF for convoying CO_2 intelligent utilization. Energy Materials. 2024 Apr 9;4(2). doi:10.20517/energymater.2023.123

275. Jeon YE, Hong J, An BS, Kim HY, Kim C, Lee J, et al. N, S-coordinated Ni single-atom catalysts for efficient CO_2 reduction in a zero-gap membrane electrode assembly electrolyzer. Mater Today Energy. 2024 Dec;46:101706. doi:10.1016/j.mtener.2024.101706

276. Sun X, Wang L, Lan X, Lu Q, Tuo Y, Ye C, et al. Positively charged nickel-sulfur dual sites for efficient CO_2 electroreduction reaction. Appl Catal B. 2024 Mar;342:123389. doi:10.1016/j.apcatb.2023.123389

277. Hicks MH, Nie W, Boehme AE, Atwater HA, Agapie T, Peters JC. Electrochemical CO_2 Reduction in Acidic Electrolytes: Spectroscopic Evidence for Local pH Gradients. J Am Chem Soc. 2024 Sep 11;146(36):25282–9. doi:10.1021/jacs.4c09512

278. Wu W, Xu L, Lu Q, Sun J, Xu Z, Song C, et al. Addressing the Carbonate Issue: Electrocatalysts for Acidic CO_2 Reduction Reaction. Advanced Materials. 2025 Jan 17;37(2). doi:10.1002/adma.202312894

279. Zeng M, Fang W, Cen Y, Zhang X, Hu Y, Xia BY. Reaction Environment Regulation for Electrocatalytic CO_2 Reduction in Acids. Angew Chem Int Ed. 2024 Jun 21;63(26). doi:10.1002/anie.202404574

280. Wei S, Hua H, Zhao Y, Luo J. Porous membranes enable selective and stable zero-gap acidic CO_2 electrolysers. Nat Commun. 2025 Oct 21;16(1):9299. doi:10.1038/s41467-025-64342-w

281. Zhao Z, Li M, Zhang L, Dai L, Xia Z. Design Principles for Heteroatom-Doped Carbon Nanomaterials as Highly Efficient Catalysts for Fuel Cells and Metal–Air Batteries. Advanced Materials. 2015 Nov 29;27(43):6834–40. doi:10.1002/adma.201503211

282. Zhang X, Lyu D, Mollamahale YB, Yu F, Qing M, Yin S, et al. Critical role of iron carbide nanodots on 3D graphene based nonprecious metal catalysts for enhancing oxygen reduction reaction. Electrochim Acta. 2018 Aug;281:502–9. doi:10.1016/j.electacta.2018.05.206

283. Jung N, Chung DY, Ryu J, Yoo SJ, Sung YE. Pt-based nanoarchitecture and catalyst design for fuel cell applications. Nano Today. 2014 Aug;9(4):433–56. doi:10.1016/j.nantod.2014.06.006

284. Fu Y, Zhao Q, Wei Q, Bowen CR, Wong WY, Yang W. Non-precious metal-based single-atom catalysts for oxygen reduction reaction: fundamentals and applications. Materials Science and Engineering: R: Reports. 2024 Sep;160:100822. doi:10.1016/j.mser.2024.100822

285. Xia W, Mahmood A, Liang Z, Zou R, Guo S. Earth-Abundant Nanomaterials for Oxygen Reduction. Angew Chem Int Ed. 2016 Feb 18;55(8):2650–76. doi:10.1002/anie.201504830

286. Wu G, Zelenay P. Nanostructured Nonprecious Metal Catalysts for Oxygen Reduction Reaction. Acc Chem Res. 2013 Aug 20;46(8):1878–89. doi:10.1021/ar400011z

287. Kim JH, Sa YJ, Jeong HY, Joo SH. Roles of Fe−N_x and Fe−Fe_3C@C Species in Fe−N/C Electrocatalysts for Oxygen Reduction Reaction. ACS Appl Mater Interfaces. 2017 Mar 22;9(11):9567–75. doi:10.1021/acsami.6b13417

288. Liu M, Yin X, Guo X, Hu L, Yuan H, Wang G, et al. High efficient oxygen reduction performance of Fe/Fe_3C nanoparticles in situ encapsulated in nitrogen-doped carbon via a novel microwave-assisted carbon bath method. Nano Materials Science. 2019 Jun;1(2):131–6. doi:10.1016/j.nanoms.2019.04.003

289. Faubert G, Côté R, Dodelet JP, Lefèvre M, Bertrand P. Oxygen reduction catalysts for polymer electrolyte fuel cells from the pyrolysis of FeII acetate adsorbed on 3,4,9,10-perylenetetracarboxylic dianhydride. Electrochim Acta. 1999 Jan;44(15):2589–603. doi:10.1016/S0013-4686(98)00382-X

290. Jaouen F, Marcotte S, Dodelet JP, Lindbergh G. Oxygen Reduction Catalysts for Polymer Electrolyte Fuel Cells from the Pyrolysis of Iron Acetate Adsorbed on Various Carbon Supports. J Phys Chem B. 2003 Feb 1;107(6):1376–86. doi:10.1021/jp021634q

291. Jaouen F, Lefèvre M, Dodelet JP, Cai M. Heat-Treated Fe/N/C Catalysts for O_2 Electroreduction: Are Active Sites Hosted in Micropores? J Phys Chem B. 2006 Mar 1;110(11):5553–8. doi:10.1021/jp057135h

292. Meng Y, Voiry D, Goswami A, Zou X, Huang X, Chhowalla M, et al. N-, O-, and S-Tridoped Nanoporous Carbons as Selective Catalysts for Oxygen Reduction and

Alcohol Oxidation Reactions. J Am Chem Soc. 2014 Oct 1;136(39):13554–7. doi:10.1021/ja507463w

293. Kramm UI, Herranz J, Larouche N, Arruda TM, Lefèvre M, Jaouen F, et al. Structure of the catalytic sites in Fe/N/C-catalysts for O_2-reduction in PEM fuel cells. Physical Chemistry Chemical Physics. 2012;14(33):11673. doi:10.1039/c2cp41957b

294. Wei X, Song S, Wu N, Luo X, Zheng L, Jiao L, et al. Synergistically enhanced single-atomic site Fe by Fe_3C@C for boosted oxygen reduction in neutral electrolyte. Nano Energy. 2021 Jun;84:105840. doi:10.1016/j.nanoen.2021.105840

295. Jiang WJ, Gu L, Li L, Zhang Y, Zhang X, Zhang LJ, et al. Understanding the High Activity of Fe–N–C Electrocatalysts in Oxygen Reduction: Fe/Fe_3C Nanoparticles Boost the Activity of $Fe–N_x$. J Am Chem Soc. 2016 Mar 16;138(10):3570–8. doi:10.1021/jacs.6b00757

296. Peera SG, Koutavarapu R, Prasada Reddy PS, Koyyada G, Alodhayb AN, Pandiaraj S, et al. Effect of N-Doped Carbon on the Morphology and Oxygen Reduction Reaction (ORR) Activity of a Xerogel-Derived Mn(II)O Electrocatalyst. Catalysts. 2024 Nov 6;14(11):792. doi:10.3390/catal14110792

297. Feng L, Yang L, Huang Z, Luo J, Li M, Wang D, et al. Enhancing Electrocatalytic Oxygen Reduction on Nitrogen-Doped Graphene by Active Sites Implantation. Sci Rep. 2013 Nov 22;3(1):3306. doi:10.1038/srep03306

298. Muhyuddin M, Berretti E, Mirshokraee SA, Orsilli J, Lorenzi R, Capozzoli L, et al. Formation of the active site structures during pyrolysis transformation of Fe-phthalocyanine into $Fe-N_x$-C electrocatalysts for the oxygen reduction reaction. Appl Catal B. 2024 Apr;343:123515. doi:10.1016/j.apcatb.2023.123515

299. Tan F, Li W, Wang J, Min C, Li Z, Zhang B, et al. Clarifying the critical roles of iron in boosting oxygen reduction: Single Fe atoms anchored on carbon vacancies as efficient active sites. Appl Catal B. 2022 May;305:121035. doi:10.1016/j.apcatb.2021.121035

300. Huang Y, Liu K, Kan S, Liu P, Hao R, Liu W, et al. Highly dispersed Fe-Nx active sites on Graphitic-N dominated porous carbon for synergetic catalysis of oxygen reduction reaction. Carbon N Y. 2021 Jan;171:1–9. doi:10.1016/j.carbon.2020.09.010

301. Jiang WJ, Gu L, Li L, Zhang Y, Zhang X, Zhang LJ, et al. Understanding the High Activity of Fe–N–C Electrocatalysts in Oxygen Reduction: Fe/Fe_3C Nanoparticles Boost the Activity of $Fe–N_x$. J Am Chem Soc. 2016 Mar 16;138(10):3570–8. doi:10.1021/jacs.6b00757

302. Zhang X, Lyu D, Mollamahale YB, Yu F, Qing M, Yin S, et al. Critical role of iron carbide nanodots on 3D graphene based nonprecious metal catalysts for enhancing

oxygen reduction reaction. Electrochim Acta. 2018 Aug;281:502–9. doi:10.1016/j.electacta.2018.05.206

303. Huang Z, Pan H, Yang W, Zhou H, Gao N, Fu C, et al. *In Situ* Self-Template Synthesis of Fe–N-Doped Double-Shelled Hollow Carbon Microspheres for Oxygen Reduction Reaction. ACS Nano. 2018 Jan 23;12(1):208–16. doi:10.1021/acsnano.7b05832

304. Wang X, Zhu H, Yang C, Lu J, Zheng L, Liang HP. Mesoporous carbon promoting the efficiency and stability of single atomic electrocatalysts for oxygen reduction reaction. Carbon N Y. 2022 May;191:393–402. doi:10.1016/j.carbon.2022.01.057

305. Li R, Wen X, Zhao Y, Fan S, Wei Q, Lan K. Metal-based mesoporous frameworks as high-performance platforms in energy storage and conversion. Energy Reviews. 2025 Mar;4(1):100108. doi:10.1016/j.enrev.2024.100108

306. Zhao XS, Su F, Yan Q, Guo W, Bao XY, Lv L, et al. Templating methods for preparation of porous structures. J Mater Chem. 2006;16(7):637–48. doi:10.1039/B513060C

307. Ghaedi H, Zhao M. Review on Template Removal Techniques for Synthesis of Mesoporous Silica Materials. Energy & Fuels. 2022 Mar 3;36(5):2424–46. doi:10.1021/acs.energyfuels.1c04435

308. Hiraide S, Yamada M, Kataoka S, Inagi Y, Endo A. Time evolution of the framework structure of SBA-15 during the aging process. Colloids Surf A Physicochem Eng Asp. 2019 Dec;583:123807. doi:10.1016/j.colsurfa.2019.123807

309. Abbaspour S, Nourbakhsh AA, Kalbasi RJ, Mackenzie KJD. Investigating the Properties of the Nanocomposite (poly(4-vinyl pyridine)/Al-SBA-15): A Precursor for β-SiAlON. Molecular Crystals and Liquid Crystals. 2012 Apr 5;555(1):104–11. doi:10.1080/15421406.2012.635078

310. Zholobenko VL, Khodakov AY, Impéror-Clerc M, Durand D, Grillo I. Initial stages of SBA-15 synthesis: An overview. Adv Colloid Interface Sci. 2008 Oct;142(1–2):67–74. doi:10.1016/j.cis.2008.05.003

311. Parant H, Muller G, Le Mercier T, Tarascon JM, Poulin P, Colin A. Flowing suspensions of carbon black with high electronic conductivity for flow applications: Comparison between carbons black and exhibition of specific aggregation of carbon particles. Carbon N Y. 2017 Aug;119:10–20. doi:10.1016/j.carbon.2017.04.014

312. Ferrari AC, Basko DM. Raman spectroscopy as a versatile tool for studying the properties of graphene. Nat Nanotechnol. 2013 Apr 4;8(4):235–46. doi:10.1038/nnano.2013.46

313. Tuinstra F, Koenig JL. Raman Spectrum of Graphite. J Chem Phys. 1970 Aug 1;53(3):1126–30. doi:10.1063/1.1674108

314. Cançado LG, Jorio A, Ferreira EHM, Stavale F, Achete CA, Capaz RB, et al. Quantifying Defects in Graphene via Raman Spectroscopy at Different Excitation Energies. Nano Lett. 2011 Aug 10;11(8):3190–6. doi:10.1021/nl201432g

315. Ferrari AC, Meyer JC, Scardaci V, Casiraghi C, Lazzeri M, Mauri F, et al. Raman Spectrum of Graphene and Graphene Layers. Phys Rev Lett. 2006 Oct 30;97(18):187401. doi:10.1103/PhysRevLett.97.187401

316. Dong C, Campell AS, Eldawud R, Perhinschi G, Rojanasakul Y, Dinu CZ. Effects of acid treatment on structure, properties and biocompatibility of carbon nanotubes. Appl Surf Sci. 2013 Jan;264:261–8. doi:10.1016/j.apsusc.2012.09.180

317. Jun S, Joo SH, Ryoo R, Kruk M, Jaroniec M, Liu Z, et al. Synthesis of New, Nanoporous Carbon with Hexagonally Ordered Mesostructure. J Am Chem Soc. 2000 Nov 1;122(43):10712–3. doi:10.1021/ja002261e

318. Ryoo R, Joo SH, Jun S. Synthesis of Highly Ordered Carbon Molecular Sieves via Template-Mediated Structural Transformation. J Phys Chem B. 1999 Sep 1;103(37):7743–6. doi:10.1021/jp991673a

319. Shu C, Song B, Wei X, Liu Y, Tan Q, Chong S, et al. Mesoporous 3D nitrogen-doped yolk-shelled carbon spheres for direct methanol fuel cells with polymer fiber membranes. Carbon N Y. 2018 Apr;129:613–20. doi:10.1016/j.carbon.2017.12.049

320. Sevilla M, Fuertes AB. The production of carbon materials by hydrothermal carbonization of cellulose. Carbon N Y. 2009 Aug;47(9):2281–9. doi:10.1016/j.carbon.2009.04.026

321. Zhao D, Feng J, Huo Q, Melosh N, Fredrickson GH, Chmelka BF, et al. Triblock Copolymer Syntheses of Mesoporous Silica with Periodic 50 to 300 Angstrom Pores. Science (1979). 1998 Jan 23;279(5350):548–52. doi:10.1126/science.279.5350.548

322. Fei H, Dong J, Feng Y, Allen CS, Wan C, Volosskiy B, et al. General synthesis and definitive structural identification of MN_4C_4 single-atom catalysts with tunable electrocatalytic activities. Nat Catal. 2018 Jan 8;1(1):63–72. doi:10.1038/s41929-017-0008-y

323. SERP, PHILIPPE. “9 Carbon Nanotubes and.” Carbon Materials for Catalysis (2008): 309.

324. Liang B, Zhu P, Gu J, Yuan W, Xiao B, Hu H, et al. Advancing Adsorption and Separation with Modified SBA-15: A Comprehensive Review and Future Perspectives. Molecules. 2024 Jul 27;29(15):3543. doi:10.3390/molecules29153543

325. Santori PG, Speck FD, Cherevko S, Firouzjaie HA, Peng X, Mustain WE, et al. High Performance FeNC and Mn-oxide/FeNC Layers for AEMFC Cathodes. J Electrochem Soc. 2020 Jan 10;167(13):134505. doi:10.1149/1945-7111/abb7e0

326. Zhou Y, Yu Y, Ma D, Foucher AC, Xiong L, Zhang J, et al. Atomic Fe Dispersed Hierarchical Mesoporous Fe–N–C Nanostructures for an Efficient Oxygen Reduction Reaction. ACS Catal. 2021 Jan 1;11(1):74–81. doi:10.1021/acscatal.0c03496

327. Mao K, Yang L, Wang X, Wu Q, Hu Z. Identifying Iron–Nitrogen/Carbon Active Structures for Oxygen Reduction Reaction under the Effect of Electrode Potential. J Phys Chem Lett. 2020 Apr 16;11(8):2896–901. doi:10.1021/acs.jpclett.0c00428

328. Liu YL, Xu XY, Shi CX, Ye XW, Sun PC, Chen TH. Iron–nitrogen co-doped hierarchically mesoporous carbon spheres as highly efficient electrocatalysts for the oxygen reduction reaction. RSC Adv. 2017;7(15):8879–85. doi:10.1039/C6RA26917F

329. Zitolo A, Ranjbar-Sahraie N, Mineva T, Li J, Jia Q, Stamatin S, et al. Identification of catalytic sites in cobalt-nitrogen-carbon materials for the oxygen reduction reaction. Nat Commun. 2017 Oct 16;8(1):957. doi:10.1038/s41467-017-01100-7

330. Li J, Ghoshal S, Liang W, Sougrati MT, Jaouen F, Halevi B, et al. Structural and mechanistic basis for the high activity of Fe–N–C catalysts toward oxygen reduction. Energy Environ Sci. 2016;9(7):2418–32. doi:10.1039/C6EE01160H

331. Watts JF, Wolstenholme J. An Introduction to Surface Analysis by XPS and AES. Wiley; 2003. doi:10.1002/0470867930

332. Seah MP. Reference data for Auger electron spectroscopy and X-ray photoelectron spectroscopy combined. Appl Surf Sci. 1999 Apr;144–145:161–7. doi:10.1016/S0169-4332(98)00788-0

333. Ryoo R, Joo SH, Jun S. Synthesis of Highly Ordered Carbon Molecular Sieves via Template-Mediated Structural Transformation. J Phys Chem B. 1999 Sep 1;103(37):7743–6. doi:10.1021/jp991673a

334. Ferrari AC, Robertson J. Interpretation of Raman spectra of disordered and amorphous carbon. Phys Rev B. 2000 May 15;61(20):14095–107. doi:10.1103/PhysRevB.61.14095

335. Hantsche H. High resolution XPS of organic polymers, the scienta ESCA300 database. By G. Beamson and D. Briggs, Wiley, Chichester 1992, 295 pp., hardcover, £ 65.00, ISBN 0-471-93592-1. Advanced Materials. 1993 Oct 29;5(10):778–778. doi:10.1002/adma.19930051035

336. Hüfner S. Photoelectron Spectroscopy. Berlin, Heidelberg: Springer Berlin Heidelberg; 2003. doi:10.1007/978-3-662-09280-4

337. Sevilla M, Mokaya R. Energy storage applications of activated carbons: supercapacitors and hydrogen storage. Energy Environ Sci. 2014;7(4):1250–80. doi:10.1039/C3EE43525C

338. Biniak S, Szymański G, Siedlewski J, Świątkowski A. The characterization of activated carbons with oxygen and nitrogen surface groups. Carbon N Y. 1997;35(12):1799–810. doi:10.1016/S0008-6223(97)00096-1

339. Lefèvre M, Proietti E, Jaouen F, Dodelet JP. Iron-Based Catalysts with Improved Oxygen Reduction Activity in Polymer Electrolyte Fuel Cells. Science (1979). 2009 Apr 3;324(5923):71–4. doi:10.1126/science.1170051

340. Kundu S, Xia W, Busser W, Becker M, Schmidt DA, Havenith M, et al. The formation of nitrogen-containing functional groups on carbon nanotube surfaces: a quantitative XPS and TPD study. Physical Chemistry Chemical Physics. 2010;12(17):4351. doi:10.1039/b923651a

341. Zitolo A, Goellner V, Armel V, Sougrati MT, Mineva T, Stievano L, et al. Identification of catalytic sites for oxygen reduction in iron- and nitrogen-doped graphene materials. Nat Mater. 2015 Sep 10;14(9):937–42. doi:10.1038/nmat4367

342. Sa YJ, Seo DJ, Woo J, Lim JT, Cheon JY, Yang SY, et al. A General Approach to Preferential Formation of Active Fe–N_x Sites in Fe–N/C Electrocatalysts for Efficient Oxygen Reduction Reaction. J Am Chem Soc. 2016 Nov 16;138(45):15046–56. doi:10.1021/jacs.6b09470

343. Biesinger MC, Payne BP, Grosvenor AP, Lau LWM, Gerson AR, Smart RStC. Resolving surface chemical states in XPS analysis of first row transition metals, oxides and hydroxides: Cr, Mn, Fe, Co and Ni. Appl Surf Sci. 2011 Jan;257(7):2717–30. doi:10.1016/j.apsusc.2010.10.051

344. Grosvenor AP, Kobe BA, Biesinger MC, McIntyre NS. Investigation of multiplet splitting of Fe 2p XPS spectra and bonding in iron compounds. Surface and Interface Analysis. 2004 Dec 7;36(12):1564–74. doi:10.1002/sia.1984

345. Yamashita T, Hayes P. Analysis of XPS spectra of Fe^{2+} and Fe^{3+} ions in oxide materials. Appl Surf Sci. 2008 Feb;254(8):2441–9. doi:10.1016/j.apsusc.2007.09.063

346. Jaouen F, Lefèvre M, Dodelet JP, Cai M. Heat-Treated Fe/N/C Catalysts for O_2 Electroreduction: Are Active Sites Hosted in Micropores? J Phys Chem B. 2006 Mar 1;110(11):5553–8. doi:10.1021/jp057135h

347. Carbon materials for catalysis. Focus on Catalysts. 2009 Aug;2009(8):8. doi:10.1016/S1351-4180(09)70357-5

348. Walker PL, Rusinko F, Austin LG. Gas Reactions of Carbon. In. 1959. p. 133–221. doi:10.1016/S0360-0564(08)60418-6

349. Zhang L, Chen Y, Zhao P, Luo W, Chen S, Shao M. Fe_3C Nanorods Encapsulated in N-Doped Carbon Nanotubes as Active Electrocatalysts for Hydrogen Evolution Reaction. Electrocatalysis. 2018 Mar 6;9(2):264–70. doi:10.1007/s12678-017-0425-3

350. Gianola G, Cosenza A, Roiron C, Pirri CF, Specchia S, Atanassov P, et al. Effect of silica leaching treatment during template-assisted synthesis on the performance of FeNC catalysts for oxygen reduction reaction. Electrochim Acta. 2025 Jun;525:146085. doi:10.1016/j.electacta.2025.146085

351. Gianola G, Lourenço MAO, Basile L, Morais T, Mafra L, Pirri C, et al. Pore structure engineering *via* hard-template synthesis: unlocking the high oxygen reduction reaction activity and stability of Fe–N@C electrocatalysts. Nanoscale Horiz. 2025;10(9):1975–87. doi:10.1039/D5NH00300H

352. Irmawati Y, Prakoso B, Balqis F, Indriyati, Yudianti R, Iskandar F, et al. Advances and Perspective of Noble-Metal-Free Nitrogen-Doped Carbon for pH-Universal Oxygen Reduction Reaction Catalysts. Energy & Fuels. 2023 Apr 6;37(7):4858–77. doi:10.1021/acs.energyfuels.2c04272

353. Yang L, Shui J, Du L, Shao Y, Liu J, Dai L, et al. Carbon-Based Metal-Free ORR Electrocatalysts for Fuel Cells: Past, Present, and Future. Advanced Materials. 2019 Mar 13;31(13). doi:10.1002/adma.201804799

354. Irmawati Y, Prakoso B, Balqis F, Indriyati, Yudianti R, Iskandar F, et al. Advances and Perspective of Noble-Metal-Free Nitrogen-Doped Carbon for pH-Universal Oxygen Reduction Reaction Catalysts. Energy & Fuels. 2023 Apr 6;37(7):4858–77. doi:10.1021/acs.energyfuels.2c04272

355. Rojas-Carbonell S, Artyushkova K, Serov A, Santoro C, Matanovic I, Atanassov P. Effect of pH on the Activity of Platinum Group Metal-Free Catalysts in Oxygen Reduction Reaction. ACS Catal. 2018 Apr 6;8(4):3041–53. doi:10.1021/acscatal.7b03991

356. Wan K, Yu Z peng, Li X hua, Liu M yao, Yang G, Piao J hua, et al. pH Effect on Electrochemistry of Nitrogen-Doped Carbon Catalyst for Oxygen Reduction Reaction. ACS Catal. 2015 Jul 2;5(7):4325–32. doi:10.1021/acscatal.5b01089

357. Wan K, Yu Z peng, Li X hua, Liu M yao, Yang G, Piao J hua, et al. pH Effect on Electrochemistry of Nitrogen-Doped Carbon Catalyst for Oxygen Reduction Reaction. ACS Catal. 2015 Jul 2;5(7):4325–32. doi:10.1021/acscatal.5b01089

358. Li X, Liu G, Popov BN. Activity and stability of non-precious metal catalysts for oxygen reduction in acid and alkaline electrolytes. J Power Sources. 2010 Oct;195(19):6373–8. doi:10.1016/j.jpowsour.2010.04.019

359. Herranz J, Jaouen F, Lefèvre M, Kramm UI, Proietti E, Dodelet JP, et al. Unveiling N-Protonation and Anion-Binding Effects on Fe/N/C Catalysts for O_2 Reduction in Proton-Exchange-Membrane Fuel Cells. The Journal of Physical Chemistry C. 2011 Aug 18;115(32):16087–97. doi:10.1021/jp2042526

360. Herranz J, Jaouen F, Lefèvre M, Kramm UI, Proietti E, Dodelet JP, et al. Unveiling N-Protonation and Anion-Binding Effects on Fe/N/C Catalysts for O_2 Reduction in Proton-Exchange-Membrane Fuel Cells. The Journal of Physical Chemistry C. 2011 Aug 18;115(32):16087–97. doi:10.1021/jp2042526

361. Gianola G, Cosenza A, Roiron C, Pirri CF, Specchia S, Atanassov P, et al. Effect of silica leaching treatment during template-assisted synthesis on the performance of FeNC catalysts for oxygen reduction reaction. Electrochim Acta. 2025 Jun;525:146085. doi:10.1016/j.electacta.2025.146085

362. Gianola G, Lourenço MAO, Basile L, Morais T, Mafra L, Pirri C, et al. Pore structure engineering *via* hard-template synthesis: unlocking the high oxygen reduction reaction activity and stability of Fe–N@C electrocatalysts. Nanoscale Horiz. 2025;10(9):1975–87. doi:10.1039/D5NH00300H

363. Ge X, Sumboja A, Wuu D, An T, Li B, Goh FWT, et al. Oxygen Reduction in Alkaline Media: From Mechanisms to Recent Advances of Catalysts. ACS Catal. 2015 Aug 7;5(8):4643–67. doi:10.1021/acscatal.5b00524

364. Zhu Q, Xiang T, Chen C, Zhang J, Wu Z, Rao S, et al. Enhancing activity and stability of Fe N C catalysts through co incorporation for oxygen reduction reaction. J Colloid Interface Sci. 2024 Jun;663:53–60. doi:10.1016/j.jcis.2024.02.144

365. Liu C, Yang R, Wang J, Liu B, Chang X, Feng P, et al. Synergistic Catalysts with Fe Single Atoms and Fe $_3$ C Clusters for Accelerated Oxygen Adsorption Kinetics in Oxygen Reduction Reaction. Angew Chem Int Ed. 2025 May 19;64(21). doi:10.1002/anie.202501266

366. Kim JH, Sa YJ, Jeong HY, Joo SH. Roles of Fe−N_x and Fe−Fe_3C@C Species in Fe−N/C Electrocatalysts for Oxygen Reduction Reaction. ACS Appl Mater Interfaces. 2017 Mar 22;9(11):9567–75. doi:10.1021/acsami.6b13417

367. Karuppannan M, Park JE, Bae HE, Cho YH, Kwon OJ. A nitrogen and fluorine enriched Fe/Fe $_3$ C@C oxygen reduction reaction electrocatalyst for anion/proton exchange membrane fuel cells. Nanoscale. 2020;12(4):2542–54. doi:10.1039/C9NR08631E

368. Hou Y, Huang T, Wen Z, Mao S, Cui S, Chen J. Metal−Organic Framework-Derived Nitrogen-Doped Core-Shell-Structured Porous Fe/Fe_3C@C Nanoboxes Supported on Graphene Sheets for Efficient Oxygen Reduction Reactions. Adv Energy Mater. 2014 Aug 4;4(11). doi:10.1002/aenm.201400337

369. Liu M, Guo X, Hu L, Yuan H, Wang G, Dai B, et al. Fe_3O_4 /Fe_3C@Nitrogen-Doped Carbon for Enhancing Oxygen Reduction Reaction. ChemNanoMat. 2019 Feb 7;5(2):187–93. doi:10.1002/cnma.201800432

370. Gandionco KA, Kim J, Bekaert L, Hubin A, Lim J. Single-atom catalysts for the electrochemical reduction of carbon dioxide into hydrocarbons and oxygenates. Carbon Energy. 2024 Mar 6;6(3). doi:10.1002/cey2.410

371. Zafar A, Shanmugam S, Zhang X. Single Atom Catalysts for Electrochemical CO_2 Reduction Reaction: Synthetic Strategies and Mechanistic Insights. Small. 2025 Sep 31;21(37). doi:10.1002/smll.202507483